

EXPERIMENTAL TWO-PHASE FLUID FLOW IN MICROCHANNELS

THÈSE N° 3437 (2005)

PRÉSENTÉE À LA FACULTÉ SCIENCES ET TECHNIQUES DE L'INGÉNIEUR

Institut des sciences de l'énergie

SECTION DE GÉNIE MÉCANIQUE

ÉCOLE POLYTECHNIQUE FÉDÉRALE DE LAUSANNE

POUR L'OBTENTION DU GRADE DE DOCTEUR ÈS SCIENCES

PAR

Rémi REVELLIN

ingénieur INSA Lyon, France
de nationalité française

acceptée sur proposition du jury:

Prof. J. Thome, directeur de thèse
Prof. J. Bonjour, rapporteur
Prof. M. Deville, rapporteur
Prof. M. Poniewski, rapporteur

Lausanne, EPFL
2006

Acknowledgments

This study has been carried out at the Laboratory of Heat and Mass Transfer (LTCM), Swiss Federal Institute of Technology Lausanne (EPFL), under the direction of Prof. John R. Thome. The project has been supported by the European Community's Human Potential Programme under contract HPRN-CT-2002-00204, [HMTMIC] funded by OFES, Bern, Switzerland, which are gratefully acknowledged.

I would like to thank Prof. Thome for giving me the opportunity to carry out this project in his laboratory, for his encouragement and guidance during this period. He was always available for research discussions. Finally, I would like to thank him for his careful reading of this manuscript.

I acknowledge Laurent Chevalley and Alfred Thomas who have successfully participated to the construction and maintenance of the test facility.

I also acknowledge my colleagues of the LTCM for their help and specially Bruno Agostini for his collaboration on the videos and the constructive discussions we had every day. I would like also to acknowledge Thierry Ursenbacher for his contribution to the image and video processing. Thank you also to Vincent Dupont for his help on the construction of the experimental stand.

Remerciements à mes amis pour leurs mails quotidiens, les entraînements en commun et leurs pas de danse.

J'aimerais finalement remercier mes parents, Jeanine et Gérard, pour leurs conseils avisés et leur soutien permanent ainsi que ma soeur Laurence, son mari Christophe et mes deux nièces Chloé et Candy pour leurs encouragements.

Abstract

Micro or mini heat spreaders are used in the interest of providing higher cooling capability for microtechnologies. Heat spreaders using micro or mini channels are not yet well studied, for this the fundamentals of two-phase heat transfer in microchannels are being studied. Here, a comprehensive experimental two-phase flow study has been carried out on two single round tubes ($D = 0.509$ and 0.790 mm) and for two different fluids: R-134a and R-245fa.

An optical measurement method for two-phase flow characterization in microtubes has been applied to determine the frequency of bubbles exiting a microevaporator, the coalescence rates of these bubbles and their lengths as well as their mean two-phase vapor velocity. Four principal flow patterns (bubbly flow, slug flow, semi-annular flow and annular flow) with their transitions (bubbly/slug flow and slug/semi-annular flow) were observed. A new type of flow pattern map for evaporating flow in microchannel has been developed. The first zone corresponds to the isolated bubble regime. It includes both bubbly flow or/and slug flow and is present up to the onset of coalescence. The second zone is the coalescing bubble regime. It is present up to the end of coalescence process. The third zone is the annular zone and is limited by the fourth zone of this diabatic map, the onset of critical heat flux. This flow pattern map can be used for heat transfer model and design of microevaporator.

The vapor velocity or cross sectional void fraction have been measured. For R-134a, the flow can be considered to be homogeneous (or near homogeneous). For R-245fa, more tests exhibit instabilities and surprisingly show vapor velocities below those of homogeneous flow. Frictional two-phase pressure drops have been measured over a wide range of conditions for the two microchannels and two fluids. Three regimes are distinguishable when regarding to the variation of the adiabatic frictional pressure drop with the vapor quality or the two-phase friction factor with the two-phase Reynolds number: a laminar regime for $Re_{TP} < 2000$, a transition regime for $2000 \leq Re_{TP} < 8000$ and a turbulent regime for $Re_{TP} \geq 8000$. The turbulent two-phase flows are best predicted by the Müller-Steinhagen correlation. New accurate CHF data have been measured with the test facility. A new microchannel version of the Katto - Ohno correlation has been developed to predict the CHF in circular, uniformly heated microchannels. Moreover, a new transition curve from annular flow to dryout has been proposed.

Version Abrégée

Les micro ou mini dissipateurs thermiques sont utilisés dans les microtechnologies pour leurs très hautes performances de refroidissement. Ces dissipateurs thermiques ne sont cependant pas encore suffisamment étudiés. Pour cette raison, une étude expérimentale des écoulements biphasiques a été réalisée sur deux tubes à section circulaire ($D = 0.509$ et 0.790 mm) et pour deux fluides différents : R-134a et R-245fa.

Une méthode de mesure optique a été appliquée afin de caractériser les écoulements liquide-vapeur en microtubes, en déterminant la fréquence des bulles quittant un microévaporateur, la vitesse de coalescence de ces bulles, leur longueur ainsi que leur vitesse moyenne. Quatre principaux régimes d'écoulement (écoulement à bulles, écoulement à bouchons, écoulement semi-annulaire et écoulement annulaire) avec leurs transitions (écoulement à bulles/bouchons et écoulement à bouchons/semi-annulaire) ont été observés. Une nouvelle forme de carte d'écoulement a été développée. La première zone correspond au régime d'écoulement à bulles isolées qui inclut l'écoulement à bulles et/ou l'écoulement à bouchons. Ce régime est présent jusqu'au début de la coalescence. La seconde zone est le régime de coalescence des bulles. Ce régime est présent jusqu'à la fin de la coalescence. La troisième zone est la zone annulaire, limitée par la quatrième zone qui est le début du flux de chaleur critique. Cette nouvelle carte d'écoulement peut être utilisée dans des modèles de transfert de chaleur et pour le dimensionnement de microévaporateurs.

La vitesse de la vapeur, ou indirectement le taux de vide, a été mesurée. Pour le R-134a, l'écoulement peut être considéré comme homogène (ou proche de l'homogène). Pour le R-245fa, des instabilités ont été observées et les résultats ont montré des vitesses de bulles de vapeur inférieures à celles d'un écoulement homogène.

Les pertes de charge par frottements ont été mesurées pour un grand intervalle de conditions expérimentales, en considérant les deux dimensions de tubes et les deux fluides. La variation du coefficient de frottement biphasique en fonction du nombre de Reynolds biphasique permet de distinguer trois régimes: un régime laminaire pour $Re_{TP} < 2000$, un régime de transition pour $2000 \leq Re_{TP} < 8000$ et un régime turbulent pour $Re_{TP} \geq 8000$. La corrélation de Müller-Steinhagen prédit correctement l'écoulement biphasique en régime turbulent. De nouvelles valeurs du flux de chaleur critique ont été mesurées avec le dispositif expérimental. Une nouvelle corrélation basée sur celle de Katto-Ohno a été développée pour prédire le flux de chaleur critique en microtubes circulaires uniformément chauffés. De plus, une nouvelle courbe de transition entre le régime annulaire et la zone d'assèchement est proposée.

Les résultats obtenus peuvent être directement utilisés pour développer un modèle de transfert de chaleur et de pertes de charge en microcanaux ainsi que pour dimensionner les micro dissipateurs thermiques.

Contents

| | |
|--|-------------|
| Acknowledgements | iii |
| Abstract | v |
| Version Abrégée | vii |
| List of Figures | xiv |
| List of Tables | xxii |
| Nomenclature | xxv |
| 1 Introduction | 1 |
| 2 Fundamental definitions and flow parameters | 5 |
| 2.1 Two-phase flow | 5 |
| 2.2 Vapor quality | 5 |
| 2.3 Mass flux | 6 |
| 2.4 Velocities | 6 |
| 2.4.1 True average velocities | 7 |
| 2.4.2 Superficial velocities | 7 |
| 2.4.3 Drift velocities | 7 |
| 2.5 Void fraction | 8 |
| 2.6 Definition of non-dimensional numbers | 9 |
| 2.6.1 Reynolds number | 9 |
| 2.6.2 Weber number | 10 |
| 2.6.3 Boiling number | 11 |

| | | |
|----------|--|-----------|
| 2.6.4 | Martinelli parameter | 11 |
| 2.7 | Conclusions | 12 |
| 3 | State of the Art Review | 13 |
| 3.1 | Critical heat flux | 13 |
| 3.1.1 | The Gambill and Lienhard study | 13 |
| 3.1.2 | The Katto and Ohno study | 14 |
| 3.1.3 | The Qu and Mudawar study | 15 |
| 3.1.4 | The Pribyl et al. study | 17 |
| 3.1.5 | Conclusions | 17 |
| 3.2 | Flow pattern maps | 18 |
| 3.2.1 | Flow patterns in conventional channels | 18 |
| 3.2.2 | Flow pattern maps in conventional channels | 20 |
| 3.2.3 | Flow patterns and flow pattern maps in microchannels | 23 |
| 3.2.4 | Conclusions | 31 |
| 3.3 | Void fraction | 32 |
| 3.3.1 | Homogeneous model | 32 |
| 3.3.2 | The general drift flux model of Zuber and Findlay | 32 |
| 3.3.3 | The Tripplet et al. study | 35 |
| 3.3.4 | The Serizawa et al. study | 36 |
| 3.3.5 | The Chung and Kawaji study | 36 |
| 3.3.6 | The Kawahara et al. study | 39 |
| 3.3.7 | Conclusions | 40 |
| 3.4 | Two-phase pressure drop | 42 |
| 3.4.1 | Homogeneous model | 42 |
| 3.4.2 | The separated flow model of Lockhart and Martinelli | 43 |
| 3.4.3 | The Friedel correlation | 44 |
| 3.4.4 | The Chisholm's method | 45 |
| 3.4.5 | The Mishima and Hibiki study | 46 |
| 3.4.6 | The Lee and Lee study | 48 |
| 3.4.7 | The Kawahara et al. study | 48 |

| | | |
|----------|--|-----------|
| 3.4.8 | The Lee and Mudawar study | 50 |
| 3.4.9 | The Zhang and Webb study | 53 |
| 3.4.10 | The Tran et al. study | 54 |
| 3.4.11 | The Cavallini et al. study | 55 |
| 3.4.12 | The Müller-Steinhagen and Heck study | 55 |
| 3.4.13 | Conclusions | 57 |
| 4 | Description of experiments | 59 |
| 4.1 | General description | 59 |
| 4.2 | Test section | 59 |
| 4.3 | Optical measurement technique | 61 |
| 4.4 | Measurements and accuracy | 68 |
| 4.4.1 | Diameter | 69 |
| 4.4.2 | Surface roughness | 69 |
| 4.4.3 | Microevaporator length | 70 |
| 4.4.4 | Distance between the lasers | 70 |
| 4.4.5 | Temperature | 70 |
| 4.4.6 | Fluid properties | 71 |
| 4.4.7 | Mass Flow | 72 |
| 4.4.8 | Mass flux | 72 |
| 4.4.9 | Pressure | 73 |
| 4.4.10 | Energy balance | 73 |
| 4.4.11 | Heat flux | 75 |
| 4.4.12 | Vapor quality | 77 |
| 4.4.13 | Vapor bubble velocity | 78 |
| 4.4.14 | Pressure drop | 79 |
| 4.4.15 | Inlet subcooling | 83 |
| 4.4.16 | Superficial velocities | 84 |
| 4.4.17 | Repeatability of the experiments | 84 |
| 4.5 | Conclusions on the test facility and measurement technique | 84 |
| 5 | Critical heat flux | 87 |

| | | |
|----------|---|------------|
| 5.1 | Experimental procedure | 87 |
| 5.2 | Experimental results | 87 |
| 5.3 | Correlations for saturated CHF | 91 |
| 5.4 | Flow patterns and critical quality | 93 |
| 5.5 | Conclusions from the CHF study | 94 |
| 6 | Flow patterns | 97 |
| 6.1 | Experimental procedure | 97 |
| 6.2 | Experimental flow patterns | 97 |
| 6.3 | Experimental flow pattern maps | 105 |
| 6.3.1 | Comparison with the Kattan et al. macroscale map | 109 |
| 6.3.2 | Comparison with the Triplet et al. adiabatic microscale map | 109 |
| 6.3.3 | Comparison with the Garimella et al. [22] transition line | 110 |
| 6.3.4 | Effect of the inlet subcooling | 110 |
| 6.3.5 | Effect of the saturation temperature | 110 |
| 6.3.6 | Effect of the microevaporator length | 112 |
| 6.3.7 | Effect of the tube diameter | 112 |
| 6.3.8 | Effect of the fluid | 114 |
| 6.4 | New flow pattern map for evaporating flows in microchannels | 115 |
| 6.4.1 | The isolated bubble regime to coalescing bubble regime transition | 115 |
| 6.4.2 | The coalescing bubble regime to annular regime transition | 118 |
| 6.5 | Conclusions from the flow pattern study in microchannels | 120 |
| 7 | Velocity and void fraction | 121 |
| 7.1 | Experimental velocity | 121 |
| 7.1.1 | Effect of the inlet subcooling | 122 |
| 7.1.2 | Effect of the saturation temperature | 122 |
| 7.1.3 | Effect of the microevaporator length | 122 |
| 7.1.4 | Effect of the diameter | 122 |
| 7.1.5 | Effect of the fluid | 124 |
| 7.1.6 | Velocities below homogeneous model predictions | 125 |
| 7.2 | Drift flux model applied to the vapor velocity | 126 |

| | | |
|----------|---|------------|
| 7.2.1 | R-134a results | 126 |
| 7.2.2 | R-245fa results | 128 |
| 7.3 | Experimental time averaged void fractions | 128 |
| 7.4 | Drift flux model applied to the cross sectional void fraction | 129 |
| 7.5 | Conclusions on the velocity and void fraction results | 131 |
| 8 | Adiabatic two-phase pressure drop | 133 |
| 8.1 | Experimental two-phase frictional pressure drop | 133 |
| 8.1.1 | Effect of the inlet subcooling | 134 |
| 8.1.2 | Effect of the saturation temperature | 134 |
| 8.1.3 | Effect of the microevaporator length | 137 |
| 8.1.4 | Effect of the microevaporator diameter | 137 |
| 8.1.5 | Effect of the fluid | 138 |
| 8.1.6 | The two-phase friction factor | 138 |
| 8.2 | Comparisons with existing prediction methods | 139 |
| 8.3 | New prediction method | 145 |
| 8.3.1 | Homogeneous model with a new two-phase friction factor | 145 |
| 8.3.2 | Lockhart-Martinelli model with a new C parameter | 146 |
| 8.4 | Conclusions on the adiabatic two-phase pressure drop | 150 |
| 9 | Conclusions | 151 |
| A | Fluid physical properties | 155 |
| | Bibliography | 156 |
| | Curriculum vitae | 163 |
| | Publications | 165 |

List of Figures

| | | |
|------|---|----|
| 1.1 | Schematic of three-zone evaporation model. | 2 |
| 1.2 | Elongated bubble in 2.0, 0.8 and 0.5 mm tubes. | 2 |
| 2.1 | Cross-sectional void fraction (ϵ). | 8 |
| 3.1 | Dependence of q_{max} on reduced pressure for R-245fa and R-134a. | 14 |
| 3.2 | Schematic of flow patterns in internal horizontal two-phase flow from Collier and Thome [14]. | 19 |
| 3.3 | Schematic of flow patterns in internal horizontal two-phase flow during evaporation from Collier and Thome [14]. | 20 |
| 3.4 | Schematic of flow patterns in internal vertical two-phase flow from Collier and Thome [14]. | 21 |
| 3.5 | Schematic of flow patterns in internal vertical two-phase flow during evaporation from Collier and Thome [14]. | 22 |
| 3.6 | Flow pattern map for horizontal channels of Kattan et al. [23] for R-134a, $D = 10$ mm, $T_{sat} = 30$ °C, $q = 10$ kW/m ² . (S =Stratified flow, SW =Stratified Wavy flow, I =Intermittent flow, A =Annular flow, M =Mist flow). | 22 |
| 3.7 | Flow pattern map of Suo and Griffith [47] for $\frac{\mu_L}{\mu_V} = 50$ and $\frac{Re_L^2}{We_L} = 0.75 \times 10^{-5}$ | 23 |
| 3.8 | Flow patterns of Kew and Cornwell [15, 16, 30]. | 25 |
| 3.9 | Flow pattern map for air/water in a 1.1 mm tube from Tripplet et al. [54]. | 26 |
| 3.10 | Flow patterns of Coleman and Garimella [11] study. | 27 |
| 3.11 | Flow pattern map of Coleman and Garimella [12] study for R-134a. | 28 |
| 3.12 | Flow patterns of Yang and Shieh [57] study. | 29 |
| 3.13 | Flow patterns of Serizawa et al. [44] for air/water in a 100 μ m inside diameter. | 30 |
| 3.14 | Comparison of measured void fractions of Tripplet et al. [53] with predictions of various correlations for the round tube: (a) homogeneous flow model; (b) Chexal et al. [7]; (c) Lockart-Martinelli-Butterworth [5]; (d) CISE [40]. | 37 |

| | | |
|------|--|----|
| 3.15 | Cross-sectional average void fraction of Serizawa et al. [44] in air-water two-phase flow in a 20 μm ID silica tube. | 38 |
| 3.16 | Relationship between void fraction and volumetric quality in the study of Chung and Kawaji [10]. (— Armand correlation, \cdots Homogeneous model). | 39 |
| 3.17 | Effect of ethanol concentration on the void fraction data for different diameter in the study of Kawahara et al. [29]. | 41 |
| 3.18 | Parameter C for round tubes and rectangular ducts of Mishima and Hibiki [38]. | 47 |
| 3.19 | Comparison between the new correlation and the measurements of Lee and Lee [32]. | 49 |
| 3.20 | Comparison of the two-phase frictional pressure gradient between microchannel data of Kawahara et al. [28] and homogeneous flow model predictions using different viscosity formulations. | 49 |
| 3.21 | Predictions of two-phase friction pressure gradient data of Kawahara et al. [28] by a Lockhart-Martinelli correlation with different C values. | 50 |
| 3.22 | Comparison of R-134a pressure drop data of Lee and Mudawar [33] with homogeneous equilibrium model predictions based on two-phase viscosity models by (a) McAdams, (b) Ackers, (c) Cicchitti et al. and (d) Dukler. | 51 |
| 3.23 | Comparison of R-134a pressure drop data of Lee and Mudawar [33] with separated flow model predictions based on correlations by (a) Lockhart and Martinelli, (b) Friedel, (c) Mishima and Hibiki and (d) Lee and Lee. | 52 |
| 3.24 | Comparison of new correlation predictions of Lee and Mudawar [33] with (a) R-134a data and (b) Qu and Mudawar's microchannel water data. | 53 |
| 3.25 | Predictions of two-phase pressure drop data of Zhang and Webb [58] with the Friedel correlation and the new correlation. | 54 |
| 3.26 | Predictions of two-phase pressure drop data of Tran et al. [52] with different correlations and the new correlation. | 55 |
| 3.27 | Predictions of two-phase pressure drop data of Cavallini et al. [6] with different correlations. | 56 |
| 4.1 | Photograph of the experimental stand. | 60 |
| 4.2 | Schematic of a) pump loop and b) reservoir loop. | 61 |
| 4.3 | Schematic diagram of the test section: a) front view and b) 3D view. | 62 |
| 4.4 | Photograph of the test section. | 63 |
| 4.5 | Schematic of the test section with thermocouple and pressure locations. | 63 |
| 4.6 | Schematic diagram of the laser instrumentation. | 64 |
| 4.7 | Photograph of the laser instrumentation. | 65 |

| | | |
|------|---|----|
| 4.8 | Example of (a) a voltage signal and (b) a histogram of its distribution showing the chosen thresholds for characterizing a slug flow. | 66 |
| 4.9 | Example of cross correlation of voltage signals from the two diodes. | 67 |
| 4.10 | Control element of vapor used for vapor velocity calculation. | 68 |
| 4.11 | Energy balance for $D = 0.509$ mm and different mass fluxes. | 75 |
| 4.12 | Vapor bubble velocity calculation from laser 1 for $D = 0.509$ mm, $L_{MEV} = 70.70$ mm, $T_{sat} = 30^{\circ}\text{C}$, $G = 500$ kg/m ² s and $\Delta T_{sub} = 3^{\circ}\text{C}$. Data shown are for increasing and decreasing heat flux. | 76 |
| 4.13 | Flow pattern determination from laser 1 for $D = 0.509$ mm, $L_{MEV} = 70.70$ mm, $T_{sat} = 30^{\circ}\text{C}$ and $\Delta T_{sub} = 3^{\circ}\text{C}$. Data shown are for increasing and decreasing heat flux. | 76 |
| 4.14 | Comparison between the velocity calculated from the cross correlation of the lasers with the video processing. | 80 |
| 4.15 | Effect of the distance between the lasers ($L_{adb,2}$) on the vapor bubble velocity calculation from laser 1 for $D = 0.509$ mm, $L_{MEV} = 70.70$ mm, $T_{sat} = 30^{\circ}\text{C}$, $G = 500$ kg/m ² s and $\Delta T_{sub} = 3^{\circ}\text{C}$ | 81 |
| 4.16 | Effect of the acquisition time on the bubble frequency (a) and vapor velocity (b). | 82 |
| 4.17 | Vapor velocity comparison at two different dates (29/04/2004 and 31/10/2004) from laser 1 for R-134a, $D = 0.509$ mm, $L_{MEV} = 70.70$ mm, $T_{sat} = 30^{\circ}\text{C}$ and $\Delta T_{sub} = 3^{\circ}\text{C}$ | 85 |
| 4.18 | Flow pattern map comparison at two different dates (29/04/2004 and 31/10/2004) from laser 1 for R-134a, $D = 0.509$ mm, $L_{MEV} = 70.70$ mm, $T_{sat} = 30^{\circ}\text{C}$ and $\Delta T_{sub} = 3^{\circ}\text{C}$ | 85 |
| 5.1 | Determination of CHF during a single test for R-134a, $G = 1000$ kg/m ² s, $T_{sat} = 30^{\circ}\text{C}$, $D = 0.509$ mm and $L_{MEV} = 70\text{mm}$ | 88 |
| 5.2 | CHF versus mass flux in 0.509 and 0.790 mm ID tubes for R-134a, $T_{sat} = 35^{\circ}\text{C}$, $\Delta T_{sub} = 8^{\circ}\text{C}$, $L_{MEV} = 70$ mm. | 89 |
| 5.3 | CHF versus microevaporator length in 0.509 and 0.790 mm ID tubes for R-134a, $G = 500$ kg/m ² s, $T_{sat} = 35^{\circ}\text{C}$, $\Delta T_{sub} = 8^{\circ}\text{C}$ | 89 |
| 5.4 | CHF versus microevaporator length for R-245fa and R-134a, $G = 500$ kg/m ² s, $T_{sat} = 35^{\circ}\text{C}$, $D = 0.509$ mm, $\Delta T_{sub} = 8^{\circ}\text{C}$ | 90 |
| 5.5 | Influence of the inlet subcooling at entrance to the microevaporator on CHF for R-134a, $G = 1000$ kg/m ² s, $T_{sat} = 35^{\circ}\text{C}$, $D = 0.509$ mm, $L_{MEV} = 70$ mm. | 90 |
| 5.6 | Influence of the saturation temperature on CHF for R-134a, $D = 0.509$ mm, $L_{MEV} = 70$ mm, $\Delta T_{sub} = 8^{\circ}\text{C}$ | 91 |
| 5.7 | Comparison of the experimental results to the Katto-Ohno correlation. | 92 |

| | | |
|------|--|-----|
| 5.8 | Comparison of the experimental results for R-245fa, $G = 500 \text{ kg/m}^2\text{s}$, $T_{sat} = 35^\circ\text{C}$, $D = 0.509 \text{ mm}$ and $\Delta T_{sub} = 8^\circ\text{C}$ to the Qu and Mudawar correlation. | 92 |
| 5.9 | Comparison of the experimental results to the new correlation. | 93 |
| 5.10 | Variation of the CHF as a function of critical vapor quality at constant heated length, $L_{MEV} = 70 \text{ mm}$ for $350 \leq G \leq 1500$ | 94 |
| 5.11 | Transition from annular to dryout for R-134a, $L_{MEV} = 70 \text{ mm}$ and $T_{sat} = 30^\circ\text{C}$ | 95 |
| 6.1 | FFT signals for $D = 0.509 \text{ mm}$, $L_{MEV} = 70.70 \text{ mm}$, $G = 500 \text{ kg/m}^2\text{s}$, $T_{sat} = 30^\circ\text{C}$ and $\Delta T_{sub} = 3^\circ\text{C}$ at entrance to the microevaporator. | 99 |
| 6.2 | Characterization of flow using the laser signal for $D = 0.509 \text{ mm}$, $L_{MEV} = 70.70 \text{ mm}$, $G = 500 \text{ kg/m}^2\text{s}$, $T_{sat} = 30^\circ\text{C}$ and $\Delta T_{sub} = 3^\circ\text{C}$ at entrance to the microevaporator. a) Bubble frequencies and flow patterns and b) percentage of small bubbles remaining versus vapor quality | 100 |
| 6.3 | Schematic of flow patterns and transitions. | 102 |
| 6.4 | Flow patterns and transitions for R-134a, $D = 0.509 \text{ mm}$, $L_{MEV} = 70.70 \text{ mm}$, $G = 500 \text{ kg/m}^2\text{s}$, $T_{sat} = 30^\circ\text{C}$ and $\Delta T_{sub} = 3^\circ\text{C}$ at entrance to the microevaporator. | 102 |
| 6.5 | Flow pattern laser signals for R-134a, $D = 0.509 \text{ mm}$, $L_{MEV} = 70.70 \text{ mm}$, $G = 500 \text{ kg/m}^2\text{s}$, $T_{sat} = 30^\circ\text{C}$ and $\Delta T_{sub} = 3^\circ\text{C}$ | 103 |
| 6.6 | Flow patterns and transitions for R-245fa, $D = 0.509 \text{ mm}$, $L_{MEV} = 70.70 \text{ mm}$, $G = 500 \text{ kg/m}^2\text{s}$, $T_{sat} = 35^\circ\text{C}$ and $\Delta T_{sub} = 6^\circ\text{C}$ | 104 |
| 6.7 | Flow patterns and transitions for R-134a, $D = 0.790 \text{ mm}$, $L_{MEV} = 70 \text{ mm}$, $G = 500 \text{ kg/m}^2\text{s}$, $T_{sat} = 30^\circ\text{C}$ and $\Delta T_{sub} = 3^\circ\text{C}$ | 104 |
| 6.8 | Flow pattern maps with transition lines for $D = 0.509 \text{ mm}$, $L = 70.70 \text{ mm}$, $T_{sat} = 30^\circ\text{C}$ and $\Delta T_{sub} = 3^\circ\text{C}$ using the two lasers. | 105 |
| 6.9 | Coalescence phenomena from laser 1 for $D = 0.509 \text{ mm}$, $L_{MEV} = 70.70 \text{ mm}$, $T_{sat} = 30^\circ\text{C}$ and $\Delta T_{sub} = 3^\circ\text{C}$ | 107 |
| 6.10 | Adiabatic coalescence for R-134a, $D = 0.509 \text{ mm}$, $G = 359 \text{ kg/m}^2\text{s}$, $T_{sat} = 30^\circ\text{C}$ and $x = 0.05$ taken with a high speed digital camera at 10000 Hz. | 108 |
| 6.11 | Comparison between present flow pattern transition observations from laser 1 for $D = 0.509 \text{ mm}$, $L_{MEV} = 70.70 \text{ mm}$, $T_{sat} = 30^\circ\text{C}$, $\Delta T_{sub} = 3^\circ\text{C}$ and Kattan-Thome-Favrat macroscale map in a mass flux vs. vapor quality format at the present test conditions. (B =Bubbly flow, B/S =Bubbly/slug flow, S =Slug flow, $S/S-A$ =Slug/semi-annular flow, $S-A$ =Semi-annular flow, A =Annular flow) | 109 |
| 6.12 | Comparison between present flow pattern transition observations from laser 1 for $D = 0.509 \text{ mm}$, $L_{MEV} = 70.70 \text{ mm}$, $T_{sat} = 30^\circ\text{C}$, $\Delta T_{sub} = 3^\circ\text{C}$ and Tripplet et al. transition lines available for air-water flow in a 1.097 mm tube diameter. | 110 |

| | | |
|------|--|-----|
| 6.13 | Comparison between present flow pattern transition observations from laser 1 for $D = 0.509$ mm, $L_{MEV} = 70.70$ mm, $T_{sat} = 30^{\circ}\text{C}$, $\Delta T_{sub} = 3^{\circ}\text{C}$ and Garimella et al. transition line between intermittent and non-intermittent flow available for condensation of R-134a in a 0.509 mm tube diameter. | 111 |
| 6.14 | Comparison between experimental transition lines from three different inlet subcoolings at entrance to the microevaporator from laser 1 for R-134a, $D = 0.509$ mm, $L_{MEV} = 70.70$ mm and $T_{sat} = 30^{\circ}\text{C}$ | 111 |
| 6.15 | Comparison between experimental transition lines from three different saturation temperatures from laser 1 for R-134a, $D = 0.509$ mm, $L_{MEV} = 70.70$ mm and $\Delta T_{sub} = 3^{\circ}\text{C}$ | 112 |
| 6.16 | Comparison between experimental transition lines from three different microevaporator lengths from laser 1 for R-134a, $D = 0.509$ mm, $\Delta T_{sub} = 3^{\circ}\text{C}$ and $T_{sat} = 30^{\circ}\text{C}$ | 113 |
| 6.17 | Comparison between experimental transition lines from two different inside diameters from laser 1 for R-134a, $L_{MEV} = 70.70$ mm, $T_{sat} = 30^{\circ}\text{C}$ and $\Delta T_{sub} = 3^{\circ}\text{C}$ | 113 |
| 6.18 | Comparison between experimental transition lines from two different fluids from laser 1 for $D = 0.509$ mm, $L_{MEV} = 70.70$ mm, $T_{sat} = 30^{\circ}\text{C}$ and $\Delta T_{sub} = 3^{\circ}\text{C}$ | 114 |
| 6.19 | New type of flow pattern map for evaporating flow in microchannel for $D = 0.5$ mm, $L_{MEV} = 70$ mm, $T_{sat} = 30^{\circ}\text{C}$, $q = 50$ kW/m ² and $\Delta T_{sub} = 0^{\circ}\text{C}$. IB: Isolated bubble regime, CB: Coalescing bubble regime, A: Annular regime (completely coalesced regime), PD: Post dryout regime. | 116 |
| 6.20 | Frequency A versus vapor quality for $D = 0.509$ mm, $L_{MEV} = 70.70$ mm, $T_{sat} = 30^{\circ}\text{C}$, $G = 700$ kg/m ² s and $\Delta T_{sub} = 3^{\circ}\text{C}$ | 116 |
| 6.21 | Comparison between the vapor quality from the model and the experimental vapor quality for the isolated bubble regime and coalescing bubble regime transition. | 118 |
| 6.22 | Comparison between the vapor quality from the model and the experimental vapor quality for the coalescing bubble regime and annular regime transition. | 119 |
| 7.1 | Vapor velocity versus vapor quality from laser 2 for R-134a, $D = 0.509$ mm, $L_{MEV} = 70$ mm, $T_{sat} = 30^{\circ}\text{C}$ and $\Delta T_{sub} = 3^{\circ}\text{C}$ | 121 |
| 7.2 | Influence of the inlet subcooling at entrance to the microevaporator on the vapor velocity from laser 2 for R-134a, $D = 0.509$ mm, $L_{MEV} = 70$ mm, $T_{sat} = 35^{\circ}\text{C}$ and $G = 1000$ kg/m ² s. | 122 |
| 7.3 | Influence of the saturation temperature on the vapor velocity from laser 2 for R-134a, $D = 0.509$ mm, $\Delta T_{sub} = 3^{\circ}\text{C}$, $L_{MEV} = 70$ mm and $G = 1000$ kg/m ² s. | 123 |
| 7.4 | Influence of the microevaporator length on the vapor velocity from laser 2 for R-134a, $D = 0.509$ mm, $\Delta T_{sub} = 3^{\circ}\text{C}$, $T_{sat} = 30^{\circ}\text{C}$ and $G = 500$ kg/m ² s. | 123 |

| | | |
|------|--|-----|
| 7.5 | Influence of the diameter on the vapor velocity from laser 2 for R-134a, $T_{sat} = 30^{\circ}\text{C}$, $\Delta T_{sub} = 3^{\circ}\text{C}$, $L_{MEV} = 70$ mm and $G = 350$ kg/m ² s. | 124 |
| 7.6 | Influence of the fluid on the vapor velocity from laser 2 for $T_{sat} = 35^{\circ}\text{C}$, $D = 0.509$ mm, $\Delta T_{sub} = 5 - 6^{\circ}\text{C}$, $L_{MEV} = 70$ mm and $G = 500$ kg/m ² s. | 124 |
| 7.7 | Vapor velocity versus vapor quality from laser 2 for R-245fa, $T_{sat} = 35^{\circ}\text{C}$, $D = 0.509$ mm, $\Delta T_{sub} = 6^{\circ}\text{C}$ and $L_{MEV} = 70$ mm. | 125 |
| 7.8 | Wall temperature measurement versus time carried out with a high-speed infrared camera for $T_{sat} = 30^{\circ}\text{C}$, $G = 300$ kg/m ² s, $D = 0.790$ mm, $q = 140$ kW/m ² and $x_{MEV,out} = 0.82$ | 126 |
| 7.9 | Drift flux model applied to R-134a and $D = 0.509$ mm results. | 127 |
| 7.10 | Drift flux model applied to R-134a and $D = 0.790$ mm results. | 127 |
| 7.11 | Drift flux model applied to all R-134a results. | 128 |
| 7.12 | Drift flux model applied to R-245fa results. | 129 |
| 7.13 | Void fractions from laser 2 for R-134a, $D = 0.509$ mm, $L_{MEV} = 70.70$ mm, $T_{sat} = 30^{\circ}\text{C}$ and $\Delta T_{sub} = 3^{\circ}\text{C}$ | 130 |
| 7.14 | Void fraction versus volumetric flow concentration for R-134a compared with the homogeneous model and the Armand's correlation. | 131 |
| 8.1 | Comparison between the total, the frictional and the momentum pressure drop as a function of vapor quality from laser 1 for R-134a, $D = 0.509$ mm, $L_{MEV} = 70.70$ mm, $T_{sat} = 30^{\circ}\text{C}$, $G = 1800$ kg/m ² s and $\Delta T_{sub} = 3^{\circ}\text{C}$. Since the momentum pressure drop is so small, the values for the total and the frictional pressured drops essentially fall on top of one another. | 134 |
| 8.2 | Two-phase frictional pressure drop as a function of the vapor quality from laser 1 for R-134a, $D = 0.509$ mm, $L_{MEV} = 70.70$ mm, $T_{sat} = 30^{\circ}\text{C}$ and $\Delta T_{sub} = 3^{\circ}\text{C}$ | 135 |
| 8.3 | Signal from diode versus time for laser 1 R-134a, $D = 0.509$ mm, $L_{MEV} = 70.70$ mm, $T_{sat} = 30^{\circ}\text{C}$, $G = 1200$ kg/m ² s and $\Delta T_{sub} = 3^{\circ}\text{C}$. Left: wavy-annular flow (a); Right: smooth and wavy-annular flow (b). | 135 |
| 8.4 | Influence of the inlet subcooling at entrance to the microevaporator on the two-phase frictional pressure drop for R-134a, $D = 0.509$ mm, $L_{MEV} = 70.70$ mm, $T_{sat} = 35^{\circ}\text{C}$ and $G = 1500$ kg/m ² s. | 136 |
| 8.5 | Influence of the saturation temperature on the two-phase frictional pressure drop for R-134a, $D = 0.509$ mm, $L_{MEV} = 70.70$ mm, $\Delta T_{sub} = 3^{\circ}\text{C}$ and $G = 1800$ kg/m ² s. | 136 |
| 8.6 | Influence of the microevaporator length on the two-phase frictional pressure drop for R-134a, $D = 0.509$ mm, $T_{sat} = 30^{\circ}\text{C}$, $\Delta T_{sub} = 3^{\circ}\text{C}$ and $G = 1800$ kg/m ² s. | 137 |

| | | |
|------|---|-----|
| 8.7 | Influence of the microevaporator diameter on the two-phase frictional pressure drop for R-134a, $T_{sat} = 30^{\circ}\text{C}$, $L_{MEV} = 70.70$ mm, $\Delta T_{sub} = 3^{\circ}\text{C}$ and $G = 1200$ kg/m ² s. | 137 |
| 8.8 | Influence of the fluid on the two-phase frictional pressure drop for $D = 0.509$ mm, $T_{sat} = 35^{\circ}\text{C}$, $L_{MEV} = 70.70$ mm, $\Delta T_{sub} = 5 - 6^{\circ}\text{C}$ and $G = 700$ kg/m ² s. | 138 |
| 8.9 | Two-phase friction factor versus two-phase Reynolds number. | 140 |
| 8.10 | Comparison between the experimental data of two-phase frictional pressure drop and different models or correlations available in the literature for macroscale or microscale. | 141 |
| 8.11 | Comparison between the experimental data of two-phase frictional pressure drop and different models or correlations available in the literature for macroscale or microscale. | 142 |
| 8.12 | Comparison between the experimental data of two-phase frictional pressure drop and different models or correlations available in the literature for macroscale or microscale. | 143 |
| 8.13 | Comparison between the experimental data of two-phase frictional pressure drop and different models or correlations available in the literature for macroscale or microscale. | 144 |
| 8.14 | Two-phase friction factor versus two-phase Reynolds number for $Re_{TP} \geq 8000$ | 146 |
| 8.15 | Comparison between the experimental data of two-phase frictional pressure drop and the homogeneous model using a new two-phase friction factors for $Re_{TP} \geq 8000$ | 147 |
| 8.16 | Two-phase multiplier versus Martinelli parameter for $Re_{TP} \geq 2000$ | 148 |
| 8.17 | Comparison between the experimental data of two-phase frictional pressure drop and the modified Lockhart-Martinelli model. | 149 |

List of Tables

| | | |
|-----|---|-----|
| 3.1 | CHF correlation of Katto-Ohno. | 16 |
| 3.2 | Experimental conditions of two-phase flow in microchannel. | 24 |
| 3.3 | Dimensions of the test section of Mishima and Hibiki [38]. | 47 |
| 3.4 | Constant and exponents for parameter C of Lee and Lee [32]. | 48 |
| 4.1 | Coefficients for the R-134a properties. | 71 |
| 4.2 | Coefficients for the R-245fa properties. | 72 |
| 4.3 | Coefficients for the vapor pressure curve calculation. | 82 |
| 4.4 | Coefficients for the pressure to temperature calculation. | 83 |
| 5.1 | Experimental conditions for CHF study. | 88 |
| 6.1 | Experimental conditions for the flow pattern study. | 98 |
| A.1 | R-134a properties. | 155 |
| A.2 | R-245fa properties. | 155 |

Nomenclature

Latin

| Symbol | Parameter | Units |
|-----------|---|---------------------|
| a | Coleman and Garimella Parameter | kg/m ² s |
| A | Cross Sectional Area | m ² |
| b | Coleman and Garimella Parameter | kg/m ² s |
| B | Chisholm Parameter | - |
| Bo | Boiling Number | - |
| C | Constant of Lockhart and Martinelli or Chisholm Parameter | m |
| C | Katto and Ohno Parameter | - |
| Co | Confinement Number | - |
| C_1 | Chung Parameter | - |
| C_2 | Chung Parameter | - |
| d | Diameter | m |
| D | Diameter | m |
| e | Surface Roughness | μm |
| E | Friedel Parameter | - |
| F | Friedel Parameter | - |
| F | Müller-Steinhagen Parameter | bar/m |
| F | Vector Quantity of Zuber and Findlay | - |
| Fr | Froude Number | - |
| f | Friction Factor | - |
| G | Mass Flux | kg/m ² s |
| g | Acceleration of Gravity | m/s ² |
| H | Friedel parameter | - |
| j | Superficial Velocity | m/s |
| K | Empirical Inlet Subcooling Parameter of Katto and Ohno | - |
| L | Length | m |
| M | Molar Mass | kg/mol |
| \dot{M} | Mass flow | kg/s |
| P | Pressure | bar |
| P | Perimeter | m |
| \dot{Q} | Volumetric Flow Rate | m ³ /s |

| | | |
|------|--------------------------------|------------------|
| Q | Heat Flow Rate | W |
| q | Heat Flux | W/m ² |
| q' | Heat Input per Unit of Length | W/m |
| R | Ideal Gas Constant $R = 8.314$ | J/molK |
| R | Radius | m |
| Re | Reynolds Number | - |
| T | Temperature | °C |
| t | Time | s |
| u | Velocity | m/s |
| V | Drift Velocity | m/s |
| We | Weber Number | - |
| x | Vapor Quality | - |
| X | Lockhart-Martinelli Parameter | - |
| Y | Chisholm Parameter | - |
| z | Longitudinal Abscissa | m |

Subscripts

| Symbol | Parameter |
|--------|---------------------------------------|
| c | CHF for Subcooled Inlet Conditions |
| co | CHF for Saturated Conditions at Inlet |
| $crit$ | Critical |
| dry | Dryout |
| ext | External |
| f | Frictional |
| $film$ | Film |
| G | Gas |
| h | Heated |
| h | Hydraulic |
| Hom | Homogeneous Model |
| int | Internal |
| in | Inlet |
| L | Liquid |
| m | Momentum |
| min | Minimum |
| MEV | Microevaporator |
| MPH | Micropreheater |
| O | Only |
| out | Outlet |
| s | Static |
| p | Pair |
| sat | Saturation |

| | |
|------------|---------------------|
| <i>sub</i> | Subcooling |
| <i>t</i> | Total |
| <i>tt</i> | Turbulent-Turbulent |
| <i>TP</i> | Two-Phase |
| <i>TS</i> | Test Section |
| <i>V</i> | Vapor |
| 0 | Initial |

Greek

| Symbol | Parameter | Units |
|---------------|---|--------------------------|
| β | Volumetric Flow Concentration, also called Volumetric Quality | - |
| δ | Film Thickness | μm |
| Δ | Difference | - |
| Δ | Error | - |
| ε | Void Fraction | - |
| λ | Lee and Lee parameter | - |
| ϕ | Two-Phase Multiplier | - |
| ψ | Lee and Lee parameter | - |
| ρ | Density | kg/m^3 |
| μ | Dynamic Viscosity | $\text{Pa}\cdot\text{s}$ |
| σ | Surface Tension | N/m |

Chapter 1

Introduction

Electronic components dissipate more and more heat due to their increasing working capacities. Irreversible damages occur when their internal temperatures reach 150°C . For this, the internal temperature of these electronic components is limited to about 100°C with a surface temperature of 85°C due to the temperature gradient. For a specific example, PC chips have a maximum surface working temperature of about 67°C . Thus, effective heat dissipation is required.

Micro or mini heat spreaders are used in the interest of providing higher cooling capability for microtechnologies. They are characterized by a high heat flux dissipation and a better heat transfer coefficient compared to conventional processes. Higher effectiveness means, for an identical power, a reduction of size and cost. Compactness also reduces the amount of charge of the fluid, which has also a direct positive impact on safety and environment. However the negative point is possibly a higher pressure drop related to the micro or mini flow channels.

The thermal performance of heat spreaders using micro or mini channels are not yet well understood, for this the fundamentals of two-phase heat transfer in microchannels are being studied. Many heat transfer design methods exist for refrigerant vaporization inside macrochannels, but these have been found to not be suitable to the small dimensions found in microchannels due to small-scale phenomena. Therefore, research is underway to investigate these small-scale phenomena and to develop new microchannel design methods.

Thome et al. [51, 19] proposed the first mechanistic heat transfer model to describe evaporation in microchannels with a *three-zone* flow boiling model that describes the transient variation in the local heat transfer coefficient during sequential and cyclic passage of (i) a liquid slug, (ii) an evaporating elongated bubble with a thin liquid film trapped between it and the channel wall and (iii) a vapor slug when film dryout has occurred. Fig. 1.1 depicts a schematic of their three-zone heat transfer model. The new model illustrates the strong dependency of heat transfer on the bubble frequency, the lengths of the bubbles and liquid slugs, and the liquid film thickness trapped between the heated wall and the bubble, and is so far only applicable to the slug flow regime.

The present study is carried out on two single round tubes ($D = 0.509$ and 0.790 mm) and for two different fluids: R-134a and R-245fa. Many questions are open:

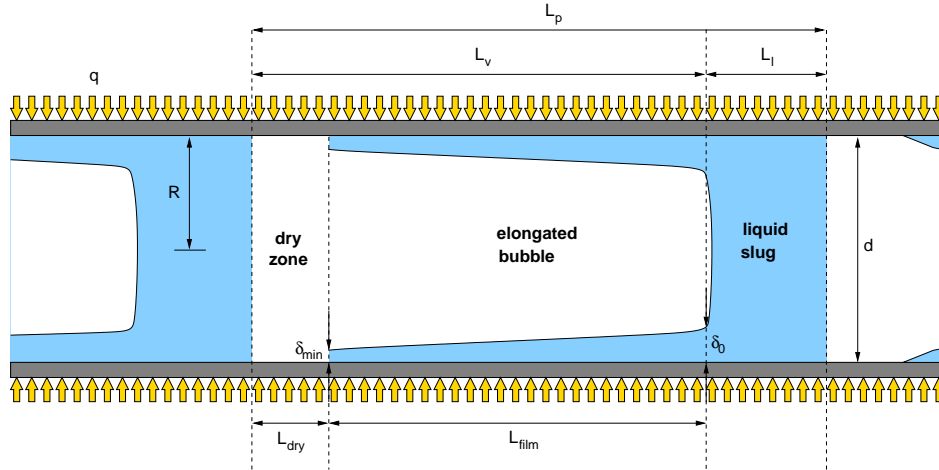


Figure 1.1: Schematic of three-zone evaporation model.

- What is the critical heat flux (CHF) in microchannels compared to conventional ones? One of the limiting factors in two-phase heat transfer is the onset of dry-out. It happens when the heat transfer surface is no longer completely wetted by the liquid phase. Vapor now completely or partially blankets the surface and heat transfer is no longer to a highly conducting liquid but to a poorly conducting gas. Such a condition can damage the microevaporator and the electronic component.
- What are the different flow patterns encountered in microchannels flow? Under what conditions do they occur? Heat transfer and pressure drop models should be based on the liquid and vapor distributions created by the flow patterns. The flow patterns are the description of the two-phase flow structure to explain under which condition the vapor is a continuous phase in the central core of the tube (annular flow) or is arranged as bubbles etc.
- How does the void fraction behave compared to that known in macrochannels? Void fraction is an important parameter used in heat transfer and pressure drop models.
- How large is the pressure drop inside microchannels? This information is valuable to engineers for designing microcooling systems.
- What phenomena govern the two-phase flow in micro or mini channels? Gravity seems to have less influence than surface tension forces. As an example, Fig. 1.2 shows elongated bubbles in 2.0, 0.8 and 0.5 mm tubes and demonstrates that the gravity has essentially no buoyancy effect for the 0.5 mm channel.

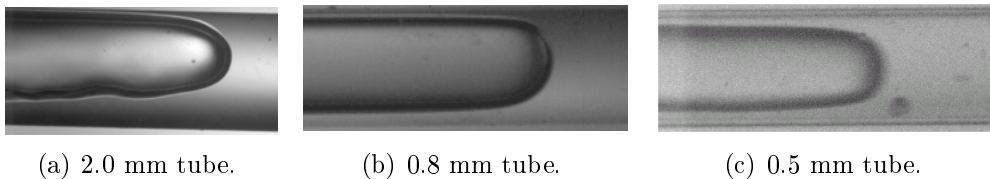


Figure 1.2: Elongated bubble in 2.0, 0.8 and 0.5 mm tubes.

For these reasons, it is opportunistic to apply an optical measurement technique to quantitatively characterize flow pattern transitions, determine void fraction, and measure the frequency, velocity and length of vapor bubbles in microchannels, in particular at the exit of microevaporators in which the flows are formed. Such an optical measurement technique has been developed here and implemented in a new multi-purpose microchannel test facility. The main objectives of this work are to increase the database for refrigerants flowing in microchannels for CHF, flow patterns, void fraction and pressure drop and to develop corresponding prediction methods. These methods are imperative for the design and optimization of efficient micro heat spreaders for cooling of electronic components.

This manuscript is organized as follows:

- Chapter 1: introduction.
- Chapter 2: presents the fundamentals of two-phase flow with the main parameters and definitions described.
- Chapter 3: reviews the state of the art. The first topic is CHF, the second one is flow patterns and flow pattern maps, the third one is void fraction and the last topic is the pressure drop.
- Chapter 4: presents a description of the new experimental facility and presents the results for the critical heat flux as well as proposing a new correlation for predicting CHF.
- Chapter 5: shows the experimental work and results carried out on flow patterns. A new diabatic flow pattern map for evaporating flows in microchannels is also presented.
- Chapter 6: shows the results on void fraction and vapor velocity as well as the drift flux model applied to the results.
- Chapter 7: presents the experimental pressure drop results and a new correlation is proposed to predict the results.
- Chapter 8: presents the general conclusions.

Chapter 2

Fundamental definitions and flow parameters

This chapter introduces the primary variables used throughout this work and derives some simple relationships between them for the case of one-dimensional two-phase flow. To distinguish between vapor and liquid the subscripts 'L' for liquid and 'V' for vapor will be used.

2.1 Two-phase flow

Classical thermodynamics tells us that a phase is a macroscopic state of the matter which is homogeneous in chemical composition and physical structure; e.g., a gas, a liquid or solid of a pure component. Two-phase flow is the simplest case of multiphase flow in which two phases are present for a pure component.

In internal convective vaporization and condensation processes, the vapor and liquid are in simultaneous motion inside the flow channel. The resulting two-phase flow is generally much more complicated physically than single-phase flow. In addition to the usual inertia, viscous, and pressure forces present in single-phase flow, two-phase flows are also affected by interfacial tension forces, the wetting characteristics of the liquid on the tube wall, and the exchange of momentum between the liquid and vapor phases in the flow.

2.2 Vapor quality

The vapor quality (x) is defined to be the ratio of the vapor mass flow rate (\dot{M}_V [kg/s]) divided by the total mass flow rate ($\dot{M}_V + \dot{M}_L$):

$$x = \frac{\dot{M}_V}{\dot{M}_V + \dot{M}_L} \quad (2.1)$$

When phase change does not take place in a channel, one needs to measure the mass flow rate of each phase, and the quality is then determined for the entire channel. In case there is a phase change in the channel, e.g. if the channel is heated and boiling takes place, then the quality will increase (inverse for condensation) in the direction of flow.

If there is not thermal equilibrium between the phases, one cannot calculate the quality merely by knowing the inlet quality and the heat flux from the wall. Unfortunately, it is very difficult to measure or calculate with precision the quality of the liquid-vapor mixture flowing in a channel where a change of phase takes place. A fictitious quality, the so called thermodynamic equilibrium quality can be calculated by assuming that both phases are saturated, i.e. that their temperatures are equal to the saturation temperature corresponding to their common pressure. The so-called thermodynamic equilibrium quality can be calculated as:

$$x = \frac{h(z) - h_L}{h_{LV}} \quad (2.2)$$

where h_L [J/kg] is the enthalpy of the saturated liquid, h_{LV} [J/kg] is the latent heat of vaporization, and $h(z)$ [J/kg] is the enthalpy at a cross section z , which can be calculated from:

$$h(z) = h_{in} + \frac{1}{\dot{M}} \int_0^z q'(z) dz \quad (2.3)$$

where h_{in} is the enthalpy of the fluid at the inlet and $q'(z)$ [W/m] is the heat input from unit of length.

2.3 Mass flux

The mass flux (G) is defined to be the ratio of the mass flow rate (\dot{M}) divided by the cross-sectional area:

$$G = \frac{\dot{M}}{A} \quad (2.4)$$

Considering the continuity law, the mass flux is the expression of the mean flow velocity multiplied by the mean density. The usual unit of the mass flux is [kg/m²s].

2.4 Velocities

In two-phase flow there are a number of velocities which can be defined. Also, in general, the phases will not have the same velocity and there will be a relative velocity between them.

2.4.1 True average velocities

The true average velocities of the phases u_V and u_L are the velocities by which the phases actually travel. The cross sectional average true velocities are determined by the volumetric flow rates \dot{Q}_V and \dot{Q}_L [m³/s] divided by the cross-sectional areas occupied by each phase:

$$u_V = \frac{\dot{Q}_V}{A_V} = \frac{\dot{Q}_V}{\epsilon A} \quad (2.5)$$

$$u_L = \frac{\dot{Q}_L}{A_L} = \frac{\dot{Q}_L}{(1 - \epsilon)A} \quad (2.6)$$

From the equation of continuity it is possible to define liquid and vapor true means velocities in a channel as follows:

$$u_V = \frac{x}{\epsilon} \frac{\dot{M}}{\rho_V A} = \frac{G}{\rho_V} \frac{x}{\epsilon} \quad (2.7)$$

$$u_L = \frac{1 - x}{1 - \epsilon} \frac{\dot{M}}{\rho_L A} = \frac{G}{\rho_L} \frac{1 - x}{1 - \epsilon} \quad (2.8)$$

2.4.2 Superficial velocities

The superficial velocities (also called volumetric fluxes) of the phases j_V and j_L are defined as the ratio of the volumetric flow rate of the phase considered over the total cross-sectional area of the two-phase flow. It might also be expressed as the phase velocity if it would flow alone in the entire cross section.

$$j_V = \frac{\dot{Q}_V}{A} = \frac{G}{\rho_V} x = \epsilon u_V \quad (2.9)$$

$$j_L = \frac{\dot{Q}_L}{A} = \frac{G}{\rho_L} (1 - x) = (1 - \epsilon) u_L \quad (2.10)$$

The total superficial velocity is defined as:

$$j = j_V + j_L \quad (2.11)$$

2.4.3 Drift velocities

The drift velocities of the phases V_{Vj} and V_{Lj} are defined as the true average velocity of the phase in relation to the total superficial velocity, namely:

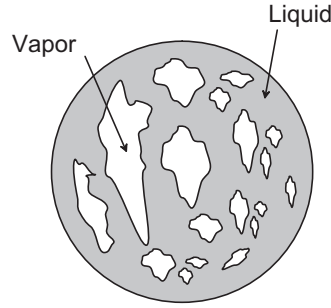


Figure 2.1: Cross-sectional void fraction (ϵ).

$$V_{Vj} = u_V - j \quad (2.12)$$

$$V_{Lj} = u_L - j \quad (2.13)$$

The drift fluxes of the phases j_{Vj} and j_{Lj} are defined as follows:

$$j_{Vj} = \epsilon V_{Vj} = \epsilon(u_V - j) \quad (2.14)$$

$$j_{Lj} = (1 - \epsilon)V_{Lj} = (1 - \epsilon)(u_L - j) \quad (2.15)$$

It follows, from Eqs. (2.14), (2.15) and (2.11) that:

$$j_{Vj} + j_{Lj} = 0 \quad (2.16)$$

2.5 Void fraction

In two-phase flow, void fraction is one of the most important parameters to be defined. It defines the cross-sectional area occupied by the gas or vapor phase respect to the total. As it determines the true average velocities of the liquid and the vapor, it represents a fundamental parameter in the calculation of pressure drop, flow pattern transitions and heat transfer coefficients.

Cross sectional void fraction is defined as:

$$\epsilon = \frac{A_V}{A_V + A_L} \quad (2.17)$$

where A_V is the sum of areas occupied by vapor and A_L is the sum of areas occupied by liquid, for example those shown in Fig. 2.1.

In two-phase flow, the superficial velocity is used to calculate the cross-sectional void fraction as written in Eq. (2.18).

$$\epsilon_V = \frac{j_V}{u_V} \quad (2.18)$$

The time average centerline void fraction, on the other hand, is calculated by assuming that its value is 1 if there is vapor and 0 if liquid. It does not take into account the radial distribution of the liquid and vapor but only that at the nose and rear of the bubble, i.e. essentially that at the centerline of the channel, in a slug flow.

2.6 Definition of non-dimensional numbers

The principal non-dimensional numbers used in the present study are defined below.

2.6.1 Reynolds number

The Reynolds number represents the ratio of the inertial forces to the viscous forces. For the particular case of forced convection inside a tubular channel, the liquid Reynolds number can be expressed in the following form:

$$Re_L = \frac{\rho_L u_L D_h}{\mu_L} \quad (2.19)$$

where D_h is the hydraulic diameter defined as the ratio of the cross-sectional area of the fluid A to the wetted perimeter P_L :

$$D_h = \frac{4A}{P_L} \quad (2.20)$$

In the case of circular tubes, $D_h = D$.

Considering one-dimensional flow and using the definition of the true average velocity from Eq. (2.6), the liquid Reynolds number can be expressed as:

$$Re_L = \frac{GD_h}{\mu_L} \frac{1-x}{1-\epsilon} \quad (2.21)$$

where the D_h for the liquid phase is expressed in the following form:

$$D_h = \frac{4A_L}{P_L} = \frac{4(1-\epsilon)A}{P_L} \quad (2.22)$$

Substituting Eq. (2.22) into (2.21) the liquid Reynolds number is defined as:

$$Re_L = \frac{4G(1-x)A}{\mu_L P_L} \quad (2.23)$$

The same approach will be used for the vapor Reynolds number which is defined as:

$$Re_V = \frac{GD_h x}{\mu_V \epsilon} \quad (2.24)$$

where the D_h for the vapor phase is expressed as:

$$D_h = \frac{4A_V}{P_V} = \frac{4A \epsilon}{P_V} \quad (2.25)$$

Finally, substituting Eq. (2.25) into (2.24), the vapor Reynolds number is expressed as:

$$Re_V = \frac{4GxA}{\mu_V P_V} \quad (2.26)$$

In the literature other definitions of the Reynolds number may be found. As the void fraction is difficult to determine, the following expressions are also used for circular tubes:

$$Re_L = \frac{G(1-x)D}{\mu_L} \quad (2.27)$$

$$Re_V = \frac{GxD}{\mu_V} \quad (2.28)$$

In that situation, each phase flows alone in the complete cross-section of the tube at its own velocity. Another type of Reynolds number may be calculated:

$$Re_{LO} = \frac{GD}{\mu_L} \quad (2.29)$$

$$Re_{VO} = \frac{GD}{\mu_V} \quad (2.30)$$

It represents the liquid or the vapor phase only flowing alone in the complete cross-section of the tube at the total mass flux. Prediction methods for two-phase frictional pressure drops use one set of these Reynolds number definitions and one must be careful to use the definition used in the particular method.

2.6.2 Weber number

The liquid Weber number expresses the ratio of inertia to surface tension forces. The reference length is the tube diameter:

$$We_L = \frac{\rho_L u_L^2 D}{\sigma} \quad (2.31)$$

Usually, in two-phase flow experiments, the liquid Weber number is expressed as:

$$We_L = \frac{G^2 D(1-x)}{\rho_L \sigma} \quad (2.32)$$

or

$$We_{LO} = \frac{G^2 D}{\rho_L \sigma} \quad (2.33)$$

for when the liquid phase only flows alone in the complete cross-section of the tube at the total mass flux.

For the vapor, the same type of definitions are obtained:

$$We_V = \frac{G^2 D x}{\rho_V \sigma} \quad (2.34)$$

or

$$We_{VO} = \frac{G^2 D}{\rho_V \sigma} \quad (2.35)$$

2.6.3 Boiling number

The Boiling number expresses the ratio between the heat flux and the potential heat flux that would have been applied for complete evaporation:

$$Bo = \frac{q}{h_{LV} G} \quad (2.36)$$

2.6.4 Martinelli parameter

The Martinelli parameter [34] is the ratio of the theoretical frictional pressure drop that would occur if each phase could flow separately in the complete cross-section of the channel with the original rate of each phase. In general form the Martinelli parameter is calculated as:

$$X_{tt} = \left[\frac{\left(\frac{dP}{dz} \right)_L}{\left(\frac{dP}{dz} \right)_V} \right]^{0.5} \quad (2.37)$$

where

$$\left(\frac{dP}{dz}\right)_L = f_L \frac{2G^2}{D\rho_L} (1-x)^2 \quad (2.38)$$

$$\left(\frac{dP}{dz}\right)_V = f_V \frac{2G^2}{D\rho_V} x^2 \quad (2.39)$$

$$(2.40)$$

with f_L , the friction factor for the liquid expressed by:

$$f_L = \frac{16}{Re_L} \text{ for } Re_L < 2000 \quad (2.41)$$

$$f_L = 0.079 Re_L^{-0.25} \text{ for } Re_L > 2000 \quad (2.42)$$

with Re_L from Eq. (2.27),

and f_V , the friction factor for the vapor expressed by:

$$f_V = \frac{16}{Re_V} \text{ for } Re_V < 2000 \quad (2.43)$$

$$f_V = 0.079 Re_V^{-0.25} \text{ for } Re_V > 2000 \quad (2.44)$$

with Re_V from Eq. (2.28).

X_{tt} can be also defined as a measure of the degree to which the two-phase mixture is closer to being a liquid ($X_{tt} \gg 1$) or being a gas ($X_{tt} \ll 1$).

2.7 Conclusions

The fundamentals parameters and definitions used for describing two-phase flows have been presented.

Chapter 3

State of the Art Review

This Chapter presents the state-of-the-art review relevant to the present investigation on critical heat flux, flow pattern maps, void fraction and two-phase frictional pressure drops.

3.1 Critical heat flux

Critical heat flux (CHF) or burnout is a limiting operating heat flux for the safe operation of heat dissipation applications and refers to the replacement of liquid being in contact with the heated surface with a vapor blanket. The thermal conductivity of the vapor is very low compared to the liquid and the surface heat transfer coefficient drops dramatically, resulting in the sudden increase of the surface temperature and possible failure of the cooled device.

CHF may occur in subcooled as well as in saturated boiling conditions. In subcooled CHF, the bulk temperature at the channel outlet is subcooled and the thermodynamic equilibrium vapor quality is lower than zero, $x < 0$. These are the typical conditions for very high mass velocities, high inlet subcoolings and relative short channels compared to their hydraulic diameters. In saturated CHF, the thermodynamic equilibrium vapor quality at the channel outlet is greater or equal to zero, $x = 0$. This is typically encountered at low mass velocities, at low inlet subcoolings and in channels with a large length to diameter ratio.

Many researchers are trying to respond to the question "what is the upper limit for the critical heat flux in microchannels in order to estimate the maximum cooling rate of a say a PC microprocessor?"

3.1.1 The Gambill and Lienhard study

Independent studies have been summarized by Gambill and Lienhard [21]. They noted that, if one could contrive to collect every vapor molecule that leaves a liquid-vapor interface without permitting any vapor molecule to return to the liquid, then

$$q_{max} = \rho_V h_{LV} \sqrt{\frac{RT}{2\pi M}} \quad (3.1)$$

where q_{max} is the highest heat flux that can conceivably be achieved in a phase transition process and R the ideal gas constant and M the molar mass. This equation is based on kinetic theory and the average speed of a Maxwellian gas. Fig 3.1 shows the variation of the upper limit of heat flux as a function of reduced pressure (P/P_{crit}) for refrigerants tested in the present study, namely R-245fa and R-134a. As can be seen, the maximum heat flux increases for both refrigerants with the increase of the reduced pressure, reaching a peak at $Pr = 0.85$. Then it starts to decrease and arrives at zero for vapor quality equal to one, $x=1$. Figure 3.1 shows the astonishingly high values of heat fluxes that might seem to be attainable. There are several reasons that this limit will be unattainable in practice. The most serious restriction is that many vapor molecules will inevitably be returned to the interface by molecular collisions. Another problem lies in the premise that all the heat ultimately passes through a liquid-vapor interface, according to Gambill and Lienhard.

From the practical point of view, the target level of CHF appears to be about $0.1q_{max}$. If burnout consistently reaches one tenth of the limit, then burnout is occurring because a molecular effusion fails to provide sufficient cooling. Molecular effusion is an unobserved until now burnout mechanism according to Gambill and Lienhard. At 35°C , the value of q_{max} is 125 MW/m^2 for R-245fa and 464 MW/m^2 for R-134a. As will be seen later, only a fraction of these values are achievable in the present microchannels.

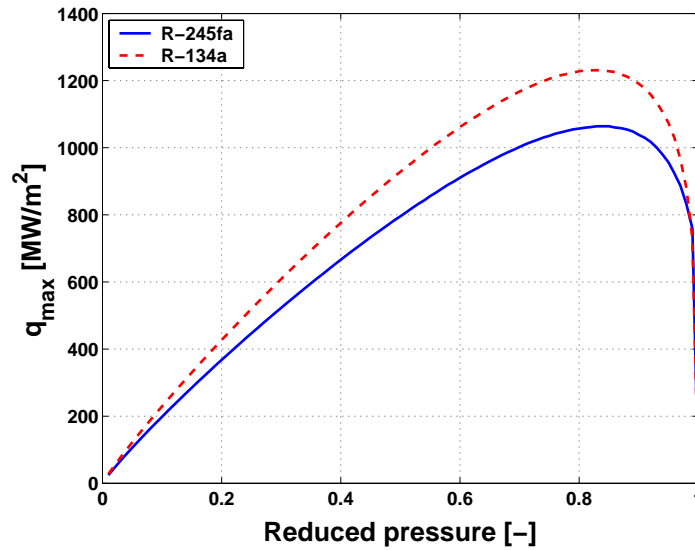


Figure 3.1: Dependence of q_{max} on reduced pressure for R-245fa and R-134a.

3.1.2 The Katto and Ohno study

One of the most widely used empirical methods developed for predicting saturated CHF in a single channel is the Katto-Ohno [25] correlation. For no liquid subcooling, they correlate CHF as:

$$\frac{q_{co}}{Gh_{LV}} = f \left[\frac{\rho_L}{\rho_V}, \frac{\sigma \rho_L}{G^2 L_h}, \frac{L_h}{D} \right] \quad (3.2)$$

For most regimes, they found a linear rise in CHF with increasing liquid subcooling. Therefore, subcooling was taken into account by the following equation:

$$\frac{q_c}{Gh_{LV}} = q_{co} \left(1 + K \frac{\Delta h_{in}}{h_{LV}} \right) \quad (3.3)$$

where q_c is the CHF for subcooled conditions, q_{co} is the saturated CHF, Δh_{in} is the inlet enthalpy of subcooling with respect to saturation and K is an empirical inlet subcooling parameter. All these parameters are calculated as described in Table 3.1.

To ascertain the applicability of the above correlation to fluids other than water, they conducted the following experiments:

- R-12 for $D = 3.0$ and 5.0 mm, $L_h/D = 200$ and 333 , $\rho_V/\rho_L = 0.109 - 0.306$ and $G = 1100 - 8800$ kg/m²s in Katto et al. [26];
- R-12 for $D = 5.0$ mm, $L_h/D = 50$, $\rho_V/\rho_L = 0.109 - 0.306$ and $G = 700 - 7000$ kg/m²s in Katto et al. [24];
- liquid helium for $D = 1.0$ mm, $L_h/D = 25 - 200$, $\rho_V/\rho_L = 0.409$ and $G = 10.5 - 108$ kg/m²s in Katto et al. [27].

Hence, for normal refrigerants this method is applicable only down to about 3.0 mm channels.

3.1.3 The Qu and Mudawar study

Qu and Mudawar [42] compared 414 data points they obtained for water channels with in $D = 1.0 - 3.0$ mm with $L_h/D = 50 - 975$ and R-113 in $D = 3.15$ mm with $L_h/D = 40$ to the correlation of Katto-Ohno. They found that this correlation is fairly accurate at predicting saturated CHF in single circular mini-channels. The mean absolute error for this correlations was 17.3% with most of the data points falling within a $\pm 40\%$ error band.

Furthermore, Qu and Mudawar [42] adapted the Katto-Ohno correlation for microchannel heat sinks containing 21 parallel 215×821 μm channels. They found that as CHF was approached, flow instabilities induced vapor backflow into the heat sink's upstream plenum mixing vapor with subcooled liquid. The backflow negated the advantages of inlet subcooling, resulting in a CHF virtually independent of inlet subcooling. Their new empirical correlation based on their experimental CHF data for water and R-113 in mini/microchannel heat sinks is as follows:

$$\frac{q_c}{Gh_{LV}} = 33.43 \left(\frac{\rho_V}{\rho_L} \right)^{1.11} We_L^{-0.21} \left(\frac{L_h}{D} \right)^{-0.36} \quad (3.4)$$

$$\begin{aligned}\frac{q_{co1}}{Gh_{LV}} &= C \left(\frac{\sigma \rho_L}{G^2 L_h} \right)^{0.043} \frac{1}{L_h/D} \\ \frac{q_{co2}}{Gh_{LV}} &= 0.1 \left(\frac{\rho_V}{\rho_L} \right)^{0.133} \left(\frac{\sigma \rho_L}{G^2 L_h} \right)^{1/3} \frac{1}{1 + 0.0031 L_h/D} \\ \frac{q_{co3}}{Gh_{LV}} &= 0.098 \left(\frac{\rho_V}{\rho_L} \right)^{0.133} \left(\frac{\sigma \rho_L}{G^2 L_h} \right)^{0.433} \frac{(L_h/D)^{0.27}}{1 + 0.0031 L_h/D} \\ \frac{q_{co4}}{Gh_{LV}} &= 0.0384 \left(\frac{\rho_V}{\rho_L} \right)^{0.60} \left(\frac{\sigma \rho_L}{G^2 L_h} \right)^{0.173} \frac{1}{1 + 0.280(\sigma \rho_L/G^2 L_h)^{0.233} L_h/D} \\ \frac{q_{co5}}{Gh_{LV}} &= 0.234 \left(\frac{\rho_V}{\rho_L} \right)^{0.513} \left(\frac{\sigma \rho_L}{G^2 L_h} \right)^{0.433} \frac{(L_h/D)^{0.27}}{1 + 0.0031 L_h/D}\end{aligned}$$

$$C = 0.25 \text{ for } L_h/D < 50$$

$$C = 0.25 + 0.0009 [L_h/D - 50] \text{ for } L_h/D = 50 \text{ to } 150$$

$$C = 0.34 \text{ for } L_h/D > 150$$

$$\begin{aligned}K_1 &= \frac{1.043}{4C (\sigma \rho_L/G^2 L_h)^{0.043}} \\ K_2 &= \frac{5}{6} \frac{0.0124 + D/L_h}{(\rho_V/\rho_L)^{0.133} (\sigma \rho_L/G^2 L_h)^{1/3}} \\ K_3 &= 1.12 \frac{1.52 (\sigma \rho_L/G^2 L_h)^{0.233} + D/L_h}{(\rho_V/\rho_L)^{0.60} (\sigma \rho_L/G^2 L_h)^{0.173}}\end{aligned}$$

for $\rho_V/\rho_L < 0.15$

→ when $q_{co1} < q_{co2}$, $q_{co} = q_{co1}$

→ when $q_{co1} > q_{co2}$

if $q_{co2} < q_{co3}$, $q_{co} = q_{co2}$

if $q_{co2} > q_{co3}$, $q_{co} = q_{co3}$

→ when $K_1 > K_2$, $K = K_1$

→ when $K_1 < K_2$, $K = K_2$

for $\rho_V/\rho_L > 0.15$

→ when $q_{co1} < q_{co5}$, $q_{co} = q_{co1}$

→ when $q_{co1} > q_{co5}$

if $q_{co5} < q_{co4}$, $q_{co} = q_{co4}$

if $q_{co5} > q_{co4}$, $q_{co} = q_{co5}$

→ when $K_1 > K_2$, $K = K_1$

→ when $K_1 < K_2$

if $K_2 < K_3$, $K = K_2$

if $K_2 > K_3$, $K = K_3$

Table 3.1: CHF correlation of Katto-Ohno.

with

$$We_L = \frac{G^2 L_{MEV}}{\rho_L \sigma} \quad (3.5)$$

This correlation predicted their experimental data with very low mean absolute error of 4%.

3.1.4 The Pribyl et al. study

Pribyl et al. [41] studied the effect of the flow patterns on CHF. They plotted experimental water CHF data obtained in three independent test facilities against vapor quality. The total number of experimental points was 4109. The tube diameters tested varied from 1.0 to 37.0 mm, heated lengths from 31 to 3000 mm and mass flux from 10 to 18580 kg/m²s. The database was sorted by regime using the Taitel- Dukler [48] map to identify annular, intermittent and bubble flows. They found that CHF varied linearly with quality in distinct segments, with a relatively sharp discontinuity and change in slope at low vapor qualities, where the Taitel- Dukler map predicts a regime transition. The most apparent difference in slope was observed between bubble and annular flow. They concluded that a change in flow regime might affect the mechanism of CHF and that within each flow regime a similar but distinct CHF mechanism could be expected to apply.

3.1.5 Conclusions

Only few studies exist on the critical heat flux in microchannels while it has been extensively studied for conventional channels for a variety of flow boiling configurations. A larger database for single uniformly heated microtubes should be developed, especially for fluids other than water and old (retired) refrigerants. Existing correlations have to be tested and modified, if needed, to predict CHF in microtube for the new refrigerants and other coolants.

3.2 Flow pattern maps

One of the most important features of a two-phase flow is the variety of flow patterns, i.e. how do the phases distribute themselves in the conduit. Are the bubbles going to be distributed uniformly throughout the liquid or are they going to coalesce and form larger bubbles? Without knowing the flow regime (pattern) one cannot calculate correctly the design parameters for defined flow conditions such as heat transfer and pressure drop. The flow patterns depend on many parameters such as pressure, geometry, inclination of the tube, etc. In the first part of this chapter, the flow patterns in conventional channels and the flow pattern maps encountered in macrochannel two-phase flow will be described. In the last part, the state-of-the-art of two-phase flow patterns and flow pattern maps in microchannels will be presented.

3.2.1 Flow patterns in conventional channels

Flow patterns in horizontal two-phase flow

The flow patterns observed in horizontal two-phase flow are complicated by asymmetry of the phases resulting from the influence of gravity. The generally accepted flow patterns are shown in Fig. 3.2 and described below:

- **Bubbly flow:** The gas or vapor phase is distributed as discrete bubbles in a continuous liquid phase. The size of bubbles does not approach the diameter of the pipe. The bubbles tend to travel in the upper half of the pipe.
- **Plug flow:** This pattern is an intermittent flow that occurs at low gas flow rates and moderate liquid rate. In this regime, liquid plugs, free of entrained gas bubbles, are separated by zones of elongated gas bubbles.
- **Slug flow:** When the gas velocity is increased in a plug flow, the liquid slugs become aerated and contain small bubbles. The flow is more chaotic compared with plug flow and the interface between gas and liquid is not as clearly defined. Plug flow and slug flow are often categorized as one flow regime called intermittent flow.
- **Stratified flow:** The two phases are separated with the all liquid at the bottom of the channel (under normal gravity conditions). This flow pattern occurs at low liquid and gas velocities. This flow regime is subdivided into two regimes: stratified smooth and stratified wavy. The stratified smooth occurs at low gas velocities.
- **Wavy flow:** As the gas velocity is increased, waves are formed on the liquid-gas interface, with the waves traveling in the direction of the flow. This flow pattern corresponds to the stratified wavy flow.
- **Annular flow:** Higher gas flow rates will cause the liquid to form a film on the tube wall, somewhat similar to that observed in vertical flow, with the important exception that the film at the bottom of the tube may be much notably thicker than the film at the top.

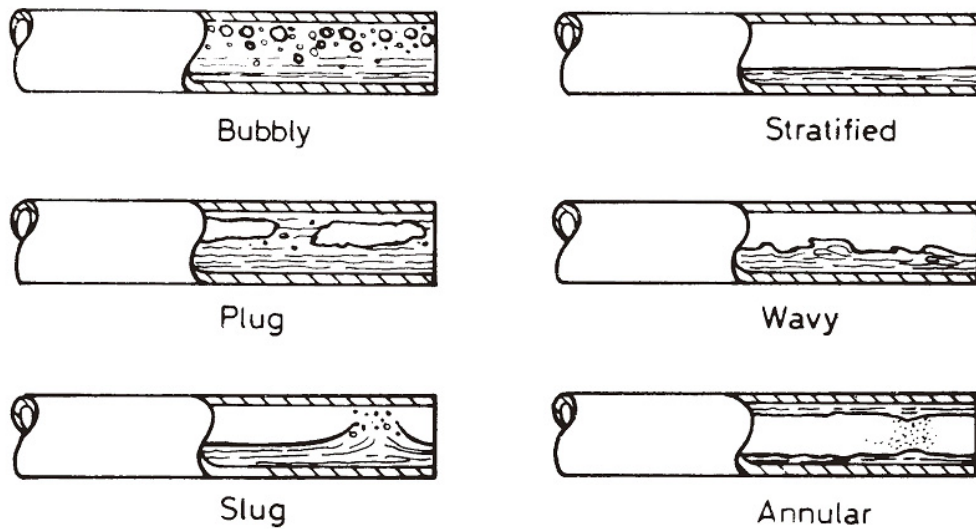


Figure 3.2: Schematic of flow patterns in internal horizontal two-phase flow from Collier and Thome [14].

Flow patterns formed during the generation of vapor in horizontal tubular channels can be influenced by departures from thermodynamic and hydrodynamic equilibrium. Figure 3.3 shows a schematic representation of a horizontal tubular channel heated by a uniform low heat flux and fed with liquid just below saturation temperature. The sequence of flow patterns shown corresponds to relatively low inlet velocity (< 1 m/s). Asymmetric phase distributions and stratification introduce additional complications. Important points to note from a heat transfer viewpoint are the possibility of intermittent drying and rewetting of the upper surfaces of the tube in slug and wavy flow and the progressive drying out over long tube lengths of the upper circumference of the tube wall in annular flow. At higher inlet liquid velocities the influence of gravity is less obvious, the phase distribution becomes more symmetrical and the flow patterns become closer to those seen in vertical flow.

Flow patterns in vertical two-phase flow

The distribution of the phases in vertical upward two-phase flow is no more influenced by the gravity. The most common flow patterns encountered in vertical upward flow are shown in Fig. 3.4 and presented below:

- **Bubbly flow:** The gas or vapor phase is dispersed as discrete bubbles in the continuous liquid. The bubbles may have different shapes and sizes but they are much smaller than the pipe diameter.
- **Slug flow:** When the quality increases, the bubbles coalesce and form larger bubbles, of a size similar to the pipe diameter. These are called Taylor bubbles and have a characteristic spherical cap nose and are somewhat abruptly terminated. The elongated gas bubbles are separated by liquid slugs, which may have smaller bubbles in them. The Taylor bubbles are separated from the wall by a thin film of liquid.

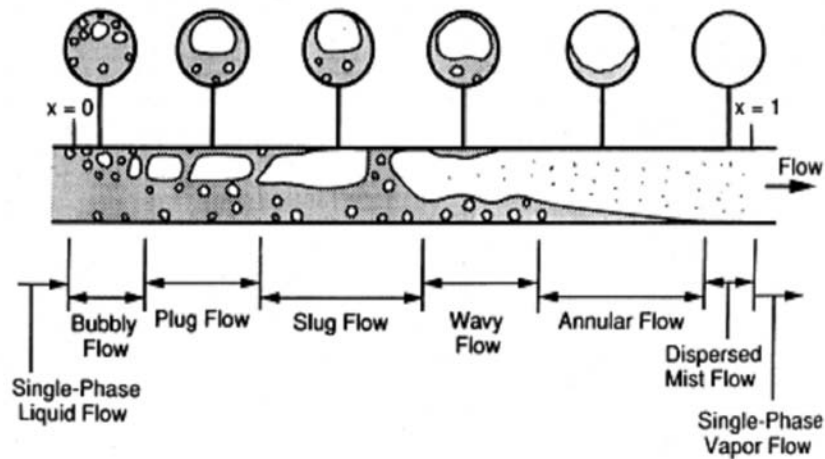


Figure 3.3: Schematic of flow patterns in internal horizontal two-phase flow during evaporation from Collier and Thome [14].

- **Churn flow:** When the velocity of the flow is increased, the slugs break-down into a seemingly unstable regime. This is a flow regime in between the slug flow and the annular flow regimes, where the liquid is displaced to the tube wall.
- **Wispy-annular flow:** When the liquid flow rate is increased, a considerable amount of liquid may be entrained in the gas core. These liquid droplets may then coalesce to form large lumps or wisps of liquid. This regime occurs at high mass velocities.
- **Annular flow:** The bulk of the liquid flows on the wall, as a film and the gas is the continuous phase at the center of the tube. Normally there is some liquid entrained in the continuous gas in the form of small droplets, and there may be some gas in the liquid film in the form of bubbles.

The formation of a two-phase mixture by vapor generation in a vertical heated tubular channel represents an important special case. The presence of a heat flux through the channel wall may alter the flow pattern from that which would have occurred in a long unheated channel at the same local flow conditions. These changes occur due to two main reasons; the departure from thermodynamic equilibrium coupled with the presence of radial temperature profiles in the channel and the departure from local hydrodynamic equilibrium throughout the channel. Figure 3.5 from Collier and Thome [14] depicts a schematic representation of a vertical tubular channel heated by a uniform heat flux and fed with liquid just below the saturation temperature.

3.2.2 Flow pattern maps in conventional channels

Many flow pattern maps exist for predicting two-phase flow regimes. They can be classified into two classes: Adiabatic flow pattern maps that usually work for air/water and diabatic flow pattern maps that work for evaporating refrigerants. Mechanistic type of heat transfer and pressure drop models are based on these flow pattern maps.

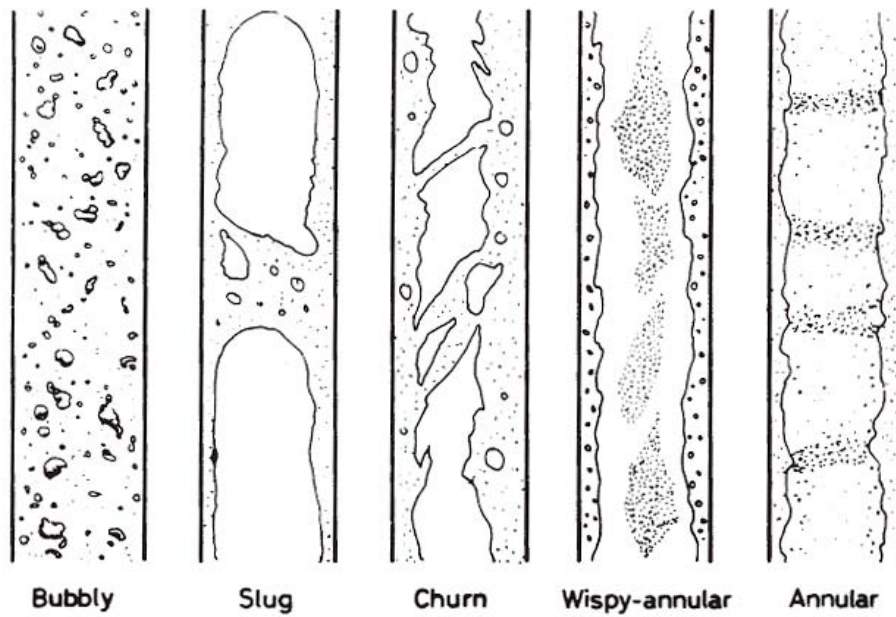


Figure 3.4: Schematic of flow patterns in internal vertical two-phase flow from Collier and Thome [14].

Kattan et al. [23] proposed an improved two-phase flow pattern map for evaporation in horizontal tubes as presented in Fig. 3.6. The new map was developed based on flow pattern data for five different refrigerants covering a wide range of mass velocities and vapor qualities. The map is valid for both adiabatic and diabatic (evaporating) flows in horizontal tubes. The smallest channel Thome and coworkers tested this map against was 0.8 mm.

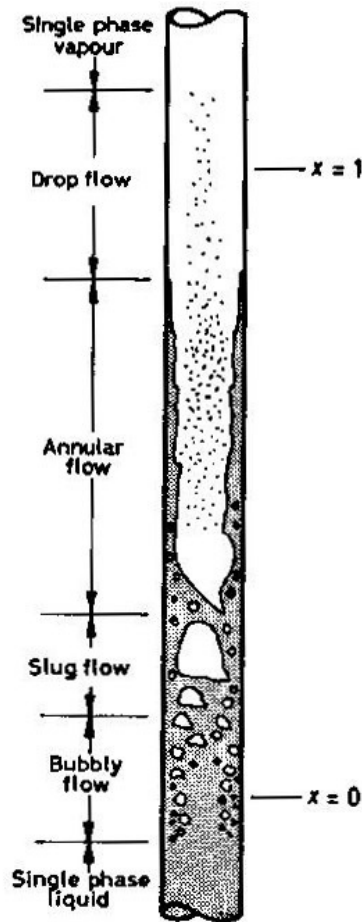


Figure 3.5: Schematic of flow patterns in internal vertical two-phase flow during evaporation from Collier and Thome [14].

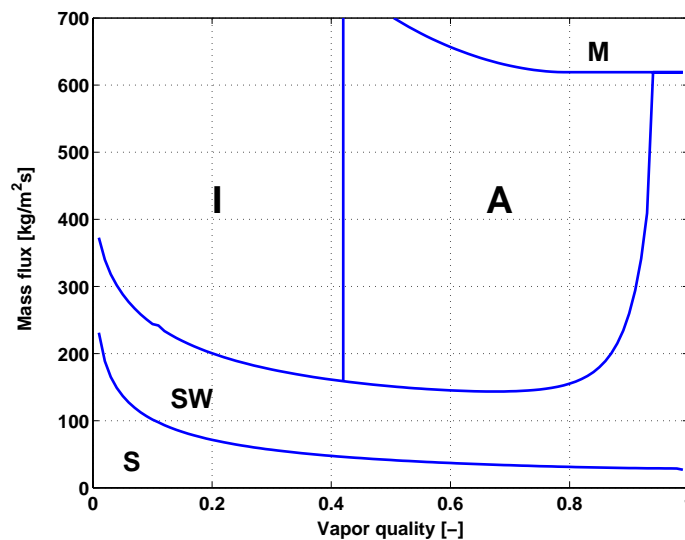


Figure 3.6: Flow pattern map for horizontal channels of Kattan et al. [23] for R-134a, $D = 10$ mm, $T_{sat} = 30$ °C, $q = 10$ kW/m². (S =Stratified flow, SW =Stratified Wavy flow, I =Intermittent flow, A =Annular flow, M =Mist flow).

3.2.3 Flow patterns and flow pattern maps in microchannels

Many studies exist now on flow patterns in microchannels. The most representative are presented here.

The Suo and Griffith study

Among the first studies to describe flow patterns in microchannels is that by Suo and Griffith [47] in 1964. The adiabatic two phase flow of gas and liquid was studied in horizontal tubes for different conditions as summarized in Table 3.2. Two flow regimes which bound the slug flow regime (S) are annular flow (A) and bubbly-slug flow (the author's definition apparently corresponds to the churn flow regime) (C), and are shown in Fig. 3.7. The authors concluded that the characteristics of the capillary slug flow regime indicates that surface tension forces predominate over gravity forces in the flow. The slug to bubbly-slug (churn) transition is correlated with the following equation:

$$Re_V \times We_V = 2.8 \times 10^5 \quad (3.6)$$

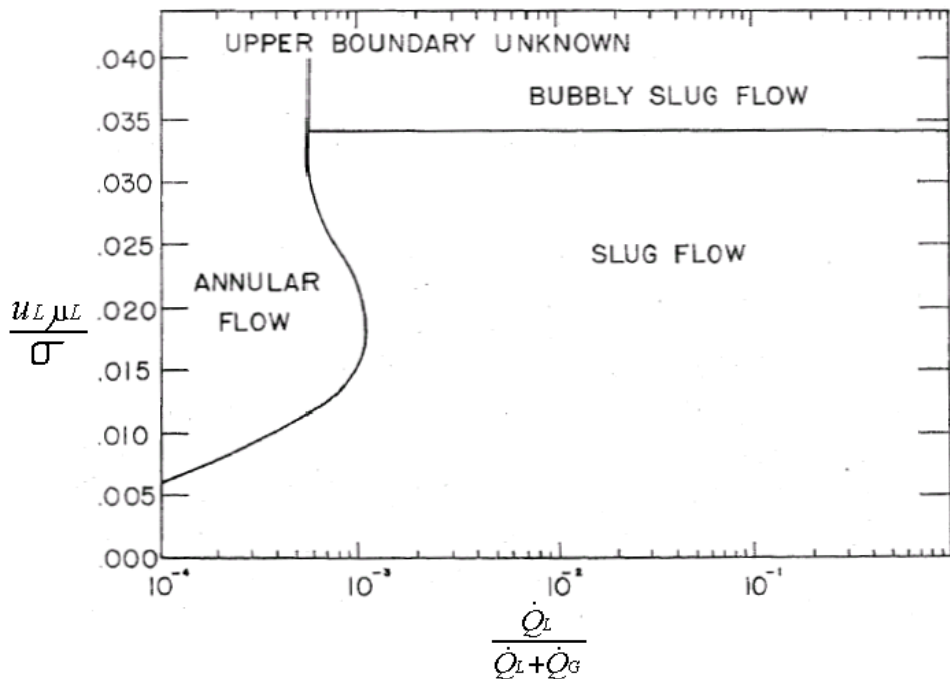


Figure 3.7: Flow pattern map of Suo and Griffith [47] for $\frac{\mu_L}{\mu_V} = 50$ and $\frac{Re_L^2}{We_L} = 0.75 \times 10^{-5}$.

The Kew and Cornwell studies

Many investigations have been carried out to determine the mechanisms involved during boiling in single and multiple narrow channels. The experimental facility of Kew and Corn-

Table 3.2: Experimental conditions of two-phase flow in microchannel.

| Year | Authors | Fluid | Size mm | L mm | Channel(s) | P bar | j_L m/s | j_V m/s | G kg/m ² s | x | q kW/m ² | Flow patterns |
|------|--------------------------|-------------------------|--|--------------------------|------------|----------|--|----------------------------------|--------------------------|--------------------------|------------------------|--|
| 1964 | Suo and Griffith [47] | Heptane/N ₂ | 0.159 | - | 1 | - | - | - | - | - | - | S, C & A |
| | | Water/N ₂ | 0.159 | - | - | - | - | - | - | - | - | - |
| | | Heptane/He | 0.1028 | - | - | - | - | - | - | - | - | - |
| | | Heptane/N ₂ | 0.1028 | - | - | - | - | - | - | - | - | - |
| | | Heptane/N ₂ | 0.1028 | - | - | - | - | - | - | - | - | - |
| 1992 | Cornwell and Kew [15] | R-113 | 0.12 x 0.9 | 300 | 75 | 1-2 | - | - | 117-627 | 3-20 | - | IB, CB, ASF & PD |
| | | | 0.325x1.1 | - | 36 | - | - | - | - | - | - | - |
| 1996 | Mertz et al. [37] | Water & R-141b | 0.1x1 | - | 101 & 1 | 1 & 2 | - | - | 50-700 | - | <300 | B, S & A |
| | | | 0.1x2 | - | 101 & 1 | - | - | - | - | - | - | - |
| | | | 0.1x3 | - | 101 & 1 | - | - | - | - | - | - | - |
| | | | 0.2x2 | - | 50 & 1 | - | - | - | - | - | - | - |
| | | | 0.2x4 | - | 50 & 1 | - | - | - | - | - | - | - |
| | | | 0.3x3 | - | 33 & 1 | - | - | - | - | - | - | - |
| | | | 0.25x1 | - | 8 | - | - | - | - | - | - | - |
| 1995 | Kew and Cornwell [16] | R-141b | 0.205 | 500 | 1 | - | - | - | 180 | 35.6 | - | IB, CB, ASF & PD |
| 1997 | Kew and Cornwell [30] | R-141b | 0.369 | 500 | 1 | 10-15 | - | - | 188-1480 | 10-100 | - | IB, CB, ASF & PD |
| | | | 0.287 | - | - | - | - | - | - | - | - | - |
| | | | 0.137 | - | - | - | - | - | - | - | - | - |
| 1999 | Thripplet et al. [54] | Air/water | 0.11 0.145 Δ 1.09 Δ 1.49 | 200 | 1 | 1 | 0.02-8 | 0.02-80 | - | - | - | B, C, S, S/A & A |
| 1999 | Coleman & Garimella [11] | Air/water | 0.5-50 0.260 0.175 0.130 0.130 0.5.6x4 0.491 | - | 1 | - | 0.01-10 | 0.1-100 | - | - | - | B, D, EB, S ₂ St, W, WA & A |
| 2000 | Coleman & Garimella [13] | R-134a | 0.1x1 0.2x2 0.3x3 0.4x4 | - | 1 | - | - | - | 150-750 | 0-1 | - | B, D, EB, S ₂ St, W, WA & A B, D, EB, S ₂ St, W, WA & A |
| 2000 | Coleman & Garimella [12] | R-134a | 0.1x1 0.2x2 0.3x3 0.4x4 | - | 1 | - | - | - | 150-750 | 0-1 | - | B, D, EB, S ₂ St, W, WA & A B, D, EB, S ₂ St, W, WA & A |
| 2000 | Sheng & Palm [45] | Water | 0.10 0.16 0.20 0.40 | 500 600 700 800 | 1 | 1 | - | - | 52-518 | - | 6.3-40 | B, CB & A |
| 2000 | Kuwahara et al. [31] | R-134a | 0.12 | - | 1 | 9.2 | - | - | 80-1260 | 0.008-0.975 | - | B, P, S, WA, & A |
| 2001 | Yang & Shieh [57] | Air/water | 0.1 0.2 0.3 0.2 | 200 400 600 400 | 1 | 1 | 0.014-134 0.006-2.1 0.006-2.1 7.7 | 0.21-75 0.13-86 0.016-91.5 | - | - | - | B, S,P, WS, D & A |
| 2001 | | R-134a | 0.3 | 600 | 1 | - | - | - | 300-1600 | 0.003-0.74 0.006-0.92 | - | B, S,P, WS, D & A |
| 2002 | Serizawa et al. [44] | Air/water & Steam/water | 0.020 0.025 0.050 | 10 | 1 | 1 | 0.003-17.52 | 0.0012-295.3 | - | - | - | B, S, R, L, A, F, RI & LD |
| 2003 | Steinke & Kandlikar [46] | Water | 0.214x0.200 | 57.15 | 6 | - | - | - | 157-1782 | - | <898 | NB, B, S, A, AN, C & DO |

Legend: A=Annular, AN=Annular Flow with Nucleation in the Thin Film, ASF=Annular-Slug Flow, B=Bubbly, C=Churn, CB=Confined bubble, D=Disperse, DO= Dry Out,
Legend: EB=Elongated Bubble, F=Frothy, IB= Isolated Bubble, L= Liquid Lump, LD=Liquid Droplets, NB=Nucleate Boiling, P=Plug, R=Liquid Ring, RI=Rivulet,
Legend: S=Slug, St=Stratified, W=Wavy, WA=Wavy-Annular, WS= Wavy-Stratified

well [15, 16, 30] was capable of accommodating either a single tubular section 500 mm long in either horizontal or vertical upflow configuration or a vertical multichannel test section (300 mm x 76 mm with either 76 or 36 channels) heated from behind and with a glass adiabatic wall in front. The test fluid was R-141b and R-113.

The flow regimes have been observed using a high speed video recorder providing 200 frames/sec. Four flow regimes may occur during evaporation in narrow channels as presented in Fig. 3.8, namely Isolated Bubble (IB), Confined Bubble (CB), Annular Slug Flow (ASF) and Partial Dryout (PD). Experimental conditions are summarized in Table 3.2. The authors concluded that in the IB regime, the heat transfer mechanism is predominantly nucleate boiling, while in the CB, ASF and PD regimes heat transfer may be by convection through and evaporation of the liquid layer separating the vapor core from the heated surface.

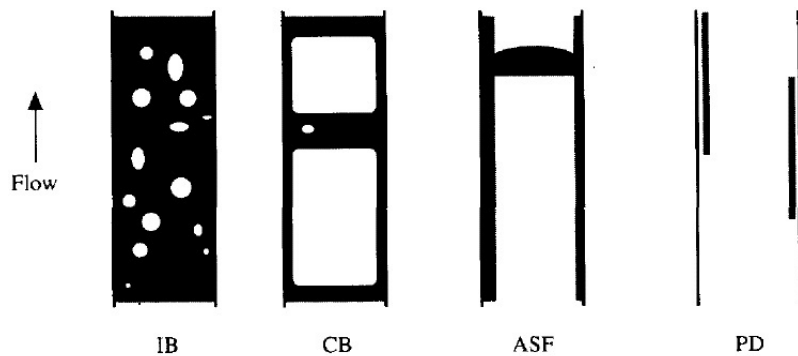


Figure 3.8: Flow patterns of Kew and Cornwell [15, 16, 30].

The Mertz et al. study

The study of flow boiling heat transfer of water and R-141b in vertical narrow rectangular channels has been carried out in Mertz et al. [37]. The experimental conditions are summarized in Table 3.2. For the multichannel test section, the flow patterns observed by the authors for water and $G = 200 \text{ kg/m}^2\text{s}$ are:

- $q \leq 20 \text{ kW/m}^2$ single bubbles
- $20 \leq q \leq 100 \text{ kW/m}^2$ confined bubbles
- $q \geq 100 \text{ kW/m}^2$ annular flow

For the multichannel tests, the flow patterns observed for R-141b and $G = 200 \text{ kg/m}^2\text{s}$ are:

- $q \leq 7 \text{ kW/m}^2$ single bubbles
- $7 \leq q \leq 20 \text{ kW/m}^2$ confined bubbles
- $q \geq 20 \text{ kW/m}^2$ annular flow

The frequencies of bubble generation increased for the smaller and flatter channels. They are estimated to be about 10 Hz for water and up to 40 Hz for R-141b. The frequencies also depended on the heat fluxes, where higher heat fluxes led to higher frequencies. For low mass fluxes and high heat fluxes, back flow was observed. For the single channel, the same conclusions as for the multichannel can be drawn.

The Tripplet et al. study

A systematic experimental investigation of two-phase flow patterns in microchannels was the objective of this study. Using air and water, experiments were conducted in circular microchannels (pyrex circular channels) with 1.1 and 1.45 mm inner diameters, and in microchannels with semi-triangular cross-sections (acrylic or polycarbonated rod was used) with hydraulic diameters 1.09 and 1.49 mm. The flow regimes in the test sections were identified visually by the authors with the aid of a strobe and a digital camera.

Flow patterns and flow pattern maps using gas and liquid superficial velocities as coordinates were similar for all the test sections. The discernible flow patterns were bubbly (B), churn (C), slug (S), slug/annular (S/A) and annular flow (A) at the experimental conditions summarized in Table 3.2, as shown in Fig 3.9. Neither of the test sections supported stratified flow, confirming the predominance of surface tension as emphasized by Tripplet et al.

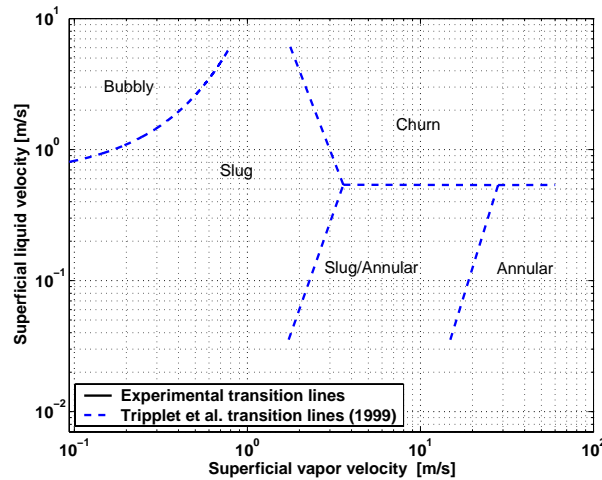


Figure 3.9: Flow pattern map for air/water in a 1.1 mm tube from Tripplet et al. [54].

The experimental data were compared with similar data of Suo and Griffith [47], Damianides and Westwater [17] with good overall agreement and with inconsistencies mainly attributable to the confusion in the identification of flow patterns. Available relevant flow regime transition models were compared with data, with poor agreement.

The Coleman and Garimella studies

Coleman and Garimella [11] investigated the effect of tube diameter and shape on flow regime transitions for two-phase flow in tubes with small hydraulic diameters. Flow patterns

for co-current flow of air/water mixtures in horizontal round and rectangular tubes are determined by high-speed video analysis to develop flow regime maps and the transitions between these flow regimes. Bubble (B), dispersed (D), elongated bubble (EB), slug (S), stratified (St), wavy (W), wavy-annular (WA) and annular flow (A) are observed. The effect of tube diameter and shape on the flow patterns for hydraulic diameters ranging from 1.3 to 5.5 mm is identified. Experimental test conditions are reported in Table 3.2. There is a suppression of the stratified flow when decreasing the tube diameter and an increase of the size of the intermittent regime. The flow map of Taitel and Dukler available for conventional channels was shown not to be valid for small diameter tubes. In 2000, Coleman and Garimella [13] proposed an experimental investigation of two-phase flow during condensation of refrigerant R-134a in a 4.91 mm round tube. The different flow patterns are presented in Fig. 3.10. In the same time the authors [12] performed experiments with four different square cross-sectional channels. A graphical flow pattern map is presented in Fig. 3.11 for R-134a.

Garimella et al. [22] proposed a correlation for during flow transition condensation of R-134a with the hydraulic diameter (in mm) as parameter to determine the transition between intermittent and non-intermittent flow as shown in Eq. (3.7).

$$x = \frac{a}{G + b} \quad (3.7)$$

with

$$a = 69.5673 + 22.595 \exp(0.2586D_h) \quad (3.8)$$

$$b = -59.9899 + 176.8137 \exp(0.3826D_h) \quad (3.9)$$


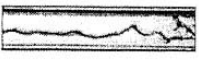














| | | FLOW REGIMES | | | |
|---|---|--|--|---|-----------|
| | | Annular | Wavy | Intermittent | Dispersed |
| Flow Patterns |  |  |  |  | |
| | Mist Flow | Discrete Wave (0) | Slug Flow | Bubbly Flow | |
| |  |  |  |  | |
| | Annular Ring | Discrete Wave (1) | Slug Flow | Bubbly Flow | |
| |  |  |  |  | |
| | Wave Ring | Discrete Wave (2) | Plug Flow | Bubbly Flow | |
|  |  |  | | | |
| Wave Packet | Disperse Wave (3) | Plug Flow | | | |
|  | Note: Numbers above denote intensity of secondary waves | | | | |
| Annular Film | Note: Numbers above denote intensity of secondary waves | | | | |

Figure 3.10: Flow patterns of Coleman and Garimella [11] study.

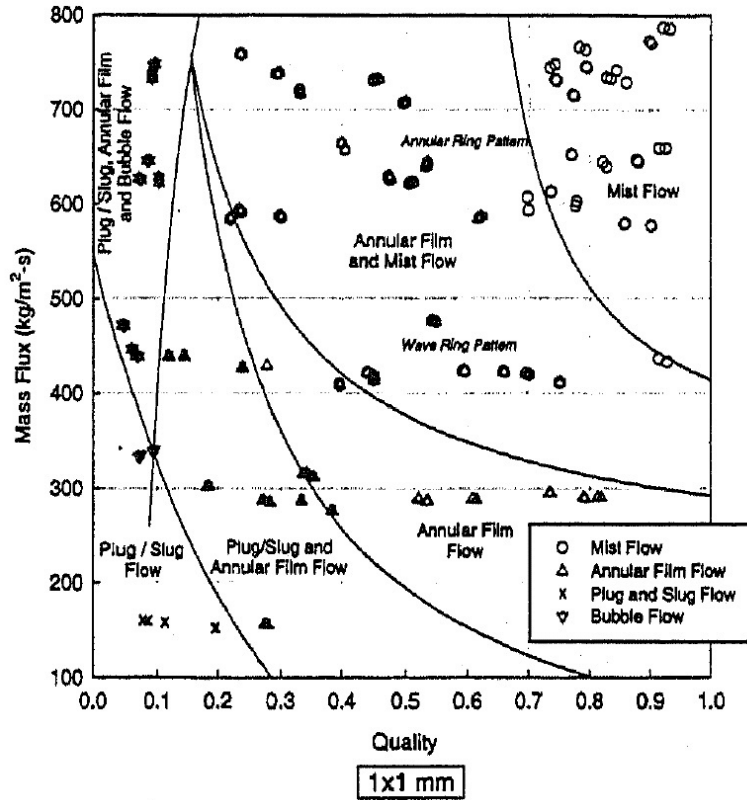


Figure 3.11: Flow pattern map of Coleman and Garimella [12] study for R-134a.

The Sheng and Palm study

Flow boiling heat transfer for water in a single glass tube has been visualized experimentally using a high-speed video camera by Sheng and Palm [45]. The experiments were done at atmospheric pressure and different flow directions (upward, downward and horizontal). Three flow regimes were sufficient to describe the patterns observed according to the authors. They are isolated bubble flow (B), slug bubble flow (probably referring to confined bubble flow (CB)) and annular flow (A). Experimental conditions are summarized in Table 3.2. The isolated bubble flow is a typical flow pattern for subcooled boiling, while the slug bubble flow and annular flow are the typical flow patterns for saturated boiling in their small diameter tubes. Horizontal and downward flow are more stable than upward flow. In horizontal flow, the flow was unsymmetrical although it is a small tube.

The Kuwahara et al. study

Kuwahara et al. [31] investigated experimentally the characteristics of flow pattern for evaporation of pure R-134a in a capillary tube of 1.2 mm inside diameter. The flow patterns were observed through a glass tube section at a constant pressure of 9.2 bar. The experimental test conditions are presented in Table 3.2. The flow patterns were visualized with a high-speed digital video camera and are: bubble (B), plug (P), slug (S), wavy-annular (WA) and annular flow (A). These flow patterns are typical of those in relatively large diameter tubes.

However, the transition points between each flow pattern are different from the modified Baker map and the Taitel-Dukler map, which are proposed for relatively large diameters.

The Yang and Shieh study

Experimental investigations of two-phase flow patterns for refrigerant R-134a and air/water in horizontal tubes was performed by Yang and Shieh [57] with experimental test conditions presented in Table 3.2. The flow patterns observed are presented in Fig. 3.12: bubble (B), slug (S), plug (P), wavy stratified (SW), dispersed (D) and annular flow (A). The authors concluded their work by saying that none of the existing flow pattern maps was able to well predict air-water and refrigerant flow in small tubes. The change in working fluid from air-water to R-134a lead to a shift in the slug to annular transition to a lower value of gas velocity. The locations of bubble to plug and slug flow transition are also significantly affected by the working fluid properties. The surface tension effect was also identified as an important parameter for flow pattern transition.

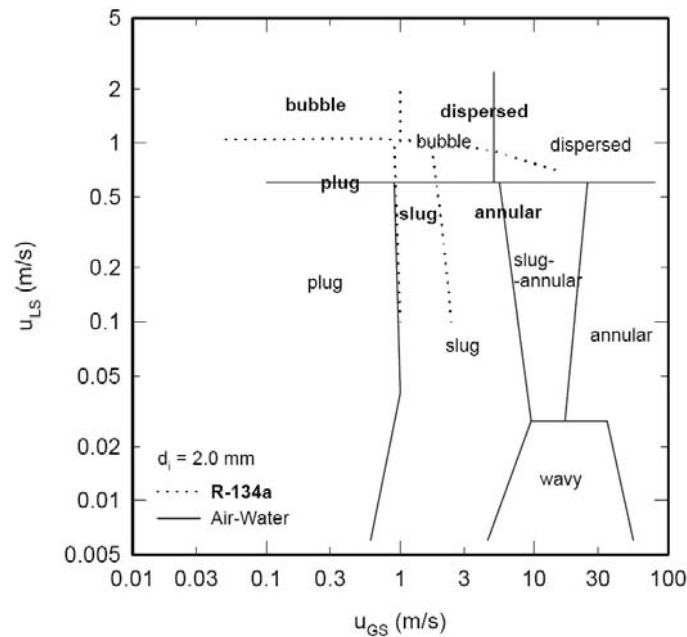


Figure 3.12: Flow patterns of Yang and Shieh [57] study.

The Serizawa et al. study

Serizawa et al. [44] viewed gas-liquid flow patterns with a microscope coupled with a high-speed video camera for air/water and steam/water flow in circular tubes of 20, 25 and 100 μm inside diameter (very small compared to the prior studies). Several distinct flow patterns, namely, dispersed bubbly flow (B), gas slug flow (S), liquid ring flow (R), liquid lump flow (L), annular flow (A), frothy flow (F), rivulet flow (Ri), liquid droplets flow (LD) and a special type of flow pattern, namely, skewed barbecue shaped flow are identified both in

air-water and steam-water systems as shown in Fig 3.13. It was confirmed that two-phase flow patterns are sensitive to the surface conditions of the inner wall of the test tube. All the experimental conditions are summarized in Table 3.2.

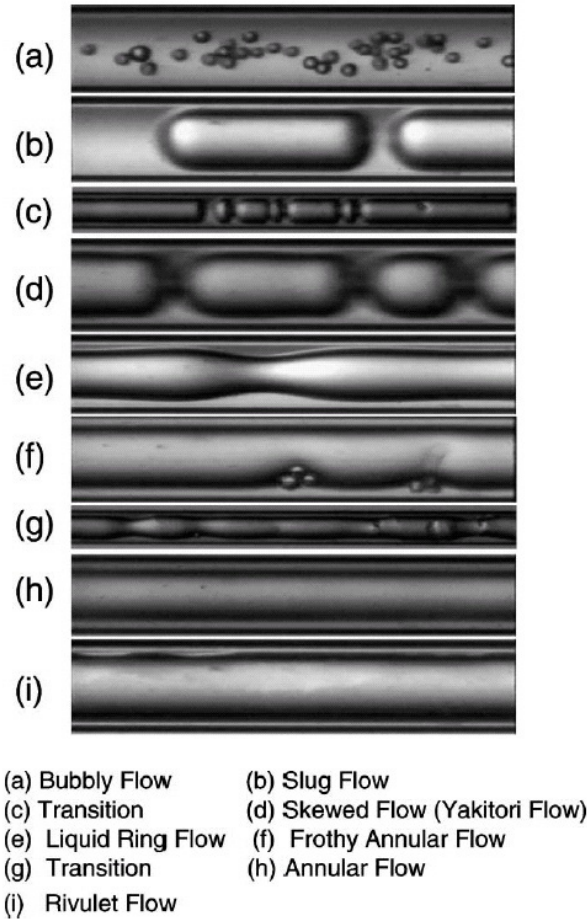


Figure 3.13: Flow patterns of Serizawa et al. [44] for air/water in a 100 μm inside diameter.

The Steinke and Kandlikar study

Steinke and Kandlikar [46] explored flow boiling and pressure drop of water in six parallel microchannels. A high-speed CCD camera was used to collect videos of the flow boiling process. The experimental test conditions are presented in Table 3.2. The following flow patterns were observed in their test section: nucleate boiling (NB), bubbly flow (B), slug flow (S), annular flow (A), annular flow with nucleation in the thin film (AN), churn (C) and dry-out (DO). Observations suggest that the conventional flow boiling patterns also occur in microchannels. They suggested that there is no difference in the theory used for conventional channels. A flow reversal was observed under certain conditions in microchannels. CHF was also observed during experimentation.

3.2.4 Conclusions

Many studies now exist on two-phase flow in microchannels and are summarized in Table 3.2. Many of them (not all presented here) are adiabatic two-phase flow experiments, i.e. liquid and gas flowing in the same pipe without any heating, generated by a gas injector or liquid-vapor mixer. The resulting flow pattern and bubble characteristics are probably imposed or influenced by the design of the injector or mixer (none of those studies addressed this issue). Only few studies were for diabatic experiments (with evaporation or condensation).

Based on the present summary of existing experimental work, one can conclude that only three principal flow patterns can be used to describe two-phase flow in microchannel : Bubbly flow, confined bubble flow and annular flow. No stratified flow is observed in microchannels due to the predominance of surface tension over gravity forces so that the tube orientation has negligible influence on the flow pattern. Too many regime designations lead to too much complexity when trying to develop a model based on these flow regimes.

The subjectivity related to the flow pattern observation and their transition determination is another difficulty. How to say if a bubble is isolated or not? How can one determine the transition from wavy-annular to annular? Many questions and uncertainties arise due to this lack of objectivity in the identification of the flow patterns. Thus, an objective method should be used to create a correct flow pattern map starting point for building heat transfer and pressure drop models.

Multiple geometries can lead to a new difficulty of fundamentally studying two-phase flow in microchannels, even if Mertz et al. found that the characteristics of two-phase flow are the same for single and multiple channels. The choice of the channel size can also be a problem because that determines either macro or microscale or the transition between them.

Thome et al. [51, 19] proposed the first mechanistic heat transfer model to describe evaporation in microchannels with a *three-zone* flow boiling model that describes the transient variation in the local heat transfer coefficient during sequential and cyclic passage of (i) a liquid slug, (ii) an evaporating elongated bubble and (iii) a vapor slug when film dryout has occurred. Fig. 1.1 depicts a schematic of their three-zone heat transfer model. The new model illustrates the strong dependency of heat transfer on the bubble frequency, the lengths of the bubbles and liquid slugs, and the liquid film thickness but is so far only applicable to the slug flow regime.

For these reasons, it is opportunistic to apply an optical measurement technique to simultaneously and quantitatively characterize flow pattern transitions, and measure the frequency, velocity and length of vapor bubbles in microchannels, in particular at the exit of microevaporators in which the flows are formed.

3.3 Void fraction

3.3.1 Homogeneous model

The homogenous model is based on the assumption that the vapor and liquid phases flow at the same average velocities. After comparison of vapor and liquid velocities defined in Eqs. (2.7) and (2.8), the void fraction can be calculated as:

$$\varepsilon = \left[1 + \left(\frac{1-x}{x} \right) \left(\frac{\rho_V}{\rho_L} \right) \right]^{-1} \quad (3.10)$$

This model represents the upper physical limit of void fractions for horizontal co-current two-phase flows. There is no surprise that the homogenous model overpredicts the real void fraction for most practical cases, where the vapor phase usually flows at the higher velocity. This ideal method is reasonably accurate only for bubbly and dispersed droplet mist flows, where the entrained phase travels at nearly the same velocity as the continuous phase. The homogenous model is also the limiting case as the pressure tends towards the critical pressure, where the difference in the phase densities disappears.

3.3.2 The general drift flux model of Zuber and Findlay

Zuber and Findlay [59] proposed the general form of the drift flux model in 1965. This model takes into account both the effect of nonuniform velocity and void profiles as well as the effect of the local relative velocity between the phases. The first effect is taken into account by a distribution parameter, whereas the weighted average drift velocity accounts for the latter.

Zuber and Findlay considered a three-dimensional problem and expressed the velocities in terms of vectors. Hence, the volumetric flux densities are defined as:

$$\vec{j}_V = \varepsilon \vec{u}_V \quad (3.11)$$

$$\vec{j}_L = (1 - \varepsilon) \vec{u}_L \quad (3.12)$$

The relative velocity between the two-phases is:

$$\vec{u}_R = \vec{u}_V - \vec{u}_L \quad (3.13)$$

and the drift velocities with respect the volumetric flux density of the mixture are:

$$\vec{V}_{Vj} = \vec{u}_V - \vec{j} \quad (3.14)$$

$$\vec{V}_{Lj} = \vec{u}_L - \vec{j} \quad (3.15)$$

and the volumetric flux density of the mixture is defined by:

$$\vec{j} = \vec{j}_V + \vec{j}_L \quad (3.16)$$

Considering the continuity equation for the liquid and gas phases, they concluded that the volumetric flux densities of the two-phases do not depend upon space coordinates but only upon time, thus:

$$\vec{j}_V + \vec{j}_L = \vec{j}(t) \quad (3.17)$$

Zuber and Findlay proposed the average value of a scalar or of a vector quantity F over the cross-sectional area of the duct defined by:

$$\langle F \rangle = \frac{1}{A} \int_A F dA \quad (3.18)$$

Introducing the expressions for the local values of the local velocities u_V calculated from (3.14) into (3.18), they obtained the average velocities (over the cross-sectional area) of the vapor; thus

$$\langle u_V \rangle = \left\langle \frac{j_V}{\varepsilon} \right\rangle = \langle j \rangle + \langle V_V j \rangle \quad (3.19)$$

However, the system input parameters readily available to a designer or to an experimenter are the average volumetric flux densities defined by

$$\langle j_V \rangle = \langle \varepsilon u_V \rangle = \frac{Q_V}{A} \quad (3.20)$$

In view of these relations, Zuber and Findlay considered the weighted mean value of the quantity F , defined by:

$$\bar{F} = \frac{\langle \varepsilon F \rangle}{\langle \varepsilon \rangle} = \frac{\frac{1}{A} \int_A \varepsilon F dA}{\frac{1}{A} \int_A \varepsilon dA} \quad (3.21)$$

whence they obtained the weighted mean velocity \bar{u}_V of the gas phase, which is

$$\bar{u}_V = \frac{\langle u_V \varepsilon \rangle}{\langle \varepsilon \rangle} = \frac{\langle j_V \rangle}{\langle \varepsilon \rangle} \quad (3.22)$$

In view of equation (3.14), the weighted mean velocity also can be expressed as:

$$\bar{u}_V = \frac{\langle \varepsilon j \rangle}{\langle \varepsilon \rangle} + \frac{\langle \varepsilon V_V j \rangle}{\langle \varepsilon \rangle} \quad (3.23)$$

In general, the average velocity $\langle u_V \rangle$ defined by Eq. (3.19) is not equal to the weighted mean velocity \bar{u}_V defined by Eqs. (3.22) and (3.23).

The weighted mean velocity \bar{u}_V can be cast in several forms which are useful for analysing experimental data and for determining the average volumetric concentration (void fraction) $\langle \varepsilon \rangle$. Thus, multiplying and dividing the first term on the right-hand side of Eq. (3.23) by $\langle j \rangle$, we obtain

$$\bar{u}_V = \frac{\langle j_V \rangle}{\langle \varepsilon \rangle} = C_o \langle j \rangle + \frac{\langle \varepsilon V_{Vj} \rangle}{\langle \varepsilon \rangle} \quad (3.24)$$

where the distribution parameter C_o is defined by:

$$C_o = \frac{\langle \varepsilon j \rangle}{\langle \varepsilon \rangle \langle j \rangle} = \frac{\frac{1}{A} \int_A \varepsilon j dA}{\left[\frac{1}{A} \int_A j dA \right] \left[\frac{1}{A} \int_A \varepsilon dA \right]} \quad (3.25)$$

Equation (3.24) can be expressed in a nondimensional form by dividing both sides of $\langle j \rangle$, thus

$$\frac{\langle \beta \rangle}{\langle \varepsilon \rangle} = C_o + \frac{\langle \varepsilon V_{Vj} \rangle}{\langle \varepsilon \rangle \langle j \rangle} \quad (3.26)$$

which after rearranging, results in the general expression for predicting the average volumetric concentration (void fraction) $\langle \varepsilon \rangle$ in the form:

$$\langle \varepsilon \rangle = \frac{\langle \beta \rangle}{C_o + \frac{\langle \varepsilon V_{Vj} \rangle}{\langle \varepsilon \rangle \langle j \rangle}} \quad (3.27)$$

where $\langle \beta \rangle$ is the average volumetric flow concentration corresponding to the homogeneous void fraction:

$$\langle \beta \rangle = \frac{\langle j_V \rangle}{\langle j \rangle} = \frac{Q_V}{Q_V + Q_L} = \left[1 + \left(\frac{1-x}{x} \right) \left(\frac{\rho_V}{\rho_L} \right) \right]^{-1} \quad (3.28)$$

In contrast to previous analyses, Zuber and Findlay derived an expression, which is applicable to any two-phase flow regime. Furthermore, the analysis takes into account both the effect of nonuniform flow and void profiles and the effect of the local relative velocity. The first effect is accounted for by the distribution parameter C_o , whereas the second one is accounted for by the weighted mean drift flux velocity $\langle \varepsilon V_{Vj} \rangle / \langle \varepsilon \rangle$. For each particular flow regime, the value of the average volumetric void fraction $\langle \varepsilon \rangle$ can be obtained from the general expression (3.27) by inserting the appropriate velocity and void profiles and the appropriate expression for the drift velocity.

Zuber and Findlay showed that the distribution parameter C_o depends on the flow structure. Analyzing experimental results in $\langle j \rangle - \bar{u}_V$ coordinates, they showed linear dependence of the

results for slug, bubbly and annular flow regimes. According to Eq. (3.24), for a particular two-phase flow pattern, the slope of such a straight line gives the value of the distribution parameter C_o , whereas the intercept of this line with the $\bar{u}_V = \frac{\langle j_V \rangle}{\langle \varepsilon \rangle}$ axis gives the value of the weighted mean drift velocity \bar{V}_{Vj} .

Without any reference to flow pattern, a mean value of $C_o = 1.13$ correlated the steam-water mixture data of Zuber *et al.* [60] at elevated pressures. For vertical slug flow they proposed $C_o = 1.2$.

The weighted mean drift flux velocity obtained by Zuber and Findlay for the vertical, slug flow regime is

$$\bar{V}_{Vj} = \frac{\langle \varepsilon V_{Vj} \rangle}{\langle \varepsilon \rangle} = 0.35 \left[\frac{gpD}{\rho_L} \right]^{0.5} \quad (3.29)$$

and for the vertical, bubbly churn-turbulent regime it is

$$\bar{V}_{Vj} = \frac{\langle \varepsilon V_{Vj} \rangle}{\langle \varepsilon \rangle} = 1.53 \left[\frac{\sigma gp}{\rho_L^2} \right]^{0.25} \quad (3.30)$$

Zuber *et al.* [60] proposed for vertical flows of steam-water mixtures at elevated pressure, a mean value of \bar{V}_{Vj} applicable without any reference to flow regime as

$$\bar{V}_{Vj} = \frac{\langle \varepsilon V_{Vj} \rangle}{\langle \varepsilon \rangle} = 1.41 \left[\frac{\sigma gp}{\rho_L^2} \right]^{0.25} \quad (3.31)$$

In the case of a horizontal flow, the weighted mean drift flux velocity without buoyancy is

$$\bar{V}_{Vj} = 0 \quad (3.32)$$

As can be seen, the drift flux model of Zuber and Findlay allows one to calculate the void fraction $\langle \varepsilon \rangle$ taking into account numerous aspects occurring in two-phase flow. They presented their model for specific flow patterns and hence there is not a continuous transition in void fraction values between different flow regimes.

3.3.3 The Triplet *et al.* study

Void fraction and two-phase frictional pressure drop in microchannels were experimentally investigated by Triplet *et al.* [53]. Using air and water, experiments were conducted in transparent circular microchannels with 1.1 and 1.45 mm inner diameters and in microchannels with semi-triangular (triangular with one corner smoothed) cross-sections with hydraulic diameters of 1.09 and 1.49 mm. Gas and liquid superficial velocities were varied in the 0.02 to 80 m/s and 0.02 to 8 m/s ranges, respectively, and void fractions were calculated by analyzing photographs taken from the test sections with the circular cross-section.

Each photograph typically covered a 6 mm-long segment of the test section. In the bubbly flow pattern, individual bubbles were assumed to be spheres or ellipsoids, depending on

their shape. In slug flow, the Taylor bubbles were divided into cylinders and spherical segments. In bubbly flow each photo typically covered a large number of bubbles, thus providing a reasonable volume-averaged estimate of the void fraction. In slug flow the flow pattern is relatively regular and average Taylor bubble and liquid slug lengths were calculated from multiple photos and used for void fraction calculation. In the annular flow pattern the vapor core was divided into several cylinders and the channel average void fraction was calculated accordingly. Slug-annular and churn flow patterns were the most difficult flow regimes to analyze according to the authors. The void fractions associated with slug-annular flow patterns were not included in the analysis due to their high uncertainty. In churn flow, an average of 0.5 local void fraction was assumed in segments of the flow field where the gas phase was dispersed. The accuracy of this approach was not addressed in their paper.

Measured void fractions were compared with several correlations as shown in Fig. 3.14. The homogeneous flow model provided the best prediction of the experimental void fractions in bubbly and slug flow patterns. The homogeneous flow model and all other tested empirical correlations significantly over predicted the void fractions in annular flow, however.

3.3.4 The Serizawa et al. study

Serizawa et al. [44] in their work visualized gas-liquid flow patterns with a microscope coupled with a high-speed video camera for air/water and steam/water flow in circular tubes of 20, 25 and 100 μm inside diameter. The cross-sectional averaged void fraction was calculated from high-speed video pictures, by assuming symmetrical shape of bubbles and gas slugs, and thus the void fraction presented here concerns only with bubbly flow and slug flow. Results for 11 observations are demonstrated in their graph shown in Fig. 3.15. Liquid ring flow is axi-symmetrical, but not included in this figure. Although the present data scatter to some extent in nature, the present data are well correlated with the Armand correlation (Armand and Treschev [4]) for air-water flow. In fact, however, statistically the homogeneous model better predicts their data.

3.3.5 The Chung and Kawaji study

Chung and Kawaji [10] investigated the effect of channel diameter on two-phase flow to identify the phenomena which distinguishes microchannels from minichannels. They conducted experiments with a mixture of nitrogen gas and water in circular channels of 530, 250, 100, and 50 μm diameter.

Different methods of image analysis were used in determining the space and ensemble-average void fraction from the video images of the gas-liquid interface. The void fraction data in the 530 and 250 μm channels were deduced from about 300 video images in each experimental run. Initially, these images were sorted by flow pattern into nine categories: (a) liquid alone; (b) gas bubble; (c) short gas slug; (d) long gas slug; (e) liquid slug; (f) nose of gas slug; (g) tail of gas slug; (h) liquid ring and (i) deformed interface. The void fraction was calculated by fitting the region occupied by gas to shapes of symmetrical volume and estimating the fraction of gas volume.

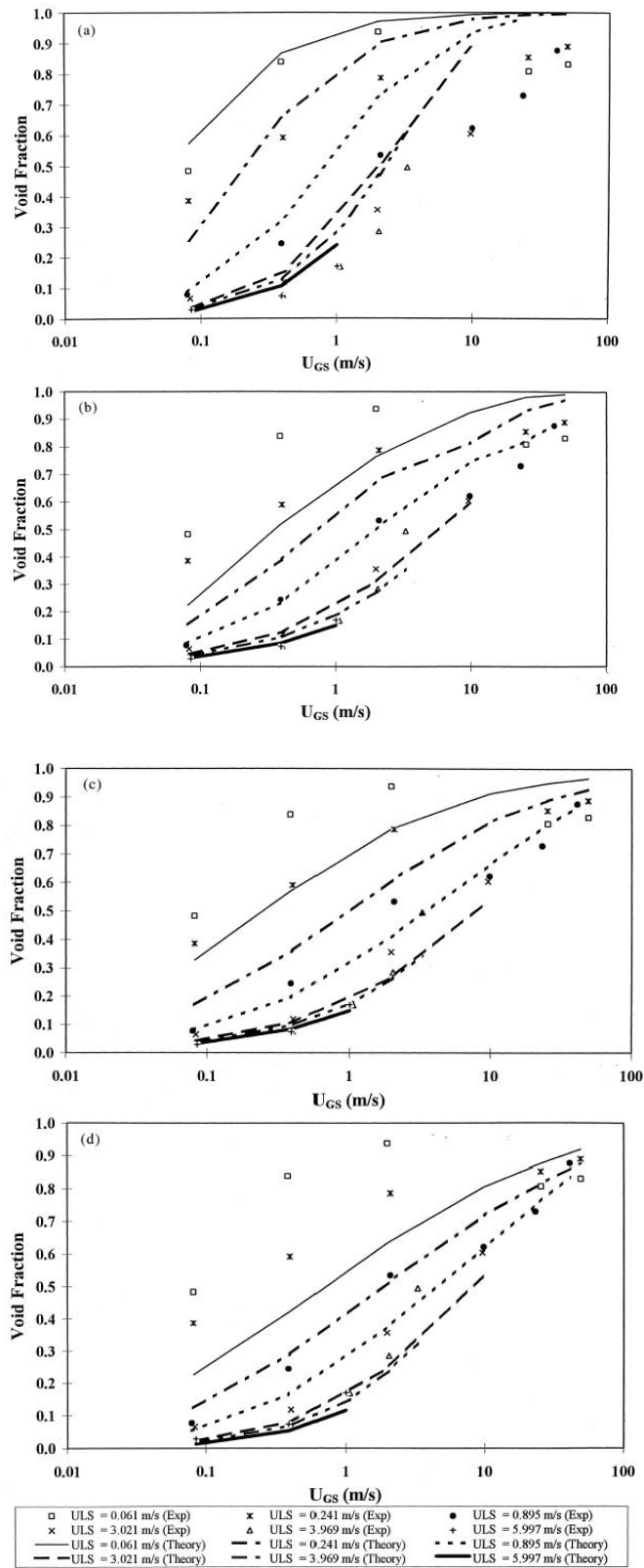


Figure 3.14: Comparison of measured void fractions of Tripplet et al. [53] with predictions of various correlations for the round tube: (a) homogeneous flow model; (b) Chexal et al. [7]; (c) Lockart-Martinelli-Butterworth [5]; (d) CISE [40].

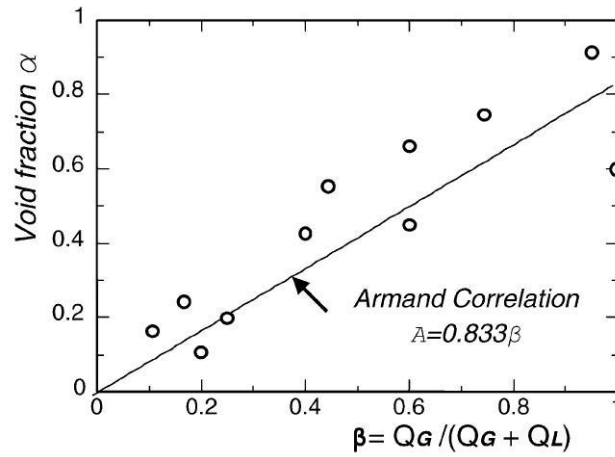


Figure 3.15: Cross-sectional average void fraction of Serizawa et al. [44] in air-water two-phase flow in a 20 μm ID silica tube.

To estimate the void fraction in the 100 and 50 μm microchannels, image analysis was performed on 200-500 video images in each run. The images were assigned a void fraction of zero when they depicted liquid flowing alone or a void fraction of unity when they depicted gas core flow with a thin-smooth liquid film or ring-shaped liquid film. The authors explained that this assignment works because the gas core flow in the images always fills the whole axial field-of-view. For a thick-smooth liquid film, the volume fraction of gas was estimated by squaring the ratio of the gas core radius to the channel radius (Kawahara et al. [28]). The effect of optical distortion on the above mentioned method of measuring the void fraction, particularly for gas core flows with ring-shaped films and thick liquid films, was already addressed by Kawahara et al. [28]. No independent method was used to verify the accuracy of this approach, such as use of a gravimetric balance without flow.

Figure 3.16 presents the time-averaged void fraction, ε , plotted against the volumetric quality, β , for all four microchannel sizes. The void fraction expression for homogeneous flow ($\varepsilon = \beta$) and the correlation for narrow channels ($\varepsilon = 0.8\beta$) recommended by Ali et al. [3] for narrow channels of $D = \sim 1$ mm are shown as a dotted and dashed line in the figures, respectively. Both show a linear relationship between the void fraction and volumetric quality. The void fraction for the 530 μm channel is predicted well by the homogeneous flow model, while that for the 250 μm channel agrees favorably with the Armand-type correlation recommended for a minichannel. On the contrary, the void fraction data for the 100 and 50 μm microchannels do not correlate with either the homogeneous flow model or an Armand-type correlation. The void fraction-to-volumetric quality relationship is instead non-linear. The following empirical correlation was fitted by them to the void fraction data for the 100 and 50 μm channels and is plotted as a solid curve in Fig. 3.16:

$$\varepsilon = \frac{C_1 \beta^{0.5}}{1 - C_2 \beta^{0.5}} \quad (3.33)$$

where C_1 and C_2 are constants based on the experimental results. $C_1 = 0.03$ and $C_2 = 0.97$ for the 100 μm circular channel; $C_1 = 0.02$ and $C_2 = 0.98$ for the 50 μm circular channel.

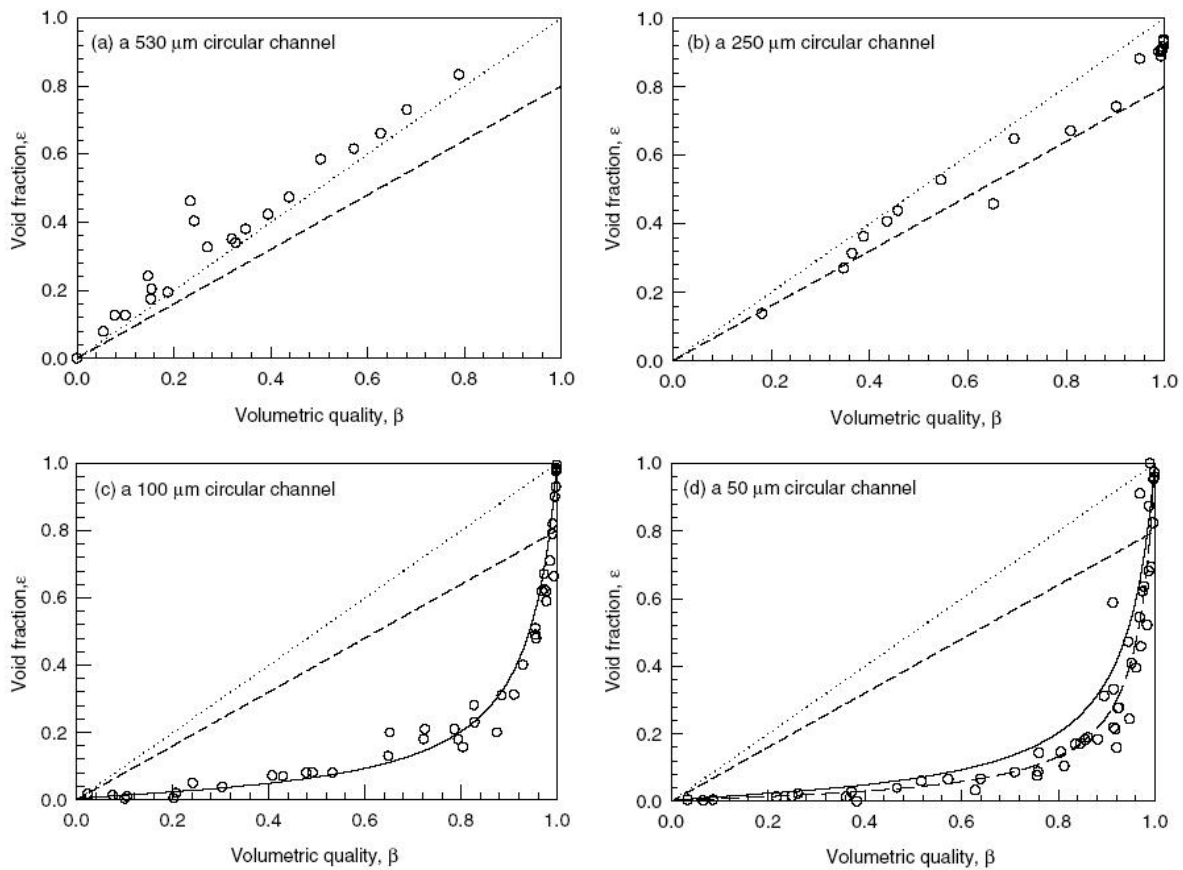


Figure 3.16: Relationship between void fraction and volumetric quality in the study of Chung and Kawaji [10]. (— Armand correlation, \cdots Homogeneous model).

3.3.6 The Kawahara et al. study

An experimental investigation has been carried out by Kawahara et al. [29] on nitrogen gas-water and nitrogen gas-water/ethanol two-phase flows in circular microchannels with diameters ranging between 50 and 251 μm . The time-average void fraction data were obtained by image analysis as that of the Chung and Kawaji [10] work, and their dependence on homogeneous void fraction was examined to determine the effects of channel diameter and fluid properties such as surface tension and liquid viscosity. From the results obtained, the following conclusions can be given.

In the 50, 75 and 100 μm diameter microchannels, the void fraction data showed (Fig. 3.17) similar nonlinear variations with homogeneous void fraction. On the other hand, the void fraction data obtained in a 251 μm channel varied linearly with homogeneous, conforming to the Armand type void fraction correlation regardless of the ethanol concentration. The liquid viscosity was, however, found to lower the void fraction in 75 and 100 μm diameter microchannels at high superficial gas velocities or $\beta > 0.8$.

These results suggest that the void fraction relation with homogeneous void fraction drastically changes in microchannels at a channel diameter between 251 and 100 μm . On the other

hand, the effects of fluid properties examined here such as surface tension and liquid viscosity were found to have much less an influence on void fraction in two-phase flow in comparison with the channel diameter. Further experiments are necessary, however, to investigate the fluid property effects over a wider range of properties.

3.3.7 Conclusions

Only a limited studies exist on void fraction in microchannels. All experimental investigations have been carried out in adiabatic two-phase flow. The evaporating process is not taken into account. The generation of the bubbles does not come from the nucleation process in a microevaporator but from a gas-liquid mixer. Thus, it is adventurous to conclude anything for diabatic conditions.

In general, for microchannels, the number of variation of the void fraction with the volumetric flow rate is linear. The data are usually well fitted by the homogeneous model or the Armand correlation. For very small microchannels, the variation of the void fraction is very nonlinear and new correlations have been found with different constants as presented by Chung and Kawaji [10]. But it is difficult to compare the results for the different channel diameters because the authors change the way to determine void fraction (cross-sectional void fraction for larger diameters and essentially a centerline void fraction for smaller ones).

The main problem in studying void fraction is the measurement technique. No method is perfect but some are more accurate than others. All should be double-checked using some type of second method. The problem with the visualization technique as proposed by the authors is the distortion effect (corrected in general but more or less accurately), the spatial distribution of the vapor (usually it is symmetrical in microchannels, however the vapor can move to the upper part of the tube when the channel diameter is increased) and the uncertainty related to the film thickness measurement (few microns). This last problem is sometimes omitted by calculating the centerline void fraction as for Chung and Kawaji [10] work. Many techniques exist for macroscale void fraction measurement, such as that of Wojtan et al. [56]. While it is a very reliable technique, however the channel size is the limitation of this dynamic measurement technique.

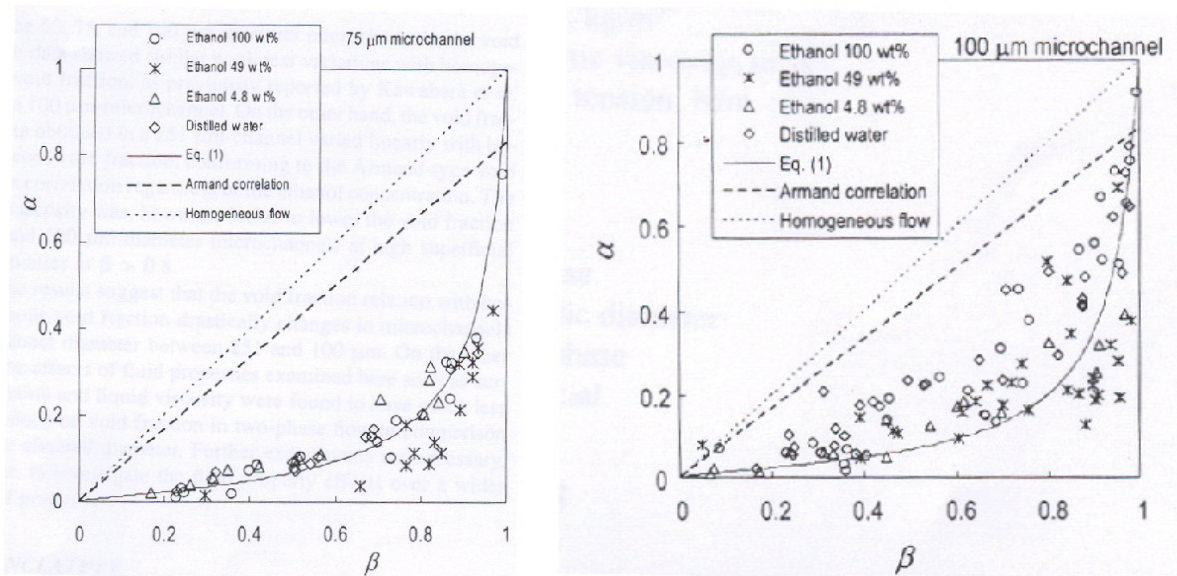
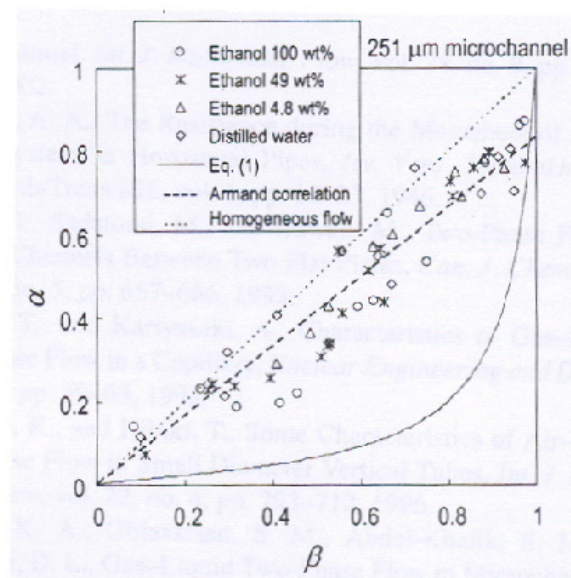
(a) Data for 75 μm microchannel.(b) Data for 100 μm microchannel.(c) Data for 251 μm microchannel.

Figure 3.17: Effect of ethanol concentration on the void fraction data for different diameter in the study of Kawahara et al. [29].

3.4 Two-phase pressure drop

3.4.1 Homogeneous model

A homogeneous fluid is a convenient concept, which makes analysis of two-phase flows easier: this ideal-fluid obeys the usual equation of a single-phase fluid and is characterized by suitably averaged properties.

The total pressure drop of a fluid is due to the variation of kinetic and potential energy and that due to friction, so that the pressure drop is the sum of the static pressure drop (elevation head), the momentum pressure drop (acceleration) and frictional pressure drop:

$$\left(\frac{dP}{dz}\right)_t = \left(\frac{dP}{dz}\right)_s + \left(\frac{dP}{dz}\right)_m + \left(\frac{dP}{dz}\right)_f \quad (3.34)$$

The static pressure drop in a horizontal microchannel is 0.

$$\left(\frac{dP}{dz}\right)_s = 0 \quad (3.35)$$

The momentum pressure drop takes into account the acceleration of the flow due to the flashing or diabatic effect and is defined as follows:

$$\left(\frac{dP}{dz}\right)_m = G^2 \frac{\Delta x}{L(\rho_L - \rho_V)} \quad (3.36)$$

where Δx is the variation of the vapor quality along the adiabatic tube.

The frictional pressure drop is given by the following equation:

$$\left(\frac{dP}{dz}\right)_f = \left(\frac{dP}{dz}\right)_{TP} = \frac{2f_{TP}G^2}{D\rho_{TP}} \left[1 + \frac{\Delta x}{2} \left(\frac{\rho_V}{\rho_L - \rho_V}\right)\right] \quad (3.37)$$

where ρ_{TP} is the two-phase mixture density and is given by

$$\rho_{TP} = \left(\frac{x}{\rho_V} + \frac{1-x}{\rho_L}\right)^{-1} \quad (3.38)$$

and f_{TP} the friction factor defined as:

$$f_{TP} = \frac{16}{Re_{TP}} \text{ for } Re_{TP} < 2000 \quad (3.39)$$

$$f_{TP} = 0.079Re_{TP}^{-0.25} \text{ for } Re_{TP} > 2000 \quad (3.40)$$

with

$$Re_{TP} = \frac{GD}{\mu_{TP}} \quad (3.41)$$

Three possible forms of the two-phase viscosity models are:

i) an equation proposed by McAdams et al. [36] in 1942:

$$\mu_{TP} = \left(\frac{x}{\mu_V} + \frac{1-x}{\mu_L} \right)^{-1} \quad (3.42)$$

ii) the definition chosen by Cicchitti et al. [8] in 1960:

$$\mu_{TP} = (x\mu_V + (1-x)\mu_L) \quad (3.43)$$

iii) the relation of Dukler et al. [18] in 1964:

$$\mu_{TP} = \rho_{TP} \left(x \frac{\mu_V}{\rho_V} + (1-x) \frac{\mu_L}{\rho_L} \right) \quad (3.44)$$

3.4.2 The separated flow model of Lockhart and Martinelli

The separated flow model considers the two-phases to be artificially separated into two streams, each flowing in its own pipe. The cross-sectional flow areas of the two pipes are proportional to the void fraction. The basic equations for the separated flow model are not dependent on the particular flow configuration adopted. It is assumed that the velocities of each phase are uniform, in any given cross-section, within the zone occupied by the phase. The first of these analyses was performed by Lockhart and Martinelli [34] in 1949.

They assumed that the gas-phase and liquid-phase pressure drops are equal, irrespective of the flow pattern so that:

$$\left(\frac{dP}{dz} \right)_f = \left(\frac{dP}{dz} \right)_L \Phi_L^2 \quad (3.45)$$

where $\left(\frac{dP}{dz} \right)_L$ is given by Eq. (2.38) and the two-phase friction multiplier is defined by:

$$\Phi_L^2 = 1 + \frac{C}{X} + \frac{1}{X^2} \quad (3.46)$$

X is the Martinelli parameter defined in Eq. (2.37). C has the following values:

| <i>Liquid</i> | <i>Gas</i> | <i>C</i> |
|---------------|----------------|----------|
| turbulent | turbulent (tt) | 20 |
| viscous | turbulent (vt) | 12 |
| turbulent | viscous (tv) | 10 |
| viscous | viscous (vv) | 5 |

3.4.3 The Friedel correlation

The Friedel [20] correlation for the two-phase frictional pressure gradient multiplier is

$$\Phi_{LO}^2 = E + \frac{3.24FH}{Fr^{0.045}We^{0.035}} \quad (3.47)$$

so that we can calculate the frictional pressure drop as

$$\left(\frac{dP}{dz}\right)_f = \left(\frac{dP}{dz}\right)_{LO} \Phi_{LO}^2 \quad (3.48)$$

where $\left(\frac{dP}{dz}\right)_{LO}$ is the pressure drop for all liquid flow defined as

$$\left(\frac{dP}{dz}\right)_{LO} = f_{LO} \frac{2G^2}{D\rho_L} \quad (3.49)$$

with f_{LO} given by Eqs. (3.50) and (3.51).

$$f_{LO} = \frac{16}{Re_{LO}} \text{ for } Re_{LO} < 2000 \quad (3.50)$$

$$f_{LO} = 0.079Re_{LO}^{-0.25} \text{ for } Re_{LO} > 2000 \quad (3.51)$$

with Re_{LO} from Eq. (2.29).

The various parameters in the two-phase multiplier equation are defined as follows:

$$Fr = \frac{G^2}{gD\rho_H^2} \quad (3.52)$$

$$E = (1-x)^2 + x^2 \frac{\rho_L f_{VO}}{\rho_V f_{LO}} \quad (3.53)$$

where f_{LO} (Eqs. (3.50) and (3.51)) and f_{VO} (Eqs. (3.54) and (3.55)) are the friction factors for the total mass flux G flowing with gas and liquid properties, respectively:

$$f_{VO} = \frac{16}{Re_{VO}} \text{ for } Re_{VO} < 2000 \quad (3.54)$$

$$f_{VO} = 0.079 Re_{VO}^{-0.25} \text{ for } Re_{VO} > 2000 \quad (3.55)$$

with Re_{VO} from Eq. (2.30).

Furthermore,

$$F = x^{0.78}(1-x)^{0.224} \quad (3.56)$$

and the empirical factor H is

$$H = \left(\frac{\rho_L}{\rho_V}\right)^{0.91} \left(\frac{\mu_V}{\mu_L}\right)^{0.19} \left(1 - \frac{\mu_V}{\mu_L}\right)^{0.7} \quad (3.57)$$

The Weber number is defined as:

$$We = \frac{G^2 D}{\sigma \rho_H} \quad (3.58)$$

where homogeneous density ρ_H in this method is defined as

$$\rho_H = \left(\frac{x}{\rho_V} + \frac{1-x}{\rho_L}\right)^{-1} \quad (3.59)$$

3.4.4 The Chisholm's method

Chisholm [9] proposed the following equation for the calculation of the frictional pressure drop:

$$\left(\frac{dP}{dz}\right)_f = \left(\frac{dP}{dz}\right)_{LO} \Phi_{LO}^2 \quad (3.60)$$

where the one-phase pressure gradient can be calculated as:

$$\left(\frac{dP}{dz}\right)_{LO} = f_{LO} \frac{2G^2}{D\rho_L} \quad (3.61)$$

where f_{LO} is given by Eqs. (3.50) and (3.51), and

$$\left(\frac{dP}{dz}\right)_{VO} = f_{VO} \frac{2G^2}{D\rho_V} \quad (3.62)$$

where f_{VO} is given by Eqs. (3.54) and (3.55).

The two-phase multiplier is:

$$\Phi_{LO}^2 = 1 + (Y^2 - 1) \left[Bx^{\frac{2-n}{2}} (1-x)^{\frac{2-n}{2}} + x^{2-n} \right] \quad (3.63)$$

where the exponent $n = 0.25$ and the Chisholm parameter Y is:

$$Y^2 = \frac{(dP/dz)_{VO}}{(dP/dz)_{LO}} \quad (3.64)$$

If the Chisholm parameter Y is $0 < Y < 9.5$, the parameter B is:

$$\begin{aligned} B &= \frac{55}{G^{0.5}} \quad \text{for } G \geq 1900 \text{ kg/m}^2\text{s} \\ B &= \frac{2400}{G} \quad \text{for } 500 < G < 1900 \text{ kg/m}^2\text{s} \\ B &= 4.8 \quad \text{for } G < 500 \text{ kg/m}^2\text{s} \end{aligned}$$

If $9.5 < Y < 28$

$$\begin{aligned} B &= \frac{520}{YG^{0.5}} \quad \text{for } G \leq 600 \text{ kg/m}^2\text{s} \\ B &= \frac{21}{Y} \quad \text{for } G > 600 \text{ kg/m}^2\text{s} \end{aligned}$$

For $Y > 28$,

$$B = \frac{15000}{Y^2 G^{0.5}}$$

3.4.5 The Mishima and Hibiki study

Mishima and Hibiki [38] measured the frictional pressure loss for air-water flows in vertical capillary tubes whose dimensions are summarized in Table 3.3 with inner diameters in the range from 1 to 4 mm.

The overall pressure loss in the pressure measuring section as shown in Table 3.3 was measured with three differential pressure transducers. The frictional pressure loss was calculated by neglecting the pressure loss due to the acceleration of the fluids and subtracting the pressure loss due to gravity from the overall pressure loss.

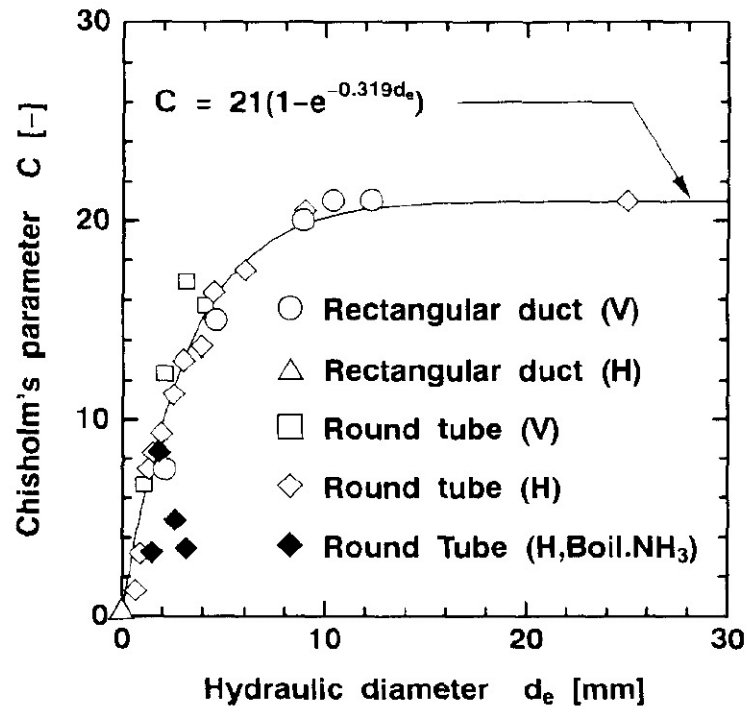
The results were compared with the Lockhart and Martinelli model (Eq. (3.45)). The frictional pressure loss was reproduced well by Chisholm's equation with a new equation for Chisholm's parameter C as a function of inner diameter defined as followed:

Table 3.3: Dimensions of the test section of Mishima and Hibiki [38].

| Diameter (mm) | Tube Material | Entrance calming sect. (mm) | Pressure measuring sect. (mm) | Exit sect. (mm) |
|------------------|------------------|--------------------------------|----------------------------------|--------------------|
| 1.05 | Glass | 220 | 210 | 220 |
| 2.05 | Glass | 320 | 310 | 320 |
| 3.12 | Glass | 420 | 510 | 420 |
| 4.08 | Glass | 500 | 1000 | 500 |
| 1.09 | Aluminum | 140 | 440 | 140 |
| 2.10 | Aluminum | 140 | 440 | 140 |
| 3.08 | Aluminum | 140 | 440 | 140 |
| 3.90 | Aluminum | 500 | 1000 | 500 |

$$C = 21 \left(1 - e^{-0.319D}\right) \quad (3.65)$$

where D is the inner diameter in mm (hence the exponent is dimensional, not dimensionless). Figure 3.18 shows the variation of C as a function of the hydraulic diameter.

Figure 3.18: Parameter C for round tubes and rectangular ducts of Mishima and Hibiki [38].

This equation predicted all the data of different studies except those for ammonia-vapor flow within an error of $\pm 12\%$. For the data for ammonia-vapor flow, the error becomes 25% . It should be noted here that the value of parameter C becomes zero when the hydraulic diameter is as small as 0.2 mm.

3.4.6 The Lee and Lee study

Lee and Lee [32] proposes new correlations for the two-phase pressure drop through horizontal rectangular channels with small gaps (heights) based on 305 data points. The gap between the upper and the lower plates of each channel ranges from 0.4 to 4 mm while the channel width was fixed to 20 mm. Water and air were used as the test fluids. The entire length of the test section was 640 mm, and three pressure taps were drilled along the centerline of the lower plate of the test section. The first one is to monitor the reference pressure of the test section and the pressure drop is measured between the two other taps using the differential pressure gauges.

The superficial velocity ranges of water and air were 0.03-2.39 and 0.05-18.7 m/s, respectively. The atmospheric pressure condition was maintained at the exit throughout the experiments. The authors expressed the two-phase frictional multiplier using the Lockhart-Martinelli type correlation but with the modification on parameter C as presented in Eq. (3.66).

$$C = A\lambda^q\psi^r Re_{LO}^s \quad (3.66)$$

where

$$\lambda = \frac{\mu_L^2}{\rho_L \sigma D} \quad (3.67)$$

and

$$\psi = \frac{\mu_L j}{\sigma} \quad (3.68)$$

The exponents A , q , r and s are given in Table 3.4.

Table 3.4: Constant and exponents for parameter C of Lee and Lee [32].

| Flow Regime | | A | q | R | S | Range of X | Range of Re_{LO} | Number of data |
|-------------|-----------|------------------------|--------|-------|-------|--------------|--------------------|----------------|
| Liquid | Gas | | | | | | | |
| Laminar | Laminar | 6.833×10^{-8} | -1.317 | 0.719 | 0.557 | 0.776-14.176 | 175-1480 | 106 |
| Laminar | Turbulent | 6.185×10^{-2} | 0 | 0 | 0.726 | 0.303-1.426 | 293-1506 | 52 |
| Turbulent | Laminar | 3.627 | 0 | 0 | 0.174 | 3.276-79.415 | 2606-17642 | 85 |
| Turbulent | Turbulent | 0.408 | 0 | 0 | 0.451 | 1.309-14.781 | 2675-17757 | 62 |

Laminar: $Re_L, Re_G < 2000$; Turbulent: $Re_L, Re_G > 2000$

The data are predicted by Eq. (3.66) and fall within a $\pm 10\%$ error band as shown in Fig. 3.19, by resorting to 10 empirical constants.

3.4.7 The Kawahara et al. study

An experimental investigation has been carried out by Kawahara et al. [28] on two-phase flow characteristics in a 100 μm diameter circular tube with a 64.5 mm length. The transparent capillary tube was made of fused silica, in which de-ionized water and nitrogen gas were injected at superficial velocities of $j_G = 0.1 - 60$ m/s for gas, and $j_L = 0.02 - 4$ m/s for liquid. The outlet pressure was atmospheric.

The present data are compared with the homogeneous flow model predictions using the different viscosity models given in Section 3.4.1. It is clear that the agreement between the

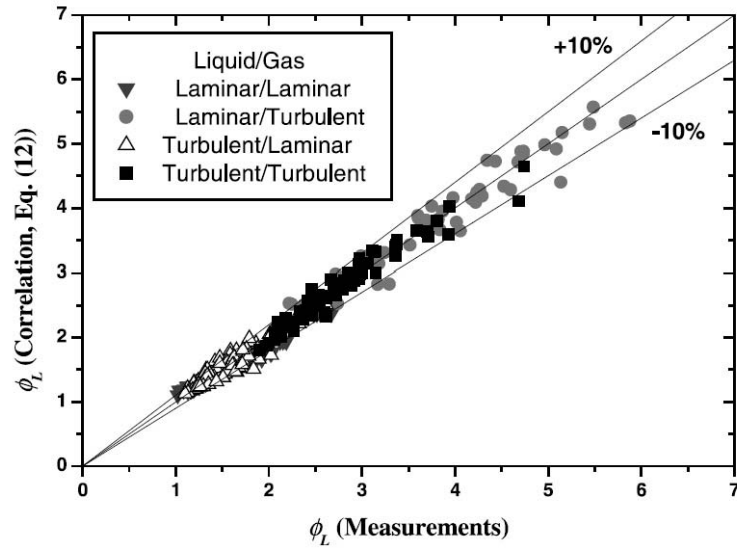


Figure 3.19: Comparison between the new correlation and the measurements of Lee and Lee [32].

experimental data and homogeneous flow model is generally poor, with reasonably good predictions (within $\pm 20\%$) obtained only with the Dukler et al. [18] model for the mixture viscosity as shown in Fig. 3.20.

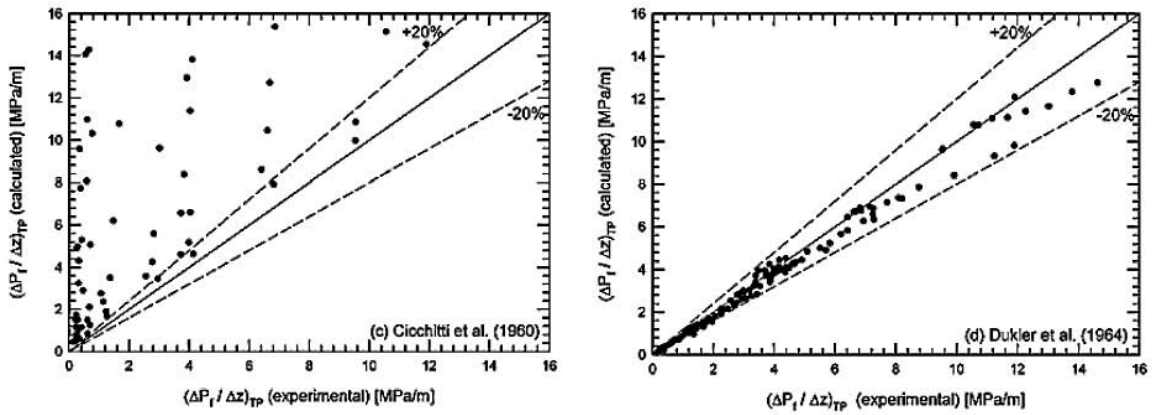


Figure 3.20: Comparison of the two-phase frictional pressure gradient between microchannel data of Kawahara et al. [28] and homogeneous flow model predictions using different viscosity formulations.

Finally, a comparison of the two-phase frictional pressure gradient data with the predictions of the Lockhart-Martinelli correlation using different C values is shown in Fig. 3.21, including $C = 5$, $C = 0.66$ from Eq. (3.65), C calculated from the Lee and Lee’s model (Eq. (3.66)), and $C = 0.24$. The conventional value of $C = 5$ again significantly over-predicted the present data, while Mishima and Hibiki’s correlation generally over-predicted the data by about 10%. On the other hand, good agreement (within $\pm 10\%$) was obtained with the use of the C value given by Lee and Lee’s model and the present value of $C = 0.24$.

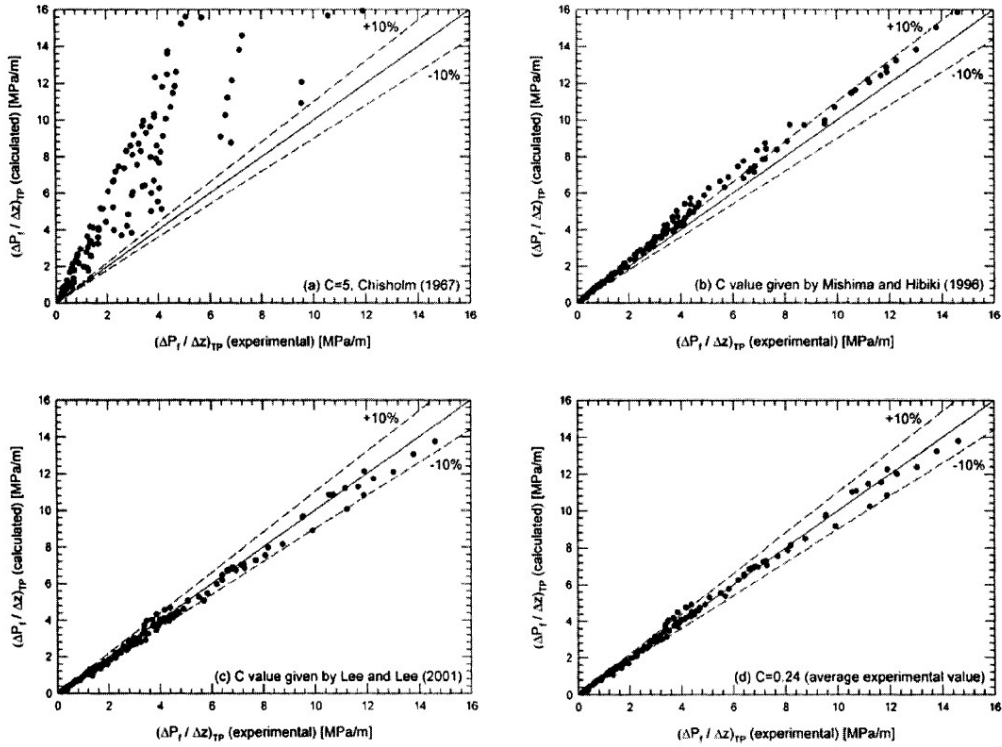


Figure 3.21: Predictions of two-phase friction pressure gradient data of Kawahara et al. [28] by a Lockhart-Martinelli correlation with different C values.

3.4.8 The Lee and Mudawar study

Lee and Mudawar [33] measured the two-phase pressure drop across a microchannel heat sink that served as an evaporator in a refrigeration cycle. The microchannels were formed by machining $231 \mu\text{m}$ wide \times $713 \mu\text{m}$ deep grooves into the surface of a copper block. Experiments were performed with refrigerant R-134a that spanned the following conditions: inlet pressure of $P_{in} = 1.44\text{-}6.60$ bar, mass flux of $G = 127\text{-}654$ kg/m²s, inlet quality of $x_{in} = 0.001\text{-}0.25$, outlet quality of $x_{out} = 0.49$ -superheat, and heat flux of $q = 31.6\text{-}93.8$ W/cm².

Figure 3.22 shows the comparison between the experimental data of Lee and Mudawar with homogeneous equilibrium model predictions for different viscosity models. As can be seen, none of the models predict the data correctly, except for the Cicchitti's model that has a low mean absolute error but does not capture the general trend.

Figure 3.23 presents the comparison between the experimental data of Lee and Mudawar with separated flow model predictions based on different correlations. The Lockhart-Martinelli, the Friedel, and the Lee and Lee predictions methods are not that bad. The other correlation shows appreciable deviation from the data.

Lee and Mudawar proposed, therefore, a new correlation based on the Lockhart and Martinelli model. They defined a new constant C as presented in Eqs. (3.69) and (3.70).

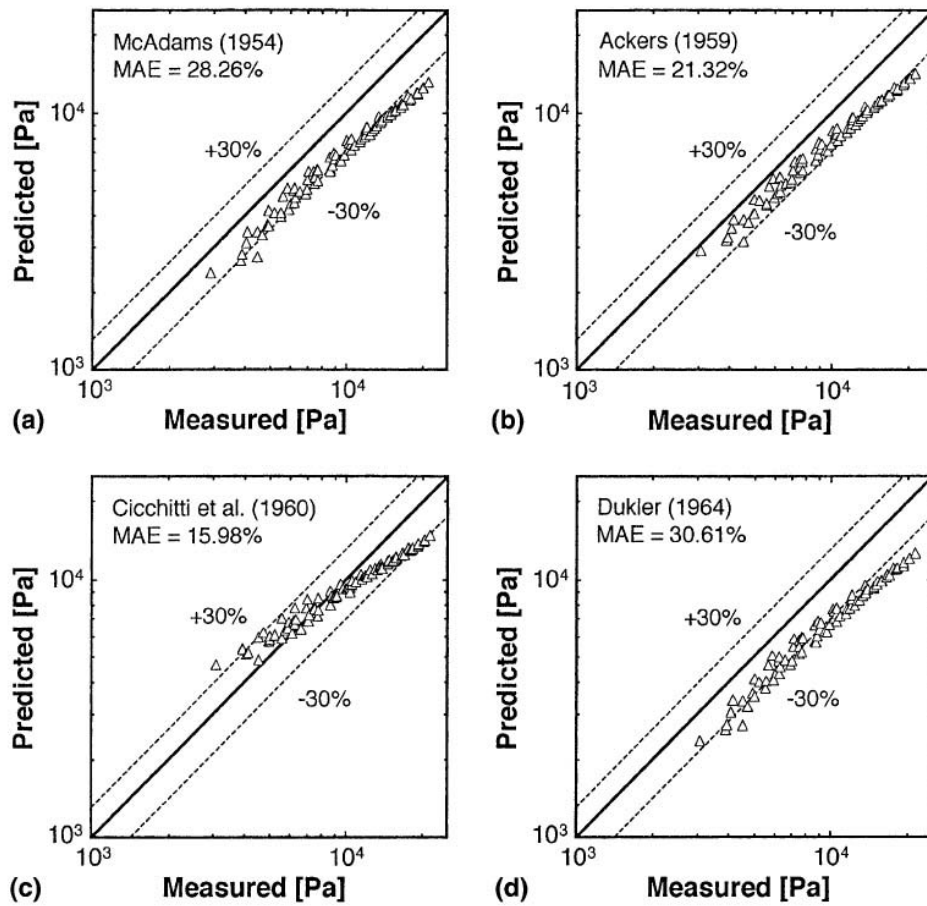


Figure 3.22: Comparison of R-134a pressure drop data of Lee and Mudawar [33] with homogeneous equilibrium model predictions based on two-phase viscosity models by (a) McAdams, (b) Ackers, (c) Cicchitti et al. and (d) Dukler.

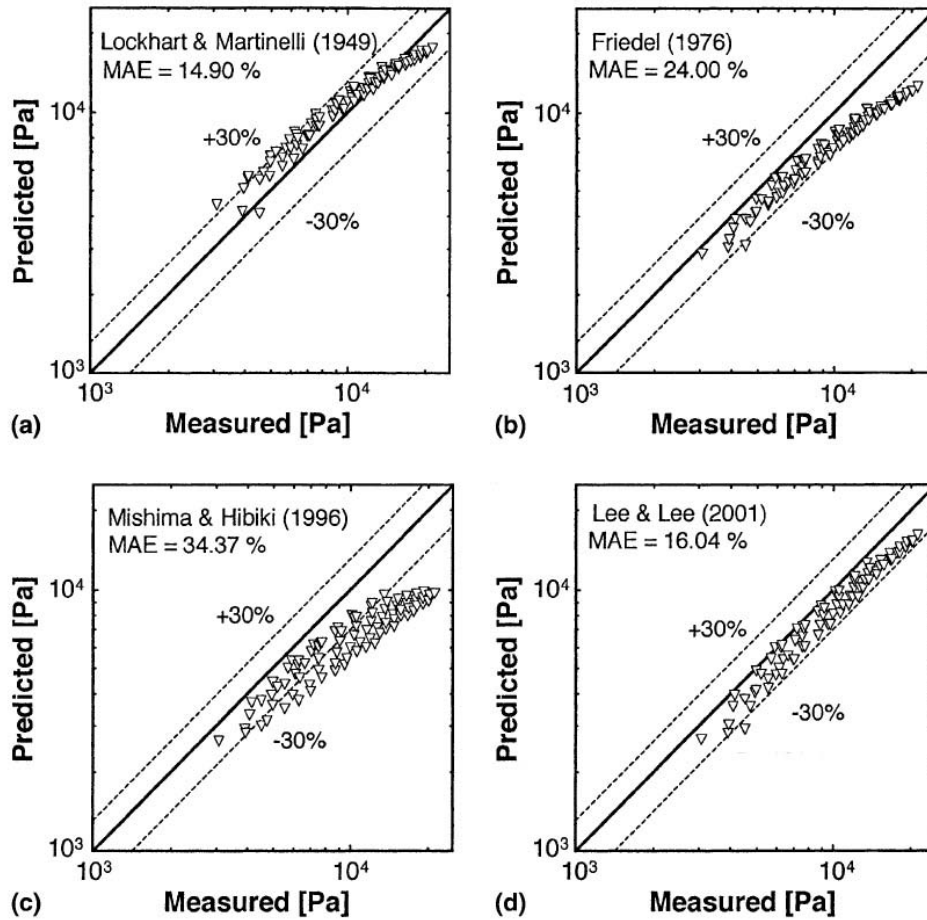


Figure 3.23: Comparison of R-134a pressure drop data of Lee and Mudawar [33] with separated flow model predictions based on correlations by (a) Lockhart and Martinelli, (b) Friedel, (c) Mishima and Hibiki and (d) Lee and Lee.

For laminar liquid and laminar vapor:

$$C_{vv} = 2.16Re_{LO}^{0.047}We_{LO}^{0.6} \quad (3.69)$$

For laminar liquid and turbulent vapor:

$$C_{vt} = 1.45Re_{LO}^{0.25}We_{LO}^{0.23} \quad (3.70)$$

Good agreement is achieved between pressure drop predictions based on the new correlation for both their present R-134a data and for prior microchannel water data as shown in Fig. 3.24.

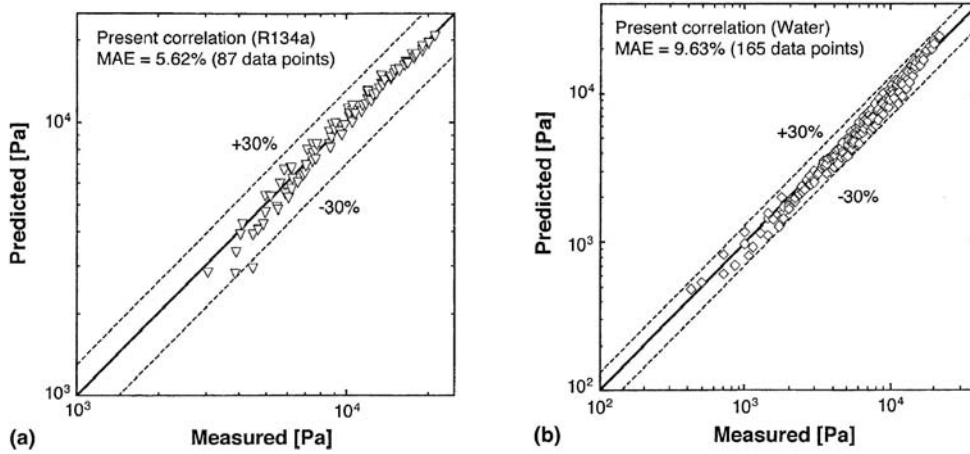


Figure 3.24: Comparison of new correlation predictions of Lee and Mudawar [33] with (a) R-134a data and (b) Qu and Mudawar's microchannel water data.

3.4.9 The Zhang and Webb study

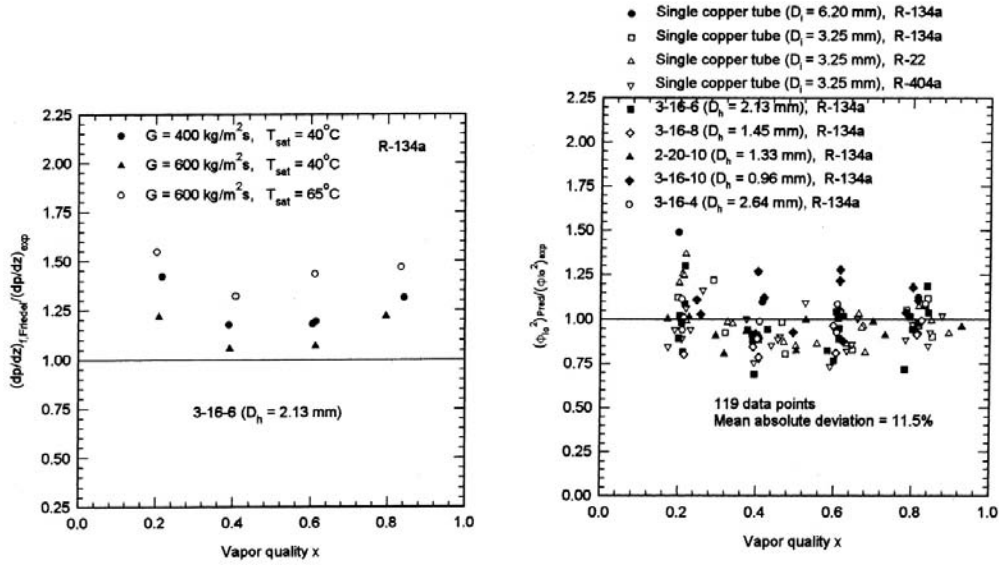
Zhang and Webb [58] measured adiabatic two-phase flow pressure drops for R-134a, R-22 and R-404a flowing in a multi-port extruded aluminum tube with a hydraulic diameter of 2.13 mm, and in two copper tubes having inside diameters of 6.25 and 3.25 mm, respectively. They found that the Friedel correlation did not predict the two-phase data accurately, especially for high reduced pressure as shown in Fig 3.25(a).

Using the data taken in their present and in a previous study, a new correlation (Eq. (3.71)) for two-phase friction pressure drop in small tubes was developed by modifying the Friedel correlation. The new correlation predicts 119 data points with a mean deviation of 11.5 % as shown in Fig 3.25(b).

$$\left(\frac{dP}{dz}\right)_f = \left(\frac{dP}{dz}\right)_{LO} \Phi_{LO}^2 \quad (3.71)$$

$$\text{with } \Phi_{LO}^2 = (1-x)^2 + 2.87x^2 \left(\frac{P}{P_{crit}}\right)^{-1} + 1.68x^{0.8}(1-x)^{0.25} \left(\frac{P}{P_{crit}}\right)^{-1.64} \quad (3.72)$$

and $\left(\frac{dP}{dz}\right)_{LO}$ given by Eq. (3.49). P_{crit} is the critical pressure, constant for each fluid.



(a) Predictions of two-phase pressure drop using the Friedel correlation (b) Predictions of two-phase pressure drop using the new correlation

Figure 3.25: Predictions of two-phase pressure drop data of Zhang and Webb [58] with the Friedel correlation and the new correlation.

3.4.10 The Tran et al. study

Two-phase flow pressure drop measurements were made by Tran et al. [52] during a phase-change heat transfer process with three refrigerants (R-134a, R-12 and R-113) at six different pressures ranging from 138 to 856 kPa, and in two sizes of round tubes (2.46 and 2.92 mm inside diameters) and one rectangular channel (4.06×1.7 mm).

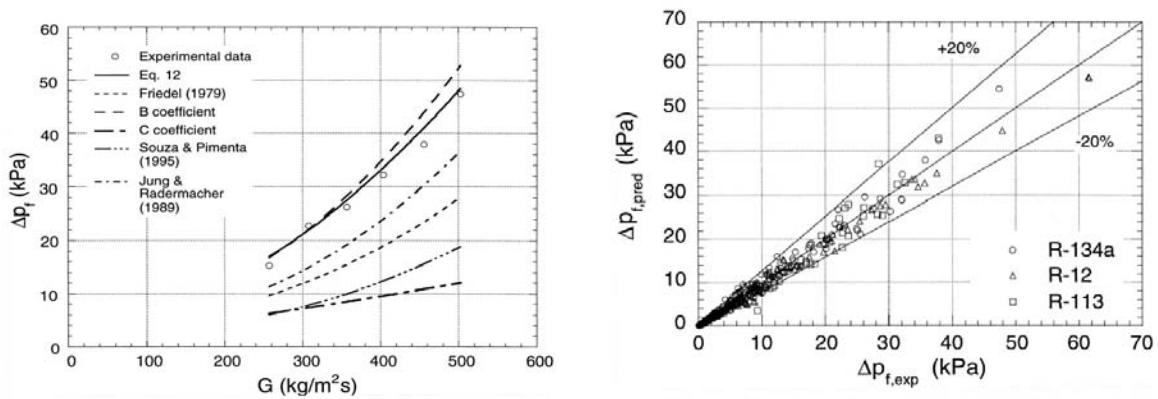
The data were compared with those from large tubes under similar conditions, and state-of-the-art correlations were evaluated using the R-134a data. The state-of-the-art large-tube correlations failed to satisfactorily predict the experimental data as shown in Fig. 3.26(a).

The data were used to develop a new correlation for two-phase pressure drop during flow boiling in small channels. The correlation was then tested against the experimental data for the three refrigerants (Fig. 3.26(b)) ; the error was $\pm 20\%$. This new correlation takes into account the effects of surface tension and channel size and is given by Eq. (3.73).

$$\left(\frac{dP}{dz}\right)_f = \left(\frac{dP}{dz}\right)_{LO} \Phi_{LO}^2 \quad (3.73)$$

$$\text{with } \Phi_{LO}^2 = 1 + (4.3Y^2 - 1) \left[Cox^{0.875}(1-x)^{0.875} + x^{1.75} \right] \quad (3.74)$$

$\left(\frac{dP}{dz}\right)_{LO}$ is given by Eq. (3.49) and Co by Eq. (3.75).



(a) Predictions of two-phase pressure drop data using different correlations

(b) Predictions of two-phase pressure drop using the new correlation

Figure 3.26: Predictions of two-phase pressure drop data of Tran et al. [52] with different correlations and the new correlation.

$$Co = \sqrt{\frac{\sigma}{D^2 g (\rho_L - \rho_V)}} \quad (3.75)$$

3.4.11 The Cavallini et al. study

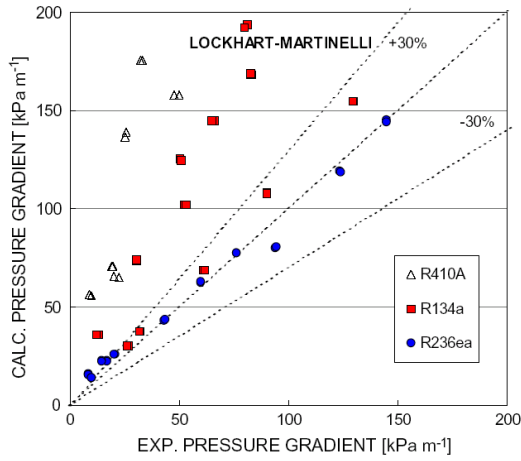
Cavallini et al. [6] presented the pressure drop characteristics of a 1.4 mm hydraulic diameter multiport minichannel tube during adiabatic two-phase flow of HFC refrigerants (R-134a, R-236ea and R-410a). The tube consists of eleven parallel rectangular cross section channels.

The experimental runs are carried out at mass fluxes ranging from 200 to 1400 kg/m²s, depending on the refrigerant under test, at constant value of vapour quality. The frictional pressure gradient is obtained from the saturation temperature drop measurement. The reduced pressure was varying from 0.1 up to 0.5.

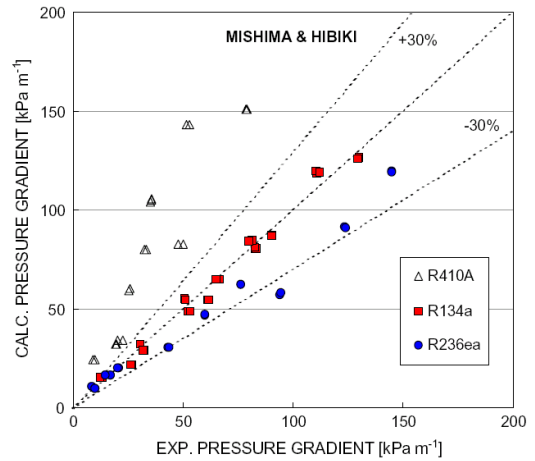
The experimental frictional pressure drop data were compared against models available in the literature for prediction of frictional pressure gradient in channels as shown in Fig. 3.27. The comparison of calculated to experimental values shows that the R-134a frictional pressure gradient in the multiport minichannel test tube can be fairly well predicted by available correlations, but no satisfactory agreement is found for R236ea data and even worse in the case of R410A data.

3.4.12 The Müller-Steinhagen and Heck study

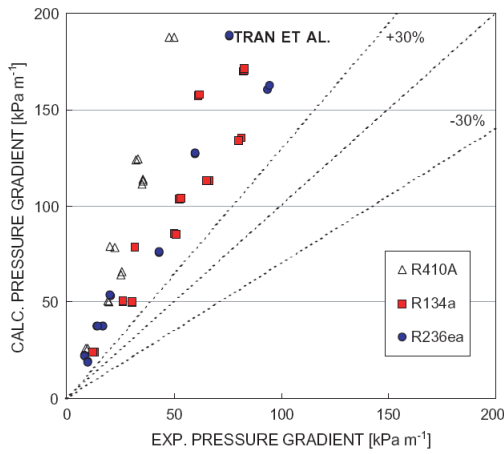
A new correlation by Müller-Steinhagen and Heck [39] for the prediction of frictional pressure drop for two-phase flow in pipes was suggested which is simple and more convenient to use than other prior methods. The correlation was developed using a data bank containing 9300 measurements of frictional pressure drop for a variety of fluids and conditions, including channel diameters from 4 to 392 mm. The correlation is given by Eq. (3.76)



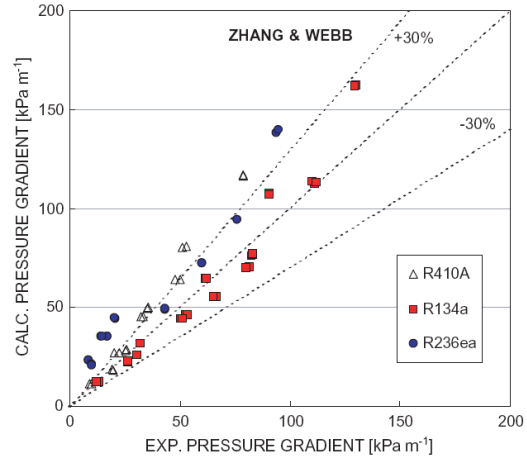
(a) Predictions of two-phase pressure drop data using the Lockhart-Martinelli correlation



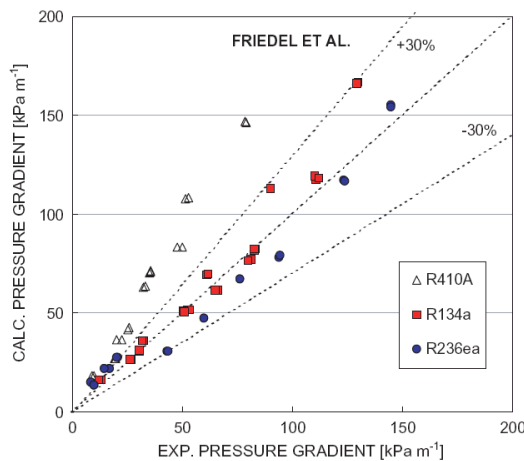
(b) Predictions of two-phase pressure drop using the Mishima and Hibiki correlation



(c) Predictions of two-phase pressure drop using the Tran et al. correlation



(d) Predictions of two-phase pressure drop using Zhang and Webb new correlation



(e) Predictions of two-phase pressure drop using the Friedel correlation

Figure 3.27: Predictions of two-phase pressure drop data of Cavallini et al. [6] with different correlations.

$$\left(\frac{dP}{dz}\right)_f = F(1-x)^{1/3} + \left(\frac{dP}{dz}\right)_{VO} x^3 \quad (3.76)$$

$$\text{With } F = \left(\frac{dP}{dz}\right)_{LO} + 2 \left[\left(\frac{dP}{dz}\right)_{VO} - \left(\frac{dP}{dz}\right)_{LO} \right] x \quad (3.77)$$

where $\left(\frac{dP}{dz}\right)_{LO}$ is given by Eq. (3.49) and $\left(\frac{dP}{dz}\right)_{VO}$ by Eq. (3.62).

3.4.13 Conclusions

Many studies exist on two-phase pressure drop in microchannels. In general, experimental data points are compared with conventional macrochannel models and correlations with poor agreement but some methods predict the data reasonably well. The Duckler et al. relation using the homogeneous model predicts the Kawahara et al. data with good agreement as well as the Cicchitti et al. relation with the Lee and Mudawar experimental data. The later does not however capture the general trend. Cavallini compared their data with the Lockhart-Martinelli correlation with poor agreement but with a better accuracy with the Friedel correlation. Tran et al. found no agreement between their data and the Friedel model.

New correlations have been proposed, typically by modification of prior methods. The Mishima and Hibiki correlation is based on the Lockart-Martinelli relation and developed a parameter C as a function of the diameter of the tube. This method predicts well the data of Kawahara et al. and Cavallini et al. results for R-134a but not those of Lee and Mudawar.

Lee and Lee predicted their data with their own correlation based on a new definition of the C parameter. Kawahara et al. found a very good agreement between this correlation and their data whereas Lee and Mudawar comparison was not so good.

Presently, no study has been shown to be accurate for a broad, independent database.

Chapter 4

Description of experiments

4.1 General description

A new experimental stand (Fig. 4.1) was built in order to control the fluid characteristics at inlet of the test section, i.e. mass flow rate, inlet subcooling and saturation pressure. The test facility is shown in Fig. 4.2 and was designed with two optional methods for controlling the flow through the heat transfer and flow visualization test sections: (i) using a speed controlled micropump (*Pump mode*) and (ii) using the pressure difference between the upstream temperature-controlled refrigerant storage vessel (called also the hot reservoir) and its downstream companion (called also the cold reservoir)(*Reservoir mode*). A Labview interface has been created to control its operation and register measurements. A microvalve has been installed between the hot reservoir and the test section to avoid oscillations when boiling starts in the test section by increasing the pressure drop in the loop, so that back flow can be suppressed and a wider range of stable operations conditions achieved.

The *Reservoir mode* is more stable for low mass flow and has been therefore preferred for performing tests with the chosen diameters. The "cold" reservoir was use for controlling the saturation condition inside the test section.

4.2 Test section

The test section consisted of an 80 mm long stainless steel tube used as a micropreheater, then a 20 mm long plastic (peek) tube for electrical insulation, followed by a 110 mm long stainless steel tube heated section as the microevaporator and then a 100 mm long glass tube for flow pattern visualization and optical measurements, as shown in Figs. 4.3 and 4.4.

The internal diameters of all these sections was 0.509 mm and 0.790 mm. Two copper clamps were attached to the preheater and to the evaporator. They were connected electrically to two Sorensen power supplies, respectively models DCS150-7E and DCS8-125E. They delivered direct current and heated the tubes by Joule effect. Two pressure transducers ($P_{TS,in}$ and $P_{TS,out}$) were installed at the inlet and outlet of the test section as shown in Fig. 4.5 where the inside diameter is 4 mm. Two 0.25 mm thermocouples ($T_{TS,in}$ and $T_{TS,out}$) were placed

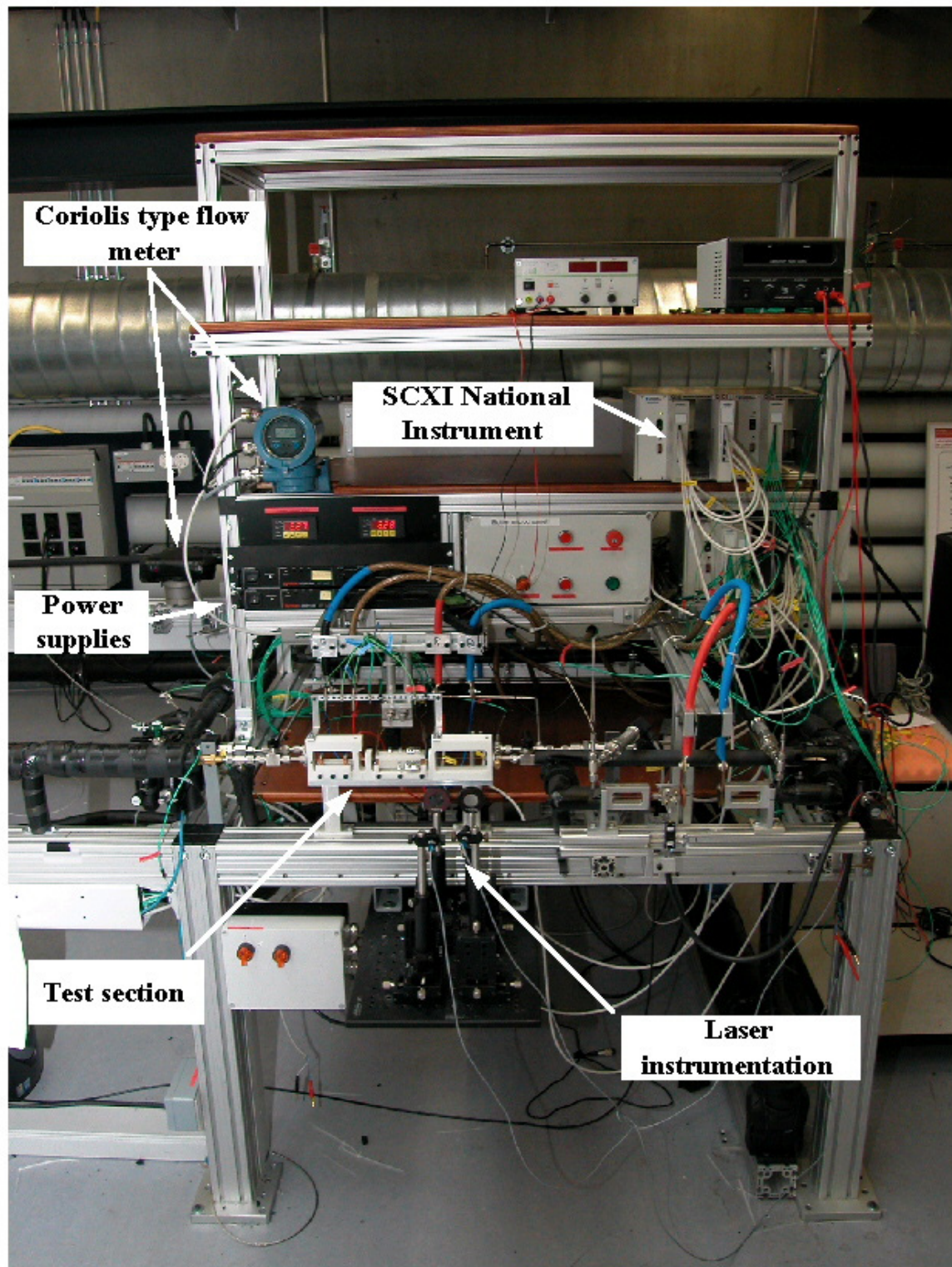


Figure 4.1: Photograph of the experimental stand.

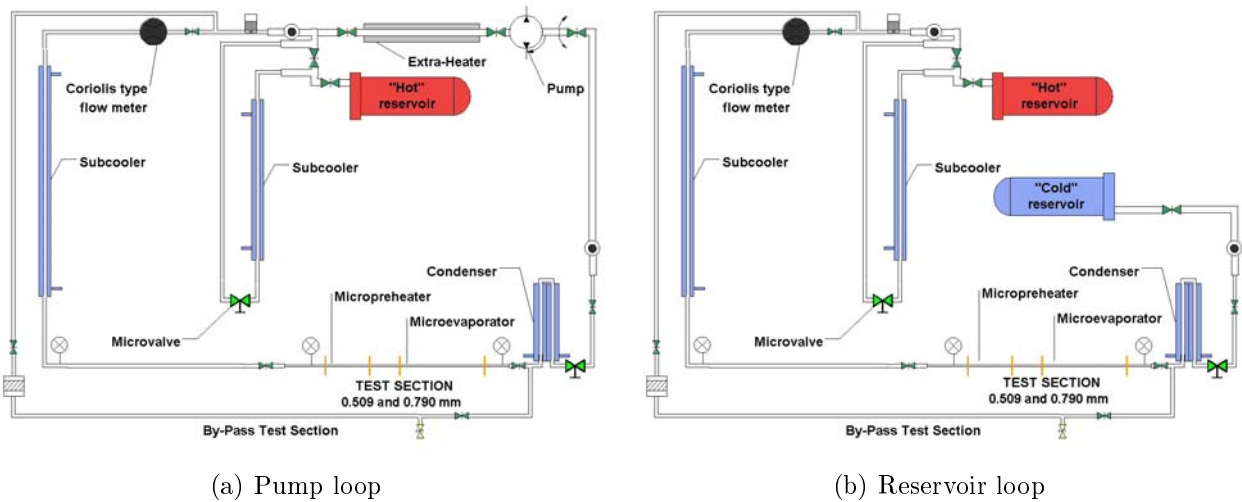


Figure 4.2: Schematic of a) pump loop and b) reservoir loop.

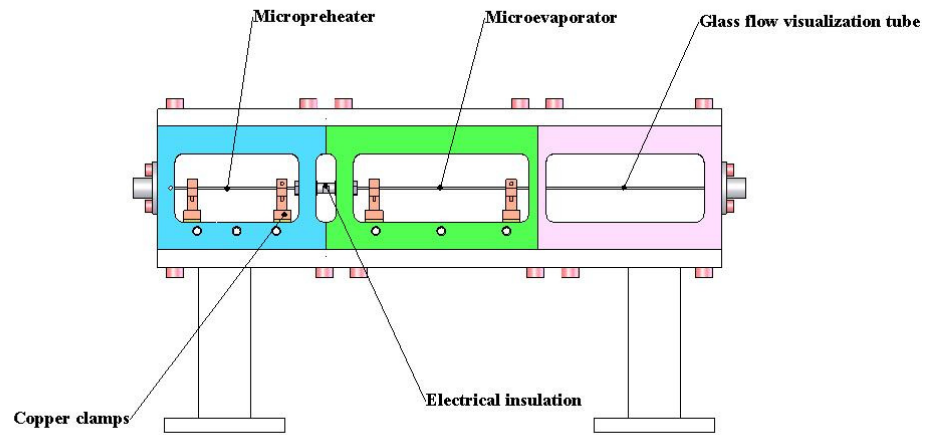
in the fluid at the same locations. Four 0.25 mm thermocouples ($T_{MPH,in}$, $T_{MPH,out}$, $T_{MEV,in}$ and $T_{MEV,out}$) were also attached on the external surface of the microtubes in an adiabatic location (before the inlet and after the outlet of the preheater and the evaporator) to measure fluid temperature. Two more 0.25 mm thermocouples ($T_{MPH,secu}$, $T_{MEV,secu}$) were installed on the two diabatic surfaces to avoid dry out and overheating. All the test section has been thermally insulated.

It is of particular importance here to note that the present setup concerns actual two-phase flows exiting a microevaporator channel and not two-phase flows generated artificially by a gas injector or liquid-vapor mixer. Hence, the bubbles observed here were nucleated in the evaporator and then flowed downstream, just like in a microchannel cooling element attached to a computer chip, for instance. Thus, here the resulting flow pattern and bubble characteristics are determined by the process itself, not imposed or influenced by the design of the injector or mixer.

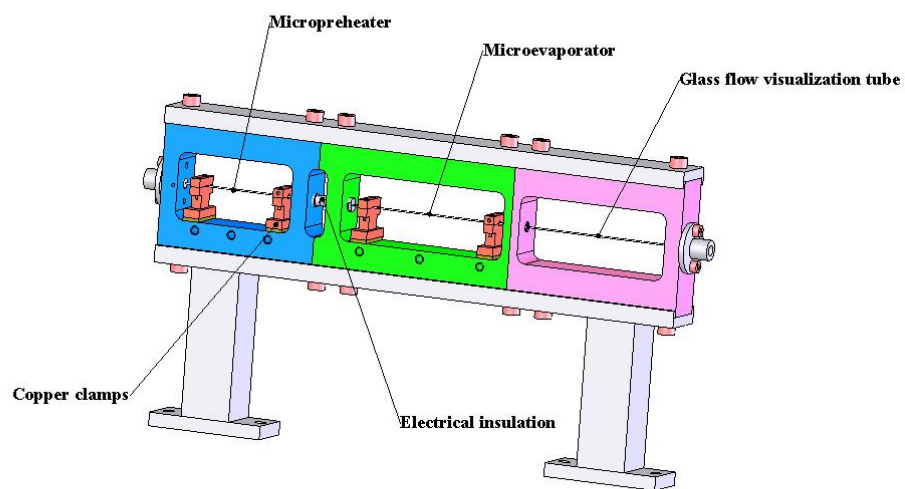
4.3 Optical measurement technique

A method to count and determine the two-phase flow characteristics has been developed. The experimental setup consisted of two laser beams, with a power less than 1 mW, directed through the glass visualization tube and the fluid at two different locations, separated by $L_{adb,2}$ that varies around 70 mm as presented in Figs. 4.6 and 4.7.

Two lenses focused the laser beams to the middle of the microtube. Two photodiodes, their faces painted over but leaving only a vertical 1 mm wide opening in the middle to isolate the signal, measured the intensity of the light. They were connected to a *National Instruments* SCXI acquisition system using a scan rate of 10 000 measurements/sec to measure the resulting voltage signals from the two diodes. A micropositioning system was used to align the laser beams with the lenses and photodiodes. The laser beams interact locally with the structure of the flow and by signal processing, it was possible to determine the velocity,



(a) front view



(b) 3D view

Figure 4.3: Schematic diagram of the test section: a) front view and b) 3D view.

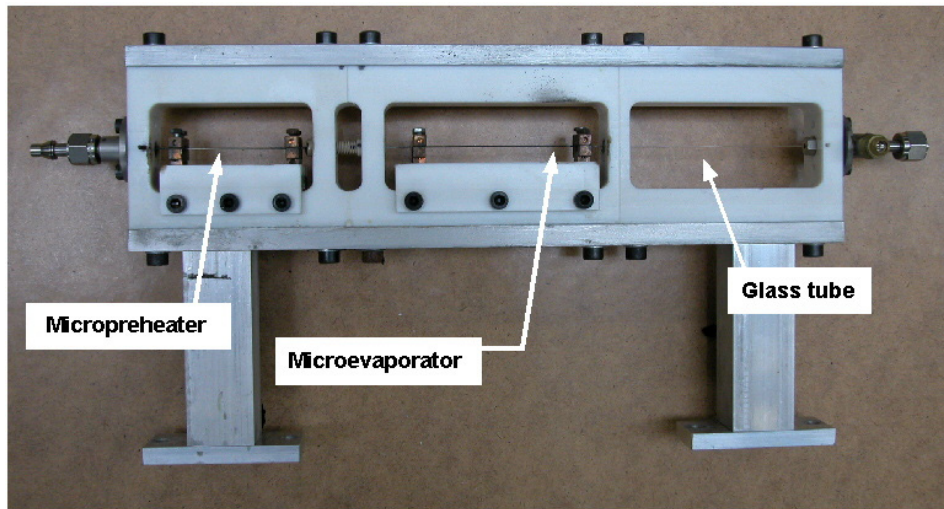


Figure 4.4: Photograph of the test section.

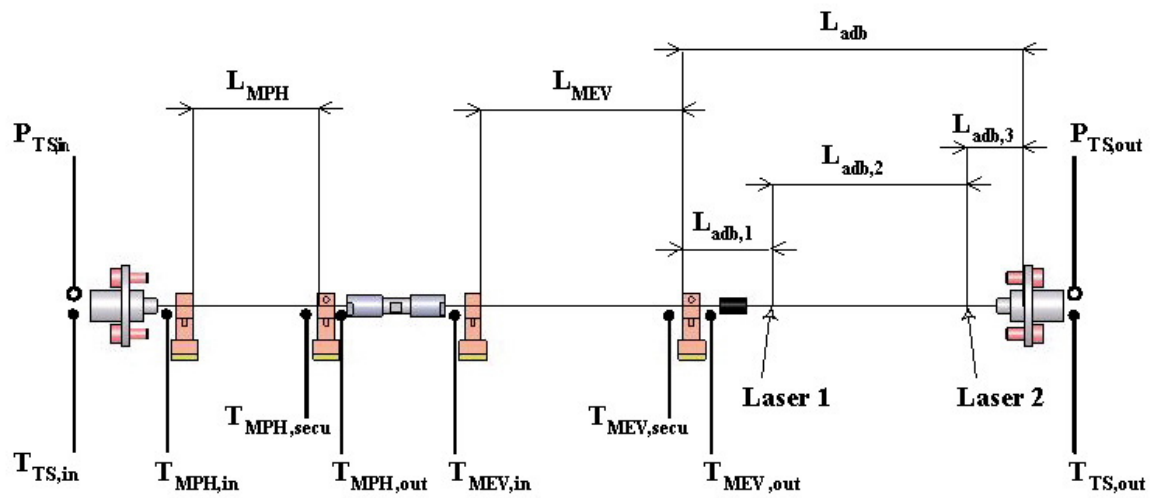


Figure 4.5: Schematic of the test section with thermocouple and pressure locations.

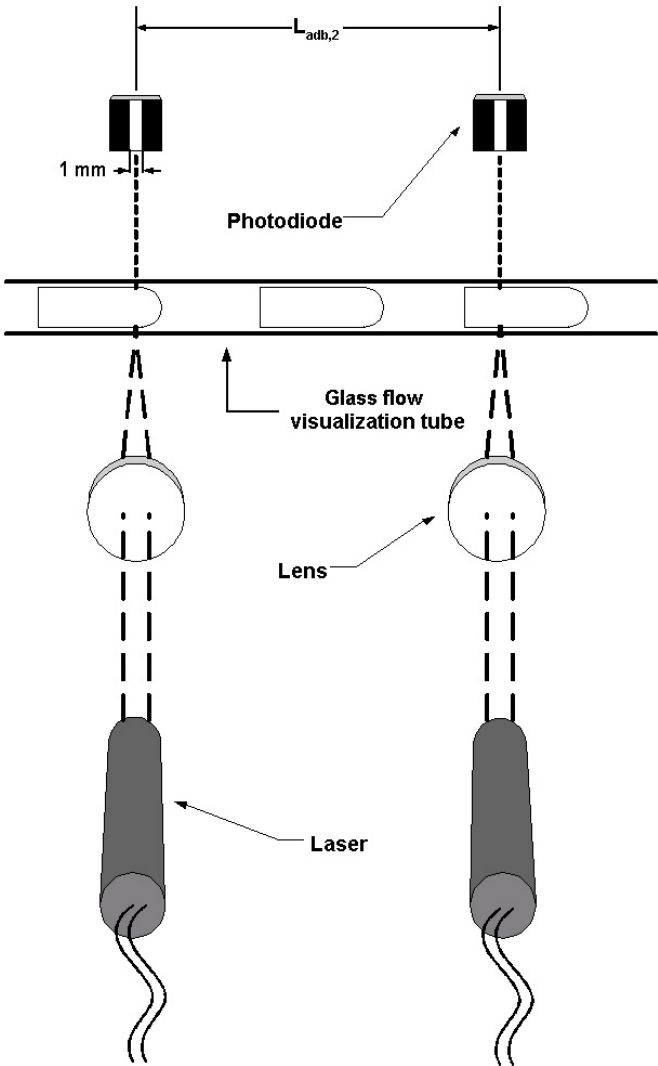


Figure 4.6: Schematic diagram of the laser instrumentation.

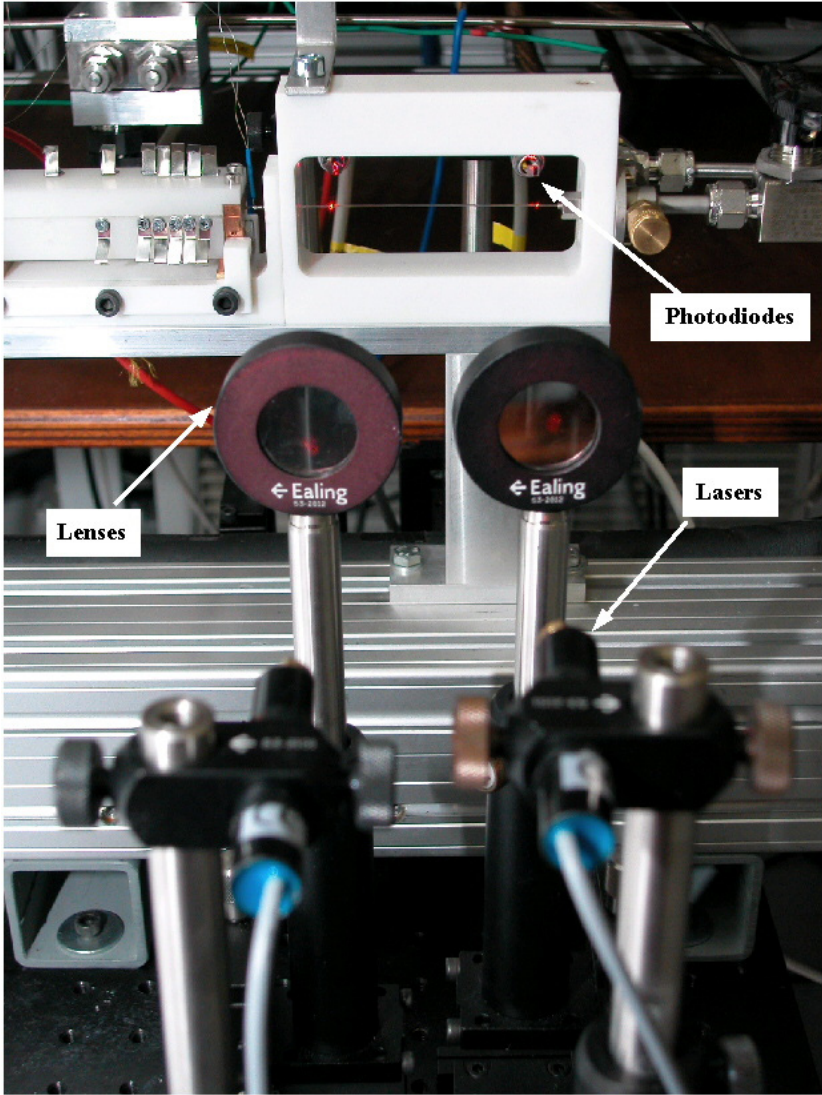


Figure 4.7: Photograph of the laser instrumentation.

length and frequency of vapor bubbles. The signals from the diodes obtained by this technique for the different flow regimes are similar to those obtained by Lowe and Rezkallah [35] using a void fraction probe for the microgravity air/water two-phase flow in a 9.525 mm I.D tube.

The processing implemented in our optical measurement technique consisted of several steps as follows:

Voltage thresholds: Fig. 4.8 shows an example of a histogram obtained by this method derived from its corresponding diode voltage signal. To count vapor bubbles, thresholds were determined in volts after first segregating the diode voltage signal into 5 mV steps. Limits were determined 20 mV after the first peak for limit A and 40 mV before the second peak for limit B. Threshold A is -440 mV for this example and threshold B is -345 mV. When the voltage signal is below limit A, the presence of liquid is detected. Signals greater than limit B mean that an annular flow or an elongated bubble is present. Between these two thresholds, either the nose or tail of a bubble or a frothy mix of liquid and vapor is present. These threshold values were kept constant for each experimental condition but could vary a bit due to periodic repositioning of the lasers, photodiodes and lenses and thus were reexamined for each set of results.

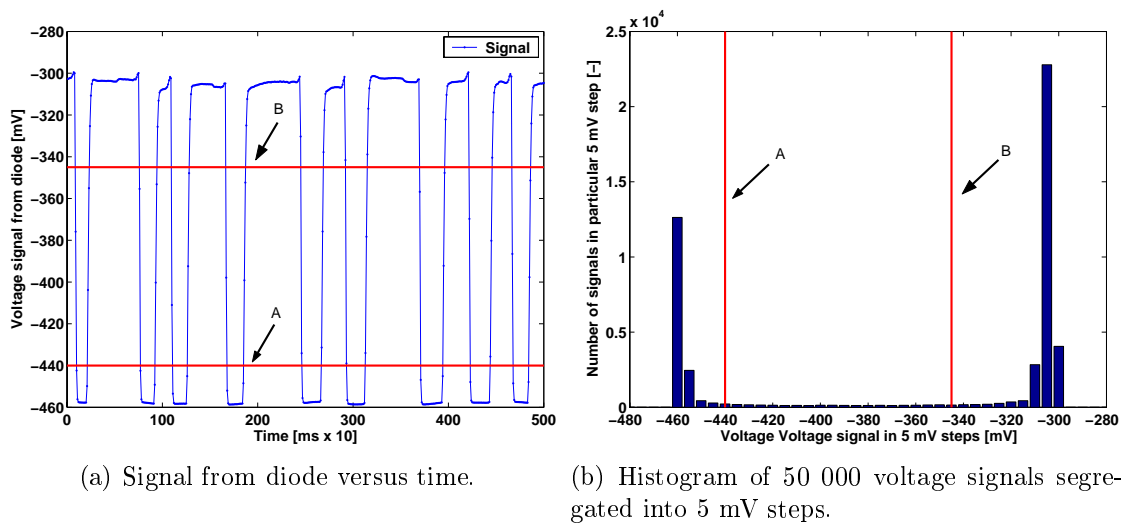


Figure 4.8: Example of (a) a voltage signal and (b) a histogram of its distribution showing the chosen thresholds for characterizing a slug flow.

Vapor bubble frequency: The program counts the number of times the voltage is less than the threshold A and divides by the elapsed time. This gives the vapor bubble frequency, i.e. bubbles separated by liquid slugs. This frequency is called f_A . The program counts also the number of times the voltage is above the threshold B and divides by the time period. The measure has been carried out on a period of 5 sec for each test (see Part 4.4.13). This gives the sum of the vapor bubble frequency and the semi-annular frequency, the latter which is annular flow with churn transition zones in place of the liquid slugs when present. This frequency is called f_B .

Vapor bubble velocity: A cross correlation of the two laser signals gives the average time delay between bubbles. It is a statistical comparison to match the bubbles. By knowing the distance between the two lasers, it is possible to determine the mean velocity of the vapor bubble. The signal obtained using this function and centering the result is composed of one high amplitude peak as shown in Fig. 4.9. It gives the average time delay between the two signals.

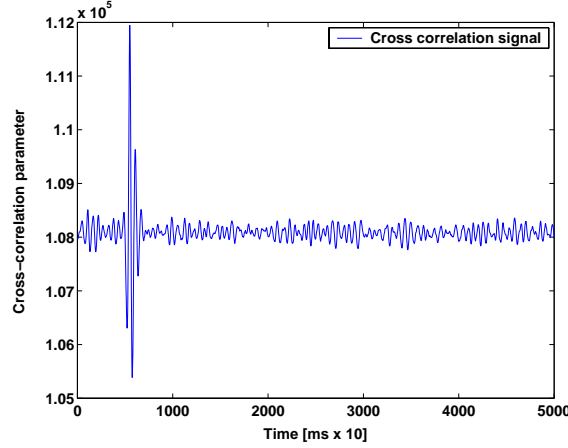


Figure 4.9: Example of cross correlation of voltage signals from the two diodes.

This method is applicable only for bubbly/slug flow, slug flow and slug/semi-annular flow. For bubbly flow, it works only at high bubble frequencies as otherwise insufficient information is available for the cross correlation function. The same problem occurs in the slug/semi-annular flow when the frequency A reaches 0 Hz. For this reason, only the velocities for the frequency A above 30 Hz will be taken into account.

The pressure drop effect in the sight glass on the vapor velocity (flashing effect) is taken into account by using simultaneously Eqs. (4.1) and (4.2) based on the mass conservation applied on a small volume of vapor as shown in Fig. 4.10. Equation (4.1) is used to incrementally calculate the local velocity $U_v(z + dz)$ from laser 1 to laser 2, assuming the initial value of $U_v(laser1)$ at z . Then the mean is calculated using Eq. (4.2) and compared to the value at the midpoint between laser 1 and 2. The iterative procedure thus gives the values of U_v at laser 1 and 2 from the known vapor density (which varies with the pressure drop) and an assumed void fraction model that gives ε_v .

$$U_v(z + dz) = \frac{\rho_v(z) \varepsilon_v(z) U_v(z)}{\rho_v(z + dz) \varepsilon_v(z + dz)} \left[\frac{x(z + dz)}{x(z)} \right] \quad (4.1)$$

$$U_{mean} = \frac{U_v(laser1) + U_v(laser2)}{2} \quad (4.2)$$

The homogeneous void fraction is assumed in the above calculation.

$$\varepsilon_{Hom} = \frac{1}{1 + \left(\frac{1-x}{x} \right) \frac{\rho_v}{\rho_l}} \quad (4.3)$$

For comparison, calculations were also performed with the Steiner [1] version of the Rouhani-Axelsson [43] drift flux equation with a difference of less than 1% on the vapor velocity. As a result, by iterations with this method it is possible to obtain the vapor velocity at each laser location.

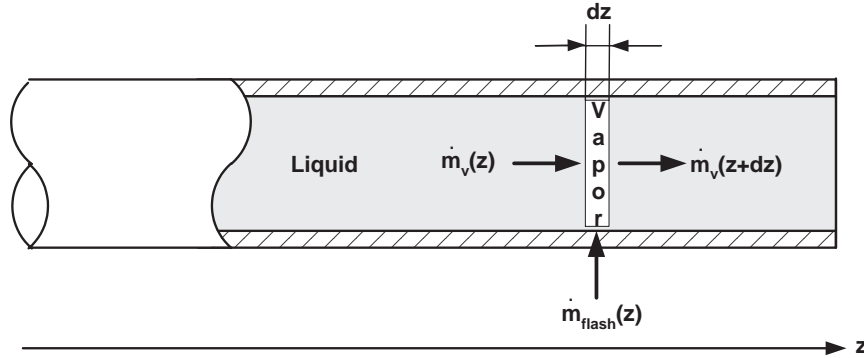


Figure 4.10: Control element of vapor used for vapor velocity calculation.

Vapor bubble length: By knowing the vapor bubble velocity (i.e. u_v) and time that a vapor bubble needs to cross the laser signal, its length can be calculated. When a bubble is smaller in length than the internal diameter of the microchannel, it is classified as a *small* bubble; otherwise, it is defined here as an *elongated* bubble.

Flow pattern identification: The method is described in Chapter 6.

4.4 Measurements and accuracy

The experimental conditions are summarized in Chapter 5 and 6.

The general formulation for error propagation permits one, see Taylor [49], to calculate the uncertainty of a function f of several independent variables x, \dots, z , provided all errors associated with these variables are independent and random:

$$\delta f = \sqrt{\left(\frac{\delta f}{\delta x} \delta x\right)^2 + \dots + \left(\frac{\delta f}{\delta z} \delta z\right)^2} \quad (4.4)$$

and the general formulation for error propagation in all cases is:

$$\delta f \leq \left|\frac{\delta f}{\delta x}\right| \delta x + \dots + \left|\frac{\delta f}{\delta z}\right| \delta z \quad (4.5)$$

This last equation that maximizes errors, will be used for the uncertainty calculations.

4.4.1 Diameter

The diameter of the microevaporator (D) and micropreheater made of stainless steel has been measured with an optical microscope. The two tubes (0.509 and 0.790 mm) have been moulded in a resin and cut into 4 pieces. The diameter has been measured 16 times in total for each tube, at different locations. The results are determined using the Student's distribution with 15 degrees of freedom and 95% confidence interval.

$$D_{int} = 0.509 \text{ mm} \pm 1 \% \text{ and } D_{ext} = 0.708 \text{ mm} \pm 1 \% \quad (4.6)$$

$$D_{int} = 0.790 \text{ mm} \pm 1 \% \text{ and } D_{ext} = 1.018 \text{ mm} \pm 1 \% \quad (4.7)$$

The diameter of the adiabatic glass tube (D_{adb}) has been measured with an optical microscope. It was not possible to cut the glass tube in different pieces so the measurement for each diameter has been carried out on two samples chosen among the numerous tubes bought and 8 measurements have been made for each diameter. The results are determined using the Student's distribution with 7 degrees of freedom and 95% confidence interval.

$$D_{int} = 0.517 \text{ mm} \pm 1.1 \% \text{ and } D_{ext} = 0.715 \text{ mm} \pm 1.6 \% \quad (4.8)$$

$$D_{int} = 0.803 \text{ mm} \pm 1.6 \% \text{ and } D_{ext} = 0.999 \text{ mm} \pm 1 \% \quad (4.9)$$

In view of the measurements and the uncertainties, we can assume that the internal and external diameters of the stainless steel and the glass tubes are the same. In the rest of this study, the diameter will always refer to the microevaporator tube.

4.4.2 Surface roughness

The stainless steel tubes (0.509 and 0.790 mm) have been opened by polishing in machine shop. The surface roughness measurements have been carried out by profilometry over a 2 mm distance line. Surface roughness for each tube is given by Eqs. (4.10) and (4.11) and corresponds to the root mean square (rms).

$$e = 3.32 \text{ } \mu\text{m} \pm 0.72 \text{ } \mu\text{m} \text{ and } \frac{e}{D} = 0.65 \% \text{ for the 0.509 mm tube} \quad (4.10)$$

$$e = 1.80 \text{ } \mu\text{m} \pm 0.27 \text{ } \mu\text{m} \text{ and } \frac{e}{D} = 0.23 \% \text{ for the 0.790 mm tube} \quad (4.11)$$

The glass tubes (0.517 and 0.803 mm) have been broken into several pieces. The surface roughness measurements have been carried out by atomic force microscopy (AFM) over a 5 μm square area. Surface roughness for each tube is given by Eqs. (4.12) and (4.13) and corresponds to the root mean square (rms).

$$e = 10.0 \text{ nm} \pm 1.20 \text{ nm} \quad \text{and} \quad \frac{e}{D} = 0.002 \% \quad \text{for the 0.517 mm tube} \quad (4.12)$$

$$e = 9.3 \text{ nm} \pm 1.6 \text{ nm} \quad \text{and} \quad \frac{e}{D} = 0.001 \% \quad \text{for the 0.803 mm tube} \quad (4.13)$$

4.4.3 Microevaporator length

The heated length of the microevaporator is defined by the internal distance between the two copper clamps. It is measured with an error less than 0.5 mm. That uncertainty comes directly from the measurement instrument (Vernier caliper).

$$\Delta L_{MEV} = 5 \times 10^{-4} \text{ m} \quad (4.14)$$

The microevaporator length varies from 20 to 70 mm. Thus the relative error ranges from 0.7 to 2.5 %.

4.4.4 Distance between the lasers

The distance between the lasers is measured with an error less than 0.5 mm. That uncertainty comes directly from the measurement instrument (Vernier caliper).

$$\Delta L_{adb,2} = 5 \times 10^{-4} \text{ m} \quad (4.15)$$

This absolute error is the same as for $\Delta L_{adb,1}$, $\Delta L_{adb,3}$ and ΔL_{adb} . The distance between the lasers ($\Delta L_{adb,2}$) is usually 70 mm. The relative error is then 0.7 %. ΔL_{adb} is equal to 120 mm.

4.4.5 Temperature

All the thermocouples are K-type (Chromel-Alumel) and come from the company *Thermo-coax*. They were connected to a *National Instrument SCXI* acquisition system using a scan rate of 1 scan/sec. They have been calibrated with two reference platinum probes in a range of temperature from 5°C to 40°C. A second degree polynomial equation has been applied to correct the measurement. The absolute error is:

$$\Delta T = 0.1^\circ\text{C} \quad (4.16)$$

The temperatures at the laser location are calculated by the following expression assuming a linear variation of the saturation pressure (temperature) along the adiabatic tube:

$$T_{laser,1} = T_{MEV,out} + \frac{T_{TS,out} - T_{MEV,out}}{L_{adb}} L_{adb,1} \quad (4.17)$$

$$T_{laser,2} = T_{MEV,out} + \frac{T_{TS,out} - T_{MEV,out}}{L_{adb}} (L_{adb,1} + L_{adb,2}) \quad (4.18)$$

The corresponding uncertainties are:

$$\Delta T_{laser,1} = \Delta T + \frac{|T_{TS,out} - T_{MEV,out}|}{L_{adb}} \left(1 + \frac{L_{adb,1}}{L_{adb}}\right) \Delta L_{adb} \quad (4.19)$$

$$\Delta T_{laser,2} = \Delta T + \frac{|T_{TS,out} - T_{MEV,out}|}{L_{adb}} \left(1 + \frac{L_{adb,1} + L_{adb,2}}{L_{adb}}\right) \Delta L_{adb} \quad (4.20)$$

with ΔT given by Eq. (4.16) and ΔL_{adb} by Eq. (4.15).

For example, if $T_{MEV,out} = 30.0^\circ\text{C}$, $T_{TS,out} = 28.5^\circ\text{C}$ (temperatures for $G = 700 \text{ kg/m}^2\text{s}$, $x_{MEV,out} = 0.54$ and $D = 0.509 \text{ mm}$), $L_{adb,1} = 20 \text{ mm}$, $L_{adb,2} = 70 \text{ mm}$ and $L_{adb} = 120 \text{ mm}$ the results are:

$$\begin{aligned} T_{laser,1} &= 29.75 \pm 0.11^\circ\text{C} \\ T_{laser,2} &= 28.88 \pm 0.11^\circ\text{C} \end{aligned}$$

It can be seen that the temperatures calculated at the laser location are still very accurate.

4.4.6 Fluid properties

The fluid properties were calculated from a temperature measurement by applying a linear regression of the 3rd order determined with the *RefProp* software.

$$\Phi = a_0 + a_1T + a_2T^2 + a_3T^3 \quad (4.21)$$

and the corresponding uncertainty is:

$$\Delta\Phi = [a_1 + 2a_2T + 3a_3T^2] \Delta T \quad (4.22)$$

The coefficients a_0 , a_1 , a_2 and a_3 for the enthalpy calculations are given in the Tables 4.1 and 4.2.

Table 4.1: Coefficients for the R-134a properties.

| Coef. | h_L | h_V |
|-------|----------|----------|
| a_0 | 200002.6 | 398600.1 |
| a_1 | 1343.4 | 583.6 |
| a_2 | 1.3 | -1.0 |
| a_3 | 0.00879 | -0.01314 |

Table 4.2: Coefficients for the R-245fa properties.

| Coef. | h_L | h_V |
|-------|----------|----------|
| a_0 | 199980.9 | 404956.0 |
| a_1 | 1299.3 | 748.6 |
| a_2 | 1.1 | 0.8 |
| a_3 | 0.00324 | -0.00789 |

For example, for a saturation temperature of 30°C the results for the enthalpies for R-134a are:

$$h_L = 241712 \text{ J/kg} \pm 0.06\%$$

$$h_V = 414853 \text{ J/kg} \pm 0.01\%$$

For R-245fa, the results are:

$$h_L = 240037 \text{ J/kg} \pm 0.06\%$$

$$h_V = 427921 \text{ J/kg} \pm 0.02\%$$

As can be seen, the relative errors made on the enthalpy calculations are negligible.

4.4.7 Mass Flow

The specifications of the Elite CMF010 Coriolis mass flow meter from *Micromotion* are indicated as follows:

$$\text{for } \dot{M} \geq 0.555 \times 10^{-3} \text{ kg/s, } \Delta\dot{M} = 0.001 \dot{M} \quad (4.23)$$

$$\text{for } \dot{M} < 0.555 \times 10^{-3} \text{ kg/s, } \Delta\dot{M} = 0.555 \times 10^{-7} \text{ kg/s} \quad (4.24)$$

4.4.8 Mass flux

The definition of the mass flux G is:

$$G = \frac{4\dot{M}}{\pi D^2}$$

The uncertainty on G is:

$$\Delta G = G \left(\frac{\Delta\dot{M}}{\dot{M}} + 2 \frac{\Delta D}{D} \right) \quad (4.25)$$

The mass flux ranged from 200 kg/m²s (for $D = 0.790$ mm) or 350 kg/m²s (for $D = 0.509$ mm) up to 2000 kg/m²s (for both tube diameters)

Thus the uncertainties are:

G=350 kg/m²s $\pm 2\%$ for $D = 0.509$ mm
 G=2000 kg/m²s $\pm 2\%$ for $D = 0.509$ mm
 G=200 kg/m²s $\pm 2\%$ for $D = 0.790$ mm
 G=2000 kg/m²s $\pm 2\%$ for $D = 0.790$ mm

The mass flux is then well measured even if the mass flow is low.

4.4.9 Pressure

The *Keller* pressure transducers are connected to a *National Instrument SCXI* acquisition system using a scan rate of 1 scan/sec. They were calibrated with an error less than 5 mbar for their present range of application.

$$\Delta P = 5 \times 10^{-3} \text{ bar} \quad (4.26)$$

The four pressures studied in this experimental work are:

6.85 bar $\pm 0.07\%$ for R-134a
 7.7 bar $\pm 0.06\%$ for R-134a
 8.86 bar $\pm 0.06\%$ for R-134a
 2.13 bar $\pm 0.23\%$ for R-245fa

The relative errors made on the pressure measurement are very small.

4.4.10 Energy balance

In order to validate the Joule heating in the microevaporator as well as the insulation around it, an energy balance test has been carried out with R-134a.

Energy Q_{in} supplied to the evaporator

The electrical power supplied by Joule effect by the *Sorensen* 8-125 (a max of 8 V and 125 A) in the evaporator is:

$$Q_{in} = UI \quad (4.27)$$

The uncertainty related to Q_{in} is given by the following equation:

$$\Delta Q_{in} = Q_{in} \left(\frac{\Delta U}{U} + \frac{\Delta I}{I} \right) \quad (4.28)$$

The dc voltage U is measured by the PCI-MIO-16XE50 of National Instrument. The corresponding uncertainty is:

$$\Delta U = 0.0002 U \quad (4.29)$$

The dc current I is measured by a dc current transformer *Z202A* and the accuracy is:
For $I < 20$ A,

$$\Delta I = 0.01 I + 0.03 \quad (4.30)$$

For $I \geq 20$ A,

$$\Delta I = 0.01 I + 0.3 \quad (4.31)$$

Sensible energy inside the liquid Q_{out}

The energy acquired by the liquid is given by the increase of the liquid enthalpy:

$$Q_{out} = \dot{M} (h_{LMEV,out} - h_{LMEV,in}) \quad (4.32)$$

$$(4.33)$$

The corresponding absolute error is thus:

$$\Delta Q_{out} = Q_{out} \left(\frac{\Delta h_{LMEV,out} + \Delta h_{LMEV,in}}{h_{LMEV,out} - h_{LMEV,in}} + \frac{\Delta \dot{M}}{\dot{M}} \right) \quad (4.34)$$

Energy balance

The energy balance is defined by:

$$Q_{in,out} = Q_{in} - Q_{out} \quad (4.35)$$

The uncertainty is:

$$\Delta Q_{in,out} = \Delta Q_{in} + \Delta Q_{out} \quad (4.36)$$

Figure 4.11 shows the energy balance experiments for $D = 0.509$ mm. It appears that the higher the heat flux, the lower the losses are. This test has been carried out for subcooled liquid. In two-phase flow experiments, the heat flux is nearly always very high and the deviation of the energy balance is less than 2-3 %.

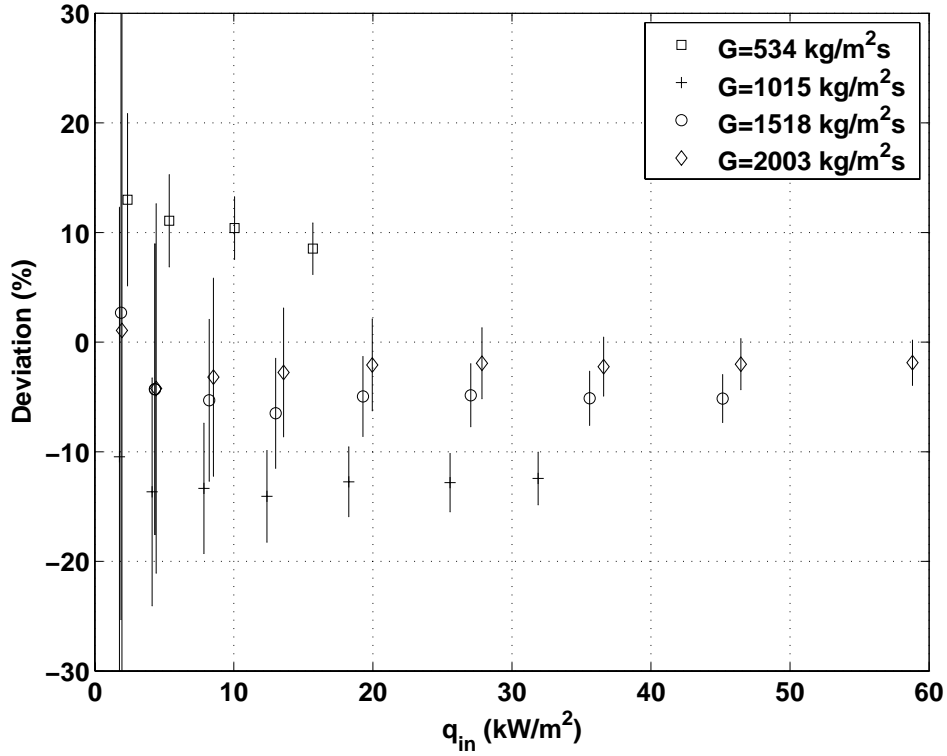


Figure 4.11: Energy balance for $D = 0.509$ mm and different mass fluxes.

4.4.11 Heat flux

Neglecting lateral (to the clamps) and radial (to insulation) losses, the heat flux is the ratio of the heat supplied by the *Sorensen* 8-125 on the internal surface of the tube:

$$q = \frac{Q_{in}}{\pi D L_{MEV}} \quad (4.37)$$

Applying the propagation error method to Eq. (4.37) leads to:

$$\frac{\Delta q}{q} = \frac{\Delta Q_{in}}{Q_{in}} + \frac{\Delta D}{D} + \frac{\Delta L_{MEV}}{L_{MEV}} \quad (4.38)$$

Heat fluxes ranged from 3.1 to 597 kW/m². Respectively, the relative errors are ± 5.5 % ($I = 1.1$ A < 20 A) and ± 5.7 % ($I = 25.4$ A > 20 A, the calibration has been changed). For $q = 199$ kW/m², the relative error is ± 3 % ($I = 8.9$ A < 20 A).

Hysteresis effect ?

As it will be explained in Section 6.1, the heat flux is increased stepwise at a constant mass flux. But one can wonder if there would be any hysteresis effect on the results due to this

increase of the heat flux. By inspecting Figs. 4.12 and 4.13, it can be seen that increasing or decreasing the heat flux has no effect on the vapor velocity calculation nor the flow pattern detection.

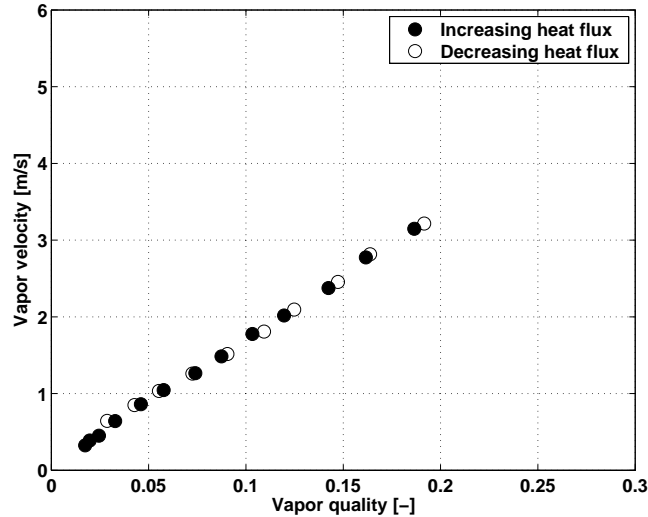


Figure 4.12: Vapor bubble velocity calculation from laser 1 for $D = 0.509$ mm, $L_{MEV} = 70.70$ mm, $T_{sat} = 30^\circ\text{C}$, $G = 500$ kg/m²s and $\Delta T_{sub} = 3^\circ\text{C}$. Data shown are for increasing and decreasing heat flux.

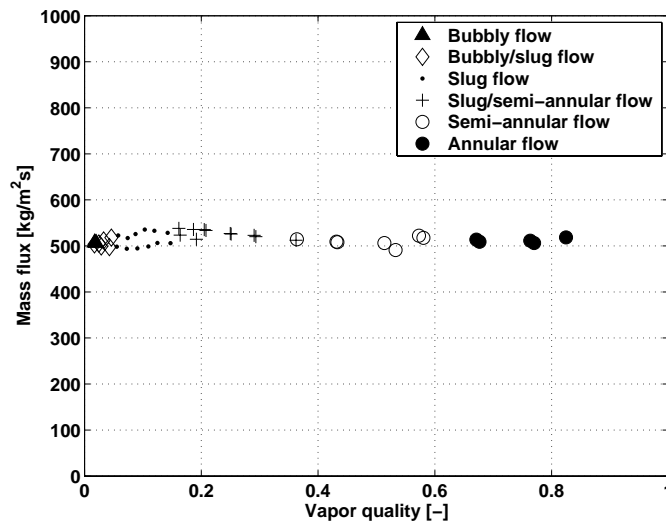


Figure 4.13: Flow pattern determination from laser 1 for $D = 0.509$ mm, $L_{MEV} = 70.70$ mm, $T_{sat} = 30^\circ\text{C}$ and $\Delta T_{sub} = 3^\circ\text{C}$. Data shown are for increasing and decreasing heat flux.

4.4.12 Vapor quality

Vapor quality at outlet of the microevaporator $x_{MEV,out}$

The vapor quality is calculated at outlet of the microevaporator with the following relation based on the definition of Eq. (2.2):

$$x_{MEV,out} = \frac{\frac{Q_{in}}{\dot{M}} + h_{L_{MEV,in}} - h_{L_{MEV,out}}}{h_{LV_{MEV,out}}} \quad (4.39)$$

The absolute error is expressed as:

$$\begin{aligned} \Delta x_{MEV,out} = & \frac{1}{h_{LV_{MEV,out}}} \left[\frac{1}{\dot{M}} \Delta Q_{in} + \frac{Q_{in}}{\dot{M}^2} \Delta \dot{M} + \Delta h_{L_{MEV,in}} \right. \\ & \left. + \Delta h_{L_{MEV,out}} + x_{MEV,out} \Delta h_{LV_{MEV,out}} \right] \end{aligned} \quad (4.40)$$

with $\Delta h_{LV_{MEV,out}}$, $\Delta h_{L_{MEV,in}}$ and $\Delta h_{L_{MEV,out}}$ given by Eq. (4.22); ΔQ_{in} given by Eq. (4.28).

Vapor quality at the outlet of the test section $x_{TS,out}$

The vapor quality at the outlet of the test section $x_{TS,out}$ is calculated with the following expression:

$$x_{TS,out} = \frac{h_{MEV,out} - h_{L_{TS,out}}}{h_{LV_{TS,out}}} \quad (4.41)$$

and the absolute error is given by Eq. (4.42).

$$\Delta x_{TS,out} = x_{TS,out} \left(\frac{\Delta h_{MEV,out}}{|h_{MEV,out} - h_{L_{TS,out}}|} + \frac{\Delta h_{L_{TS,out}}}{|h_{MEV,out} - h_{L_{TS,out}}|} + \frac{\Delta h_{LV_{TS,out}}}{h_{LV_{TS,out}}^2} \right) \quad (4.42)$$

Vapor quality at the laser location $x_{laser,1}$ and $x_{laser,2}$

The vapor quality at each laser location is calculated with Eqs. (4.43) and (4.44) assuming a linear variation of the vapor quality (due to flashing effect) along the adiabatic tube.

$$x_{laser,1} = x_{MEV,out} + \frac{x_{TS,out} - x_{MEV,out}}{L_{adb}} L_{adb,1} \quad (4.43)$$

$$x_{laser,2} = x_{MEV,out} + \frac{x_{TS,out} - x_{MEV,out}}{L_{adb}} (L_{adb,1} + L_{adb,2}) \quad (4.44)$$

and the corresponding uncertainties are given by Eqs. (4.45) and (4.46)

$$\begin{aligned}\Delta x_{laser,1} &= \frac{L_{adb,1}}{L_{adb}} \Delta x_{TS,out} + \left(1 - \frac{L_{adb,1}}{L_{adb}}\right) \Delta x_{MEV,out} \\ &+ \frac{|x_{TS,out} - x_{MEV,out}|}{L_{adb}} \left(1 + \frac{L_{adb,1}}{L_{adb}}\right) \Delta L_{adb}\end{aligned}\quad (4.45)$$

$$\begin{aligned}\Delta x_{laser,2} &= \frac{L_{adb,1} + L_{adb,2}}{L_{adb}} \Delta x_{TS,out} + \left(1 - \frac{L_{adb,1} + L_{adb,2}}{L_{adb}}\right) \Delta x_{MEV,out} \\ &+ \frac{|x_{TS,out} - x_{MEV,out}|}{L_{adb}} \left(1 + \frac{L_{adb,1} + L_{adb,2}}{L_{adb}}\right) \Delta L_{adb}\end{aligned}\quad (4.46)$$

With $\Delta x_{MEV,out}$ and $\Delta x_{TS,out}$ given by Eq. (4.40) and Eq. (4.42) respectively. ΔL_{adb} is expressed by Eq. (4.15).

If one takes the same example as for the temperature (Part 4.4.5), i.e. if $T_{MEV,out} = 30.0^\circ\text{C}$, $T_{TS,out} = 28.5^\circ\text{C}$, $G = 700 \text{ kg/m}^2\text{s}$, $D = 0.509 \text{ mm}$, $L_{adb,1} = 20 \text{ mm}$, $L_{adb,2} = 70 \text{ mm}$ and $L_{adb} = 120 \text{ mm}$, the results are:

$$\begin{aligned}x_{MEV,out} &= 0.54 \pm 1.9\% \\ x_{TS,out} &= 0.55 \pm 1.8\% \\ x_{laser,1} &= 0.541 \pm 1.9\% \\ x_{laser,2} &= 0.547 \pm 1.8\%\end{aligned}$$

The relative error on the vapor quality is small for most of the results. Only the results for vapor qualities less than about 0.01 have large uncertainties (that is, restricted to results in bubbly flow regime).

4.4.13 Vapor bubble velocity

The vapor bubble velocity is given by:

$$u_V = \frac{L_{adb,2}}{t_{CC}} \quad (4.47)$$

t_{CC} is obtained by the cross correlation of the two signals. The corresponding relative error is:

$$\frac{\Delta u_V}{u_V} = \frac{\Delta L_{adb,2}}{L_{adb,2}} + \frac{\Delta t_{CC}}{t_{CC}} \quad (4.48)$$

where $\Delta L_{adb,2}$ is given by Eq. (4.15). The error made when determining the peak location of the cross correlation is at maximum 1 data point as explained in Unserbacher [55]. So the absolute error for Δt_{CC} is:

$$\Delta t_{CC} = 0.1 \text{ ms} \quad (4.49)$$

The uncertainty made on this measurement is very small. As an example, if the velocity is $u_V = 0.2 \text{ m/s}$, $t_{CC} = 35 \text{ ms}$ with $L_{adb,2} = 70 \text{ mm}$, the relative error on u_V is 1 %.

In order to verify the velocity calculation, a comparison of the velocity calculated from the cross correlation of the two lasers versus those obtained by video processing has been carried out for different conditions. Two examples are presented in Fig. 4.14. It is shown that the video calculation is at most 20 % higher than the calculation with the lasers. This difference comes from the fact that for the video processing, only 50 long bubbles were taken for measurement (it is easier to process long bubbles than small ones) while for the cross correlation calculation, all the bubbles (2500 bubbles on average) were processed with different sizes. As the velocity is proportional to the length of the vapor bubble, the cross correlation result is always less than that from the video processing. The cross correlation method is thus validated and seems to give a more accurate result than video processing.

Influence of the distance between the lasers

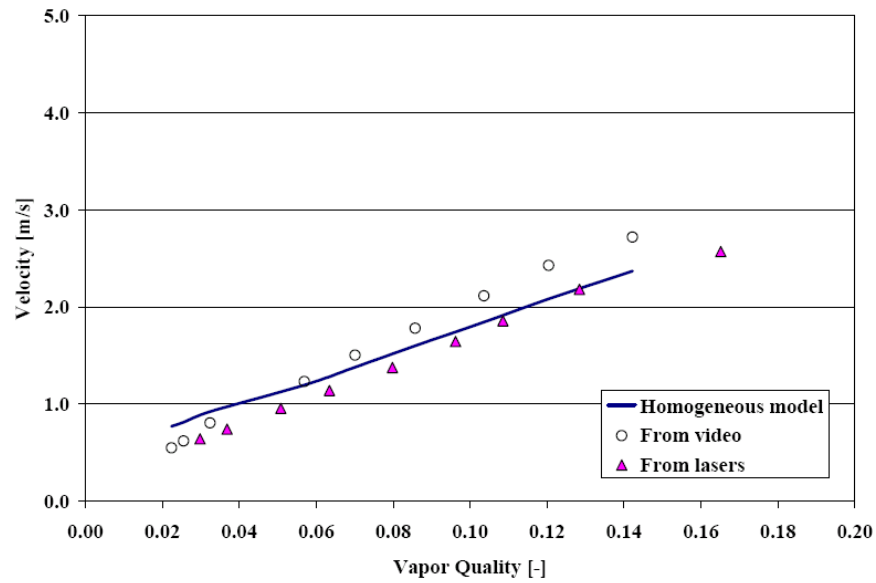
As shown in Fig. 4.15, the distance between the lasers ($L_{adb,2}$) has no effect on the results. The distance of 70 mm has been chosen because it gives the best accuracy within the limits of the present setup. The tests have been carried out only between 50 and 70 mm because it was not physically possible to increase that range (the lenses and micrometer positioning system limit the space available).

Influence of the acquisition time

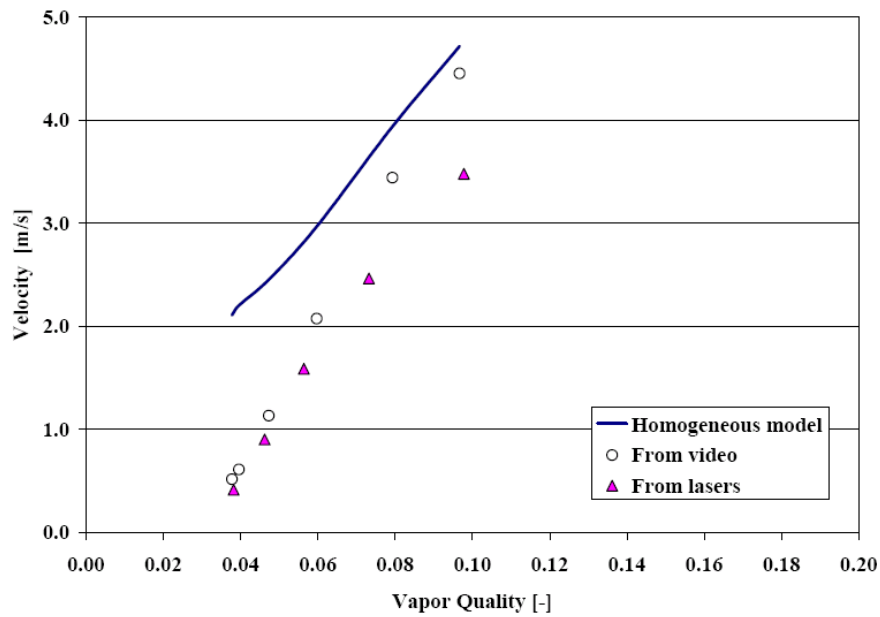
Figure 4.16 shows the effect of the acquisition time of the laser on the bubble frequency and vapor velocity. The black circle corresponds to 5 s of acquisition, the acquisition time chosen in this study. As a conclusion, the acquisition time has no effect on the bubble frequency or the cross correlation to determine the vapor velocity. As there are 10 000 acquisitions/sec, the files are quickly huge, that is why a compromise of 5 s for the acquisition time has been chosen. The ratio information/size of the file is very good.

4.4.14 Pressure drop

Accurate measurements of two-phase pressure drops along microchannels presents numerous experimental challenges. Presently, the pressure drops are calculated in the two-phase flow region from the **temperature difference** in the saturation pressure along the test length (Note that this approach is particularly suited to microchannels since it avoids disturbing the flow with small pressure taps, which could affect flow regimes, could act as bubble nucleation sites, create a capillary pressure differential, etc. This method actually becomes more accurate with increasing pressure drop). The first thermocouple is $T_{MEV,out}$ and second one is $T_{TS,out}$, both in adiabatic locations. This second saturation temperature is taken



(a) R-134a $G = 500 \text{ kg/m}^2\text{s}$, $T_{sat} = 30^\circ\text{C}$, $D = 0.509 \text{ mm}$ and $L_{MEV} = 70 \text{ mm}$.



(b) R-245fa $G = 500 \text{ kg/m}^2\text{s}$, $T_{sat} = 35^\circ\text{C}$, $D = 0.509 \text{ mm}$ and $L_{MEV} = 70 \text{ mm}$.

Figure 4.14: Comparison between the velocity calculated from the cross correlation of the lasers with the video processing.

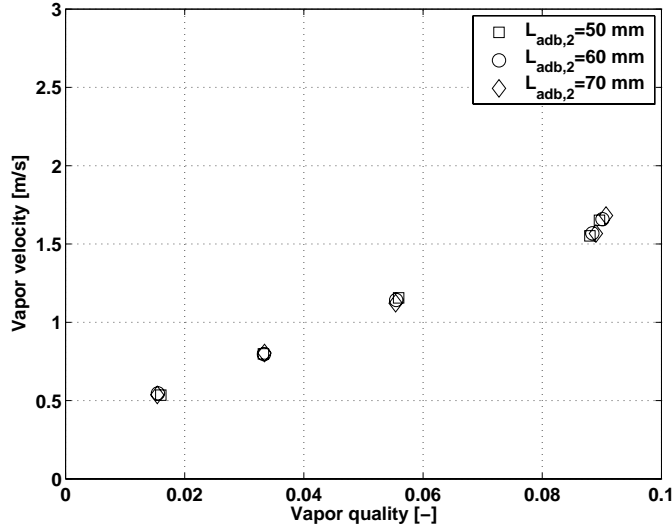


Figure 4.15: Effect of the distance between the lasers ($L_{adb,2}$) on the vapor bubble velocity calculation from laser 1 for $D = 0.509$ mm, $L_{MEV} = 70.70$ mm, $T_{sat} = 30^\circ\text{C}$, $G = 500$ kg/m²s and $\Delta T_{sub} = 3^\circ\text{C}$.

directly in the fluid in the 4 mm diameter tube, right after the test section. Due to the sudden enlargement, the saturation pressure might be reduced. To take into account this phenomena, the Eq. (4.50) is used. If the void fraction remains unchanged across the enlargement and if we assume a homogeneous flow, it becomes:

$$P_2 - P_1 = \left[\frac{G_1^2 \sigma (1 - \sigma)}{\rho_L} \right] \left[1 + \left(\frac{\rho_L}{\rho_L - \rho_V} \right) x \right] \quad (4.50)$$

where σ is the ratio between the cross sections 1 ($D = 0.509$ mm) and 2 ($D = 4$ mm). This equation allowed the real saturation temperature (pressure) right before the sudden enlargement to be calculated. After calculation, it appears that the difference between the two pressures across the enlargement is less than 0.2 % for R-134a and less than 3.5 % for R-245fa. It is rather negligible but taken into account anyway.

The total length between these two thermocouples is $L_{adb} = 120$ mm and this is maintained constant. The relation between saturation temperature and saturation pressure is given by:

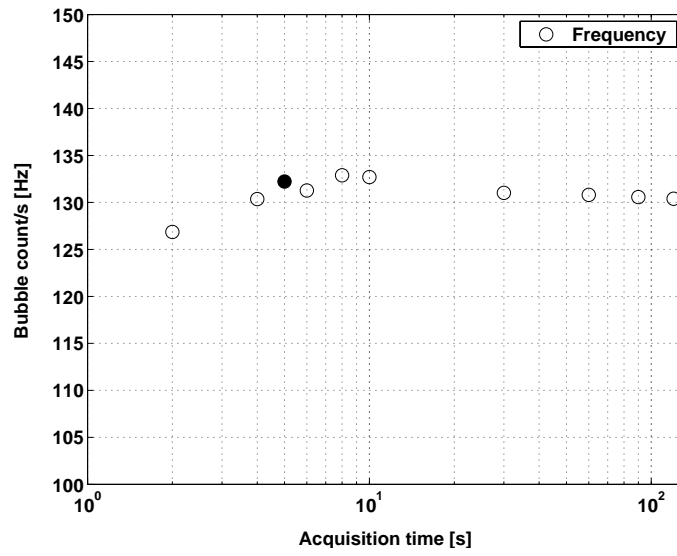
$$P_{sat} = b_0 + b_1 T_{sat} + b_2 T_{sat}^2 + b_3 T_{sat}^3 + b_4 T_{sat}^4 \quad (4.51)$$

where b_0, \dots, b_4 are given by Table 4.3.

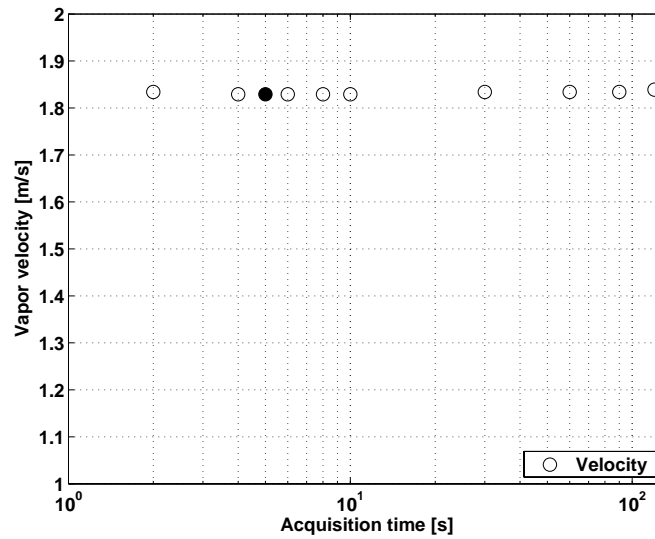
The corresponding absolute error is:

$$\Delta P_{sat} = (b_1 + 2b_2 T_{sat} + 3b_3 T_{sat}^2 + 4b_4 T_{sat}^3) \Delta T_{sat} \quad (4.52)$$

The total two-phase pressure drop expressed in bar/m is calculated with the following equation:



(a)



(b)

Figure 4.16: Effect of the acquisition time on the bubble frequency (a) and vapor velocity (b).

Table 4.3: Coefficients for the vapor pressure curve calculation.

| Coef. | R-134a | R-245fa |
|-------|--------------------|--------------------|
| b_0 | 2.928 | 0.5359 |
| b_1 | 0.1061 | 0.0245 |
| b_2 | 0.0015 | 0.0004 |
| b_3 | 9×10^{-6} | 4×10^{-6} |
| b_4 | 2×10^{-8} | 1×10^{-8} |

$$\left(\frac{dP}{dz}\right)_t = \frac{(P_{MEV,out} - P_{TS,out})}{L_{adb}} \quad (4.53)$$

And the absolute error is:

$$\Delta\left(\left(\frac{dP}{dz}\right)_t\right) = \frac{1}{L_{adb}} [\Delta P_{MEV,out} + \Delta P_{TS,out} + (P_{MEV,out} - P_{TS,out}) \frac{\Delta L_{adb}}{L_{adb}}] \quad (4.54)$$

with $\Delta P_{TS,out}$ and $\Delta P_{MEV,out}$ given by Eq. (4.52). As an example, if $\left(\frac{dP}{dz}\right)_t = 8.8$ bar/m, the uncertainty is $\pm 4.1\%$ and if $\left(\frac{dP}{dz}\right)_t = 1.3$ bar/m, the uncertainty is $\pm 25\%$. These values should be kept in mind in the comparisons between measured data and prediction methods in Chapter 8.

4.4.15 Inlet subcooling

The inlet subcooling is calculated with Eq. (4.55).

$$\Delta T_{sub} = T_{sat_{MEV,in}} - T_{MEV,in} \quad (4.55)$$

$T_{sat_{MEV,in}}$ is calculated with the pressure transducer $P_{TS,in}$ and applying the conventional correlation for pressure drop for flow of a subcooled liquid. Then the relation between the saturation pressure and the saturation temperature is given by Eq. (4.56).

$$T_{sat} = c_0 + c_1 P_{sat} + c_2 P_{sat}^2 + c_3 P_{sat}^3 + c_4 P_{sat}^4 \quad (4.56)$$

where c_0, \dots, c_4 are given by Table 4.4.

The absolute error made on the inlet subcooling is then:

$$\Delta(\Delta T_{sub}) = (c_1 + 2c_2 P_{sat} + 3c_3 P_{sat}^2 + 4c_4 P_{sat}^3) \Delta P + \Delta T \quad (4.57)$$

Table 4.4: Coefficients for the pressure to temperature calculation.

| Coef. | R-134a | R-245fa |
|-------|---------|---------|
| c_0 | -40.873 | -14.007 |
| c_1 | 19.769 | 33.198 |
| c_2 | -2.5113 | -5.9872 |
| c_3 | 0.1957 | 0.5951 |
| c_4 | -0.0062 | -0.0225 |

For the subcoolings tested in the present study from 2 to 15°C, this represents an error of 0.1°C in the value of the subcooling, as the dominant term in Eq. (4.57) is ΔT .

4.4.16 Superficial velocities

Equations (2.9) and (2.10) give the definition of the superficial velocity for the vapor and the liquid respectively. Equation (2.11), is the total superficial velocity.

The corresponding uncertainties are:

$$\frac{\Delta j_V}{j_V} = \frac{\Delta G}{G} + \frac{\Delta x}{x} + \frac{\Delta \rho_V}{\rho_V} \quad (4.58)$$

$$\frac{\Delta j_L}{j_L} = \frac{\Delta G}{G} + \frac{\Delta x}{1-x} + \frac{\Delta \rho_L}{\rho_L} \quad (4.59)$$

$$\frac{\Delta j}{j} = \frac{\Delta j_L + \Delta j_V}{j} \quad (4.60)$$

If one takes the same example as for the temperature (Part 4.4.5), i.e. if $T_{MEV,out} = 30.0^\circ\text{C}$, $T_{TS,out} = 28.5^\circ\text{C}$, $G = 700 \text{ kg/m}^2\text{s}$, $D = 0.509 \text{ mm}$, $L_{adb,1} = 20 \text{ mm}$, $L_{adb,2} = 70 \text{ mm}$ and $L_{adb} = 120 \text{ mm}$, the results are:

$$\begin{aligned} j_V &= 1166 \text{ m/s} \pm 4.1\% \\ j_L &= 22 \text{ m/s} \pm 5.2\% \\ j &= 1188 \text{ m/s} \pm 4.2\% \end{aligned}$$

4.4.17 Repeatability of the experiments

The repeatability of the experiments has been regularly tested and verified. In Figs. (4.17) and (4.18), two identical experiments have been repeated on two different dates about six months apart (29/04/2004 and 31/10/2004). It is clear that the experimental stand yielded experiments with a very good repeatability in the results.

4.5 Conclusions on the test facility and measurement technique

A new multipurpose microchannel test facility has been built to study the characteristics of two-phase flows and boiling heat transfer. The facility is computer controlled and provide very accurate results. Furthermore, a laser assisted technique has been developed and perfected to quantitatively identify flow patterns, obtain bubble frequencies and lengths and measure bubble velocities.

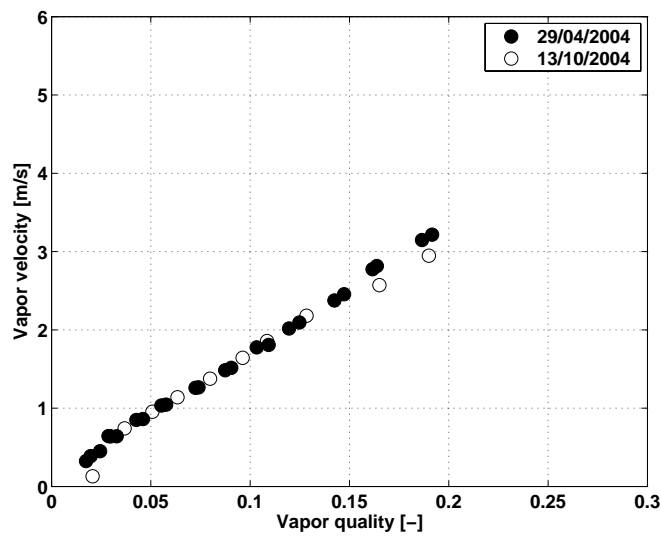


Figure 4.17: Vapor velocity comparison at two different dates (29/04/2004 and 31/10/2004) from laser 1 for R-134a, $D = 0.509$ mm, $L_{MEV} = 70.70$ mm, $T_{sat} = 30^{\circ}\text{C}$ and $\Delta T_{sub} = 3^{\circ}\text{C}$.

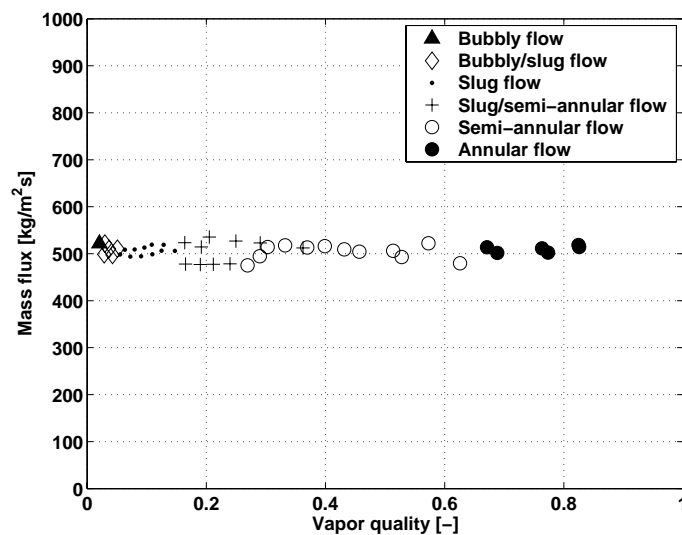


Figure 4.18: Flow pattern map comparison at two different dates (29/04/2004 and 31/10/2004) from laser 1 for R-134a, $D = 0.509$ mm, $L_{MEV} = 70.70$ mm, $T_{sat} = 30^{\circ}\text{C}$ and $\Delta T_{sub} = 3^{\circ}\text{C}$.

Chapter 5

Critical heat flux

The critical heat flux is the maximum heat flux that can be dissipated by an evaporating two-phase flow without a large excursion in the heated channel's wall temperature. Presently, it has been measured with saturated conditions near the channel exit (where the beginning of the dryout process instigating CHF occurs). The imposed boundary condition along the microchannel is a uniform heat flux imposed electrically with a DC current.

5.1 Experimental procedure

The flow in the test loop is imposed by the pressure difference in the hot and cold reservoirs. The required mass flow is regulated by the microvalve situated after the subcooler (see Fig. 4.2). The refrigerant saturation temperature is adjusted by the pressure in the cold reservoir and the liquid subcooling by the power provided to the preheater. After stabilization of the initial conditions, the test section is heated stepwise by the Sorensen power supply controlled by the computer. All experimental data are acquired by the National Instrument acquisition system at a frequency of 1 Hz. Figure 5.1 shows the evolution of the heat flux during a single test at a mass flux of $1000 \text{ kg/m}^2\text{s}$ with refrigerant R-134a.

As can be seen, the heat flux increases almost linearly with a small increase of the wall temperature (less than 8°C). The maximum heat flux is obtained at $q = 163 \text{ kW/m}^2$ and is termed CHF. At this point, considerable vapor is being formed, making it difficult for the liquid to continuously wet the surface. The decline in the heat transfer coefficient causes the sudden wall temperature increase, which is detected by the thermocouple $T_{MEV,secu}$ noted in Section 4.2. To avoid the burnout of the test section, the power supply is cut when $\Delta T > 40^\circ\text{C}$. The same procedure is performed for all experimental points.

5.2 Experimental results

There were 33 experimental CHF points obtained during this study for the conditions presented in Table 5.1. In this section the main trends in the CHF variation will be presented.

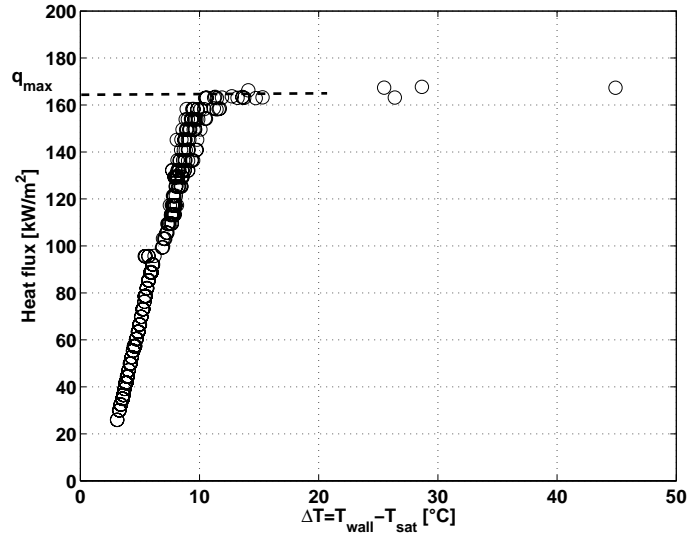


Figure 5.1: Determination of CHF during a single test for R-134a, $G = 1000 \text{ kg/m}^2\text{s}$, $T_{sat} = 30^\circ\text{C}$, $D = 0.509 \text{ mm}$ and $L_{MEV} = 70\text{mm}$.

Figure 5.2 shows the evolution of CHF as a function of mass flux in the 0.509 and 0.790 mm microchannels. All conditions (the heated length of the microevaporator and the temperature of subcooling of refrigerant) were the same for both microtube diameters. As can be seen, CHF increased with increasing mass flux. The CHF for the 0.790 mm microchannel is higher than that for the 0.509 mm channel and the difference becomes greater as the mass flux increases.

Table 5.1: Experimental conditions for CHF study.

| Parameter | Range | Units |
|------------------|-----------------|-------------------------|
| Fluid | R-134a, R-245fa | - |
| D | 0.509, 0.790 | mm |
| L_{MEV} | 20 - 70 | mm |
| G | 400 - 1600 | $\text{kg/m}^2\text{s}$ |
| q | 3.2 - 597 | kW/m^2 |
| T_{sat} | 30, 35 | $^\circ\text{C}$ |
| ΔT_{sub} | 2 - 15 | $^\circ\text{C}$ |
| We_{LO} | 293 - 21044 | - |
| ρ_V/ρ_L | 0.009 - 0.041 | - |
| L_{MEV}/D | 25 - 141 | - |

The influence of the heated length on CHF in both microtube diameters at constant mass flux is depicted in Fig. 5.3. The highest CHF was measured for the shortest heated length. With the extension of the heated length from 20 to 70 mm for the 0.790 mm diameter tube, the drop in the CHF value is 400 kW/m^2 ! It confirms that the heated length, besides the mass flux, is one of the most important parameters in the design of heat sinks. Fig. 5.3 shows also that the 0.790 mm microtube CHF is systematically higher than that for the 0.509 mm microtube. This increase ranges from 30% to 50%.

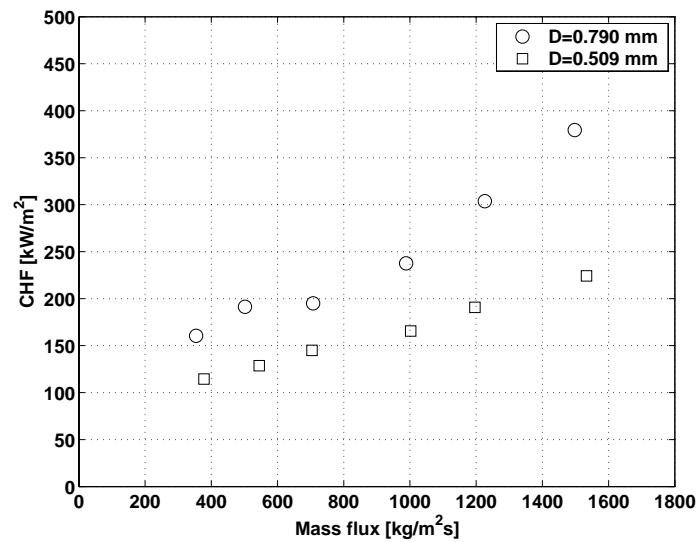


Figure 5.2: CHF versus mass flux in 0.509 and 0.790 mm ID tubes for R-134a, $T_{sat} = 35^{\circ}\text{C}$, $\Delta T_{sub} = 8^{\circ}\text{C}$, $L_{MEV} = 70$ mm.

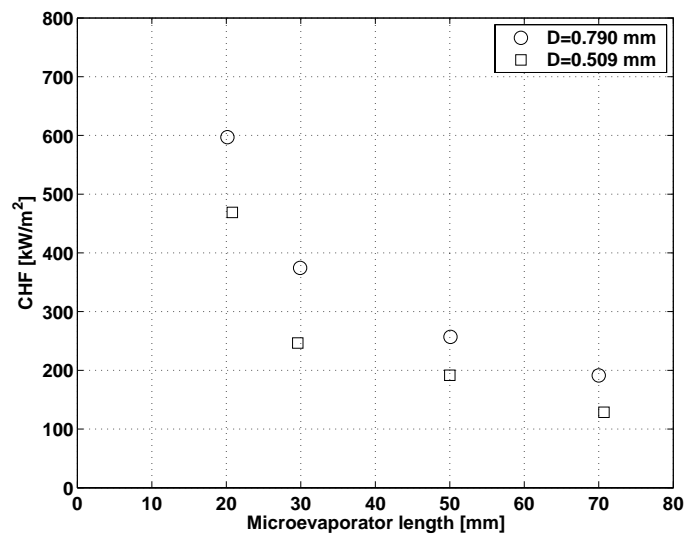


Figure 5.3: CHF versus microevaporator length in 0.509 and 0.790 mm ID tubes for R-134a, $G = 500$ kg/m²s, $T_{sat} = 35^{\circ}\text{C}$, $\Delta T_{sub} = 8^{\circ}\text{C}$.

The effect of the refrigerant on CHF is depicted in Fig. 5.4. The tests were run at the same experimental conditions for refrigerants R-134a and R-245fa. The values of CHF measured for R-245fa are higher than for R-134a, except at the heated length $L_{MEV} = 20\text{mm}$.

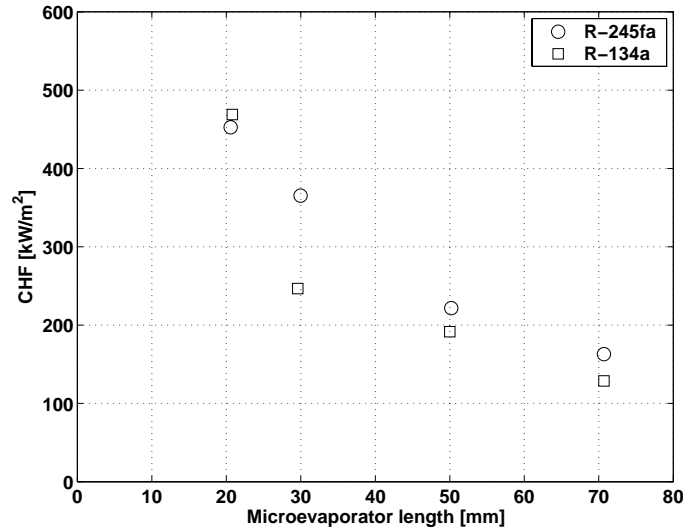


Figure 5.4: CHF versus microevaporator length for R-245fa and R-134a, $G = 500 \text{ kg/m}^2\text{s}$, $T_{sat} = 35^\circ\text{C}$, $D = 0.509 \text{ mm}$, $\Delta T_{sub} = 8^\circ\text{C}$.

Figure 5.5 shows the influence of the liquid subcooling on CHF. Only three experimental points have been acquired. Measurements for larger subcoolings were not possible. These limited experimental data show that CHF does not change significantly for the present subcoolings ranging from 4.5 to 12°C . This observation is in agreement with the results of Qu and Mudawar [42] for microchannel heat sinks.

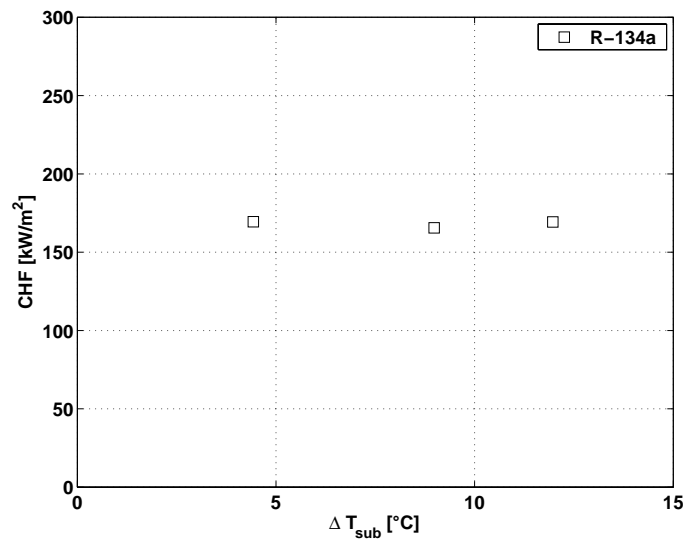


Figure 5.5: Influence of the inlet subcooling at entrance to the microevaporator on CHF for R-134a, $G = 1000 \text{ kg/m}^2\text{s}$, $T_{sat} = 35^\circ\text{C}$, $D = 0.509 \text{ mm}$, $L_{MEV} = 70 \text{ mm}$.

The effect of the refrigerant saturation temperature able to be tested over a narrow range

here is depicted in Fig. 5.6. CHF has been measured at various mass fluxes for saturation temperatures of 30 and 35°C. At mass fluxes lower than 1000 kg/m²s, there is only a slight difference in CHF for both saturation temperatures. With the increase of mass flux above 1000 kg/m²s, the effect of saturation temperature becomes more significant and CHF becomes somewhat higher for the saturation temperature of 35°C. This effect of saturation temperature seems to be logical according to the correlation of Katto-Ohno [25] in which the predicted CHF is a function of ρ_V/ρ_L and mass flux, G . The density ratio ρ_V/ρ_L increases with saturation temperature and the increase in CHF is magnified as the mass flux increases.

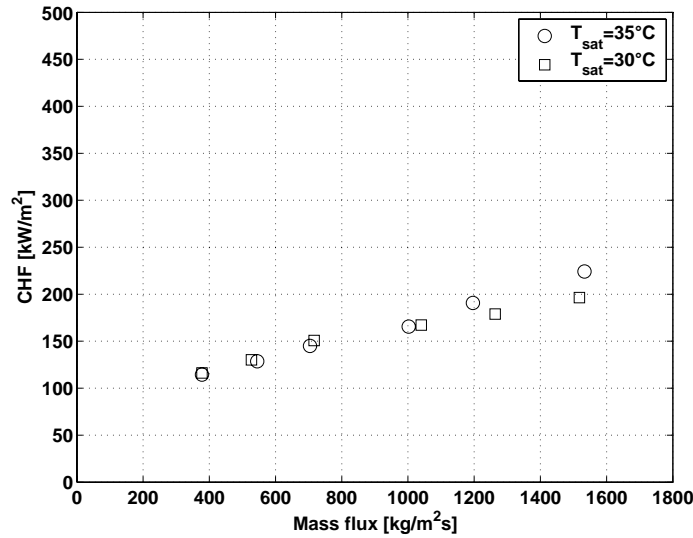


Figure 5.6: Influence of the saturation temperature on CHF for R-134a, $D = 0.509$ mm, $L_{MEV} = 70$ mm, $\Delta T_{sub} = 8^\circ\text{C}$.

5.3 Correlations for saturated CHF

The above trends in CHF for different experimental conditions show that CHF is affected by the mass flux, the microevaporator length, the microchannel diameter, the density ratio of the refrigerant and by the saturation temperature. All these effects are captured by the Katto-Ohno [25] correlation. However, the experimental data do not show almost any influence of the refrigerant subcooling on CHF (which are quite small here compared to most macroscale studies). Figure 5.7 depicts the comparison of all experimental data obtained in the 0.509 mm and 0.790 mm ID microchannels with the Katto-Ohno correlation with its subcooling effect deactivated, i.e. $K=0$ (refer to Eq. (3.3) for this correlation).

Only 41.2% of data fall within a $\pm 15.0\%$ error band but the comparison represents an extrapolation of their method to channel sizes below 1.0 mm.

The experimental data have also been compared to Eq. (3.4) of Qu and Mudawar [42]. This correlation was developed for rectangular multichannels based on the CHF data for water and R-113. As can be seen in Fig. 5.8, the predictions show the same trend in CHF as the data but the experimental values are significantly overpredicted.

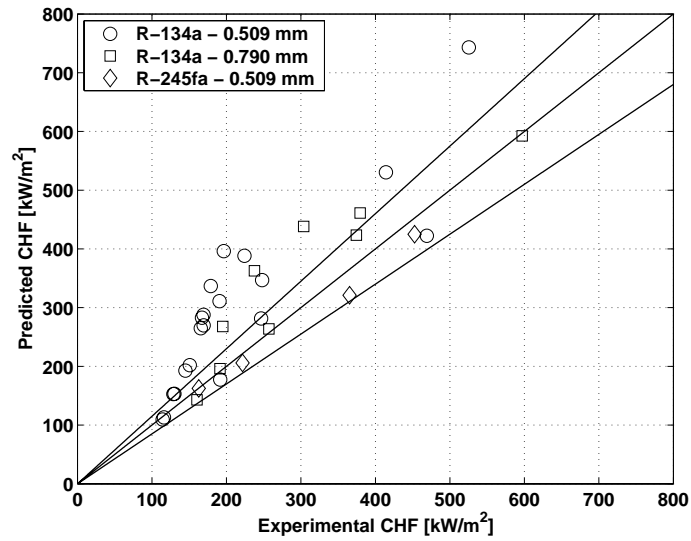


Figure 5.7: Comparison of the experimental results to the Katto-Ohno correlation.

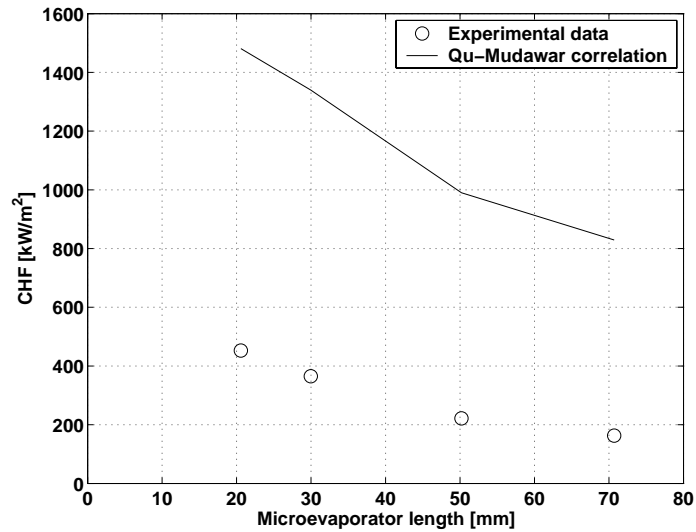


Figure 5.8: Comparison of the experimental results for R-245fa, $G = 500 \text{ kg/m}^2\text{s}$, $T_{sat} = 35^\circ\text{C}$, $D = 0.509 \text{ mm}$ and $\Delta T_{sub} = 8^\circ\text{C}$ to the Qu and Mudawar correlation.

Therefore, it has been decided to find new empirical factors based on the experimental data of this study to predict CHF in single, circular, uniformly heated microchannels. The analysis of experimental data using a least-squares fitting resulted in a new version of the Katto-Ohno correlation as

$$\frac{q_c}{Gh_{LV}} = 0.437 \left(\frac{\rho_V}{\rho_L} \right)^{0.073} We_{LO}^{-0.24} \left(\frac{L_{MEV}}{D} \right)^{-0.72} \quad (5.1)$$

with

$$We_{LO} = \frac{G^2 L_{MEV}}{\sigma \rho_L} \quad (5.2)$$

This microchannel expression above is comparable to the expressions in Table 3.1. Figure 5.9 compares the prediction of this new CHF correlation with the experimental data. The experimental points are predicted with 82.4% of data falling within a $\pm 15\%$ error band. This correlation is recommended for predicting CHF in single, uniformly heated, circular microchannels over the range of conditions cited in Table 5.1. Because of the lack of experimental data for higher reduced pressures, it is suggested to limit the use of this correlations to $\rho_V/\rho_L < 0.041$.

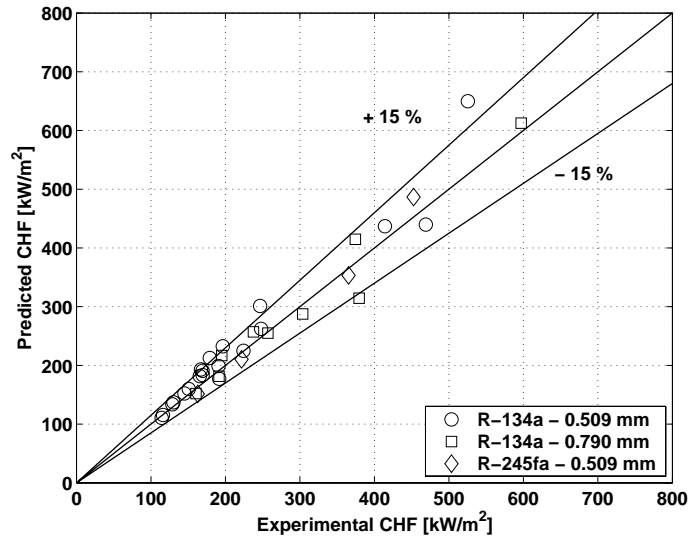


Figure 5.9: Comparison of the experimental results to the new correlation.

5.4 Flow patterns and critical quality

The critical vapor quality was obtained from the energy balance as follows

$$x_{crit} = \frac{q_c}{G(h_{LV} + h_{sub})} \frac{4L_{MEV}}{D} \quad (5.3)$$

where q_c is CHF predicted by Eq. (5.1).

Figure 5.10 depicts the variation of some of the present CHF data as a function of critical vapor quality (x_{crit}) in tube diameters of 0.509 mm and 0.790 mm. Flow patterns have been determined using the experimental flow pattern map explained later in the Chapter 6 and show that the present experimental points fall in the annular flow regime. It can be observed in Fig. 5.10 that CHF decreases almost linearly for all three experimental series without any significant change in the slope, which tends to confirm the Pribyl et al. [41] conclusion cited in Section 3.1.4.

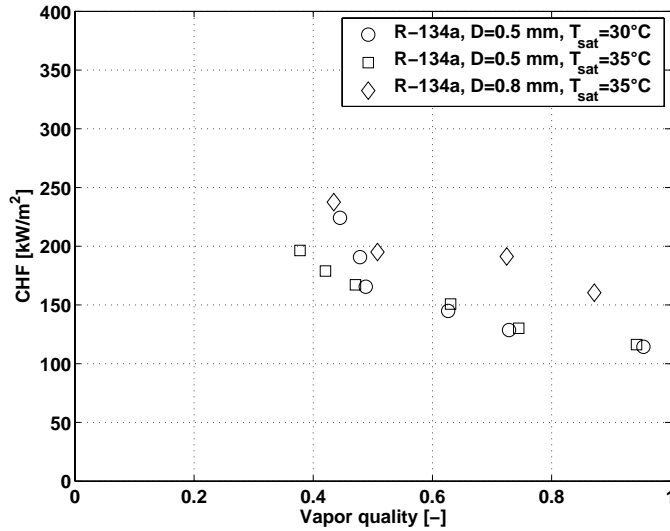


Figure 5.10: Variation of the CHF as a function of critical vapor quality at constant heated length, $L_{MEV} = 70$ mm for $350 \leq G \leq 1500$.

The dashed curve in Fig. 5.11 represents x_{crit} calculated from Eq. (5.3). Some discrepancies at higher mass velocities can be observed between the calculated and experimental critical vapor qualities. The main reason for this is the inaccuracy in the CHF prediction, which is more significant at higher G ($\pm 15\%$ error lines are included to show this). Nevertheless, Eq. (5.3) allows one to calculate x_{crit} with the reasonable accuracy and gives the transition curve from annular flow to dryout, assuming a uniform heat flux.

5.5 Conclusions from the CHF study

New accurate CHF data have been measured with the test facility in 0.509 and 0.790 mm ID microchannels. The experimental data have shown that the parameters dominating CHF are: mass flux, microevaporator length, microchannel internal diameter and thermal properties of refrigerant. No influence of the liquid subcooling has been found. Based on the experimental data, a new microchannel version of the Katto - Ohno correlation has been developed to predict the CHF in circular, uniformly heated microchannels. The new correlation predicts experimental points with the 82.4% of the data falling within a $\pm 15.0\%$ error band. Due to the lack of experimental data for higher reduced pressures and different flow patterns, it is

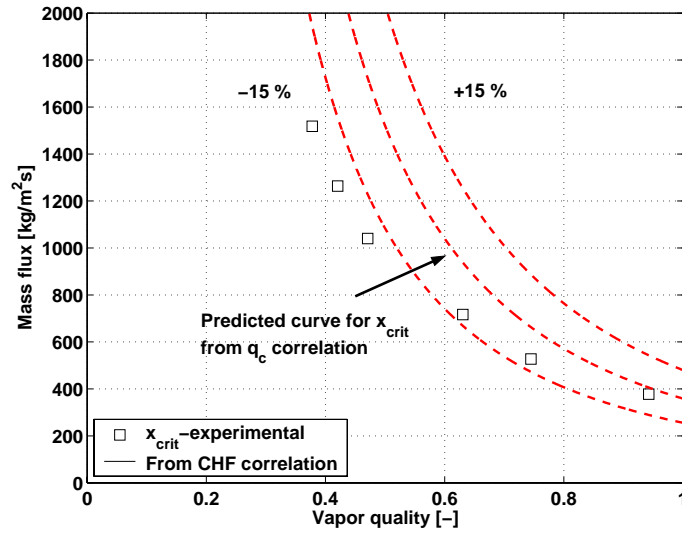


Figure 5.11: Transition from annular to dryout for R-134a, $L_{MEV} = 70$ mm and $T_{sat} = 30^\circ\text{C}$.

recommended to use this correlation for $\rho_V/\rho_L < 0.041$ and only for annular flow. Moreover, a new transition curve from annular flow to dryout has been proposed.

Chapter 6

Flow patterns

In this chapter, a description of the two-phase flow patterns observed, the method to quantitatively detect them using the laser signals, an analysis of bubble characteristics, comparison of the flow patterns observed to several flow pattern prediction maps, and a new diabatic flow pattern map will be presented.

6.1 Experimental procedure

The flow in the test loop is imposed by the pressure difference in the hot and cold reservoirs. The required mass flow is regulated by the microvalve situated after the subcooler (see Fig. 4.2). The refrigerant saturation temperature is adjusted by the pressure in the cold reservoir and the liquid subcooling by the power provided to the preheater. After stabilization, the test section is heated stepwise by the Sorensen power supply controlled by the computer. All experimental data are acquired by the National Instrument acquisition system at a frequency of 1 Hz. The laser measurements were acquired at 10000 Hz. All the results are postprocessed with a Matlab code to determine all the desired parameters.

There were 4480 experimental flow pattern points obtained during this study for the conditions presented in Table 6.1.

6.2 Experimental flow patterns

Four principal flow patterns and two intermediate transition regimes have been observed in the present study. Only three principal flow patterns (bubbly flow, slug flow and annular flow) were able to be identified by FFT (Fast Fourier Transform) of pulsed signals, as shown in Fig. 6.1, but these signals were not sufficient to identify the transitions. While bubbly flow exhibited almost white noise in FFT, slug flow was characterized by periodic frequencies between 80 and 170 Hz in this particular case. Annular flow was characterized by a dominant frequency smaller than 30 Hz . Semi-annular flow however does not exhibit a characteristic trace to be distinctively recognized by FFT signal processing alone, but the

Table 6.1: Experimental conditions for the flow pattern study.

| Parameter | Range | Units |
|--------------------------------|--|---------------------|
| Fluid | R-134a, R-245fa | - |
| D | 0.509, 0.790 | mm |
| L_{MEV} | 30 - 70 | mm |
| G | 210 - 2094 | kg/m ² s |
| q | 3.1 - 415 | kW/m ² |
| T_{sat} | 26, 30, 35 | °C |
| P_{sat} | 6.9, 7.7, 8.9 (for R-134a), 2.1 (for R-245fa) | bar |
| ΔT_{sub} | 2 - 6 | °C |
| $x_{MEV,out}$ | 0 - 0.95 | - |
| f_A | 0 - 928 | Hz |
| f_B | 0 - 717 | Hz |
| $\left(\frac{dP}{dz}\right)_t$ | 0 - 14.5 | bar/m |

difference between the bubbly flow and the semi-annular signals can be determined by also comparing their raw signals (shown later) and this has been verified by flow visualization using a high speed camera. By examining the evolution of peak and valley bubble count rates versus vapor quality, it was possible to determine the rate of coalescence of small bubbles into elongated bubbles and even elongated bubbles into semi-annular flow. The transitions were thus in fact detected by bubble count rates of signal peaks and valleys on the A and B thresholds and by the percentage of small bubbles remaining as shown in Fig. 6.2 and not the sometime ambiguous FFT signals. The microscale flow patterns observed are defined as follows:

Bubbly flow: In bubbly flow, the vapor phase is distributed as discrete bubbles in a continuous liquid phase and the bubbles are smaller in length than the diameter of the tube as shown in Fig. 6.3(a). This regime is detected when the percentage of surviving small bubbles is 100% and their average frequency f_A is greater than 0 bubbles/s. This flow pattern covers a very small range of vapor quality and is more or less non-existent at high mass flux. Fig. 6.4(a) shows a picture taken with a high definition video camera and Fig. 6.5(a) shows the voltage/time signal of the diode for this flow with the periodic passage of small bubbles. The average frequency f_A of bubbles here is 131 bubbles/s.

Bubbly/slug flow: In bubbly/slug flow, bubbly flow (described above) and slug flow (described below) are both present as shown in Fig. 6.3(b). It is detected when the percentage of surviving small bubbles is in the range from 1 to 99% and the average frequency f_A is greater than 0 bubbles/s. Fig. 6.4(b) shows a picture taken with a high definition video camera and Fig. 6.5(b) the corresponding signal. The average frequency f_A increases rapidly with the heat flux in the evaporator, reaches a peak and then decreases due to coalescence of small and elongated bubbles.

Slug flow: In slug flow (also called elongated bubble flow by some authors), the vapor bubbles are approximately the same diameter as the tube as shown in Fig. 6.3(c). The

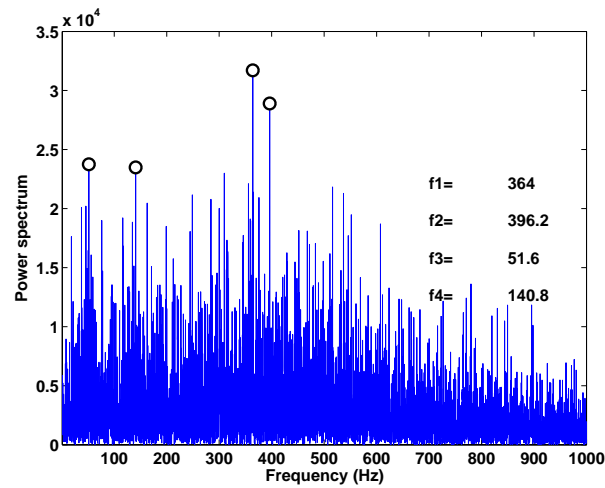
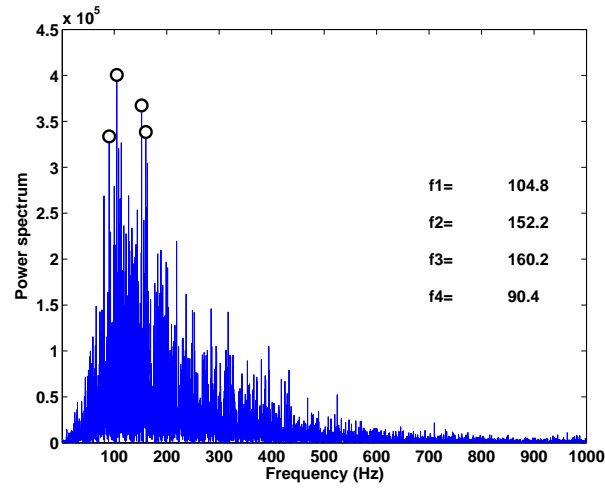
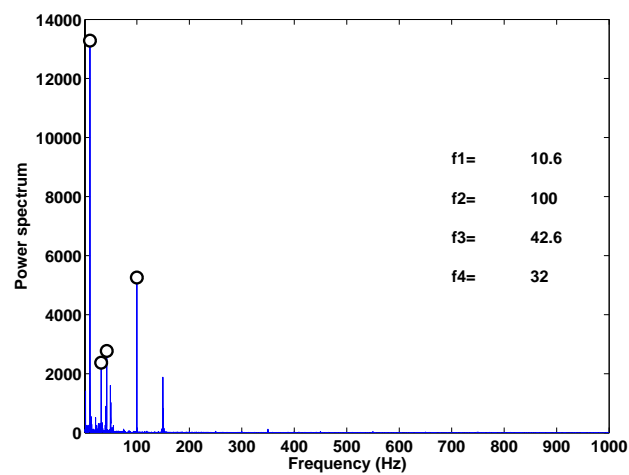
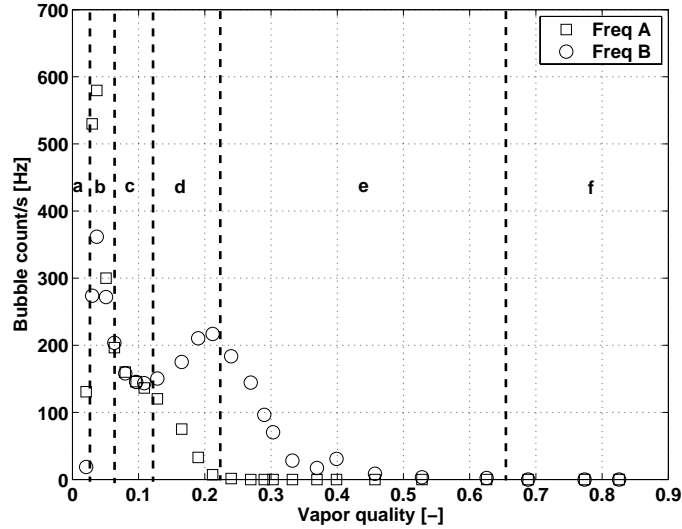
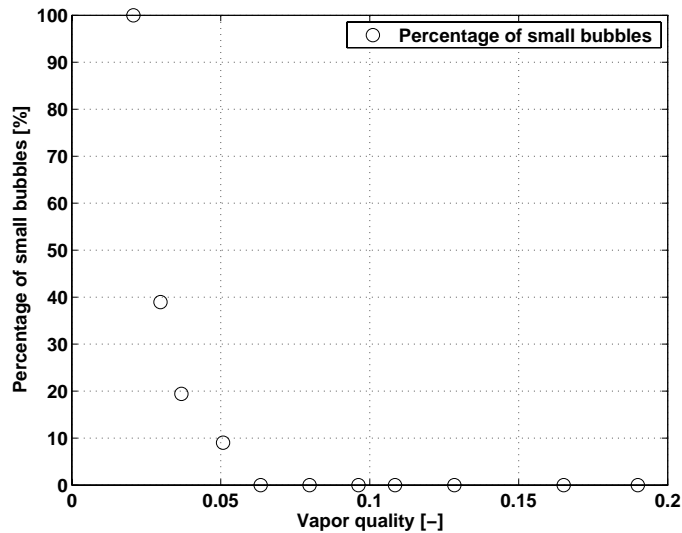
(a) FFT signal on bubbly flow for $x = 0.02$ (b) FFT signal on slug flow for $x = 0.11$ (c) FFT signal on annular flow for $x = 0.82$

Figure 6.1: FFT signals for $D = 0.509$ mm, $L_{MEV} = 70.70$ mm, $G = 500$ kg/m²s, $T_{sat} = 30^\circ\text{C}$ and $\Delta T_{sub} = 3^\circ\text{C}$ at entrance to the microevaporator.



(a) a: Bubbly flow, b: Bubbly/slug flow, c: Slug flow, d: Slug/semi-annular flow, e: Semi-annular flow, f: Annular flow.



(b)

Figure 6.2: Characterization of flow using the laser signal for $D = 0.509$ mm, $L_{MEV} = 70.70$ mm, $G = 500$ kg/m²s, $T_{sat} = 30^\circ\text{C}$ and $\Delta T_{sub} = 3^\circ\text{C}$ at entrance to the microevaporator. a) Bubble frequencies and flow patterns and b) percentage of small bubbles remaining versus vapor quality .

nose of the bubble has a characteristic hemispherical cap and the vapor in the bubbles is separated from the tube wall by a thin film of liquid. The liquid flow is contained mostly in the liquid slugs which separate successive vapor bubbles. The length of the vapor bubbles can vary considerably. This flow pattern is detected when the percentage of surviving small bubbles is 0%, f_B is the same as f_A and f_A is still greater than 0 bubbles/s. Fig. 6.4(c) shows a picture taken with a high definition video camera and Fig. 6.5(c) the corresponding signal. In this signal, the low voltage zones refer to passage of liquid slugs and the small amplitude spikes represent small bubbles entrained in the slugs (if any); on the other hand, the high voltage zones refer to passage of elongated bubbles and variations in the signal correspond to interfacial waves on the liquid film. The count rates decrease with increasing vapor quality due to coalescence of elongated bubbles but at a slower rate than in the case of small bubbles.

Slug/semi-annular flow: In slug/semi-annular flow, the slug (described above) and semi-annular (described below) flows are both present. The vapor velocity increases with heat flux and the rear of elongated bubbles are more and more deformed, see Fig. 6.3(d) and Fig. 6.4(d) as shear forces are more and more important. When coalescence occurs, transitions are no longer clean but instead create a churn-like zone where the liquid slug was. This regime is distinguishable when the signal is between threshold A and B as shown in Fig. 6.5(d). This transition starts when f_A and f_B are not the same and stops when f_A equals 0 bubbles/s corresponding to the maximum of f_B .

Semi-annular flow: In semi-annular flow, liquid slugs are nonexistent as shown in Fig. 6.3(e) and 6.4(e). A liquid film forms at the tube wall with a continuous central vapor core. It is separated by churning liquid zones due to the previous deformation of the rear ends of elongated bubbles and the coalescence of bubbles. This flow pattern is represented by the signal of Fig. 6.5(e). Limits of this transition are the end of slug/semi-annular flow and the beginning of annular flow, which is indicated by a value of f_B equal to 0 Hz. It is interesting to emphasize that the churning liquid disappears gradually from the beginning of this transition up to the end.

Annular flow: In annular flow, a liquid film flows on the tube wall with a continuous central vapor core as shown in Fig. 6.3(f). It is the same definition as for semi-annular flow, except that the churning liquid zones do not exist anymore. Annular flow is characterized by f_A and f_B equal to 0 Hz. The corresponding identification signal is shown in Fig. 6.5(f) and illustrates two types of annular flow: wavy and smooth, where the wavy annular flow signals have a small scale fluctuation from the waves on the annular film. These two types of annular flow can be seen in Fig. 6.4(f) and Fig. 6.4(g).

The flow patterns are also represented in Fig. 6.6 for R-245fa in a 0.509 mm ID tube and in Fig. 6.7 for R-134a with $D = 0.790$ mm.

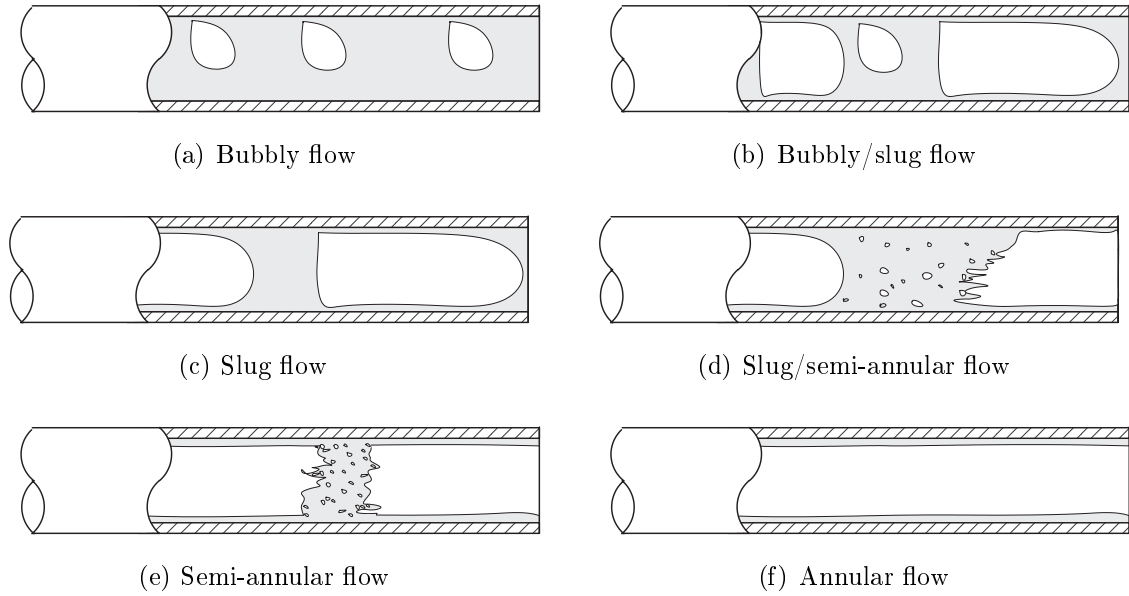
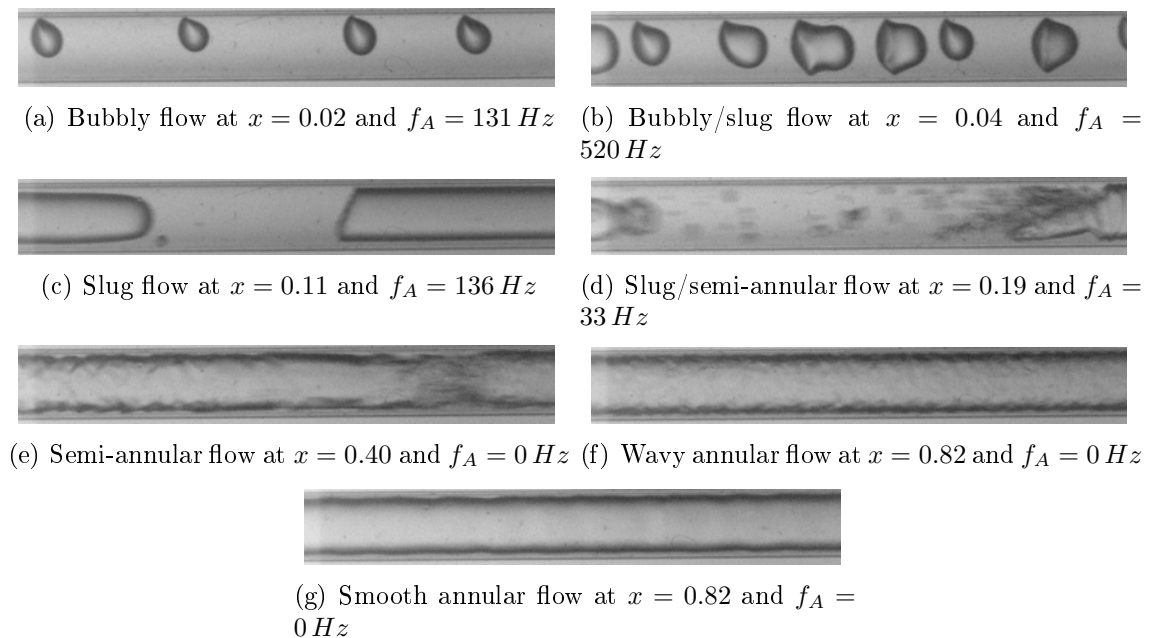
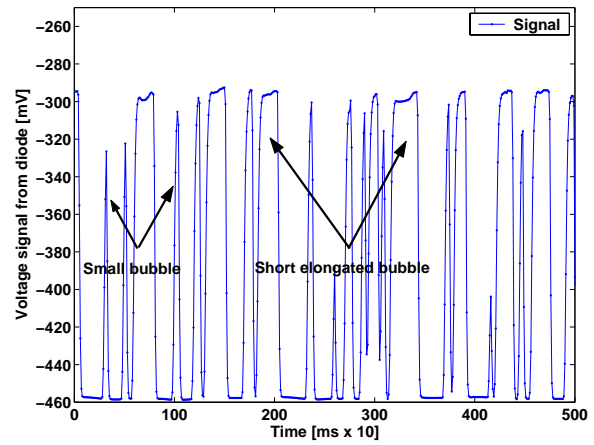
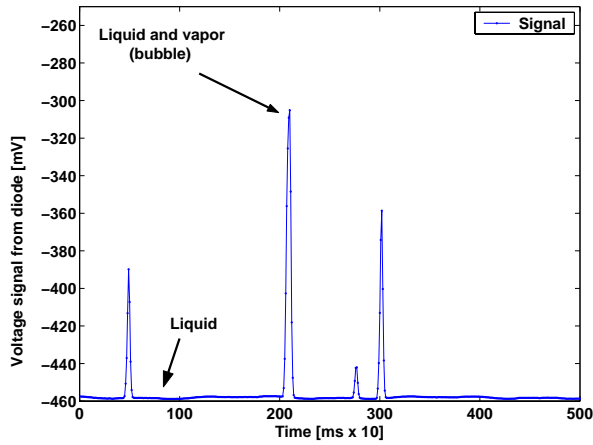
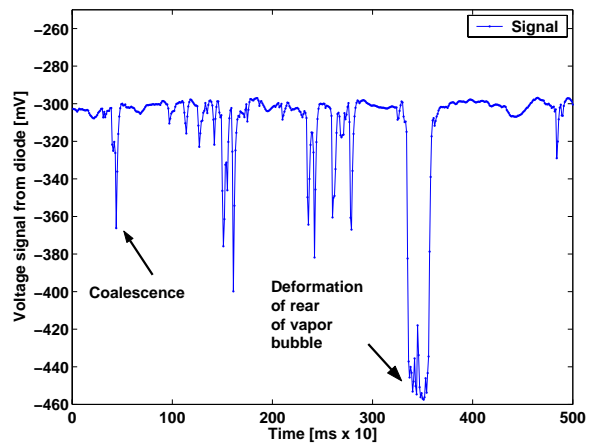
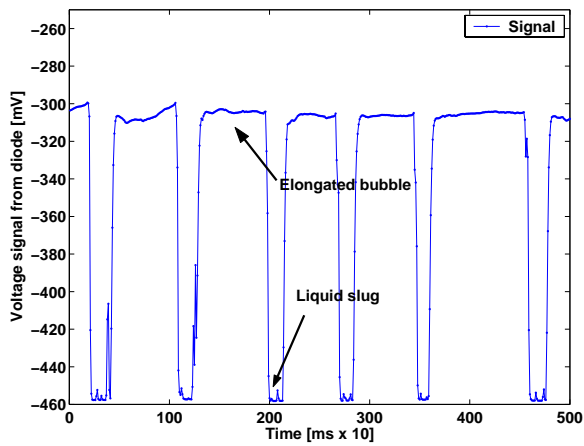


Figure 6.3: Schematic of flow patterns and transitions.

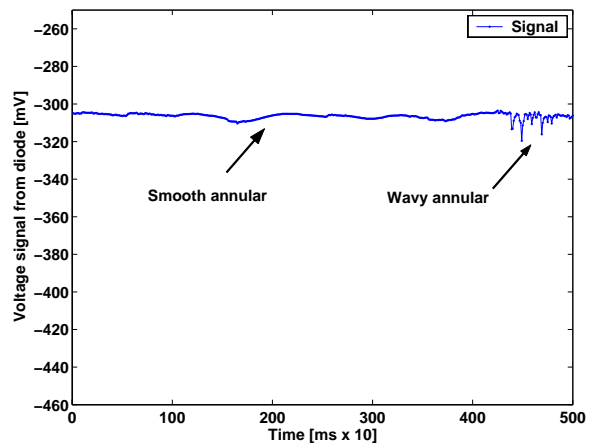
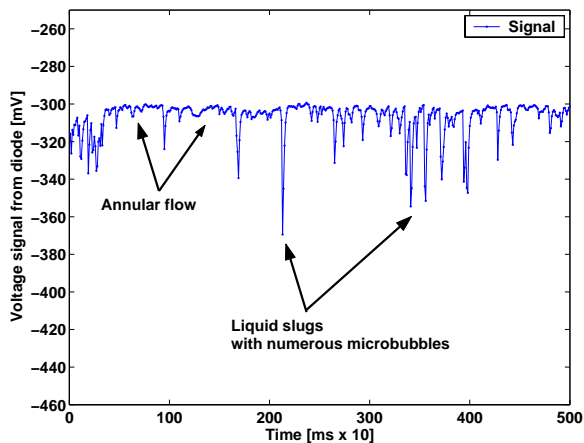
Figure 6.4: Flow patterns and transitions for R-134a, $D = 0.509 \text{ mm}$, $L_{MEV} = 70.70 \text{ mm}$, $G = 500 \text{ kg/m}^2\text{s}$, $T_{sat} = 30^\circ\text{C}$ and $\Delta T_{sub} = 3^\circ\text{C}$ at entrance to the microevaporator.



(a) Bubbly flow signal at $x = 0.02$ and $f_A = 131 \text{ Hz}$ (b) Bubbly/slug flow signal for at $x = 0.04$ and $f_A = 520 \text{ Hz}$



(c) Slug flow signal at $x = 0.11$ and $f_A = 136 \text{ Hz}$ (d) Slug/semi-annular flow signal at $x = 0.19$ and $f_A = 33 \text{ Hz}$



(e) Semi annular flow signal at $x = 0.40$ and $f_A = 0 \text{ Hz}$ (f) Annular flow signal at $x = 0.82$ and $f_A = 0 \text{ Hz}$

Figure 6.5: Flow pattern laser signals for R-134a, $D = 0.509 \text{ mm}$, $L_{MEV} = 70.70 \text{ mm}$, $G = 500 \text{ kg/m}^2\text{s}$, $T_{sat} = 30^\circ\text{C}$ and $\Delta T_{sub} = 3^\circ\text{C}$.

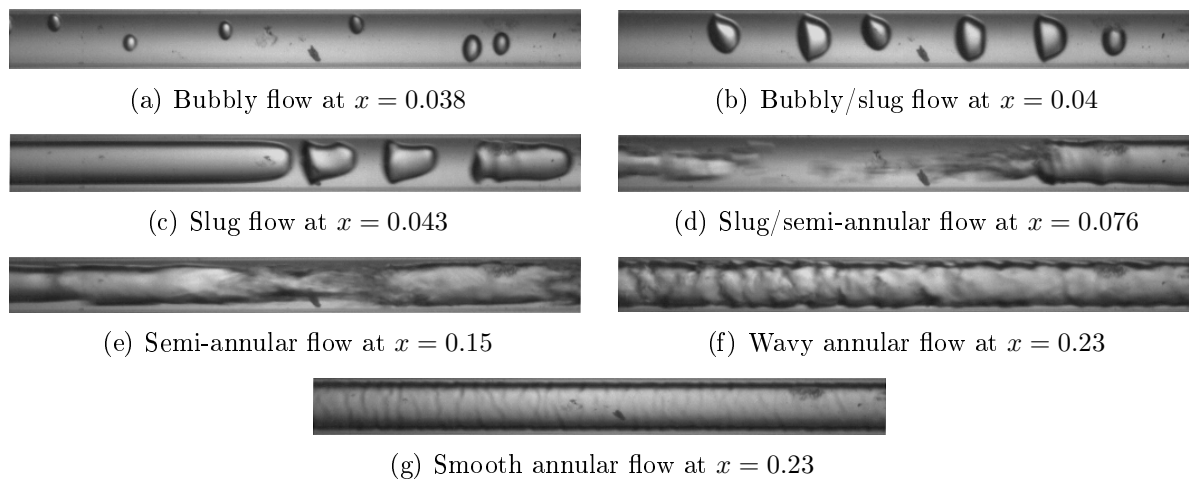


Figure 6.6: Flow patterns and transitions for R-245fa, $D = 0.509$ mm, $L_{MEV} = 70.70$ mm, $G = 500$ kg/m²s, $T_{sat} = 35^\circ\text{C}$ and $\Delta T_{sub} = 6^\circ\text{C}$.

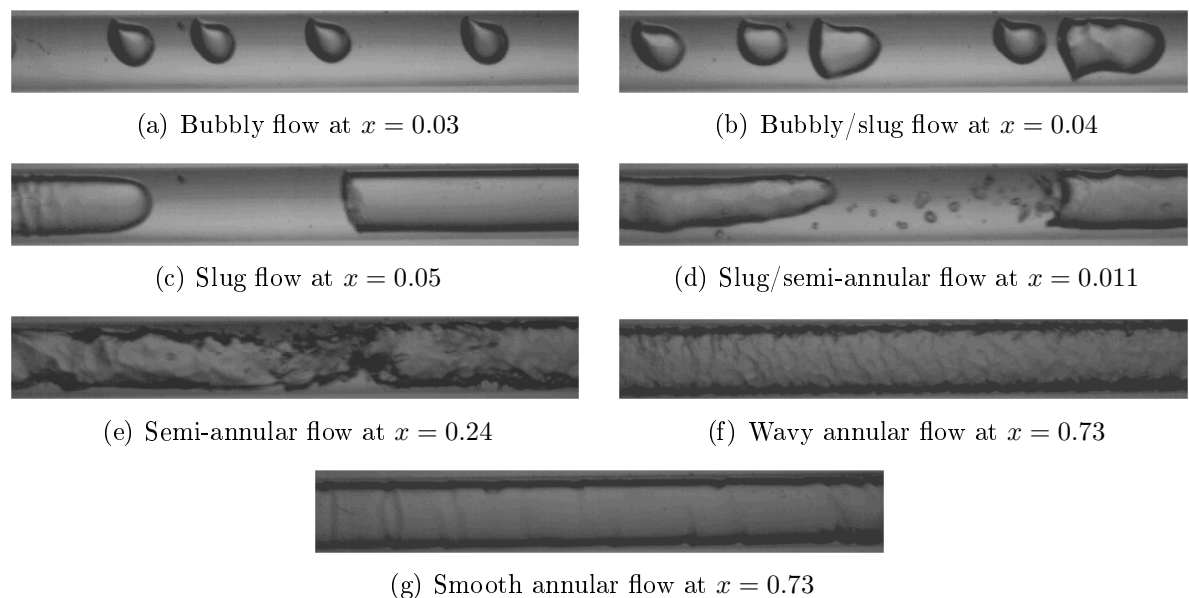
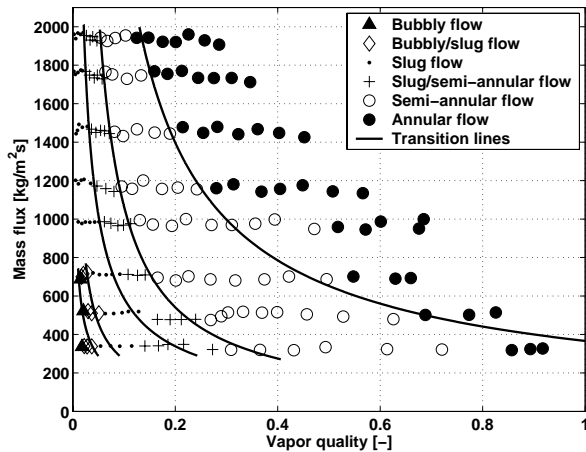


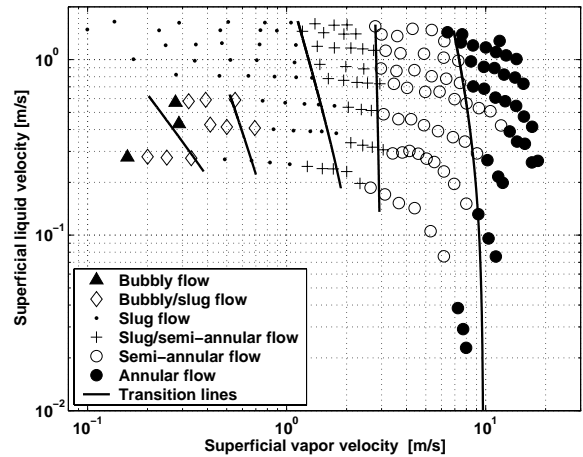
Figure 6.7: Flow patterns and transitions for R-134a, $D = 0.790$ mm, $L_{MEV} = 70$ mm, $G = 500$ kg/m²s, $T_{sat} = 30^\circ\text{C}$ and $\Delta T_{sub} = 3^\circ\text{C}$.

6.3 Experimental flow pattern maps

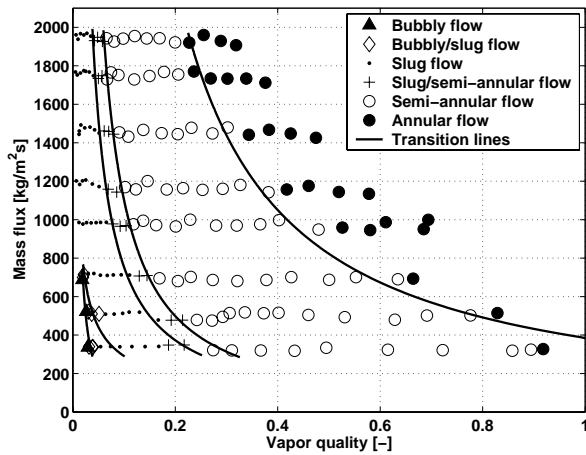
Two-phase flow patterns based on the present observations with the two laser signals are presented in Fig. 6.8 in two different formats: mass flux versus vapor quality and superficial liquid velocity versus superficial vapor velocity, which are calculated from the test results with Eqs. (2.10) and (2.9) respectively. The transition lines are determined with a least squared method.



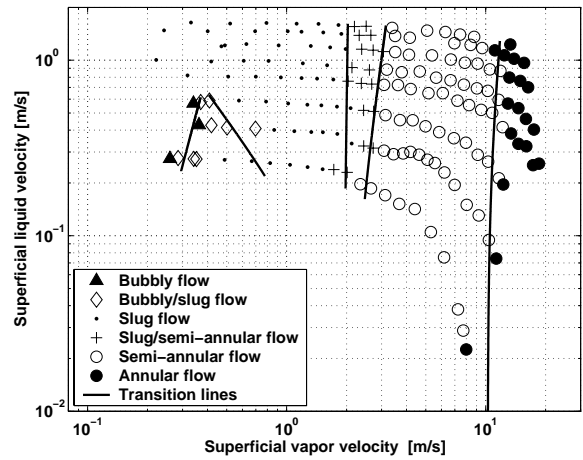
(a) Flow pattern observations from laser 1 with transition lines.



(b) Flow pattern map from laser 1 with transition lines.



(c) Flow pattern observations from laser 2 with transition lines.



(d) Flow pattern map from laser 2 with transition lines.

Figure 6.8: Flow pattern maps with transition lines for $D = 0.509$ mm, $L = 70.70$ mm, $T_{sat} = 30^\circ\text{C}$ and $\Delta T_{sub} = 3^\circ\text{C}$ using the two lasers.

Notably, the higher the mass flux, the earlier annular flow is reached. Bubbly flow is more or less nonexistent for mass fluxes greater than 1000 kg/m²s. The most important observation to make about the flow patterns in the present study is that their **transitions are controlled primarily by the rate of coalescence**, which is not recognized as a contributing factor by any of the existing microscale (nor macroscale) flow pattern maps.

Coalescence phenomena

Figure 6.9 shows coalescence phenomena as described by f_A for eight different mass fluxes where the frequency of bubbles (small and/or elongated) that go past the observation point is plotted versus local vapor quality. The upward slope shows a dependency between the heat flux in the evaporator (or vapor quality) and the average frequency (count rate). The higher the heat flux is, the larger the average frequency. The average frequency then reaches a maximum and starts to decrease. The downward slope in average bubble frequency indicates the relative rate of coalescence. *Rate 1* refers to the zone of coalescence of small bubbles into elongated bubbles until no more small bubbles exist (a "best" line indicates this trend); *Rate 2* refers to the coalescence between elongated bubbles into even larger elongated bubbles or semi-annular flow (a "best" line also indicates this trend). The higher the mass flux, the higher are the slopes of *rate 1* and *rate 2*.

The second rate comprises two types of coalescence, one clean (slug flow) and the other one affected by the deformation of the rear of the bubbles that leads to semi-annular flow, but the rate stays the same. The *rate 2* tends to increase when increasing mass flux, meaning that slug/semi-annular flow tends to disappear as well as slug flow. But in our case, the mass flux is not high enough to reach this situation. The relationship between coalescence and flow pattern transition is one of the most important observations in this study because of its influence on determining on the present flow pattern transitions, in sharp contrast to the classic macroscale transition theory of Taitel and Dukler [48].

The coalescence is illustrated in Fig. 6.10 with the following pictures taken in the adiabatic sight glass for $D = 0.509$ mm and R-134a.

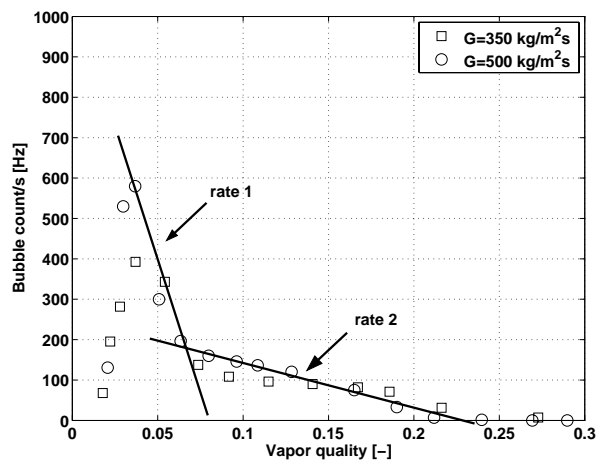
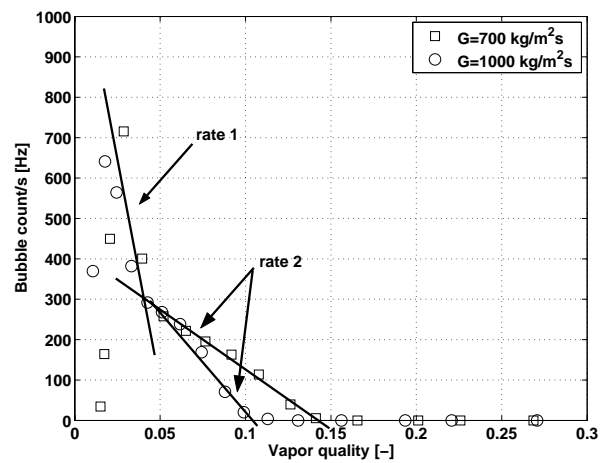
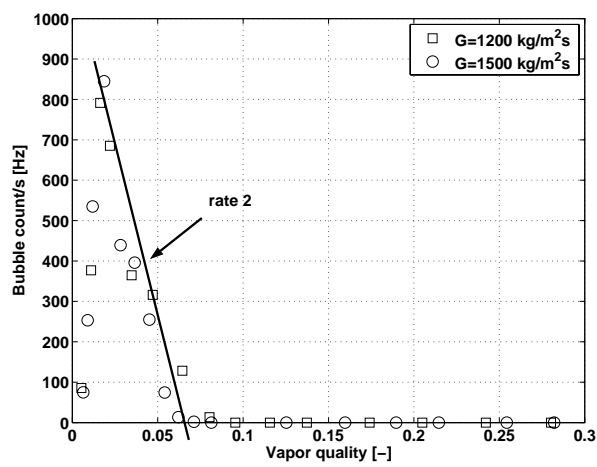
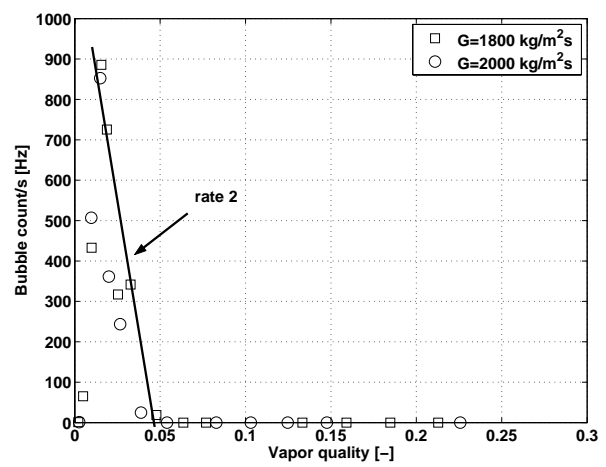
(a) $G = 350 \text{ kg m}^{-2} \text{ s}^{-1}$ and $G = 500 \text{ kg m}^{-2} \text{ s}^{-1}$.(b) $G = 700 \text{ kg m}^{-2} \text{ s}^{-1}$ and $G = 1000 \text{ kg m}^{-2} \text{ s}^{-1}$.(c) $G = 1200 \text{ kg m}^{-2} \text{ s}^{-1}$ and $G = 1500 \text{ kg m}^{-2} \text{ s}^{-1}$.(d) $G = 1800 \text{ kg m}^{-2} \text{ s}^{-1}$ and $G = 2000 \text{ kg m}^{-2} \text{ s}^{-1}$.

Figure 6.9: Coalescence phenomena from laser 1 for $D = 0.509 \text{ mm}$, $L_{MEV} = 70.70 \text{ mm}$, $T_{sat} = 30^\circ\text{C}$ and $\Delta T_{sub} = 3^\circ\text{C}$.

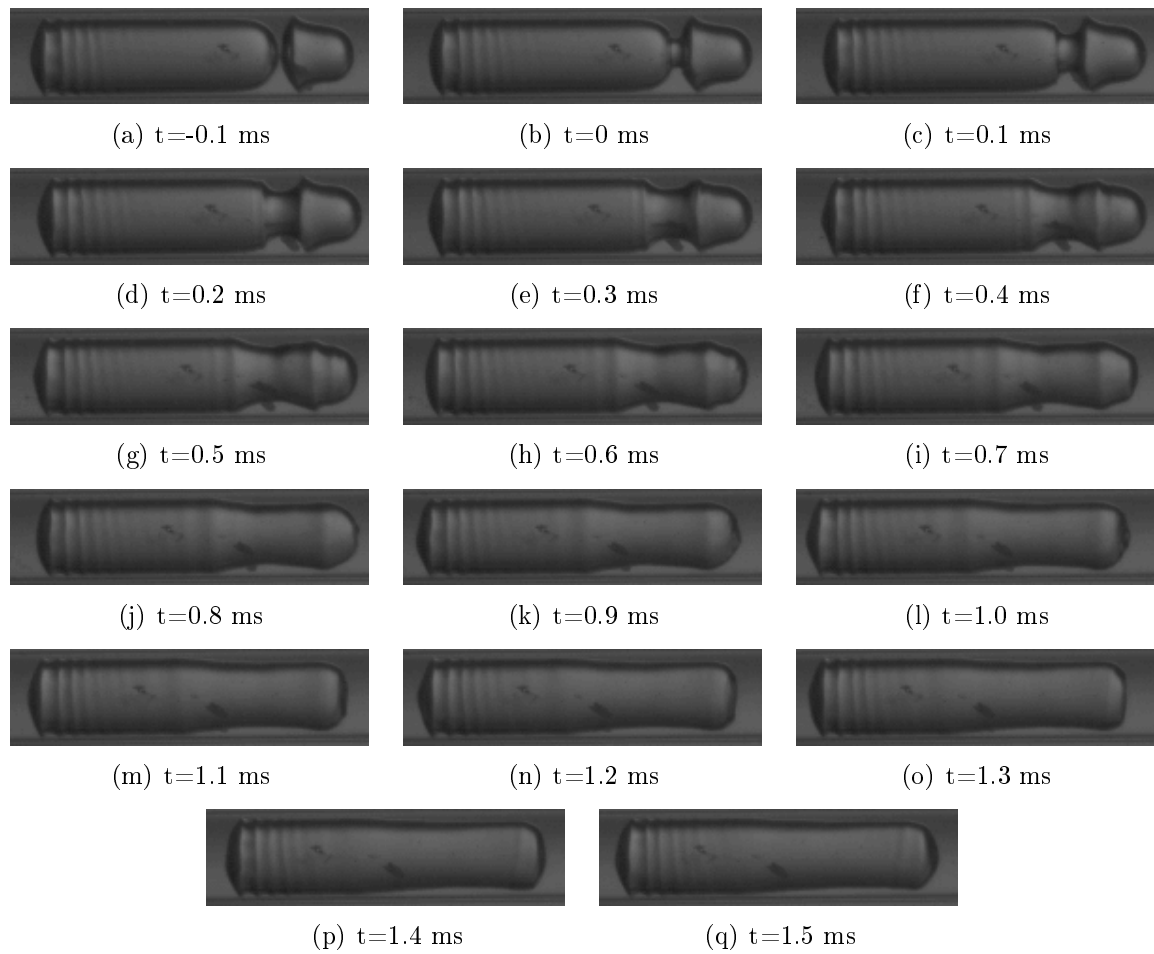


Figure 6.10: Adiabatic coalescence for R-134a, $D = 0.509$ mm, $G = 359$ kg/m²s, $T_{sat} = 30^\circ\text{C}$ and $x = 0.05$ taken with a high speed digital camera at 10000 Hz.

6.3.1 Comparison with the Kattan et al. macroscale map

A comparison with the macroscale map of Kattan et al. [23] for refrigerants inside horizontal macrochannels shows a significant difference in the transition line locations and also the flow patterns encountered (Fig. 6.11), illustrating that the current observations cannot be classified as macroscale two-phase flows. Stratified and stratified wavy flow are not present anymore in the microchannel due to the predominance of surface tension forces over gravity forces. The lower ends of the experimental transition lines are also close ($>350 \text{ kg/m}^2\text{s}$) to the flow instability threshold of the current experimental setup, which were always avoided in the present project.

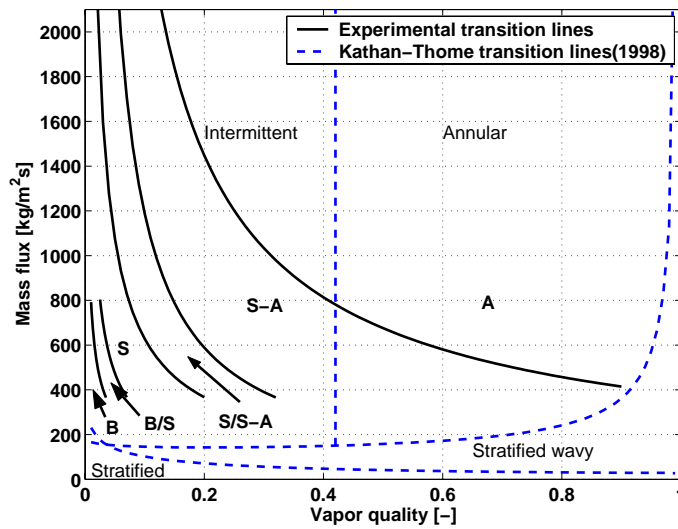


Figure 6.11: Comparison between present flow pattern transition observations from laser 1 for $D = 0.509 \text{ mm}$, $L_{MEV} = 70.70 \text{ mm}$, $T_{sat} = 30^\circ\text{C}$, $\Delta T_{sub} = 3^\circ\text{C}$ and Kattan-Thome-Favrat macroscale map in a mass flux vs. vapor quality format at the present test conditions. (B =Bubbly flow, B/S =Bubbly/slug flow, S =Slug flow, $S/S-A$ =Slug/semi-annular flow, $S-A$ =Semi-annular flow, A =Annular flow)

6.3.2 Comparison with the Tripplet et al. adiabatic microscale map

Fig. 6.12 shows a comparison between the present experimental transition lines from laser 1 and those of Tripplet et al. [54] available for air/water flow in a 1.097 mm tube diameter. The results are not in good agreement when extrapolating their air-water map to R-134a. Obviously, the diameter is not the same and the comparison cannot be perfect but the trends should be about the same but are not. The reason is perhaps that in their air/water flow, the vapor is not created by the boiling process but is dependent of the mixer design and its hydraulic characteristics, not boiling nucleation of the initial bubbles as in a microevaporator. The flow patterns encountered are however the same.

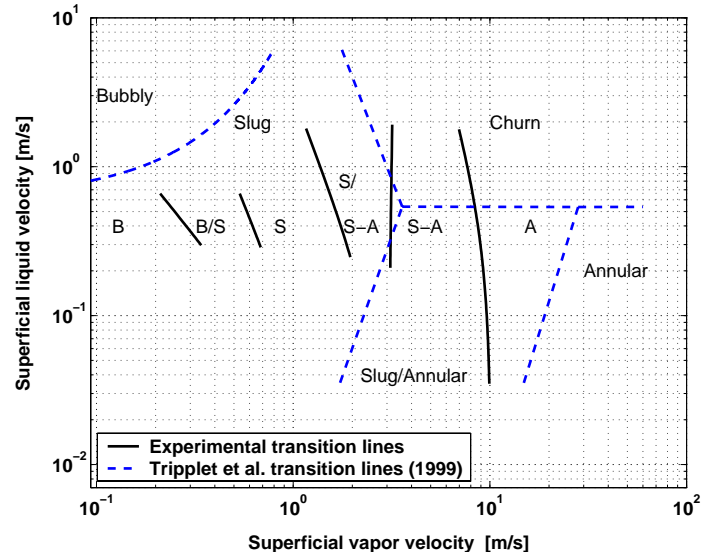


Figure 6.12: Comparison between present flow pattern transition observations from laser 1 for $D = 0.509$ mm, $L_{MEV} = 70.70$ mm, $T_{sat} = 30^\circ\text{C}$, $\Delta T_{sub} = 3^\circ\text{C}$ and Tripplet et al. transition lines available for air-water flow in a 1.097 mm tube diameter.

6.3.3 Comparison with the Garimella et al. [22] transition line

Fig. 6.13 shows a comparison between the present experimental transition lines from laser 1 and that of Garimella et al. [22] given by Eq. (3.7), the latter of which is a natural occurrence during condensation of saturated vapor. Their equation is available for condensation of R-134a and determines the transition between intermittent and non-intermittent flow. As can be seen, the Garimella et al. transition is close to that between slug/semi-annular and semi-annular flow observed in the present study, especially at high mass flux, giving a similar trend. The coalescence process will obviously be different in an evaporating process compared to a condensing one.

6.3.4 Effect of the inlet subcooling

Fig. 6.14 presents transition lines for three different inlet subcoolings: 2, 3 and 5°C . It shows no significant effect of this parameter on the transition lines. No bubbly flow has been observed for $\Delta T_{sub} = 2$ and 3°C but it would probably have been seen at the lower mass fluxes but the tests could not be run at those conditions due to instabilities.

6.3.5 Effect of the saturation temperature

The effect of the saturation temperature is shown in Fig. 6.15 for tests at inlet saturation temperatures of 26, 30 and 35°C (6.9, 7.7 and 8.9 bar saturation pressures). No bubbly flow has been observed for $T_{sat} = 35^\circ\text{C}$ for the same reason explained in Section 6.3.4. No significant difference in the locations of the transition lines were observed except for the semi-annular/annular transition. For $T_{sat} = 30^\circ\text{C}$, the transition appears earlier, which

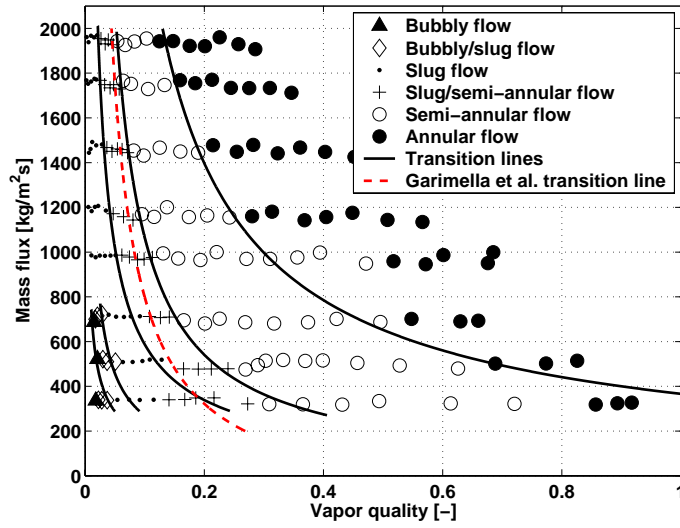


Figure 6.13: Comparison between present flow pattern transition observations from laser 1 for $D = 0.509$ mm, $L_{MEV} = 70.70$ mm, $T_{sat} = 30^{\circ}\text{C}$, $\Delta T_{sub} = 3^{\circ}\text{C}$ and Garimella et al. transition line between intermittent and non-intermittent flow available for condensation of R-134a in a 0.509 mm tube diameter.

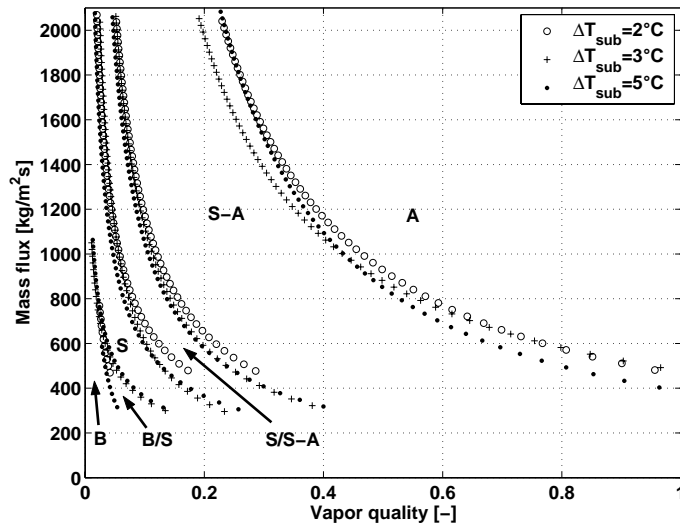


Figure 6.14: Comparison between experimental transition lines from three different inlet subcoolings at entrance to the microevaporator from laser 1 for R-134a, $D = 0.509$ mm, $L_{MEV} = 70.70$ mm and $T_{sat} = 30^{\circ}\text{C}$.

is not consistent with the two others. An appropriate explanation could be the relative subjectivity related to determining this threshold quantitatively. Furthermore, it is probably appropriate to talk about transition "zones" or "regions" instead of "lines".

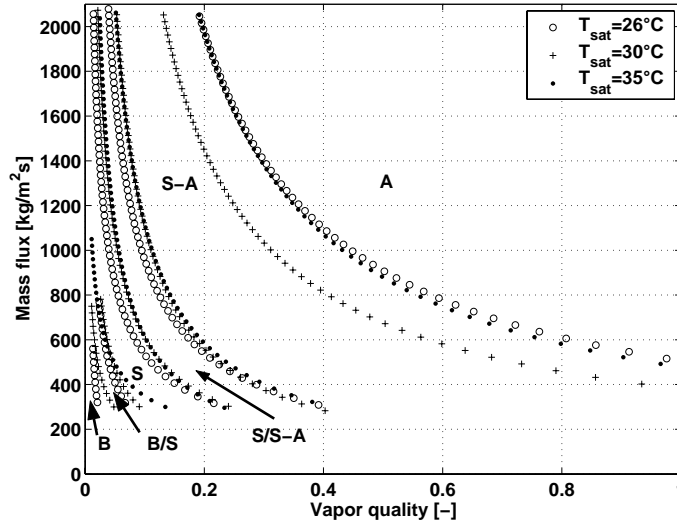


Figure 6.15: Comparison between experimental transition lines from three different saturation temperatures from laser 1 for R-134a, $D = 0.509$ mm, $L_{MEV} = 70.70$ mm and $\Delta T_{sub} = 3^\circ\text{C}$.

6.3.6 Effect of the microevaporator length

Fig. 6.16 presents the influence of the heated length of the microevaporator on the transitions between the different flow regimes. No significant difference in the location of the transition lines have been observed except for the semi-annular/annular transition. For $L_{MEV} = 50$ mm, the transition appears to be inconsistent with the two other transitions, for the same reasons explained in Section 6.3.5.

6.3.7 Effect of the tube diameter

The effect of the inside diameter is shown in Fig. 6.17. Bubbly flow for $D = 0.790$ mm would probably have been seen at the lower mass fluxes but the tests could not be run at those conditions due to instabilities in the microevaporator. Bubbly/slug flow is present over a wider range of mass flux for the 0.790 mm tube. Except for the semi-annular/annular transition (for the same reasons explained in Section 6.3.5), no significant difference is observable in the locations of the transition lines. One may conclude that the two-phase mechanisms for the two different inside diameters are the same. For R-134a, 0.790 mm still seems to be a microchannel based on the form of its experimental transition lines. A significant difference in the flow regime transition curves on a flow map could be a way to determine whether it is microscale or macroscale.

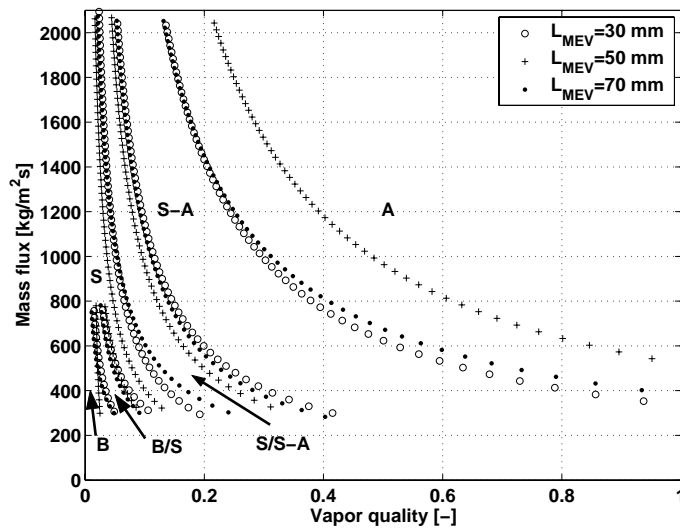


Figure 6.16: Comparison between experimental transition lines from three different microevaporator lengths from laser 1 for R-134a, $D = 0.509$ mm, $\Delta T_{sub} = 3^{\circ}\text{C}$ and $T_{sat} = 30^{\circ}\text{C}$.

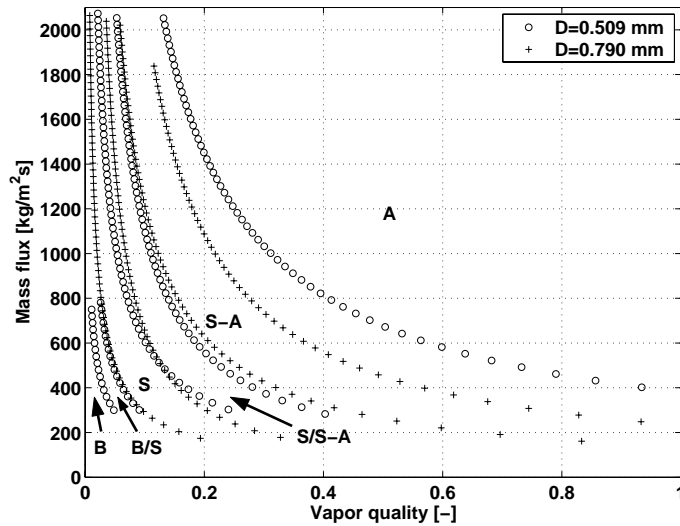


Figure 6.17: Comparison between experimental transition lines from two different inside diameters from laser 1 for R-134a, $L_{MEV} = 70.70$ mm, $T_{sat} = 30^{\circ}\text{C}$ and $\Delta T_{sub} = 3^{\circ}\text{C}$.

6.3.8 Effect of the fluid

Fig. 6.18 presents the difference in the transition line locations between R-134a and R-245fa. The latter is a low pressure fluid (2.1 bar vs. 8.9 bar of R-134a at 35°C). To avoid a below atmospheric pressure in the test section due to the high pressure drop with R-245fa, the tests were stopped when reaching atmospheric pressure at the end of the evaporator and this is why annular flow was not reached at high mass flux. No bubbly flow was observed for the two fluids but it would probably have been seen at the lower mass fluxes but the tests could not be run at those conditions because the flow would have been unstable. One may observe that the transition lines tend to be more vertical for R-245fa than for R-134a, diverging at low mass fluxes, where the difference is significant and the flow transitions appear earlier in terms of vapor quality for R-245fa. However, one may conclude that the two-phase flow transitions for R-245fa obey the same mechanisms as for R-134a.

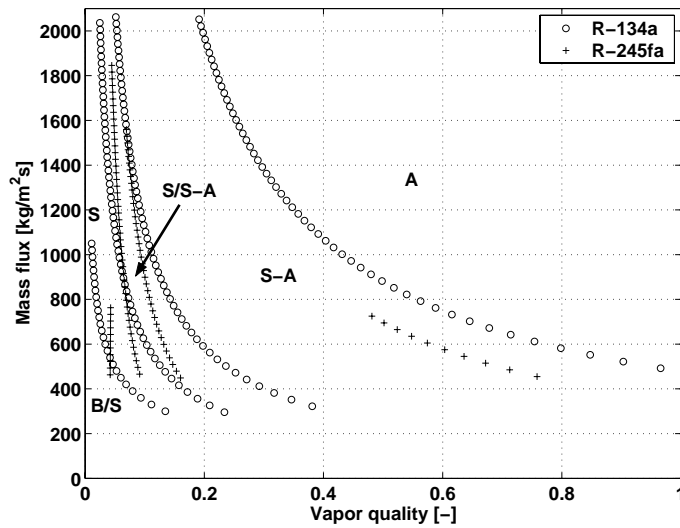


Figure 6.18: Comparison between experimental transition lines from two different fluids from laser 1 for $D = 0.509$ mm, $L_{MEV} = 70.70$ mm, $T_{sat} = 30^\circ\text{C}$ and $\Delta T_{sub} = 3^\circ\text{C}$.

6.4 New flow pattern map for evaporating flows in microchannels

Heat transfer coefficient and frictional pressure drop characteristics are based on the different flow patterns. The Thome et al. [51, 19] three zone model (Fig. 1.1) is currently applicable for slug flow (elongated bubble flow) with no coalescence phenomena. It can be extended to intermittent flow with coalescence and take into account the variation of the heat transfer coefficient due to the variation of the bubble frequency and velocity and the non-homogeneous void fraction. Heat transfer coefficient is controlled primarily by conduction through the liquid film surrounding the elongated bubbles, or by convection or conduction in the annular flow liquid film but is greatly influenced by any dryout zones. To advance their 3-zone heat transfer model beyond slug flow, an annular flow heat transfer model should be added to it. It could be a "single zone model". Furthermore, as can be observed in Figs. 6.5 and 6.8, the normal definition of flow pattern transition does not work here since coalescence is changing the flow pattern along the channel length. Hence, a new approach seems to be appropriate here to describe what is expected to occur inside a heated microchannel.

For these reasons a new type of flow pattern map for evaporating flow in microchannel has been proposed. The first flow pattern zone corresponds to the isolated bubble (IB) regime. It includes both bubbly flow or/and slug flow and is present up to the onset of coalescence. The second zone is the coalescing bubble (CB) regime. It is present up to the end of the coalescence process. The third zone is the annular (A) zone and is limited by the fourth zone of this diabatic map, the post dryout (PD) zone, which is marked by the critical vapor quality signaling the onset of critical heat flux. Figure 6.19 shows an example of this new type of flow pattern map. The saturation conditions are those at inlet of the microevaporator.

The transition lines are shown with accuracy limits of the new transition prediction methods to be presented in the next sections. The lower end of the transition lines represent an extrapolation below mass velocities tested, where flow instabilities begin. It could be imagined in the future the addition of a two-phase flow instability threshold line to this flow pattern map as a further useful guide that could be provided by the map.

Prediction methods for the transitions of this new type of flow pattern map are presented in the next parts. To utilize the map, one takes the imposed mass velocity and imposed uniform heat flux along the circular microchannel up to the desired local length from the inlet to find the corresponding vapor quality and location on the map. The saturation conditions are those at inlet of the microevaporator.

6.4.1 The isolated bubble regime to coalescing bubble regime transition

Figure 6.20 presents a typical bubble frequency variation versus vapor quality. As explained in Section 6.3, there are different trends evident in this graph. Presently, the location of the start of coalescence is of interest. The vapor quality for this maximum frequency will be the first transition, that between the isolated bubble regime and the coalescing bubble regime.

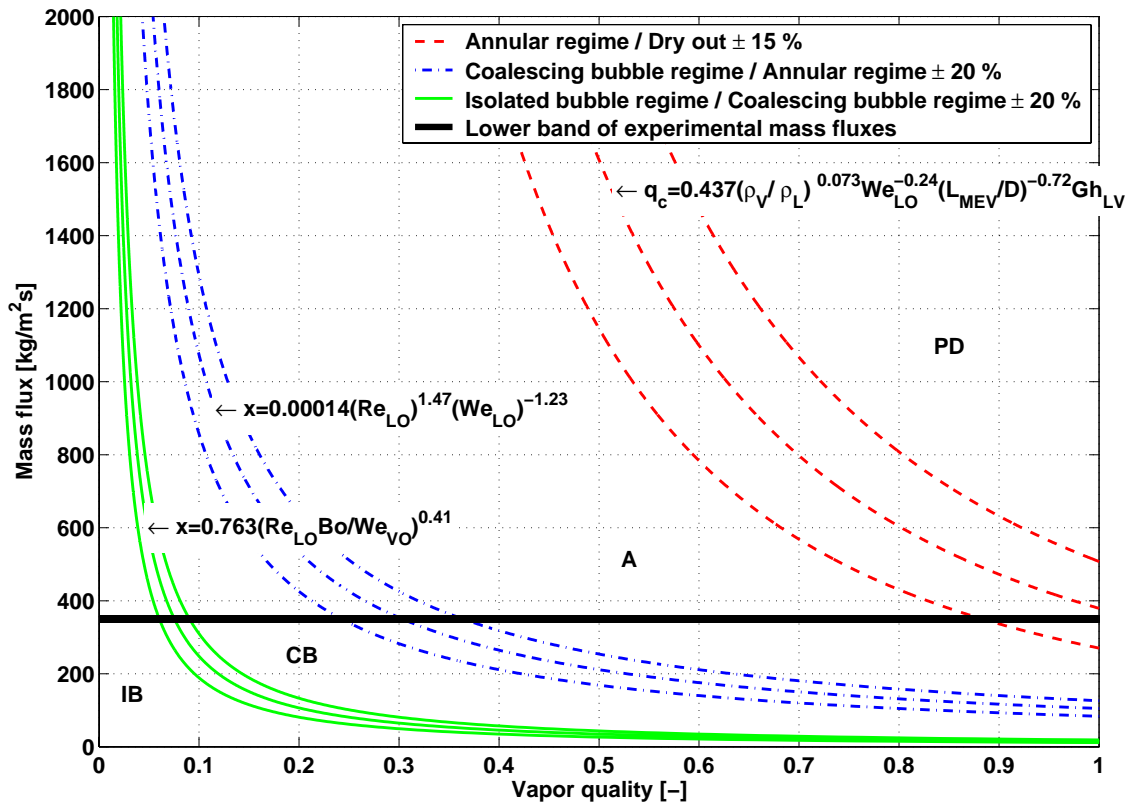


Figure 6.19: New type of flow pattern map for evaporating flow in microchannel for $D = 0.5$ mm, $L_{MEV} = 70$ mm, $T_{sat} = 30^\circ\text{C}$, $q = 50$ kW/m² and $\Delta T_{sub} = 0^\circ\text{C}$. IB: Isolated bubble regime, CB: Coalescing bubble regime, A: Annular regime (completely coalesced regime), PD: Post dryout regime.

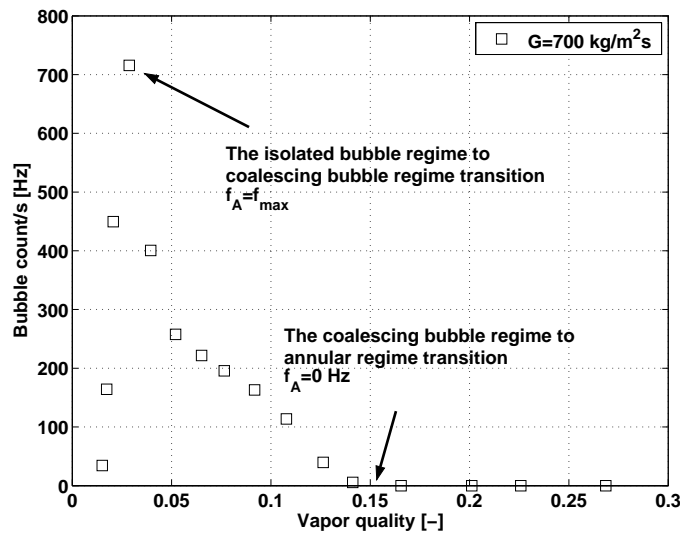


Figure 6.20: Frequency A versus vapor quality for $D = 0.509$ mm, $L_{MEV} = 70.70$ mm, $T_{sat} = 30^\circ\text{C}$, $G = 700$ kg/m²s and $\Delta T_{sub} = 3^\circ\text{C}$.

All the bubble frequency data from all the tests for both fluids and tube diameters have been used to develop the prediction of this transition (representing 200 test conditions) and a least square method has been applied to determine the empirical coefficients. Different combinations of non-dimensional numbers have been tried. Only the Boiling number, the liquid Reynolds number and the vapor Weber number were found to have a significant influence on this transition. The correlation is given by Eq. (6.1):

$$x_{IB/CB} = 0.763 \left(\frac{Re_{LO} Bo}{We_{VO}} \right)^{0.41} \quad (6.1)$$

where Bo is given by Eq. (2.36), Re_{LO} by Eq. (2.29) and We_{VO} by Eq. (2.35). Rearranging to see the effects of individual variables, this expression becomes:

$$x_{IB/CB} = 0.763 \left(\frac{q\rho_V\sigma}{\mu_L h_{LV} G^2} \right)^{0.41} \quad (6.2)$$

It is intuitive to see the Boiling number effect because it is directly related to the boiling mechanisms by the heat flux, representing the quantity of heat absorbed by the flow relative to the maximum possible in the evaporation process. It has a direct influence on the number of bubbles and their sizes. Also, the higher the heat flux is, the higher is the bubble nucleation rate and hence the frequency of isolated bubbles. Furthermore, the higher the heat flux, the longer is the isolated bubble regime region. The viscosity forces of the liquid are taken into account in the Reynolds number and the surface tension forces in the Weber number. When the flow becomes more turbulent, coalescence occurs earlier.

The vapor density is taken into account in the vapor Weber number. The size of the vapor bubbles formed, related directly to the vapor density, will decrease as the pressure increases, and smaller bubbles would intuitively delay the onset of coalescence and increase the value of $x_{IB/CB}$ as in Eq. (6.2). Notably, the channel diameter drops out of the expression since the bubble coalescence phenomenon seems to be a one-dimensional process related to the respective velocities of the colliding bubbles.

In general, the higher the heat flux, the higher is the vapor quality for the transition. When the mass flux is increased, the transition vapor quality is decreased. The tube diameter as well as the inlet subcooling and the microevaporator length have no effect on the transition according to a parameter study on their influence. Finally, the higher the saturation temperature, the higher the $x_{IB/CB}$ vapor quality transition is.

Figure 6.21 shows the vapor quality calculated with Eq. (6.1) versus the experimental vapor qualities at the maximum bubble frequency. Here, 60.5 % of the data fall within a $\pm 20\%$ error band and 70 % within a $\pm 25\%$ error band. The higher uncertainties occur at the lower vapor qualities. The difficulty here is to determine accurately the maximum of the frequency. The gradient of the frequency versus vapor quality is so high that a small variation of the vapor quality (i.e. the microevaporator heat flux) can significantly change the frequency. The exact start of the coalescence is therefore difficult to determine accurately, even using experimental steps of about 0.01 in x as in Figs. 6.9 and 6.20 in the IB regime. Furthermore, the accuracy in the energy balances at very low vapor qualities is responsible for part of the

scatter. Facing these experimental limitations, Eq. (6.1) is actually quite successful in predicting the IB/CB transition in Fig. 6.21.

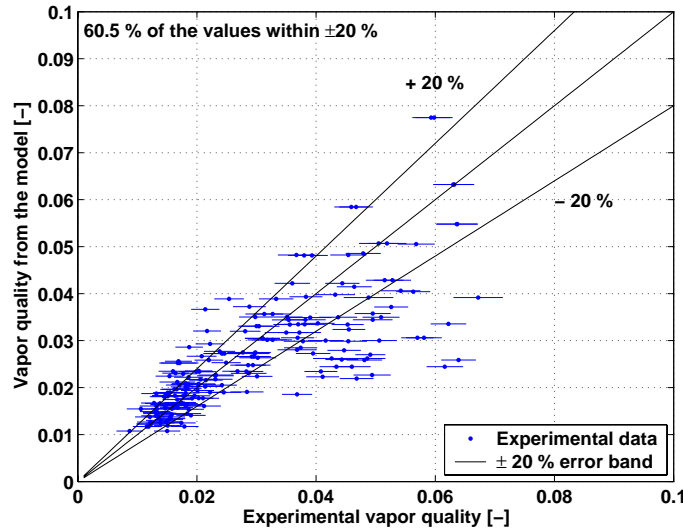


Figure 6.21: Comparison between the vapor quality from the model and the experimental vapor quality for the isolated bubble regime and coalescing bubble regime transition.

6.4.2 The coalescing bubble regime to annular regime transition

The coalescing bubble to annular flow regime transition corresponds to the vapor quality when the frequency A reaches 0 Hz as shown in Fig. 6.20. It is the end of the presence of liquid slugs and the end of coalescence as all the vapor bubbles have coalesced.

All the data for both fluids and tube diameters have been used and a least square method has been applied to determine the empirical coefficients. Different combinations of non-dimensional numbers have been tried. Only the liquid Reynolds number and the liquid Weber number were found to have an influence on the transition. The correlation is given by Eq. (6.3):

$$x_{CB/A} = 0.00014 Re_{LO}^{1.47} We_{LO}^{-1.23} \quad (6.3)$$

where Re_{LO} is given by Eq. (2.29) and We_{LO} by Eq. (2.33).

The exponents of the two non-dimensional numbers are very close to each other in terms of absolute value. The ratio between the liquid Reynolds number and the liquid Weber number represents the ratio between the surface tension forces to the kinematic viscosity (μ_L/ρ_L). When the kinematic viscosity is low (i.e. the liquid density high or the dynamic viscosity low), the vapor quality transition is higher. When the surface tension forces increase, the coalescing bubble regime resists to higher vapor qualities, as would be the case for water for example. In general, the heat flux, the subcooling and the microevaporator length were not found to have any parametric influence on this transition. The vapor quality transition increases with the saturation temperature.

Figure 6.22 shows the vapor quality calculated with Eq. (6.3) versus the experimental vapor quality. Here, 84.6 % of data fall within a $\pm 20\%$ error band and 73 % within a $\pm 15\%$ error band. The $\pm 20\%$ band was shown on Fig. 6.19 and can be interpreted as the transition zone between the coalescing bubble and the annular regimes. Furthermore, providing information on the accuracy of prediction of the location of the transition is more valuable than simply providing information on the number of observations correctly identified by the map, the latter which is the usual approach.

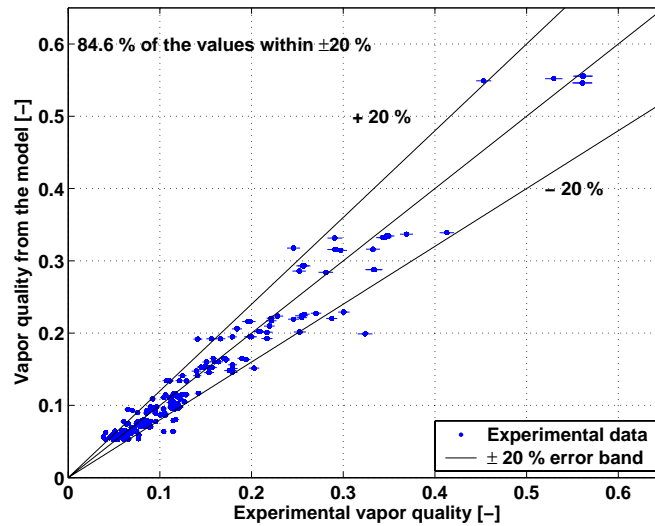


Figure 6.22: Comparison between the vapor quality from the model and the experimental vapor quality for the coalescing bubble regime and annular regime transition.

6.5 Conclusions from the flow pattern study in microchannels

Four principal flow patterns (bubbly flow, slug flow, semi-annular flow and annular flow) with their transitions (bubbly/slug flow and slug/semi-annular flow) were observed in the present experiments with R-134a and R-245fa in 0.509 mm and 0.790 mm circular channels. Regime changes were detected by bubble frequency analysis combined with a small bubble coalescence study. The higher the mass flux is, the earlier the transitions are encountered in terms of vapor quality. Bubbly flow tends to disappear at high mass flux because small bubbles quickly coalesce to form elongated ones.

Many observations have been made on the transitions between flow regimes. The two-phase flow pattern transitions observed with R-134a did not compare well to a leading macroscale flow map for refrigerants nor to a microscale map for air-water flows. No significant influence of the inlet subcooling nor the saturation pressure has been observed on the flow pattern transitions within the small variation able to be tested here. A shorter heated length did not influence the locations of the transition lines. The diameter effect did not show any significant influence, although bubbly/slug flow is present over a wider range of mass flux. The transition lines tended to be more vertical for R-245fa than for R-134a, diverging at low mass fluxes. However, the two-phase flow transitions for R-245fa are quite similar to those of R-134a. The comparison with the Garimella et al. transition for intermittent/non-intermittent regimes shows a good agreement with the experimental transition line between slug/semi-annular flow and semi-annular flow.

A new type of flow pattern map for evaporating flows in microchannels has been proposed with its eventual use in mechanistic types of models for flow boiling and two-phase pressure drops in mind. The first zone corresponds to the isolated bubble regime. It includes both bubbly flow or/and slug flow and is present up to the onset of coalescence. The second zone is the coalescing bubble regime. It is present up to the end of coalescence process. The third zone is the annular zone and is limited by the fourth zone (post dryout zone) of this diabatic map, and begins at the onset of critical heat flux. This flow pattern map can be used to determine the feasible operating range of microevaporators, where the local vapor quality must be less than x_{crit} . Furthermore, it can be used to create an isolated bubble heat transfer model similar to the three-zone model in Fig. 1.1, a coalescing bubble model for the CB regime and an annular flow model for that regime. This map can in the future have an instability curve added to it (another operating limit) to capture the onset of back flow or oscillating flow at low mass fluxes, a topic beyond the objectives of the present study.

Chapter 7

Velocity and void fraction

7.1 Experimental velocity

There are 1584 experimental velocity points obtained during this study for the conditions presented in Table 6.1. The velocity of the vapor bubbles is determined using a cross-correlation of the two signals from the lasers as explained in Section 4.3. Velocity is used for the flow pattern detection to see whether it is bubbly flow (the size of the bubbles are less than the inside diameter of the tube) or elongated bubble flow. Figure 7.1 shows some typical results for R-134a of the vapor bubble velocity versus vapor quality. As can be seen, the vapor velocity increases with the vapor quality as well as with the mass flux. The results are only for frequencies A above 30 Hz, otherwise the cross correlation does not have enough information to process. Hence, most bubbly flows are not able to be analyzed with this technique. The cross-correlation technique works for the following flow patterns: bubbly/slug, slug and slug/semi-annular flow.

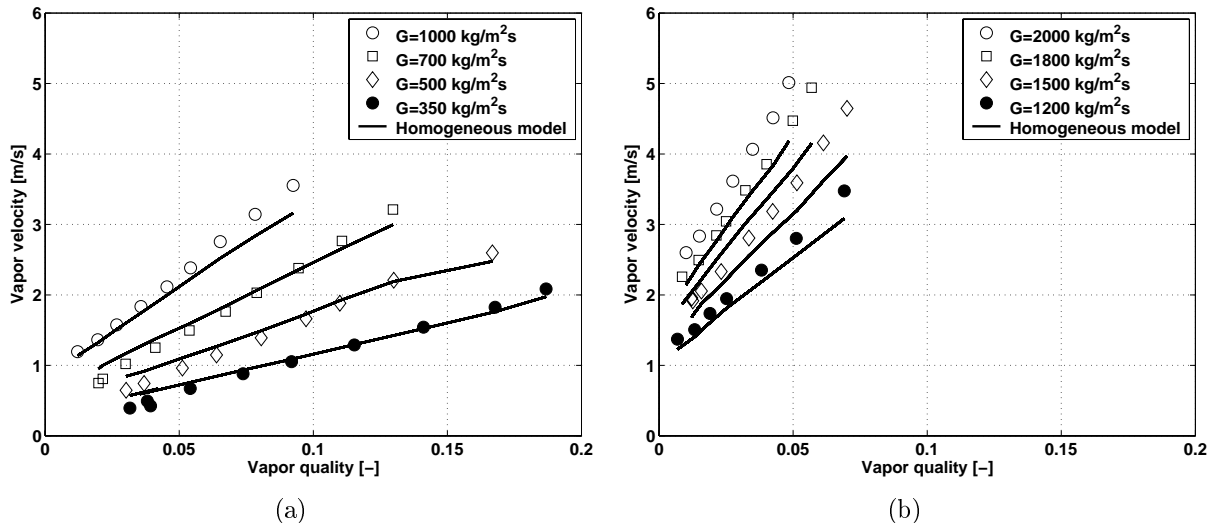


Figure 7.1: Vapor velocity versus vapor quality from laser 2 for R-134a, $D = 0.509$ mm, $L_{MEV} = 70$ mm, $T_{sat} = 30^{\circ}\text{C}$ and $\Delta T_{sub} = 3^{\circ}\text{C}$.

7.1.1 Effect of the inlet subcooling

Figure 7.2 shows the influence of the inlet subcooling at entrance to the microevaporator on the vapor velocity. As a conclusion, a small level of inlet subcooling has no influence on the vapor bubble velocity in the saturated flow boiling region downstream.

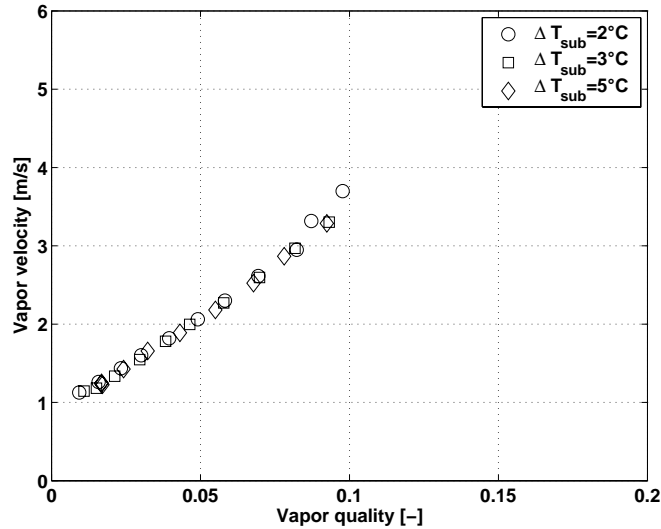


Figure 7.2: Influence of the inlet subcooling at entrance to the microevaporator on the vapor velocity from laser 2 for R-134a, $D = 0.509$ mm, $L_{MEV} = 70$ mm, $T_{sat} = 35^\circ\text{C}$ and $G = 1000$ kg/m²s.

7.1.2 Effect of the saturation temperature

Figure 7.3 shows the influence of the saturation temperature on the vapor velocity. As expected, the higher the saturation temperature, the lower the vapor bubble velocity is. This comes from the fact that ρ_V increases when the temperature increases (see Eq. (2.7)).

7.1.3 Effect of the microevaporator length

Figure 7.4 shows the influence of the microevaporator length on the vapor velocity in the aforementioned flow regimes. As can be seen, the microevaporator length has no influence.

7.1.4 Effect of the diameter

Figure 7.5 shows the influence of the diameter on the vapor velocity. As can be seen, the diameters tested here have no influence.

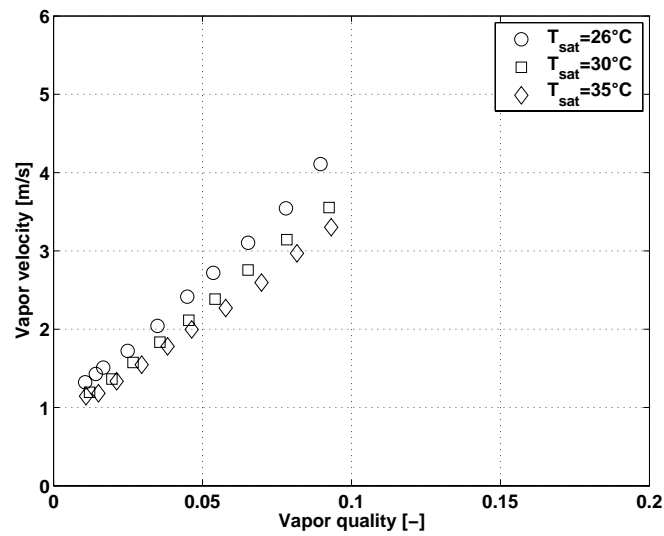


Figure 7.3: Influence of the saturation temperature on the vapor velocity from laser 2 for R-134a, $D = 0.509$ mm, $\Delta T_{sub} = 3^{\circ}\text{C}$, $L_{MEV} = 70$ mm and $G = 1000$ kg/m²s.

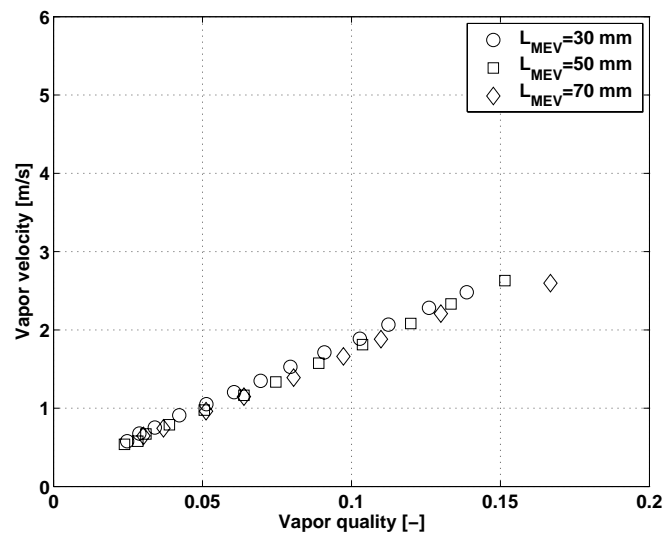


Figure 7.4: Influence of the microevaporator length on the vapor velocity from laser 2 for R-134a, $D = 0.509$ mm, $\Delta T_{sub} = 3^{\circ}\text{C}$, $T_{sat} = 30^{\circ}\text{C}$ and $G = 500$ kg/m²s.

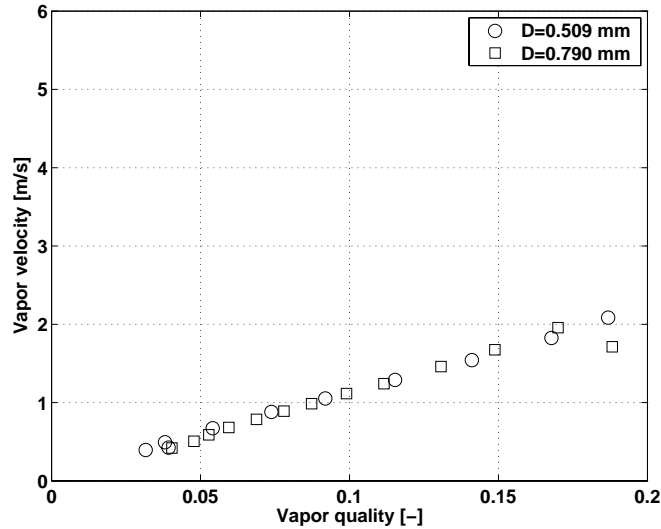


Figure 7.5: Influence of the diameter on the vapor velocity from laser 2 for R-134a, $T_{sat} = 30^\circ\text{C}$, $\Delta T_{sub} = 3^\circ\text{C}$, $L_{MEV} = 70$ mm and $G = 350$ kg/m²s.

7.1.5 Effect of the fluid

Figure 7.6 shows the influence of the fluid on the vapor velocity. The fluid properties have a strong influence on the velocity. R-245fa has a higher velocity than R-134a, which is expected when regarding the values of ρ_V (refer to Appendix A where tabular values of the physical properties of the test fluids are presented). The density of the vapor for R-134a is 3 times higher than for R-245fa.

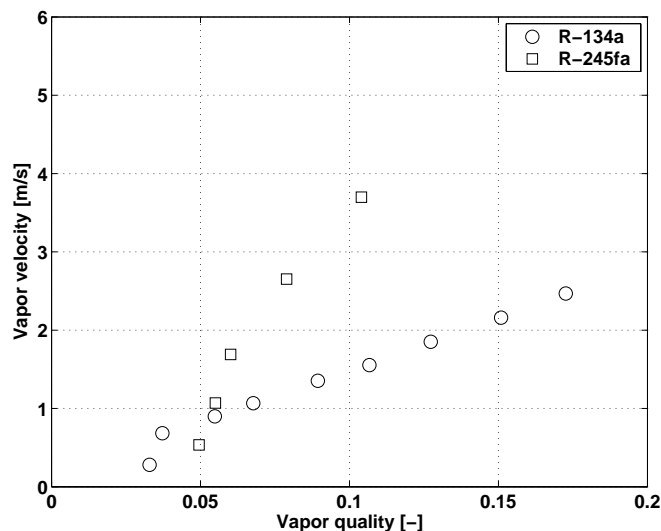


Figure 7.6: Influence of the fluid on the vapor velocity from laser 2 for $T_{sat} = 35^\circ\text{C}$, $D = 0.509$ mm, $\Delta T_{sub} = 5 - 6^\circ\text{C}$, $L_{MEV} = 70$ mm and $G = 500$ kg/m²s.

7.1.6 Velocities below homogeneous model predictions

Figure 7.7 shows some of the results plotted as vapor velocity versus vapor quality where the vapor velocity is below the homogeneous model prediction, which is quite unusual. This phenomena happens at low vapor quality and low mass flux for R-134a and always for R-245fa. These velocity measurements have been specifically verified with the high-speed video image processing as shown in Fig. 4.14, where the image processing and the laser measurement were in pretty good agreement. Two reasons could be proposed to explain this unexpected below homogeneous vapor flow velocity:

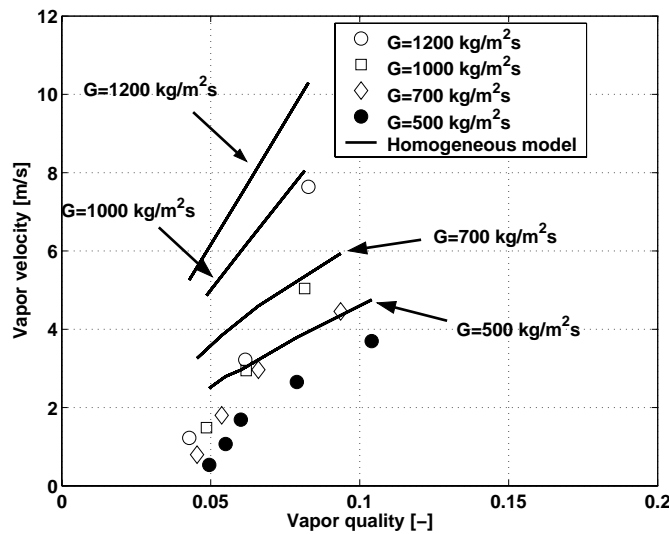


Figure 7.7: Vapor velocity versus vapor quality from laser 2 for R-245fa, $T_{sat} = 35^{\circ}\text{C}$, $D = 0.509 \text{ mm}$, $\Delta T_{sub} = 6^{\circ}\text{C}$ and $L_{MEV} = 70 \text{ mm}$.

A low level of flow instability inside the microtube and perhaps some back flow of vapor. Even though a microvalve has been installed there may be still small oscillations not detectable by the pressure transducers nor the thermocouples. Figure 7.8 shows the wall temperature measurement versus time carried out with a high-speed infrared camera at a high frequency of acquisition (900 Hz). An oscillation of the wall temperature is observed at about 8 Hz with an amplitude of 9°C . These oscillations are not detected by the thermocouples nor the pressure transducers because those signals are acquired at a frequency of only 1 Hz. Thus the flow is apparently stable looking at the 1 Hz signals but an 8 Hz instability is in fact present. In such an oscillating flow, it is logical to envision some compressibility effects on the bubbles trapped between liquid slugs flowing in opposite directions.

Thus, the actual reason why the vapor velocity can go below homogeneous is not necessarily readily evident from the information available here. Vapor velocities below homogeneous in microchannels have been observed and documented experimentally for the first time in this study. Results should represent the real functioning of a microevaporator, with or without multichannels.

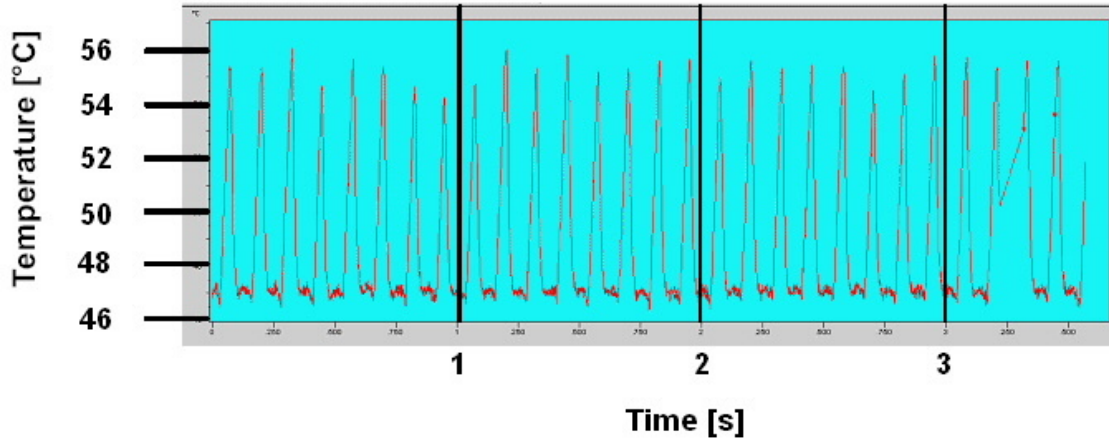


Figure 7.8: Wall temperature measurement versus time carried out with a high-speed infrared camera for $T_{sat} = 30^\circ\text{C}$, $G = 300 \text{ kg/m}^2\text{s}$, $D = 0.790 \text{ mm}$, $q = 140 \text{ kW/m}^2$ and $x_{MEV,out} = 0.82$.

7.2 Drift flux model applied to the vapor velocity

In order to predict the vapor bubble velocity, the general drift flux model of Zuber and Findlay described earlier in Chapter 3.3.2 is used.

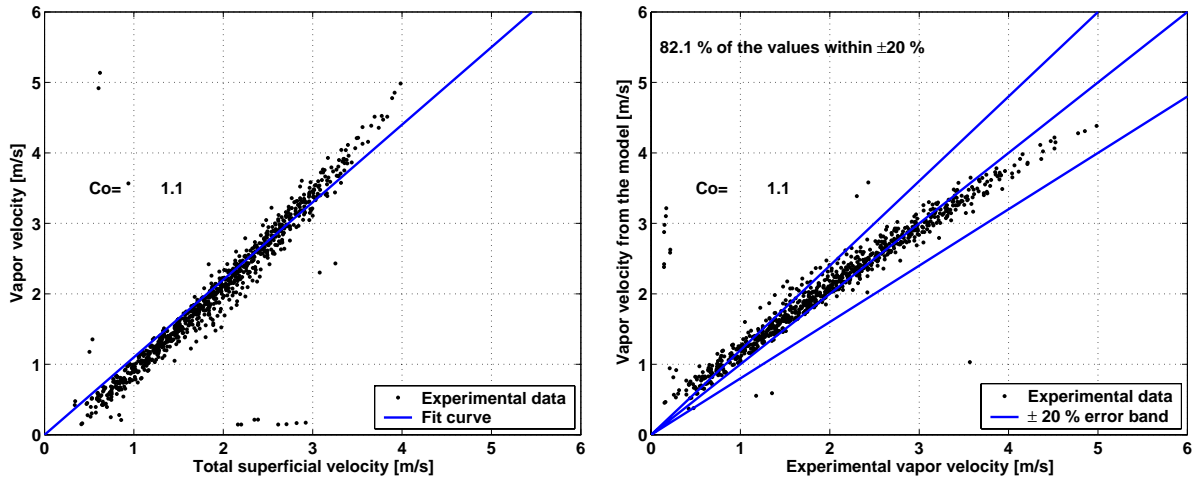
The idea here was to base the velocity (or void fraction) prediction on the flow pattern prediction for a future use in a heat transfer or pressure drop model. For that reason, two zones was defined: the first one for isolated bubble (IB) regime and the second one for the coalescing bubble (CB) regime. However, after processing the data, it appears that the bubble velocity is not affected by the different flow patterns. The data were therefore processed without any differentiation in the flow patterns.

To predict the vapor bubble velocity, results have been plotted as vapor bubble velocity versus the total superficial velocity (j) using Eq. (2.11). As the tube orientation is horizontal and as we are in the presence of a microtube, the gravity has no effect. As a result $\bar{V}_{Vj} = 0$. This factor represents the bubble rise velocity in a tube of stagnant liquid. By regarding Eq. (3.26), it appears that C_o represents an empirical factor correcting the one-dimensional homogeneous theory to account for the fact that the void and velocity profiles across the channel can vary independently of one another.

7.2.1 R-134a results

Figure 7.9 represents the drift flux model applied to R-134a and $D = 0.509 \text{ mm}$. All the data are well "aligned" and a factor of $C_o = 1.1$ has been calculated with a least square method. In fact the data would be better fitted if \bar{V}_{Vj} was allowed to be below zero ($\bar{V}_{Vj} = -0.21$) but that is not usual for a horizontal drift flux flow. The reason for this negative value is the same as that given in Part 7.1.6. The vapor is slowed down by instabilities or compressibility. It is like a negative bubble rise velocity in a tube of stagnant liquid. This negative value of \bar{V}_{Vj} may be a quantitative characterization of small instabilities or compressibility.

More than 82 % of the data fall within a $\pm 20\%$ error band (87 % in $\pm 25\%$). The drift flux model with $C_o = 1.1$ is thus in good agreement with the results. Results show that the flow is close to the homogeneous flow ($C_o = 1$).

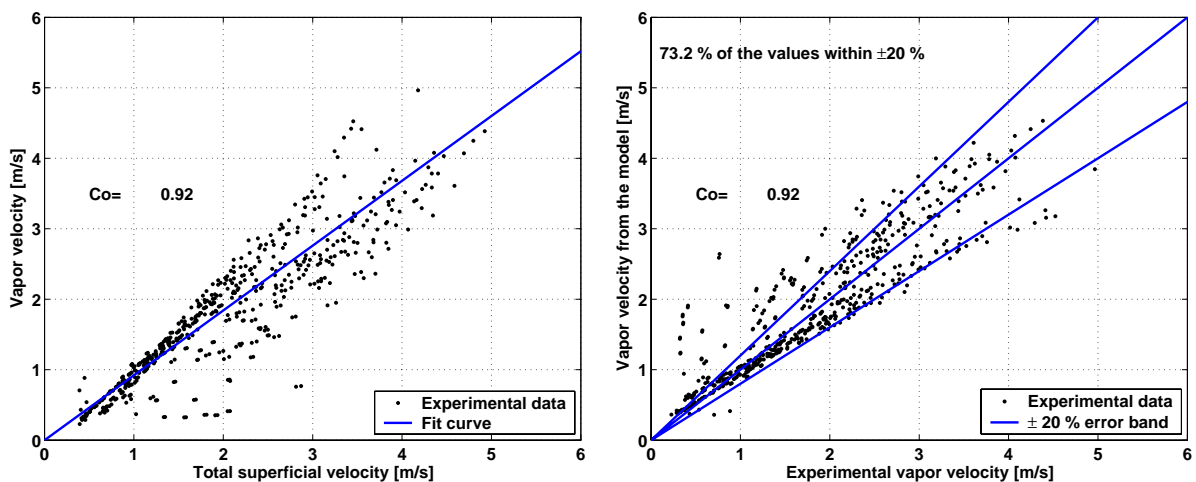


(a) Vapor velocity versus superficial velocity for R-134a and $D = 0.509$ mm.

(b) Comparison between the vapor velocity from the drift flux model and the experimental vapor velocity for R-134a and $D = 0.509$ mm.

Figure 7.9: Drift flux model applied to R-134a and $D = 0.509$ mm results.

Figure 7.10 represents the drift flux model applied to R-134a and $D = 0.790$ mm. The results are more scattered than for $D = 0.509$ mm. $C_o = 0.92$ has been determined with the least square method and more than 73 % of the data fall within a $\pm 20\%$ error band (80 % in $\pm 25\%$). One can make the same comments as in the previous paragraph about \bar{V}_{Vj} and a probable negative value that would better fit the data.



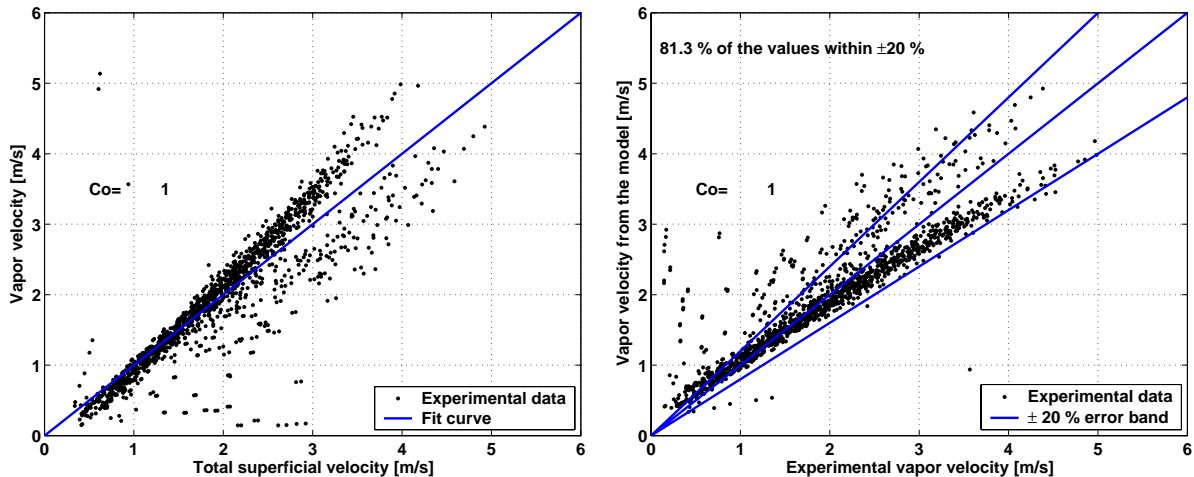
(a) Vapor velocity versus superficial velocity for R-134a and $D = 0.790$ mm.

(b) Comparison between the vapor velocity from the drift flux model and the experimental vapor velocity for R-134a and $D = 0.790$ mm.

Figure 7.10: Drift flux model applied to R-134a and $D = 0.790$ mm results.

Figure 7.11 represents the drift flux model applied to all R-134a data. The two different

diameters are plotted. A mean value of $C_o = 1.0$ has been found and suggests a homogeneous flow. More than 81 % of the data fall within a $\pm 20\%$ error band (86 % in $\pm 25\%$). Thus, use of the homogeneous model at the low vapor qualities (< 0.20) seems to be relatively appropriate here.



(a) Vapor velocity versus superficial velocity for R-134a.

(b) Comparison between the vapor velocity from the drift flux model and the experimental vapor velocity for R-134a.

Figure 7.11: Drift flux model applied to all R-134a results.

7.2.2 R-245fa results

Figure 7.12 represents the drift flux model applied to R-245fa and $D = 0.509$ mm. A value of $C_o = 0.6$ has been found. About 33 % of the data fall within a $\pm 20\%$ error band (50 % in $\pm 25\%$), which is not a good result. The data are strongly scattered. Instabilities were much more visible for R-245fa than for R-134a. This probably explained the results and the value of $C_o = 0.6$.

7.3 Experimental time averaged void fractions

In order to determine the time averaged cross sectional void fraction, Eq. (2.9) is used. It is an indirect calculation of the void fraction by using the superficial velocities and the vapor bubble velocities. The time averaged centerline void fraction is also determined. It is calculated by assuming that its value is 1 if there is vapor and 0 if liquid and then processing the signal accordingly. It does not take into account the radial distribution of the liquid and vapor but only that at the nose and rear of the bubble, i.e. essentially that at the centerline of the channel. When semi-annular flow is reached, it becomes 1 as expected and is used as a further quantitative check on that transition and thus a limit on the measurement of vapor velocities.

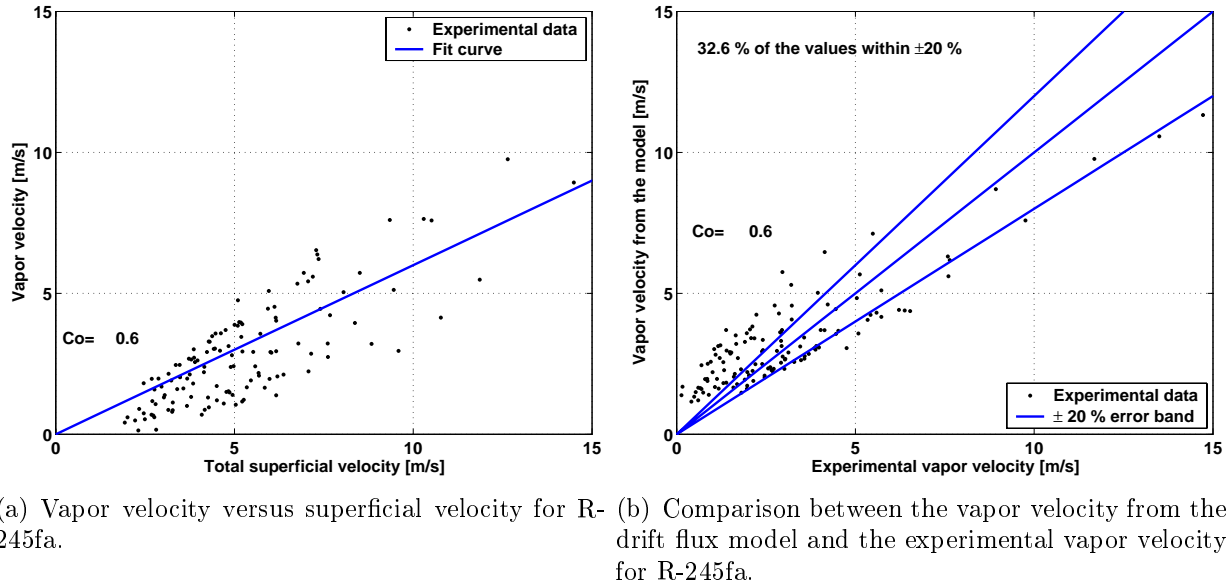


Figure 7.12: Drift flux model applied to R-245fa results.

Fig. 7.13 shows the time averaged centerline (c-l) void fractions and the cross sectional (c-s) void fractions from laser 2 versus the thermodynamic vapor quality. The cross sectional void fractions are also compared to those predicted with the homogeneous model.

As can be seen, the time averaged centerline (c-l) void fraction is most of the time greater than the time averaged cross sectional (c-s) void fraction as expected. The higher the vapor quality, the higher the void fraction is. However, the higher the mass flux, the lower the void fraction becomes.

7.4 Drift flux model applied to the cross sectional void fraction

As the cross sectional void fraction is derived from the vapor velocity measurement, the conclusion will be the same when applying the drift flux model. Figure 7.14 shows the void fraction versus the volumetric flow concentration (Eq. (3.28)) for R-134a. Results are in good agreement with the homogeneous model while the Armand correlation under predicts the data. The Armand correlation is derived from the drift flux model with $C_o = 1.2$ and $\bar{V}_{Vj} = 0$. The present results for R-134a agree well with the Tripplet et al. [53], Serizawa et al. [44], and Chung and Kawaji [10] conclusions saying that cross sectional void fraction in microchannels are well predicted by the homogeneous model, which was the void fraction model assumed in the development of the 3-zone model by Thome et al. [50].

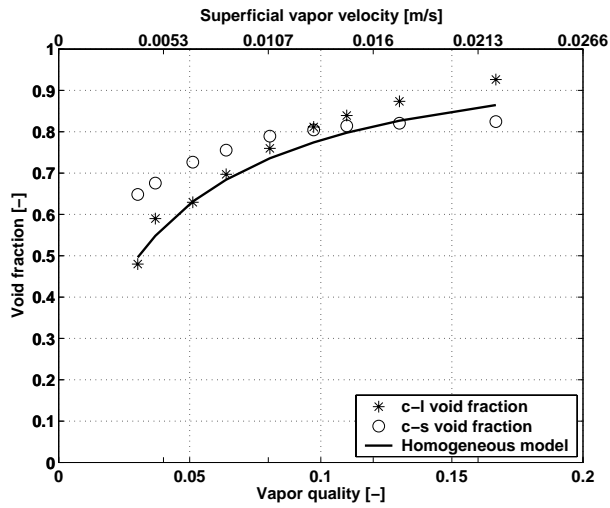
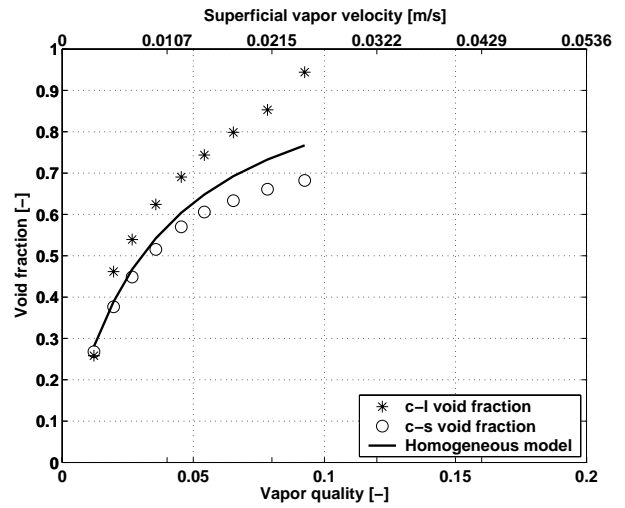
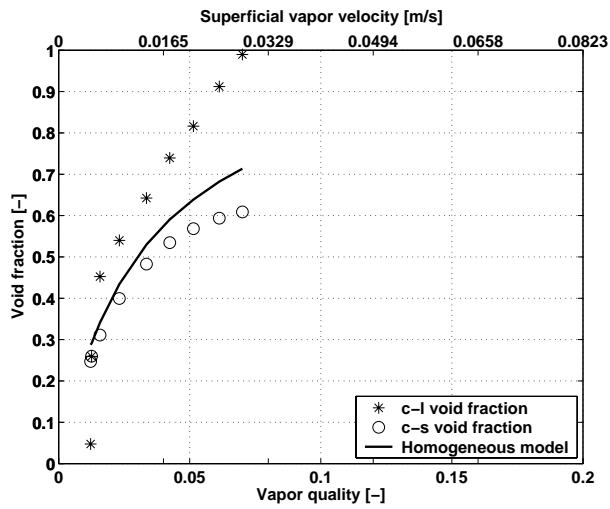
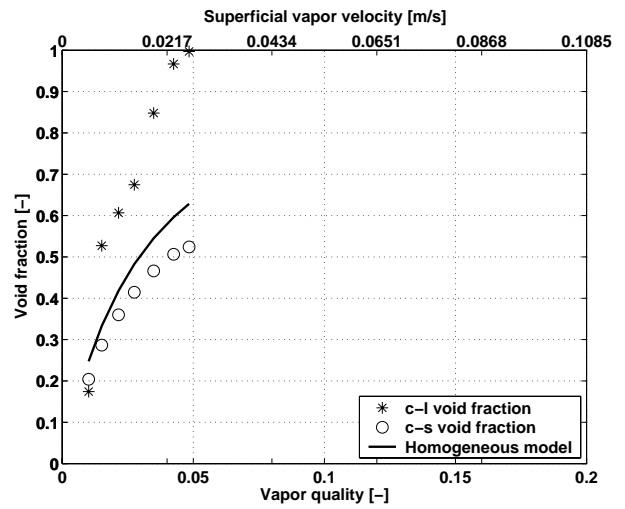
(a) $G = 500 \text{ kg/m}^2\text{s}$.(b) $G = 1000 \text{ kg/m}^2\text{s}$.(c) $G = 1500 \text{ kg/m}^2\text{s}$.(d) $G = 2000 \text{ kg/m}^2\text{s}$.

Figure 7.13: Void fractions from laser 2 for R-134a, $D = 0.509 \text{ mm}$, $L_{MEV} = 70.70 \text{ mm}$, $T_{sat} = 30^\circ\text{C}$ and $\Delta T_{sub} = 3^\circ\text{C}$.

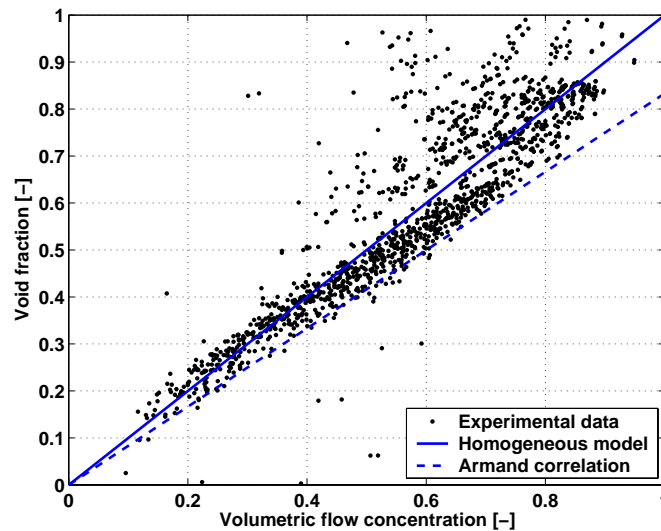


Figure 7.14: Void fraction versus volumetric flow concentration for R-134a compared with the homogeneous model and the Armand's correlation.

7.5 Conclusions on the velocity and void fraction results

Bubble vapor velocities were measured using a cross-correlation technique from two laser signals for a wide range of mass velocities for R-134a and R-245fa in two sizes of microchannels for the following types of flow regimes where the method is applicable: bubbly/slug, slug and slug/semi-annular flow. The vapor velocity and cross sectional void fraction backed out from the velocity data showed that these parameters were dependent on the vapor quality, the mass flux, the saturation temperature and the fluid. The inlet subcooling, the microevaporator length and the diameter had no influence on the results.

Some results for R-134a and all the results for R-245fa were surprisingly below the homogeneous prediction. The minor flow instabilities in the test section, not detectable with conventional instrumentation, may explain this phenomena. The flow is slowed down or blocked due to the pressure variation inside the microevaporator, which may also create a compressibility effect.

The general expression for predicting the true average velocity of the vapor and therefore the average cross-sectional void fraction of the present results is:

$$u_V = C_o G \left(\frac{x}{\rho_V} + \frac{1-x}{\rho_L} \right) \quad (7.1)$$

where:

$C_o = 1.1$ for R-134a and $D = 0.509$ mm.

$C_o = 0.92$ for R-134a and $D = 0.790$ mm.

$C_o = 1$ for R-134a based on results for both tubes.

$C_o = 0.6$ for R-245fa and $D = 0.509$ mm.

For R-134a, since $C_o = 1$ the flow can be considered as a homogeneous flow. More than 81 % of the data fall within a $\pm 20\%$ error band (86 % in $\pm 25\%$) when fitting the data with $C_o = 1$. For R-245fa, more tests with some modifications to avoid instabilities have to be performed to better investigate the reason for the vapor velocities falling significantly below that of a homogeneous flow.

Chapter 8

Adiabatic two-phase pressure drop

In this Chapter, the adiabatic two-phase pressure drops measured in the sight glass shown in Figs. 4.4 and 4.5 are presented. The method used to measure pressure drops and its error analysis were presented earlier in Section 4.4.14. As it is experimentally a challenge to measure two-phase pressure drops in microchannels without disturbing the flow, in this study they were obtained indirectly using the saturation temperatures at the inlet and outlet. This resulted in satisfactory accuracy of 4.1 % at high pressure drops (at 8.8 bar/m) but a sizable error of 25 % at low pressure drops (1.3 bar/m). However, as shown in this chapter, the method gives a very good consistency in the data. The term "adiabatic" will be omitted to lighten the text in this chapter.

8.1 Experimental two-phase frictional pressure drop

The experimental procedure is the same as for the flow patterns. There were 2210 experimental two-phase pressure drops data points measured in this study for the conditions presented in Table 6.1. 30 data points are not taken into account as their values are below zero due to small instabilities and error measurements. The two-phase total pressure drop is calculated using Eq. (4.53). According to Eqs. (3.34) and (3.36), the momentum pressure drop is subtracted from the total pressure drop to obtain the two-phase frictional pressure drop $\left(\frac{dP}{dz}\right)_f$. The momentum pressure drop is caused by the slight flashing effect due to the pressure drop but it is negligible (less than 0.1 %) as shown in Fig. 8.1, but is taken into account anyway.

The general trend for the two-phase frictional pressure drop is illustrated in Fig. 8.2. The data are plotted according to the vapor quality at the laser 1. In general, the higher the mass flux, the higher the vapor quality, the higher the two-phase frictional pressure drop is (the expected trend). However, a change in the trend can be observed for $G=1000 \text{ kg/m}^2\text{s}$ and $G=1200 \text{ kg/m}^2\text{s}$. Three arrows show this change. It corresponds to a change in flow pattern. Figure 8.3 shows the voltage signal from the laser reading diode versus time during 1 second for two different vapor qualities corresponding to the data points (a) and (b) in Fig. 8.2(b). The flow is annular according to the flow pattern map of Fig. 6.8 but the annular

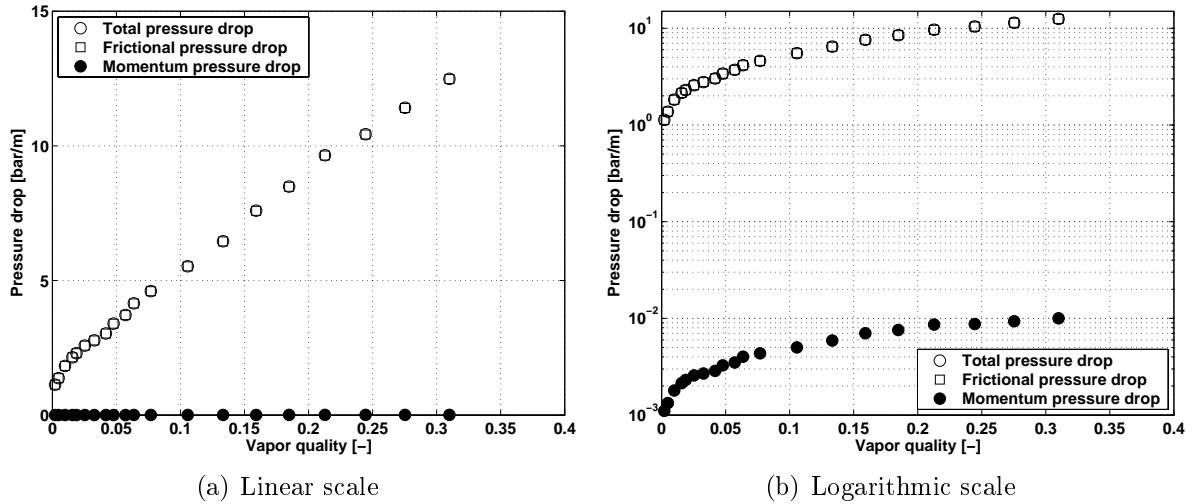


Figure 8.1: Comparison between the total, the frictional and the momentum pressure drop as a function of vapor quality from laser 1 for R-134a, $D = 0.509$ mm $L_{MEV} = 70.70$ mm, $T_{sat} = 30^\circ\text{C}$, $G = 1800$ kg/m²s and $\Delta T_{sub} = 3^\circ\text{C}$. Since the momentum pressure drop is so small, the values for the total and the frictional pressuredrops essentially fall on top of one another.

flow tends to be separated into smooth annular and wavy annular flow as shown in Figs. 6.6 and 6.7. (This can happen also for semi-annular flow which exhibits both smooth annular and churn flow zones). The friction factor is definitely less for smooth than for wavy annular flow so the two-phase pressure drop is less for case (b) than for case (a).

For very low vapor quality one can surprisingly observe the two-phase frictional pressure drops decreasing with increasing vapor quality. Afterwards the two-phase frictional pressure drop increases with the vapor quality with two different gradients, where the higher gradient is for lower vapor qualities. The change in the gradient of the two-phase frictional pressure drop will be explained later.

8.1.1 Effect of the inlet subcooling

As expected, the inlet subcooling at the entrance to the microevaporator had no effect on the saturated two-phase frictional pressure drops as shown in Fig. 8.4. The small inlet subcoolings tested here had no influence on the flow patterns and thus the two-phase mechanisms are not affected.

8.1.2 Effect of the saturation temperature

As presented in Fig. 8.5, the saturation temperature influences the two-phase frictional pressure drop. The higher the saturation temperature, the lower the two-phase frictional pressure drop is. The saturation temperature modifies the density and the dynamic viscosity of the mixture. The results here show the expected tendency from macroscale theory.

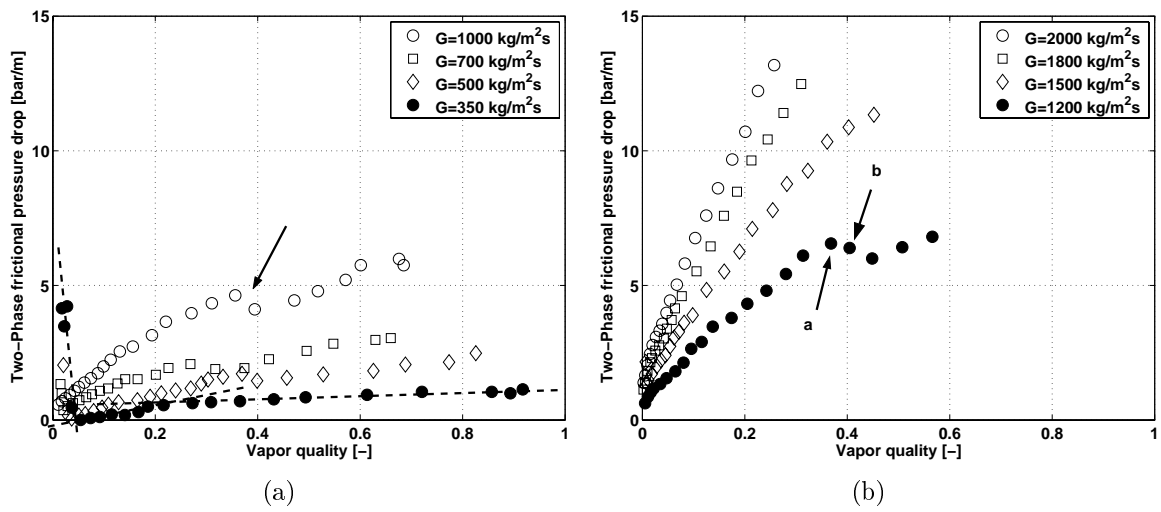


Figure 8.2: Two-phase frictional pressure drop as a function of the vapor quality from laser 1 for R-134a, $D = 0.509$ mm, $L_{MEV} = 70.70$ mm, $T_{sat} = 30^\circ\text{C}$ and $\Delta T_{sub} = 3^\circ\text{C}$.

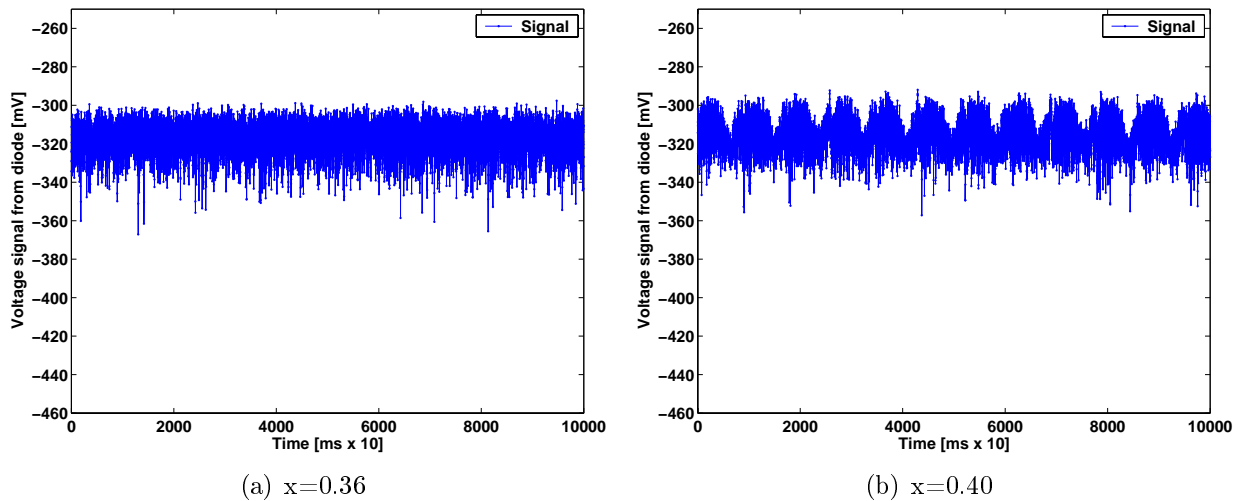


Figure 8.3: Signal from diode versus time for laser 1 R-134a, $D = 0.509$ mm, $L_{MEV} = 70.70$ mm, $T_{sat} = 30^\circ\text{C}$, $G = 1200$ kg/m²s and $\Delta T_{sub} = 3^\circ\text{C}$. Left: wavy-annular flow (a); Right: smooth and wavy-annular flow (b).

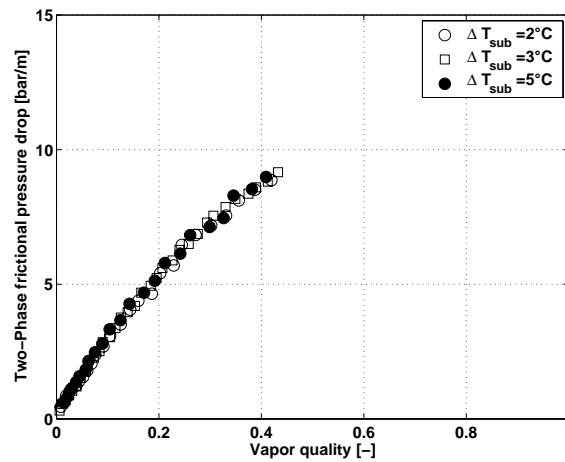


Figure 8.4: Influence of the inlet subcooling at entrance to the microevaporator on the two-phase frictional pressure drop for R-134a, $D = 0.509$ mm, $L_{MEV} = 70.70$ mm, $T_{sat} = 35^\circ\text{C}$ and $G = 1500$ kg/m²s.

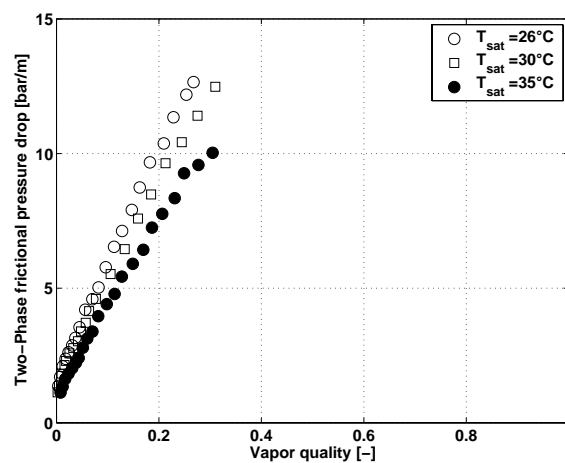


Figure 8.5: Influence of the saturation temperature on the two-phase frictional pressure drop for R-134a, $D = 0.509$ mm, $L_{MEV} = 70.70$ mm, $\Delta T_{sub} = 3^\circ\text{C}$ and $G = 1800$ kg/m²s.

8.1.3 Effect of the microevaporator length

As the microevaporator length has no effect on the flow patterns, it was expected that the two-phase frictional pressure drops measured in the sight glass tube would not be affected by this variation. Figure 8.6 shows this to be the case.

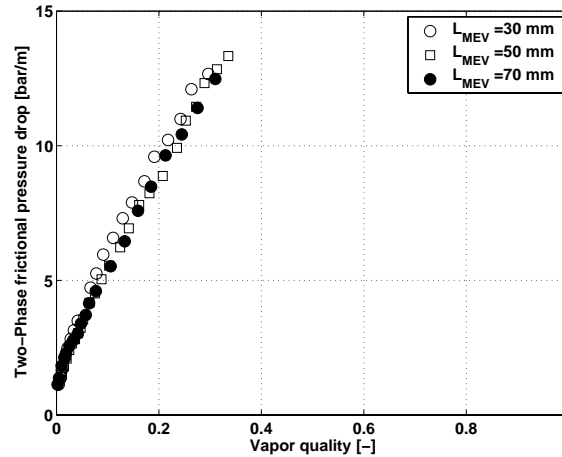


Figure 8.6: Influence of the microevaporator length on the two-phase frictional pressure drop for R-134a, $D = 0.509$ mm, $T_{sat} = 30^\circ\text{C}$, $\Delta T_{sub} = 3^\circ\text{C}$ and $G = 1800$ kg/m²s.

8.1.4 Effect of the microevaporator diameter

As can be seen in Fig. 8.7, the diameter of the sight glass tube has a strong influence on the two-phase frictional pressure drop. As expected, the larger the diameter, the lower the two-phase pressure drop is. The same trends are observed for both diameters.

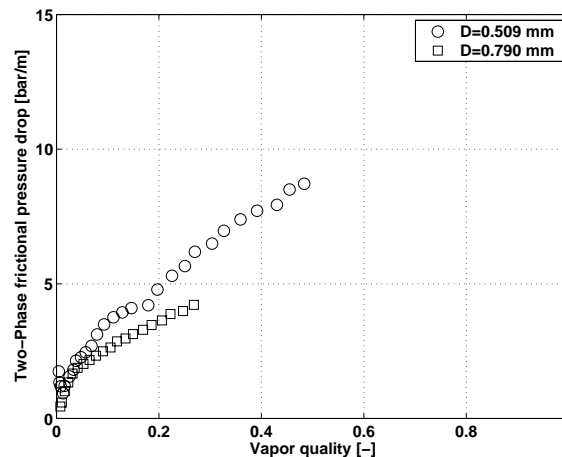


Figure 8.7: Influence of the microevaporator diameter on the two-phase frictional pressure drop for R-134a, $T_{sat} = 30^\circ\text{C}$, $L_{MEV} = 70.70$ mm, $\Delta T_{sub} = 3^\circ\text{C}$ and $G = 1200$ kg/m²s.

8.1.5 Effect of the fluid

The fluid has an important influence on the two-phase frictional pressure drop. The values for R-245fa are strongly higher than those for R-134a. Actually $\rho_V(\text{R-134a}) \simeq 3\rho_V(\text{R-245fa})$ and $2\mu_L(\text{R-134a}) \simeq \mu_L(\text{R-245fa})$, so the density and the dynamic viscosity of the two-phase mixture are affected in the same way and the result is the increase of the pressure drop for R-245fa.

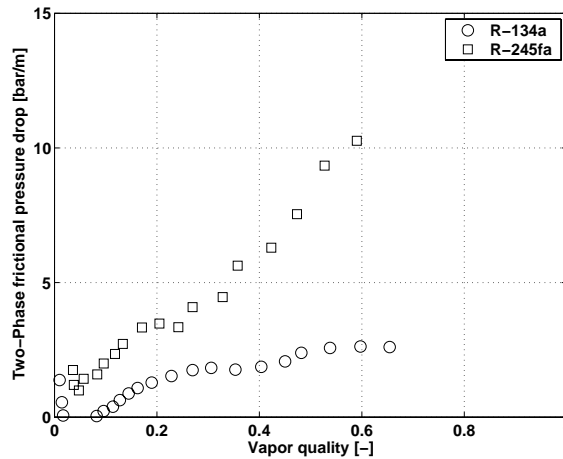


Figure 8.8: Influence of the fluid on the two-phase frictional pressure drop for $D = 0.509$ mm, $T_{sat} = 35^\circ\text{C}$, $L_{MEV} = 70.70$ mm, $\Delta T_{sub} = 5 - 6^\circ\text{C}$ and $G = 700$ kg/m²s.

8.1.6 The two-phase friction factor

As observed in the previous figures, the variation of the two-phase frictional pressure drop can be divided into three different zones. Firstly, the two-phase frictional pressure drop decreases, secondly the two-phase frictional pressure drop increases with a certain gradient and thirdly the two-phase frictional pressure drop increases with a lower gradient as can be seen in Fig. 8.8.

It is possible to plot the pressure drop data as the two-phase friction factor versus the two-phase Reynolds number as shown in Fig. 8.9. Equations (3.42) and (3.38) are used to calculate respectively μ_{TP} and ρ_{TP} . The two-phase friction factors are determined from the measured pressure gradients using Eq. (3.37). The values of Re_{TP} are obtained using Eq. (3.41). Three different zones are detected. An analogy with the behavior of the single phase friction factor is made as follows:

- $Re_{TP} < 2000$: The first zone is called the laminar zone. The two-phase friction factor diminishes when increasing the two-phase Reynolds number.
- $2000 \leq Re_{TP} < 8000$: The second zone is the transition zone. The two-phase friction factor increases with the Reynolds number or decreases, depending to the conditions. A case could also be made here to set the upper boundary at 4500 rather than 8000

in viewing Fig. 8.9 but in (b) and (c) some transition effects still appear to fall in this range.

- $Re_{TP} \geq 8000$: The third zone corresponds to the turbulent zone. The data are grouped and decrease with increasing two-phase Reynolds number.

The two-phase friction factor behavior is the same as for the single phase friction factor. It is interesting to emphasize here that each zone corresponds to each trend observed earlier when plotting the two-phase frictional pressure drop versus the vapor quality.

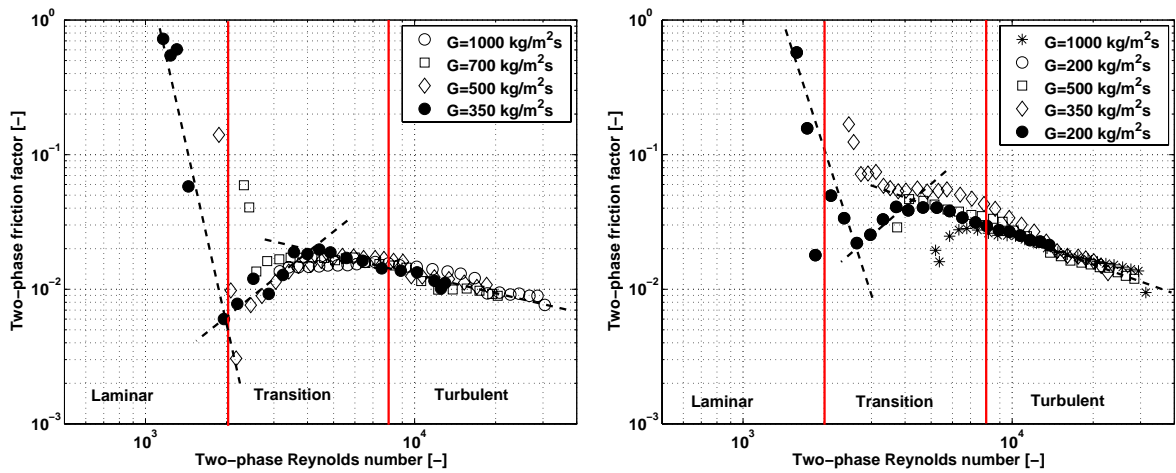
The laminar zone corresponds most often to the bubbly or bubbly/slug regime. Usually, the pressure drop should not decrease and then increase afterwards as there should be a continuous increase of the pressure drop with the two-phase Reynolds number. However, macroscale two-phase pressure drop data nearly always fall only in the turbulent zone and this trend is not thus observed. Furthermore, it is interesting to emphasize that the transition zone occurs in the same range of Reynolds number as for single phase flow. The laminar zone will be ignored for this study as it is difficult to make a detailed analysis since it corresponds to only 74 data points, or 3.3 % of the database.

The rest of the database will be divided into two sets of data (936 data points for the transition zone and 1200 data points for the turbulent region) and compared to available correlations or models.

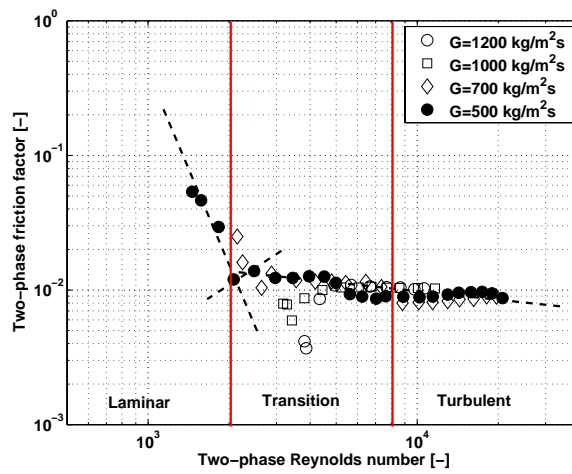
8.2 Comparisons with existing prediction methods

The comparison between the present experimental data (for R-134a, R-245fa and both sight glass tube diameters) and twelve models and correlations available in the literature (described in Chapter 3.4) is shown in Figs. 8.10, 8.11, 8.12 and 8.13, segregating the data into the respective transition (left graph) and turbulent (right graph) regions. The data are plotted according to the saturation conditions at the laser 1. No prediction method works very well to predict the present experimental data, except for the Müller-Steinhagen and Heck [39] correlation that predicts more than 62 % of the data within a ± 20 % error band for the turbulent data. Furthermore, it predicts 83 % of the data for R-134a in the 0.509 mm tube within this ± 20 % error band. For R-134a in the 0.790 mm tube, the results are not well predicted, as only 29 % of the data fall within a ± 20 % error band while 62 % of the data are within ± 20 % for R-245fa.

The homogeneous model tends to regroup the data about as well as the Zhang and Webb or Mishima and Hibiki correlations. The homogeneous models under predict the data. In fact, some methods over predict the data while others under predict them. A new prediction method has been developed and is proposed below.



(a) R-134a, $D = 0.509\text{ mm}$, $T_{sat} = 30^\circ\text{C}$, $L_{MEV} = 70.70\text{ mm}$, $\Delta T_{sub} = 3^\circ\text{C}$.
 (b) R-134a, $D = 0.790\text{ mm}$, $T_{sat} = 30^\circ\text{C}$, $L_{MEV} = 70.70\text{ mm}$, $\Delta T_{sub} = 3^\circ\text{C}$.



(c) R-245fa, $D = 0.509\text{ mm}$, $T_{sat} = 35^\circ\text{C}$, $L_{MEV} = 70.70\text{ mm}$, $\Delta T_{sub} = 6^\circ\text{C}$.

Figure 8.9: Two-phase friction factor versus two-phase Reynolds number.

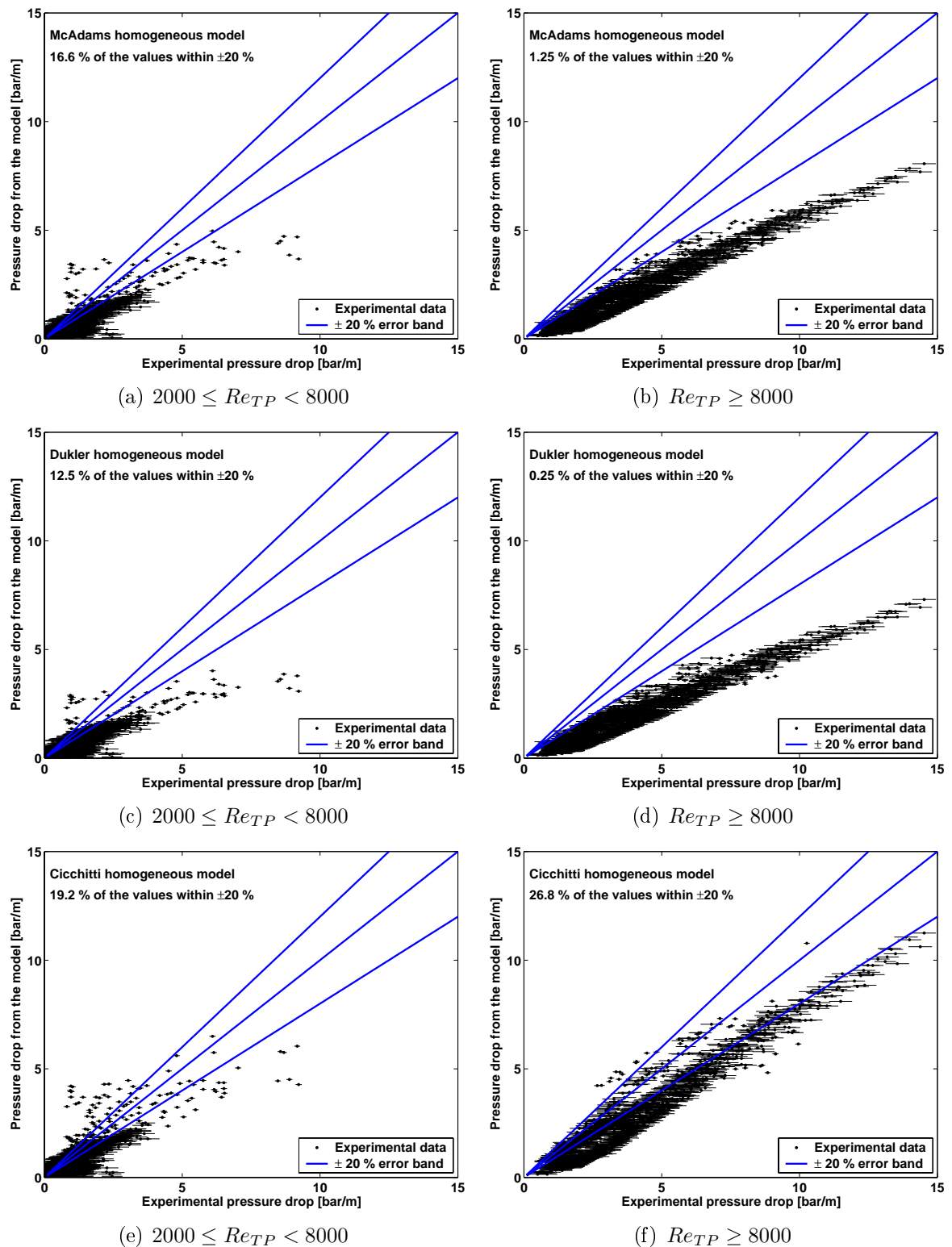


Figure 8.10: Comparison between the experimental data of two-phase frictional pressure drop and different models or correlations available in the literature for macroscale or microscale.

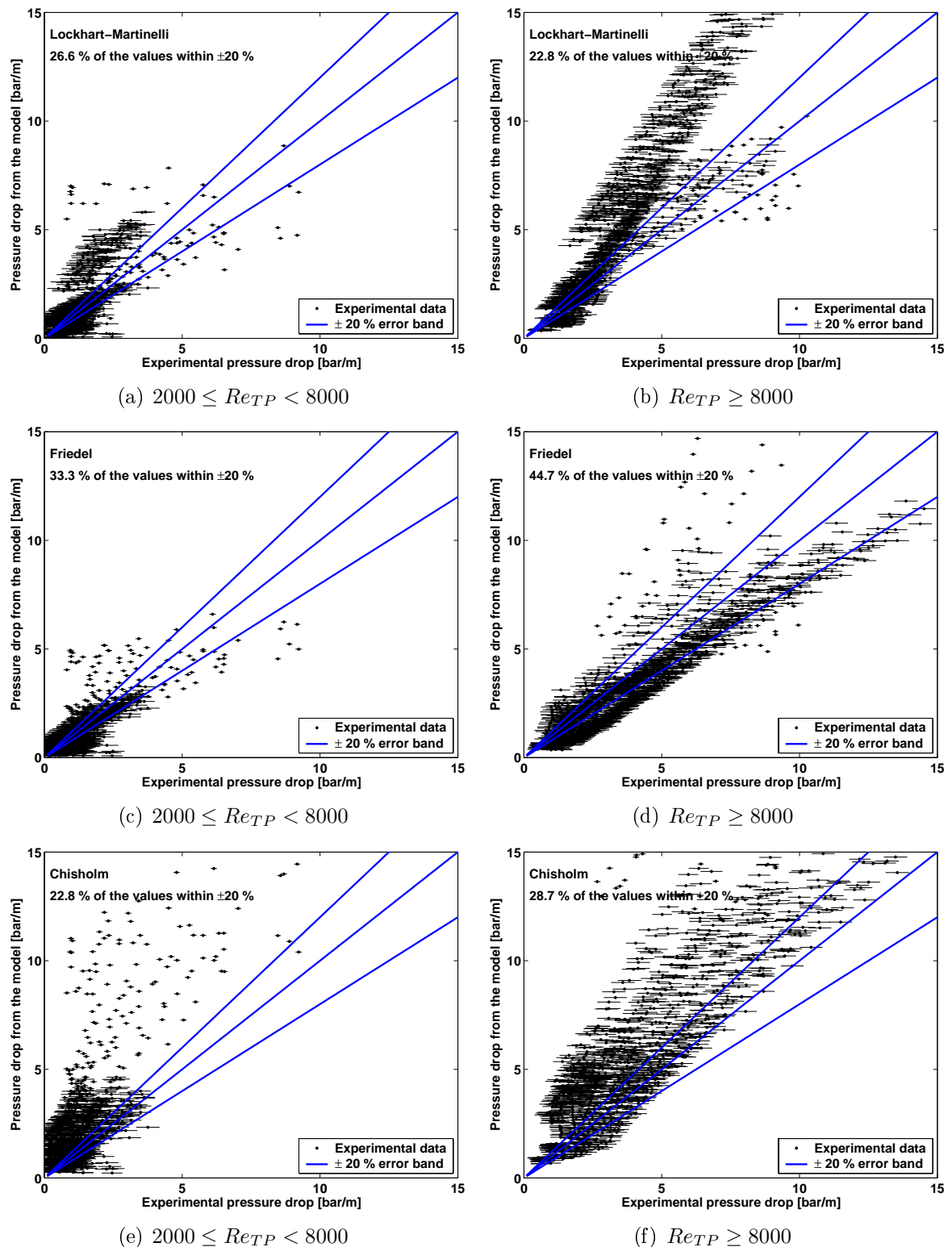


Figure 8.11: Comparison between the experimental data of two-phase frictional pressure drop and different models or correlations available in the literature for macroscale or microscale.

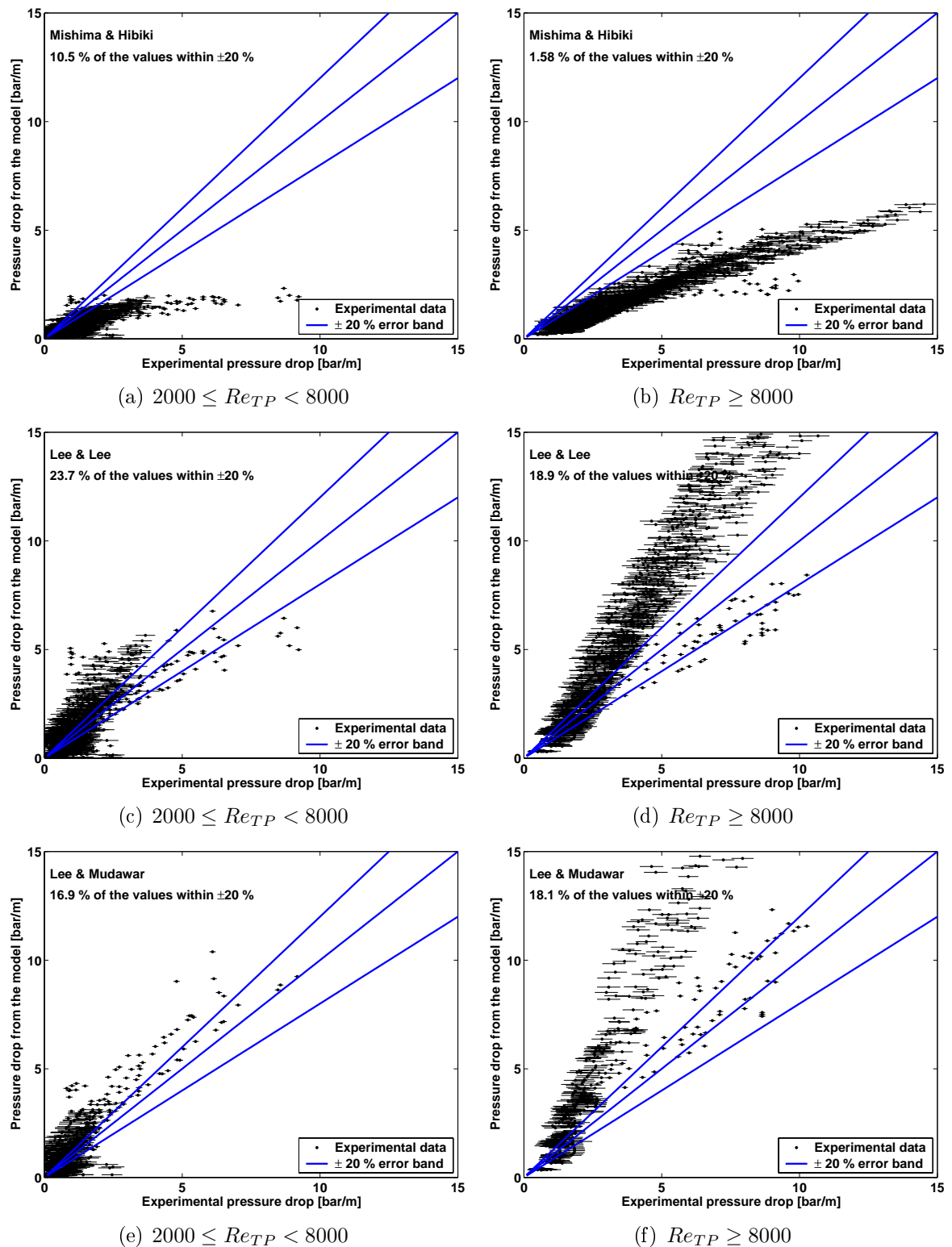


Figure 8.12: Comparison between the experimental data of two-phase frictional pressure drop and different models or correlations available in the literature for macroscale or microscale.

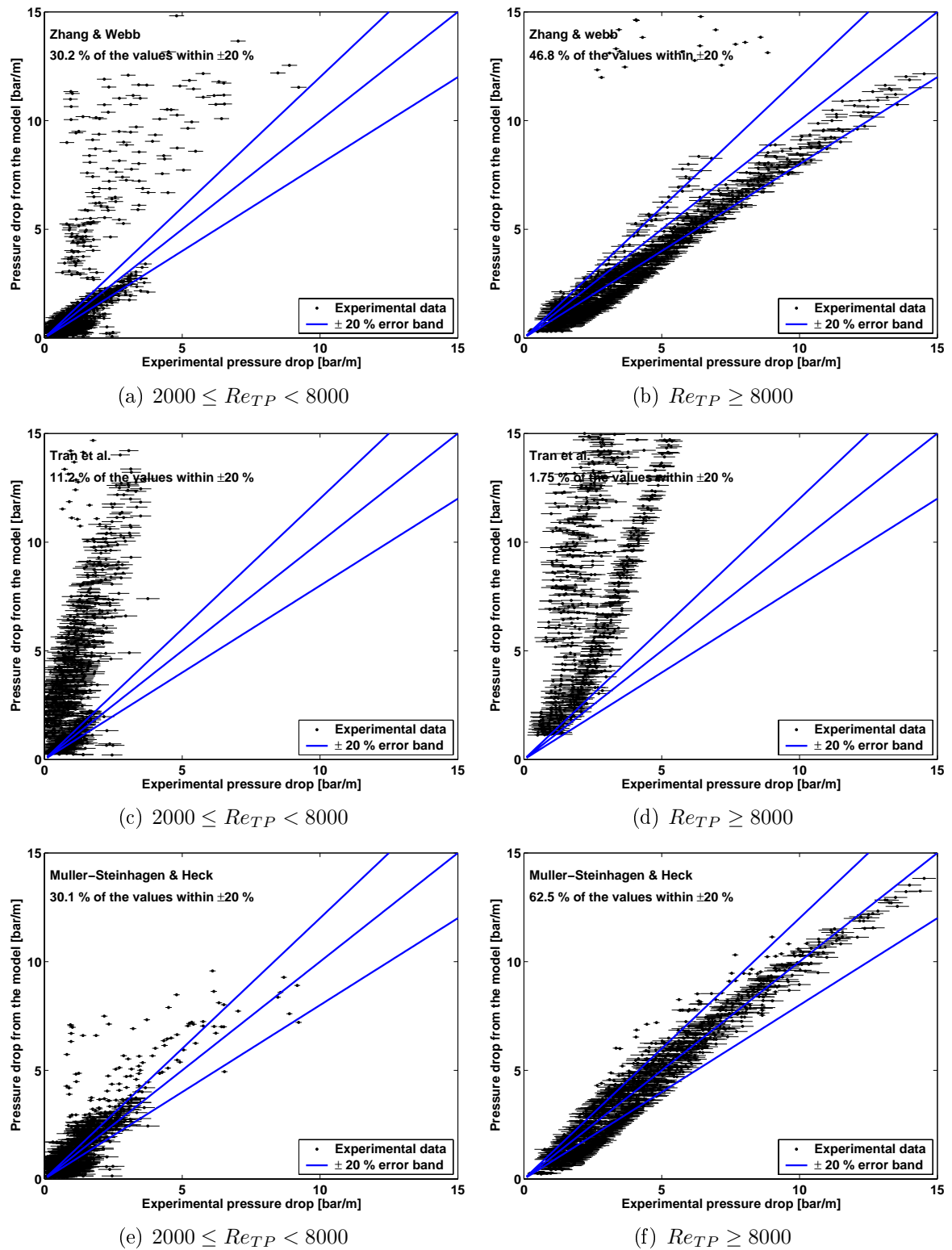


Figure 8.13: Comparison between the experimental data of two-phase frictional pressure drop and different models or correlations available in the literature for macroscale or microscale.

8.3 New prediction method

Two possibilities are offered to develop a new prediction method: In first, modification of the homogeneous model using the two-phase friction factor. This assumption is not far away from reality as it has been shown previously that the homogeneous model predicted the void fraction rather well. Moreover, Agostini and Bontemps [2] found that homogeneous model predicted their R-134a two-phase pressure drop data very well. Secondly, the classic Lockhart-Martinelli method can be modified with a new C parameter. Both approaches are widely used in the literature to predict two-phase pressure drops.

8.3.1 Homogeneous model with a new two-phase friction factor

Based on Part 8.1.6, it is possible to determine a new two-phase friction factor for the turbulent data where $8000 \leq Re_{TP}$. Figure 8.14 shows the new predicted two-phase friction factor determined with a least square method and given by the following Equations:

$$f_{TP} = 0.08Re_{TP}^{-1/5} \text{ for } D = 0.509 \text{ mm} \quad (8.1)$$

$$f_{TP} = 6Re_{TP}^{-3/5} \text{ for } D = 0.790 \text{ mm} \quad (8.2)$$

The friction factor commonly used in single phase flow for smooth tubes is also plotted for comparison. The two-phase friction factor is higher than that for single phase flow as expected. Actually, the two-phase friction takes into account the friction between the liquid and the wall as well as the friction between the liquid and the vapor whereas the single phase friction is affected only by the friction between the liquid and the wall. This difference was thus expected.

There are two different relations for f_{TP} , one for each tube. This could be explained by the fact that even if the sight glass tubes come from the same manufacturer, there could be a difference between them; however, they are very smooth (see Section 4.4.2) as can be expected with good optical quality glass and hence surface roughness can be excluded as influencing the results. More likely, it is the buoyancy effect that is responsible, which is greater for the 0.790 mm tube than for the 0.509 mm tube as shown in Fig. 1.2 and this effect explains the difference in the results. Supporting this conclusion, the data for R-134a and R-245fa in the 0.509 mm glass tube are well grouped together and are well predicted by Eq. (8.1) whereas those for the 0.790 mm tube are well predicted by Eq. (8.2).

Figure 8.15 presents the comparison between the 1200 experimental data points for the turbulent zone with the homogeneous model using a new two-phase friction factor expressions. It can be seen that the data are very well predicted. The trends are captured and the data are well grouped with 85.7 % of the data falling in a ± 20 % error band and more than 96 % within ± 30 %. The transition zone data cannot however currently be correctly predicted by any of the existing methods as shown in Figs. 8.10, 8.11, 8.12 and 8.13 and no method is proposed here for this regime. In fact none of the literature methods were specifically developed to handle the transition regime, so the lack of accuracy is not surprising. On

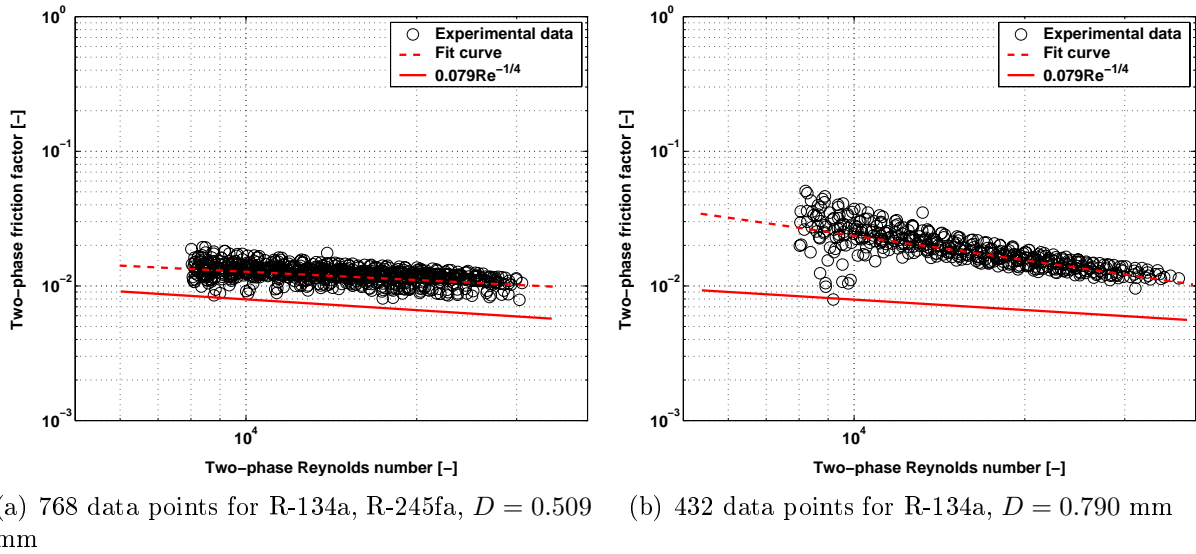


Figure 8.14: Two-phase friction factor versus two-phase Reynolds number for $Re_{TP} \geq 8000$.

the other hand, most literature methods eliminate the transition regime in the two-phase analysis, jumping directly from laminar to turbulent (see for example Friedel [20] with his Eqs. (3.54) and (3.55)). Figure 8.9 provides a very good example of why this is not at all appropriate.

8.3.2 Lockhart-Martinelli model with a new C parameter

Predicting the data with the lockhart-Martinelli method presented in Section 3.4.2 by modifying the C parameter is also possible and has been done by others as noted in Chapter 3.4. Figure 8.16 shows the two-phase multiplier as a function of the Martinelli parameter using the new values of C instead of the original values in Section 3.4.2 (which did not work well as was shown in Fig. 8.11 for the transition and turbulent data). The data have been plotted according to the different values of Re_L and Re_V . Only the data for $Re_{TP} \geq 2000$ are used. As can be seen, $C = 10$ fits the results for the 0.509 mm tube whatever are the conditions for the Reynolds number. For the 0.790 diameter tube, the data are more scattered and different values of C are found:

| <i>Liquid</i> | <i>Gas</i> | C |
|---------------|----------------|-----|
| turbulent | turbulent (tt) | 15 |
| viscous | turbulent (vt) | 22 |
| turbulent | viscous (tv) | 22 |
| viscous | viscous (vv) | 30 |

The data are more grouped for the turbulent zone than for the transition zone.

If we now compare the prediction method with the results (Fig. 8.17) for the two different zones defined earlier, it appears that the prediction method does not capture the trends for the transition region but does give a better results for the turbulent region; however the

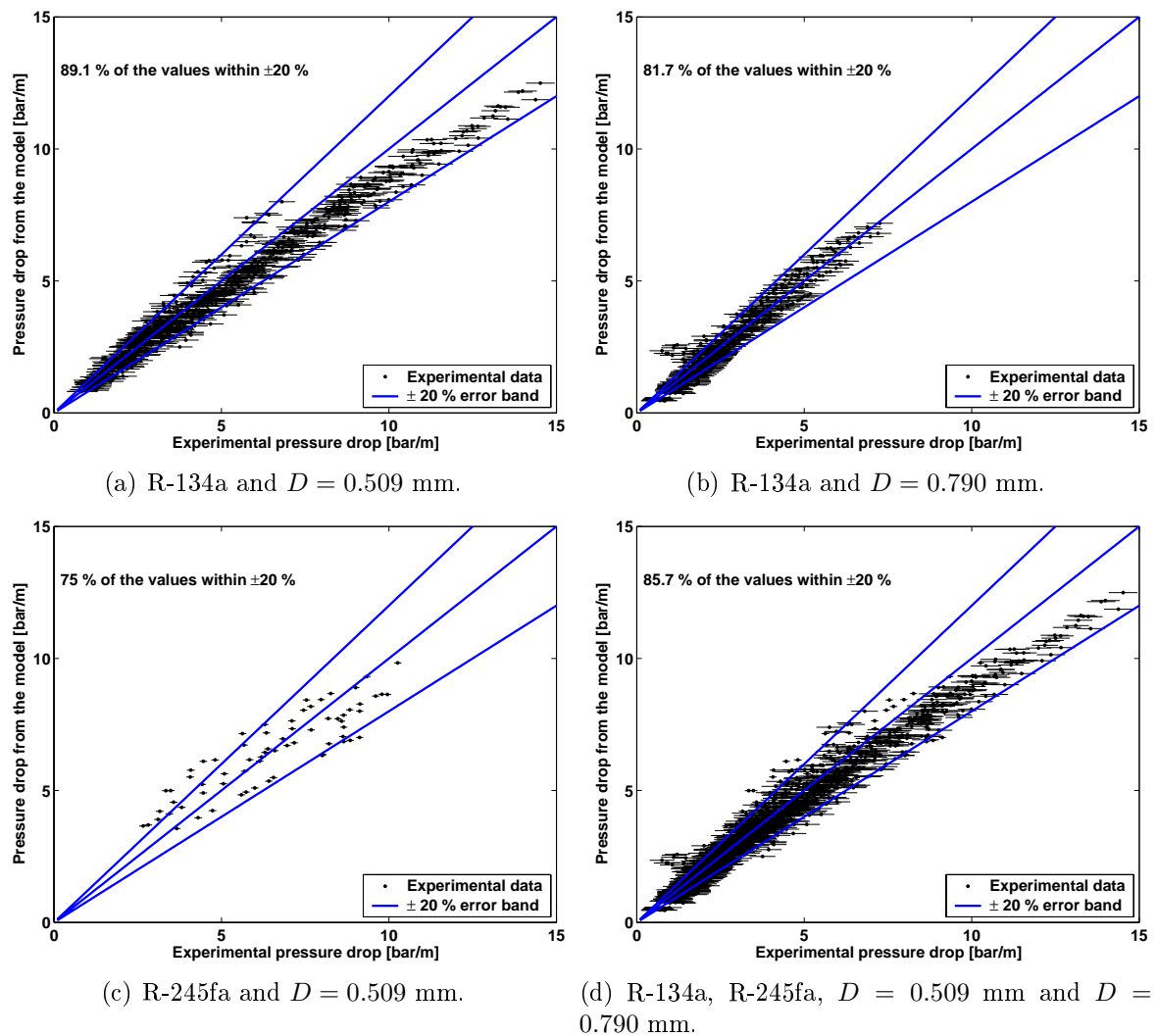
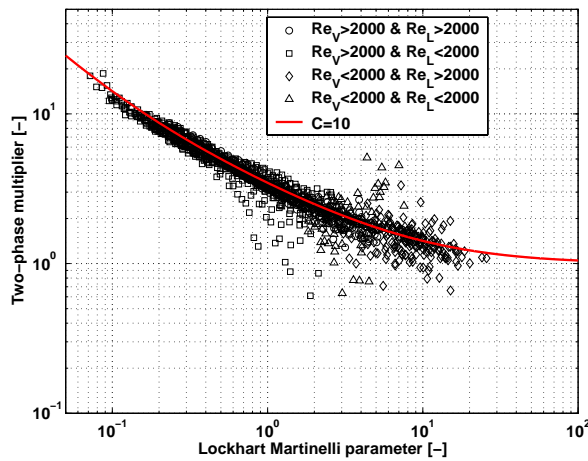
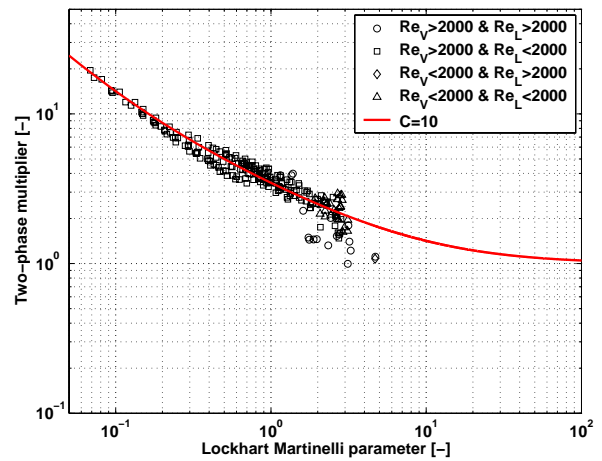
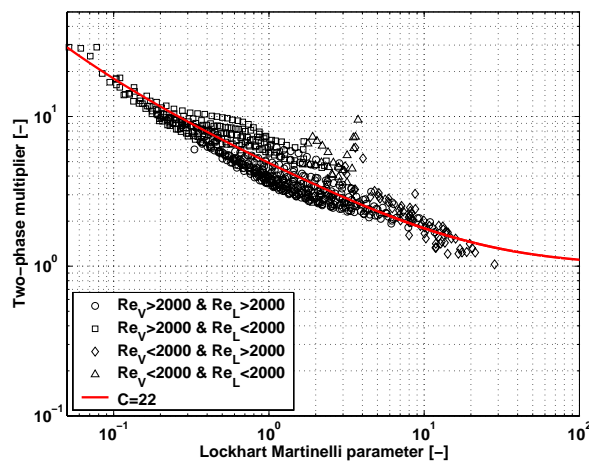


Figure 8.15: Comparison between the experimental data of two-phase frictional pressure drop and the homogeneous model using a new two-phase friction factors for $Re_{TP} \geq 8000$.

(a) R-134a and $D = 0.509$ mm.(b) R-245fa and $D = 0.509$ mm.(c) R-134a and $D = 0.790$ mm.Figure 8.16: Two-phase multiplier versus Martinelli parameter for $Re_{TP} \geq 2000$.

statistics are still poor with only 67.1 % of the data falling in a ± 20 % error band (versus only 22.8 % in Fig. 8.11(b)) against 85.7 % for the modified homogeneous model.

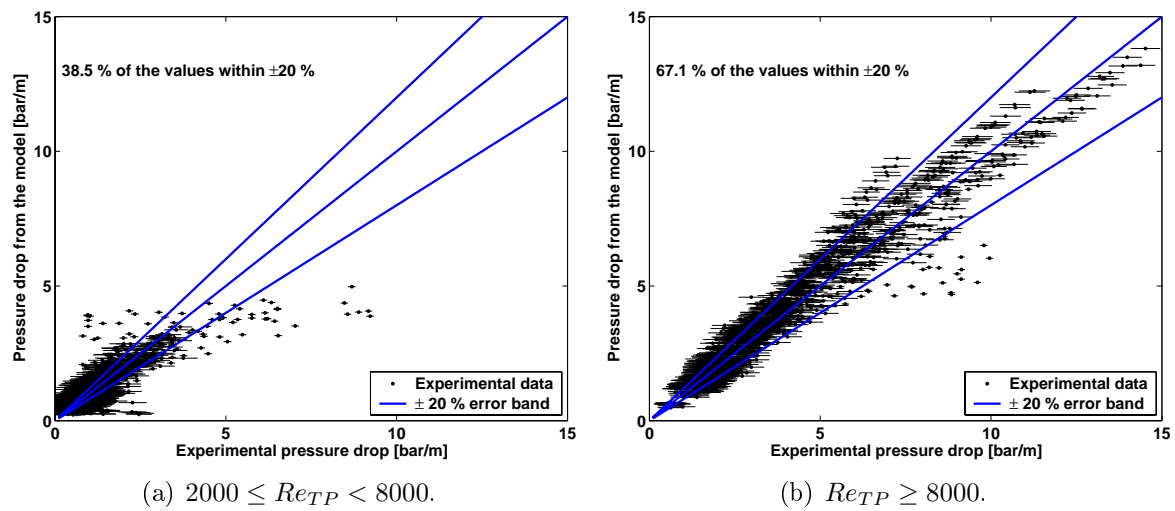


Figure 8.17: Comparison between the experimental data of two-phase frictional pressure drop and the modified Lockhart-Martinelli model.

8.4 Conclusions on the adiabatic two-phase pressure drop

In this study, 2210 experimental two-phase frictional pressure drop data points were taken in 0.790 and 0.509 mm adiabatic glass tubes for R-134a and R-245fa for a wide range of test conditions. The following conclusions can be made here:

- Three zones were distinguishable when regarding to the variation of the pressure drop with the vapor quality or the two-phase friction factor versus the two-phase Reynolds number: a laminar zone for $Re_{TP} < 2000$ (74 data points), a transition zone for $2000 \leq Re_{TP} < 8000$ (936 data points) and a turbulent region for $Re_{TP} \geq 8000$ (1200 data points). An analogy with the single phase friction factor can explain these transitions and trends.
- The laminar zone is actually not taken into account as the gradient for the pressure drop versus vapor quality is negative. This zone corresponds to small instabilities.
- The transition region is not predicted well at all by any of the prediction methods. In the literature, only a few data are available for this region and most methods ignore this region, jumping directly from laminar to turbulent flow at $Re_{TP} = 2000$.
- The turbulent zone can be reasonably well predicted by the Müller-Steinhagen correlation.
- A new prediction method is proposed here using the homogeneous model and determining a new two-phase friction factor f_{TP} for the two different tubes. More than 85.7 % of the data fall in a ± 20 % error band and more than 96 % within ± 30 %. The trend is captured for both diameters and both fluids.

In summary, none of the methods are able to capture the laminar, transition and turbulent trends in the present two-phase friction factors shown in Fig. 8.9, not even the Lockhart-Martinelli method with its different C values for laminar-laminar, turbulent-laminar, laminar-turbulent and turbulent-turbulent combinations in the liquid and vapor phases. Since most methods either ignore the transition regime and laminar regime all together, or jump directly from a laminar to turbulent formulation, it is not surprising that databases containing transition regime data are poorly predicted (as these data are not usually segregated from the database as was done here). Proposing a new prediction method that captures all these three regimes is beyond the time frame of the present project. Also, more laminar data and more accurate measurements at low pressure drops are required to do this.

Chapter 9

Conclusions

Experimental two-phase fluid flow in microchannels (0.509 and 0.790 mm) has been studied. The work and results are summarized below.

1. A new multi purpose microchannel test facility has been built and brought online with computerized data acquisition and control.
2. An optical measurement method has been developed to characterize flow pattern transitions of two-phase flow in microtubes. It consists of shining two microlaser beams through a glass tube and the fluid at two different locations, using two lenses to focus the laser beams to the middle of the microtube, and using two photodiodes to recuperate the intensity of the light, whose signals are used to distinguish whether liquid, vapor or liquid and vapor are present in the cross section. Bubble frequency, percentage of surviving small bubbles, lengths of bubbles and flow pattern transitions are parameters that are able to be determined by this technique. Mean vapor velocity is also calculable from the measurements at some test conditions.
3. Four principal flow patterns (bubbly flow, slug flow, semi-annular flow and annular flow) with their transitions (bubbly/slug flow and slug/semi-annular flow) were observed in the present experiments with R-134a and R-245fa in 0.509 mm and 0.790 mm circular channels. No influence of the liquid subcooling, the microevaporator length, the saturation temperature nor the diameter has been found. Changing the fluid affects the transition lines. A new type of flow pattern map for evaporating flow in microchannel has been developed, in particular a diabatic map as opposed to the adiabatic maps found in the literature. The first zone corresponds to the isolated bubble regime. It includes both bubbly flow or/and slug flow and is present up to the onset of coalescence. The second zone is the coalescing bubble regime. It is present up to the end of coalescence process. The third zone is the annular zone and is limited by the fourth zone of this diabatic map, the onset of critical heat flux. This flow pattern map can be used for heat transfer models and for the design of microevaporators.
4. New accurate CHF data have been measured with the test facility. The experimental data have shown that the parameters dominating CHF are: mass flux, microevaporator length, microchannel internal diameter and thermal properties of the refrigerant. No

influence of the liquid subcooling was found for the small range tested. Based on the experimental data, a new microchannel version of the Katto - Ohno correlation has been developed to predict the CHF in circular, uniformly heated microchannels. The new correlation predicts experimental points with 82.4% of the data falling within a $\pm 15.0\%$ error band. Due to the lack of experimental data for higher reduced pressures and different flow patterns, it is recommended to use this correlation only for $\rho_V/\rho_L < 0.041$ and only when the local condition at the exit is annular flow. Moreover, a new transition curve from annular flow to dryout has been proposed in the new diabatic flow pattern map developed here.

5. The vapor velocity or cross sectional void fraction is dependent on the vapor quality, the mass flux, the saturation temperature and the fluid. The inlet subcooling, the microevaporator length and the diameter were found to have no influence on the results. For R-134a, the flow can be considered as a homogeneous flow as more than 81 % of the data fall within a $\pm 20\%$ error band around the homogeneous void fraction (86 % in $\pm 25\%$). For R-245fa, more tests with some modifications to avoid instabilities have to be performed as the void fractions observed often were above the homogeneous curve.
6. Two-phase pressure drops were measured over a wide range of experimental test conditions in the two sizes of microchannel sight glass tubes for the two refrigerants. Three zones were distinguishable when plotting the variation of the diabatic frictional pressure drop versus the vapor quality or the two-phase friction factor versus the two-phase Reynolds number: a laminar regime for $Re_{TP} < 2000$, a transition regime for $2000 \leq Re_{TP} < 8000$ and a turbulent regime for $Re_{TP} \geq 8000$. An analogy with the single phase friction factor can thus be made. The laminar zone, quite surprisingly, yields a negative gradient for the pressure drop versus vapor quality apparently due to small instabilities in the flow. The transition regime is not predicted well at all by any of the prediction methods for two-phase frictional pressure drops available in the literature. This is not unexpected since only a few data are available for this region in the literature and most methods ignore this regime, jumping directly from laminar to turbulent flow at $Re_{TP} = 2000$. However, the turbulent zone is best predicted by the Müller-Steinhagen correlation. Also, a new homogeneous two-phase frictional pressure drop has been proposed here with a limited range of application.

In summary, an important new database has been created for two-phase fluid flow in microchannels. Numerous prediction methods have been compared to the results obtained here and several new methods have been proposed for predicting:

- * CHF in microchannels
- * Diabatic flow pattern map for microevaporators
- * Microchannel void fractions
- * Two-phase frictional pressure drops in the turbulent regime

However, many questions on two-phase flows in microchannels are still open:

- How to predict the onset of two-phase flow instabilities in microchannels?

- How thin is the liquid film trapped between the wall and the elongated bubbles and how can it be predicted?
- What are the coalescence mechanisms? How does coalescence affect pressure drop in microchannels?
- Where are the transitions between macro, mini and microchannels? What parameters have to be studied to explain the transitions?
- How can the two-phase frictional pressure drops be predicted over the laminar, transition and turbulent two-phase Reynolds number regimes?

All these questions should be investigated in the future to improve the thermal/hydraulic design methods and better understand the phenomena occurring in micro or mini heat exchanger.

Appendix A

Fluid physical properties

Table A.1: R-134a properties.

| Temp [°C] | Pressure [bar] | Density (L) [kg/m ³] | Density (V) [kg/m ³] | Enthalpy (L) [kJ/kg] | Enthalpy (V) [kJ/kg] | Viscosity (L) [μPa-s] | Viscosity (V) [μPa-s] | Surf Tension [N/m] |
|--------------|-------------------|-------------------------------------|-------------------------------------|-------------------------|-------------------------|--------------------------|--------------------------|-----------------------|
| 0 | 2.928 | 1295 | 14.43 | 200 | 398.6 | 271.1 | 10.73 | 0.01156 |
| 5 | 3.497 | 1278 | 17.13 | 206.8 | 401.5 | 254.4 | 10.94 | 0.01084 |
| 10 | 4.146 | 1261 | 20.23 | 213.6 | 404.3 | 238.8 | 11.15 | 0.01014 |
| 15 | 4.884 | 1243 | 23.76 | 220.5 | 407.1 | 224.3 | 11.36 | 0.00944 |
| 20 | 5.717 | 1225 | 27.78 | 227.5 | 409.7 | 210.7 | 11.58 | 0.00876 |
| 25 | 6.654 | 1207 | 32.35 | 234.5 | 412.3 | 197.9 | 11.81 | 0.00808 |
| 30 | 7.702 | 1187 | 37.54 | 241.7 | 414.8 | 185.8 | 12.04 | 0.00742 |
| 35 | 8.87 | 1168 | 43.42 | 249 | 417.2 | 174.3 | 12.29 | 0.00677 |
| 40 | 10.17 | 1147 | 50.09 | 256.4 | 419.4 | 163.4 | 12.55 | 0.00613 |
| 45 | 11.6 | 1125 | 57.66 | 263.9 | 421.5 | 153 | 12.82 | 0.0055 |
| 50 | 13.18 | 1102 | 66.27 | 271.6 | 423.4 | 143.1 | 13.12 | 0.00489 |

Table A.2: R-245fa properties.

| Temp [°C] | Pressure [bar] | Density (L) [kg/m ³] | Density (V) [kg/m ³] | Enthalpy (L) [kJ/kg] | Enthalpy (V) [kJ/kg] | Viscosity (L) [μPa-s] | Viscosity (V) [μPa-s] | Surf Tension [N/m] |
|--------------|-------------------|-------------------------------------|-------------------------------------|-------------------------|-------------------------|--------------------------|--------------------------|-----------------------|
| 0 | 0.5359 | 1404 | 3.251 | 200 | 404.9 | 581.6 | 9.465 | 0.01725 |
| 5 | 0.6698 | 1391 | 4.01 | 206.5 | 408.7 | 537.7 | 9.64 | 0.01661 |
| 10 | 0.8293 | 1378 | 4.903 | 213.1 | 412.5 | 498.5 | 9.814 | 0.01597 |
| 15 | 1.018 | 1365 | 5.946 | 219.7 | 416.4 | 463.3 | 9.989 | 0.01533 |
| 20 | 1.238 | 1352 | 7.157 | 226.4 | 420.2 | 431.5 | 10.16 | 0.01469 |
| 25 | 1.494 | 1339 | 8.555 | 233.2 | 424.1 | 402.7 | 10.34 | 0.01405 |
| 30 | 1.79 | 1325 | 10.16 | 240.1 | 427.9 | 376.4 | 10.51 | 0.01341 |
| 35 | 2.13 | 1311 | 11.99 | 247 | 431.8 | 352.3 | 10.69 | 0.01277 |
| 40 | 2.518 | 1297 | 14.08 | 254 | 435.7 | 330.1 | 10.87 | 0.01213 |
| 45 | 2.958 | 1282 | 16.44 | 261 | 439.6 | 309.7 | 11.05 | 0.01149 |
| 50 | 3.454 | 1268 | 19.11 | 268.2 | 443.4 | 290.8 | 11.23 | 0.01085 |

Bibliography

- [1] Verein Deutscher Ingenieure VDI-Wärmeatlas (VDI Heat Atlas), chapter HBB, VDI-Gesellschaft Verfahrenstechnik und Chemieingenieurwesen (GVC). Düsseldorf, 1993.
- [2] B. Agostini and A. Bontemps. Vertical flow boiling of refrigerant R-134a in small channels. *intjhf*, 26:296–306, 2005.
- [3] M. I. Ali, M. Sadatomi, and M. Kawaji. Two-phase flow in narrow channels between two flat plates. *Can. J. Chem. Eng.*, 71:657–666, 1993.
- [4] A. A. Armand and G. G. Treschev. The resistance during the movement of a two-phase system in horizontal pipes. *Izv Vses Teplotek Inst 1*, pages 16–23, 1946.
- [5] D. Butterworth. A comparison of some void fraction relationships for co-current gas-liquid flow. *Int. J. Multiphase Flow*, 1:845–850, 1975.
- [6] A. Cavallini, D. D. Col, L. Doretti, M. Matkovic, L. Rossetto, and C. Zilio. Two-phase frictional pressure gradient of R-236ea, R-134a and R-410a inside multi-port minichannels. *Exp. Thermal Fluid Sci.*, 29:861–870, 2005.
- [7] B. Chexal, M. Merilo, J. Maulbetsch, J. Horowitz, J. C. Harrison, J. W. C. Peterson, W. Kastner, and H. Schmidt. Void fraction technology for design and analysis. In *Electric power institute*, Palo Alto, CA, 1997.
- [8] A. Chiccitti, C. Lombardi, M. Silvestri, G. Soldaini, and R. Zavattarelli. Two-phase cooling experiments-pressure drop, heat transfer and burnout measurements. *Energia Nucleare*, 7(6):407–425, 1960.
- [9] D. Chisholm. Pressure gradients due to friction during the flow of evaporating two-phase mixtures in smooth tubes and channels. *Int. J. Heat Mass Transfer*, 16:347–348, 1973.
- [10] P. M. Y. Chung and M. Kawaji. The effect of channel diameter on diabatic two-phase flow characteristics in microchannels. *Int. J. Multiphase Flow*, 30:735–761, 2004.
- [11] J. W. Coleman and S. Garimella. Characterization of two-phase flow patterns in small diameter round and rectangular tubes. *Int. J. Heat Mass Transfer*, 42:2869–2881, 1999.
- [12] J. W. Coleman and S. Garimella. Two-phase flow regime transitions in microchannel tubes: the effect of hydraulic diameter. In *Proceedings of the ASME Heat Transfer Division*, volume 4, pages 71–83, 2000.

- [13] J. W. Coleman and S. Garimella. Visualization of refrigerant two-phase flow during condensation. In *Proceedings of the NHTC'00: 34th National Heat Transfer Conference*, pages 523–536, Pittsburgh, Pennsylvania, August 20-22, 2000.
- [14] J. G. Collier and J. R. Thome. *Convective boiling and condensation, third edition*. Oxford University Press, Oxford, 1994.
- [15] K. Cornwell and P. A. Kew. Boiling in small channels. In P. Pilavachi, editor, *Proceedings of CEC Conference on Energy Efficiency in Process Technology*, pages 624–638, Athens, Greece, 1992. Elsevier.
- [16] K. Cornwell and P. A. Kew. Evaporation in microchannel heat exchangers. In *Proceedings 4th U.K. National Conference on Heat Transfer*, pages 289–294, Manchester, U.K., 1995.
- [17] C. A. Damianides and J. M. Westwater. Two-phase flow patterns in a compact heat exchanger and in small tubes. In *Proceedings 2nd U.K. National Conference On Heat Transfer*, volume 2, pages 1257–1268, Glasgow, Scotland, 1988.
- [18] A. E. Dukler, M. Wicks, and R. G. Cleveland. Pressure drop and hold-up in two-phase flow part A—a comparison of existing correlations and part B—an approach through similarity analysis. *AIChE Journal*, 10(1):38–51, 1964.
- [19] V. Dupont, J. R. Thome, and A. M. Jacobi. Heat transfer model for evaporation in microchannels. part 2: comparison with the database. *Int. J. Heat Mass Transfer*, 47:3387–3401, 2004.
- [20] L. Friedel. Improved friction pressure drop correlations for horizontal and vertical two-phase pipe flow. In *European Two-Phase Flow Group Meeting*, Ispra, Italy, 1979. Paper E2.
- [21] W. R. Gambill and J. H. Lienhard. An upper bound for the critical boiling heat flux. *J. Heat Transfer*, 11:815–818, 1989.
- [22] S. Garimella, J. D. Killion, and J. W. Coleman. An experimental validated model for two-phase pressure drop in the intermittent flow regime for circular channel. *J. of Fluid Engineering*, 124:205–214, 2002.
- [23] N. Kattan, J. R. Thome, and D. Favrat. Flow boiling in horizontal tubes: Part 1—development of a diabatic two-phase flow pattern map. *J. Heat Transfer*, 120:140–147, 1998.
- [24] Y. Katto and S. Ashida. CHF in high pressure regime for forced convection boiling in uniformly heated vertical tube of low length-to-diameter-ratio. In *Proceedings 7th Int. Heat Transfer Conf.*, volume 4, pages 291–296, 1982.
- [25] Y. Katto and H. Ohno. An improved version of the generalized correlation of critical heat flux for the forced convective boiling in uniformly heated vertical tubes. *Int. J. Heat Mass Transfer*, 27(9):1641–1648, 1984.

- [26] Y. Katto and S. Yokoya. CHF of forced convection boiling in uniformly heated vertical tubes, experimental study of hp-regime by the use of R12. *Int. J. Multiphase Flow*, 8:165–181, 1982.
- [27] Y. Katto and S. Yokoya. Critical heat flux of liquid helium (i) in forced convective boiling. *Int. J. Multiphase Flow*, 10:401–413, 1984.
- [28] A. Kawahara, P. M. Y. Chung, and M. Kawaji. Investigation of flow pattern, void fraction and pressure drop in a microchannel. *Int. J. Multiphase Flow*, 28:1411–1435, 2002.
- [29] A. Kawahara, M. Sadatomi, K. Okayama, M. Kawaji, and P. M. Y. Chung. Effects of channel diameter and liquid properties on void fraction in adiabatic two-phase flow through microchannels. *Heat Transfer Engineering*, 26(3):13–19, 2005.
- [30] P. A. Kew and K. Cornwell. Correlations for the prediction of boiling heat transfer in small-diameter channels. *Applied Thermal Engineering*, 17:705–715, 1997.
- [31] K. Kuwahara, S. Koyama, J. Yu, C. Watanabe, and N. Osa. Flow pattern of pure refrigerant hfc134a evaporating in a horizontal capillary tube. In *Proceedings of the symposium of Energy Engineering in the 21st Century*, volume 2, pages 445–450, Hong Kong, 2000. Begell House.
- [32] H. J. Lee and S. Y. Lee. Pressure drop correlations for two-phase flow within horizontal rectangular channels with small heights. *Int. J. Multiphase Flow*, 27:783–796, 2001.
- [33] J. Lee and I. Mudawar. Two-phase flow in high heat flux microchannel heat sink for refrigeration cooling applications: Part i-pressure drop characteristics. *Int. J. Heat Mass Transfer*, 48:928–940, 2005.
- [34] R. C. Lockhart and R. W. Martinelli. Proposed correlation of data for isothermal two-phase, two component flow in pipes. *Chemical Engineering Progress*, 45:39–48, 1949.
- [35] D. C. Lowe and K. S. Rezkallah. Flow regime identification in microgravity two-phase flows using void fraction signals. *Int. J. Multiphase Flow*, 25:433–457, 1999.
- [36] W. H. McAdams, W. K. Woods, and R. L. Bryan. Vaporization inside horizontal tubes-ii-benzene-oil mixtures. *Trans. ASME*, 64:193, 1942.
- [37] R. Mertz, A. Wein, and M. Groll. Experimental investigation of flow boiling heat transfer in narrow channels. *Calore e Tecnologia*, 14:47–54, 1996.
- [38] K. Mishima and T. Hibiki. Some characteristics of air-water flow in small diameter vertical tubes. *Int. J. Multiphase Flow*, 22:703–712, 1996.
- [39] H. Muller-Steinhagen and K. Heck. A simple friction pressure drop correlation for two-phase flow pipes. *Cem. Eng. Process.*, 20:297–308, 1986.
- [40] A. Premoli, D. Fransesco, and A. Prina. A dimensionless correlation for determining the density of two-phase mixtures. *Lo Termotecnica*, 25:17–26, 1971.

- [41] D. J. Pribyl, A. Bar-Cohen, and A. E. Bergles. An investigation of critical heat flux and two-phase flow regimes for upward steam and water flow. In *Proceedings of the 5th international conference in boiling heat transfer*, Jamaica, May 4-8, 2003.
- [42] W. Qu and I. Mudawar. Measurement and correlation of critical heat flux in two-phase microchannel heat sinks. *Int. J. Heat Mass Transfer*, 47:2045–2059, 2004.
- [43] S. Z. Rouhani and E. Axelsson. Calculation of volume void fraction in subcooled and quality region. *Int. J. Heat Mass Transfer*, 13:383–393, 1970.
- [44] A. Serizawa, Z. Feng, and Z. Kawara. Two-phase flow in microchannels. *Exp. Thermal Fluid Sci.*, 26:703–714, 2002.
- [45] C. H. Sheng and B. Palm. The visualization of boiling in small-diameter tubes. In *Heat Transport and Transport Phenomena in Microsystems*, Banff, 2001.
- [46] M. E. Steinke and S. G. Kandlikar. Flow boiling and pressure drop in parallel flow microchannels. In *1st International Conference on Microchannels and Minichannels*, pages 1–12, Rochester, U.S., 2003.
- [47] M. Suo and P. Griffith. Two-phase flow in capillary tubes. *J. Basic Engineering*, pages 576–582, 1964.
- [48] Y. Taitel and A. E. Dukler. A model for predicting flow regime transitions in horizontal and near horizontal gas-liquid flow. *AIChE Journal*, 22(1):47–55, 1976.
- [49] J. Taylor. *Incertitudes et analyse des erreurs dans les mesures physiques*. Dunod, 2000.
- [50] J. R. Thome. Boiling in microchannels: a review of experiment and theory. *Int. J. Heat Fluid Flow*, 25:128–139, 2004.
- [51] J. R. Thome, V. Dupont, and A. M. Jacobi. Heat transfer model for evaporation in microchannels. part 1: presentation of the model. *Int. J. Heat Mass Transfer*, 47:3375–3385, 2004.
- [52] T. N. Tran, M. C. Chyu, M. W. Wambsganss, and D. M. France. Two-phase pressure drop of refrigerants during flow boiling in small channels: an experimental investigation and correlation development. *Int. J. Multiphase Flow*, 26:1739–1754, 2000.
- [53] K. A. Triplett, S. M. Ghiaasiaan, S. I. Abdel-Khalik, A. LeMouel, and B. N. McCord. Gas-liquid two-phase flow in microchannels part ii : void fraction and pressure drop. *Int. J. Multiphase Flow*, 25:395–410, 1999.
- [54] K. A. Triplett, S. M. Ghiaasiaan, S. I. Abdel-Khalik, and D. L. Sadowski. Gas-liquid two-phase flow in microchannels part i : two-phase flow patterns. *Int. J. Multiphase Flow*, 25:377–394, 1999.
- [55] T. Ursenbacher. *Traitement de Vélocimétrie par images digitales de particules par une technique robuste de distorsion d'images*. PhD thesis, Ecole polytechnique Fédérale de Lausanne, 2000.

- [56] L. Wojtan, T. Ursenbacher, and J. R. Thome. Technique for measurement of void fraction in horizontal tubes. In *3rd Conference on Enhancement Technology for the Process Industries*, Davos, Switzerland, 2001.
- [57] C. Y. Yang and C. C. Shieh. Flow pattern of air-water and two-phase r-134a in small circular tubes. *Int. J. Multiphase Flow*, 27:1163–1177, 2001.
- [58] M. Zhang and R. L. Webb. Correlation of two-phase friction for refrigerants in small-diameter tubes. *Exp. Thermal Fluid Sci.*, 25:131–139, 2001.
- [59] N. Zuber and J. A. Findlay. Average volumetric concentration in two-phase flow systems. *J. Heat Transfer*, 87:463–458, 1965.
- [60] N. Zuber, F. W. Staub, G. Bijwaard, and P. G. Kroeger. Steady state and transient void fraction in two-phase flow systems. *GEAP 5417*, 1967.

Curriculum vitae

PERSONAL DATA:

Name: Rémi Revellin
Date of Birth: 23.01.1978
Birthplace: Lyon, France
Nationality: French

EDUCATION:

2002-2005 PhD-Student at the Laboratory of Heat and Mass Transfer at the EPFL (Swiss Federal Institute of Technology) Lausanne Switzerland, under the Direction of Professor J.R. Thome.
Main Research Interests: Two-Phase Flow, Critical Heat Flux, Pressure Drops, Microchannels.

1996-2002 MSc in Energetics and Environmental Engineering at INSA (National Institute of Applied Sciences) Lyon, France.
Master Thesis Title: "Modélisation d'un Dissipateur Thermique pour le Refroidissement de Composants Electroniques"

1993-1996 A-levels (Baccalauréat) with honours (grade A) in Maths, Physics and Chemistry, Lycée Charlie Chaplin, Décines, France.

Publications

Articles

R. Revellin, V. Dupont, J.R. Thome, I. Zun. Characterization of two-phase flows in microchannels: optical measurement technique and flow parameter results for R-134a in a 0.5 mm channel. *Submitted at the International Journal of Multiphase Flow in September 2005.*

R. Revellin, J.R. Thome. Experimental investigation of R-134a and R-245fa two-phase flow in microchannels for different flow conditions. *Submitted at the International Journal of Experimental Thermal and Fluid Science in October 2005.*

L. Wojtan, R. Revellin, J.R. Thome. Investigation of critical heat flux in single, uniformly heated microchannels. *Submitted at the International Journal of Experimental Thermal and Fluid Science in October 2005.*

Conferences

R. Revellin, J.R. Thome. Experimental investigation of R-134a and R-245fa two-phase flow in microchannels for different flow conditions. *ECI International Conference on Heat Transfer and Fluid Flow in Microscale, Castelvecchio Pascoli (Italy), 25-30 September 2005.*

L. Wojtan, R. Revellin, J.R. Thome. Investigation of critical heat flux in single, uniformly heated microchannels. *ECI International Conference on Heat Transfer and Fluid Flow in Microscale, Castelvecchio Pascoli (Italy), 25-30 September 2005.*

R. Revellin, J.R. Thome. Optical investigation of R-134a two-phase flows in a microchannel. *Thermophysical Properties and Transfer Processes of Refrigerants, Vicenza (Italy), 31 August-2 September 2005.*

R. Revellin, J.R. Thome. New diabatic flow pattern map for evaporating flows in microchannels. *International Heat Transfer Conference, Sydney (Australia), 13-18 August 2006.*